

**Phase Behavior and Ordering Kinetics of Block Copolymers  
in Solution During Solvent Removal**

Michael J. Heinzer, Jr.

Dissertation submitted to the Faculty of  
Virginia Polytechnic Institute and State University  
in partial fulfillment of the requirements for the degree of  
DOCTOR OF PHILOSOPHY  
in  
Chemical Engineering

Donald G. Baird, Chairman

Richey M. Davis

Stephen M. Martin

James E. McGrath

August 25, 2011  
Blacksburg, VA

Keywords: copolymer, rheology, SAXS, ordering kinetics, solution-cast films

# **Phase Behavior and Ordering Kinetics of Block Copolymers in Solution During Solvent Removal**

**Michael J. Heinzer Jr.**

## **Abstract**

This dissertation is part of an effort to understand and to facilitate the modeling of the ordering kinetics of block copolymers in solution during the extraction of solvent from a solution-cast film. Central to this work was determining a suitable method for measuring the ordering kinetics during solvent removal and being able to interpret the measurements in terms of structure development. It was also necessary to assess a model for quantifying the ordering kinetics to use in conjunction with a mass transfer model to predict structure formation during solvent extraction.

Changes in the dynamic mechanical response (DMR) over time of block copolymer solutions at fixed concentrations following solvent removal were explored as a means to track the growth of ordered domains. It was found that DMR measurements performed following solvent extraction were sensitive to the nucleation and growth process of the phase separation process over a wide range of concentrations, beginning near the order-disorder transition concentration. Based on complimentary small angle X-ray measurements, it was determined that the changes in the DMR are caused by the development of individual microstructures. The SAXS experiments also indicated that the DMR is insensitive to late stages of the growth process. Ultimately, DMR measurements under-predicted the ordering times at several concentrations and did not detect ordering at concentrations above which SAXS data indicated ordering was still occurring.

The ability to use the parallel and series rules of mixtures for determining  $\phi(t)$  in conjunction with the Avrami equation to quantitatively model the ordering kinetics was also determined. These models allowed the ordering kinetics during solvent removal to be qualitatively analyzed. However, using the two different rules of mixtures resulted in a wide range of possible ordering times for a given copolymer concentration, making these approximations unsuitable for modeling a real solvent extraction process. Further, the parameters of the model were insensitive to the type of microstructures developing.

As a continuation of this work, a new apparatus to track block copolymer ordering *in situ* during solvent extraction was designed. Experiments using the apparatus allowed the ordering kinetics and domain dimensions as a function of concentration to be monitored in real-time under several solvent removal conditions. These experiments study the ordering kinetics in a manner more akin to real processing conditions and will allow future assessment of the ability of iso-concentration ordering kinetics to predict phase separation during film processing.

## Acknowledgements

I would like to thank Dr. Donald G. Baird for his constant support and guidance throughout the duration of this project, which has made the completion of this dissertation possible. I would also like to extend gratitude to Dr. Stephen M. Martin, whose valuable advice regarding the research and support of many aspects of this work was critical to the success of this dissertation. In addition, I would like to thank my remaining committee members for guidance and much appreciated input: Dr. James E. McGrath and Dr. Richey M. Davis.

I also thank the following people who have, in some capacity, impacted my life and helped in the achievement of my goals:

- My parents, for their constant support and encouragement that kept me believing in myself through this entire process
- My sisters, Elizabeth and Kathryn
- My grandparents, Joe & Irene Koczeniak and Charles & Pam Heinzer
- All my aunts, uncles and cousins
- The Von Hollen family
- Adam, Lindsay, CD, and Lucy for their valued friendship while here at Virginia Tech
- Past and present members of the Polymer Processing lab including: Kevin O., Chen, Gregorio, Chris M., Myoungbae, Aaron, Desmond, Chris S., Dave, Kevin M., and John.
- Sam, Roey, Ralph, Brian, Scott, Jen, Laura, Shally
- Members of the Chemical Engineering Department, especially: Dr. Walz, Diane, Tina, Jane, Nora, Mike Vaught, and Riley Chan

## **Original Contributions**

The following are considered original and significant contributions to this research:

- Experiments to track the iso-concentration ordering kinetics of a block copolymer solution following solvent removal using dynamic mechanical testing previously developed in our lab were followed in this work. These experiments tracked ordering kinetics following concentration quenches through the order-disorder concentration, as opposed to the temperature quenches commonly performed in literature. The following improvements were made to the experimental procedures:
  - Using thinner samples and increasing the initial concentration of the solution, the solvent removal time was reduced from eight hours to 30 to 45 minutes, allowing early stages of ordering to be measured and more accurate predictions of the ordering time to be made.
  - The thinner samples and faster solvent removal required improvements to be made to the solvent trap system. These modifications prevented solvent loss over a longer time period than could previously be achieved. This allowed the ordering kinetics to be monitored over a longer time than realized before.
- Small angle X-ray scattering experiments that paralleled the DMR experiments were designed and carried out. These experiments were novel in the way in which the study of ordering kinetics was approached (concentration quenches). These were also the first experiments conducted in this lab to compliment the DMR measurements and to determine the phase behavior of the model block copolymer systems used in this work.

- A cell capable of simultaneously monitoring solvent loss from a block copolymer film and tracking the phase separation of the copolymer using SAXS was designed and fabricated. Experiments allowing the ordering kinetics to be studied under different solvent removal conditions were designed and carried out using the cell. Meaningful data normalization and analysis was also determined as it pertains to ordered structure development. To the author's knowledge, these are the first such *in situ* measurements of the ordering kinetics of block copolymer solutions during solvent removal.

### **Format of Dissertation**

This dissertation is written in journal format. Chapters 3, 4 and 5 are self-contained papers that have been submitted for journal publication. Pertinent details regarding the experiments, results and conclusions are separately described in each paper. With the exception of the literature review (Chapter 2) and recommendations (Chapter 6), all figures and tables referenced in a chapter are provided following the reference section of the respective chapter.

## Table of Contents

1.0 Introduction.....	1
1.1 Project Background and Research Objectives.....	2
1.2 References.....	13
2.0 Literature Review.....	17
2.1 Block Copolymers.....	18
2.1.1 Block Copolymer Melt Phase Behavior.....	19
2.1.1.1 Thermodynamics of Phase Separation.....	19
2.1.1.2 Melt Phase Morphologies.....	21
2.1.1.3 Weak Segregation Limit.....	23
2.1.1.4 Intermediate Segregation Limit.....	25
2.1.1.5 Strong Segregation Limit.....	25
2.1.2 Block Copolymers in Solution.....	26
2.1.2.1 Dilute Solutions.....	27
2.1.2.2 The Dilution Approximation and Theoretical Phase Diagrams....	30
2.1.2.3 Experimental Styrenic Block Copolymer Phase Diagrams.....	31
2.1.2.4 Experimental Pluronic Phase Diagrams.....	36
2.2 Ordering Kinetics.....	38
2.2.1 Structure factor and small angle X-ray scattering (SAXS).....	39
2.2.2 Rheology of Block Copolymers.....	41
2.2.3 Free Energy Diagrams.....	46
2.2.4 Nucleation and Growth.....	49
2.2.5 The Avrami Equation.....	53

2.2.5.1	Original Avrami Equation.....	53
2.2.5.2	Extension of the Avrami Equation to Polymer Systems.....	57
2.2.6	Spinodal Decomposition.....	59
2.2.7	Order-Disorder Kinetics.....	60
2.2.8	Order-Order Kinetics.....	65
2.3	Solution-cast Block Copolymer Films.....	67
2.3.1	Solution-casting.....	68
2.3.2	Modeling Film Drying.....	72
2.3.3	Processing Conditions Affecting Film Morphology.....	84
2.4	References.....	91
3.0	Iso-concentration Ordering Kinetics Of Block Copolymers In Solution During Solvent Extraction Using Dynamic Oscillatory Measurements.....	100
3.1	Abstract.....	101
3.2	Introduction.....	102
3.3	Experimental.....	106
3.3.1	Materials.....	106
3.3.2	Solution Preparation.....	107
3.3.3	Equilibrium SAXS Measurements.....	107
3.3.4	Iso-concentration Rheology Measurements.....	107
3.3.5	Iso-concentration SAXS Measurements.....	108
3.4	Results and Discussion.....	109
3.4.1	Phase Behavior.....	109
3.4.2	Rheology of Ordering SB/toluene Solutions.....	110
3.4.3	Small Angle X-ray Scattering Measurements.....	115

3.4.4	Avrami fitting.....	117
3.4.5	Effect of microstructure on Avrami exponent.....	124
3.5	Conclusions.....	125
3.6	Acknowledgements.....	127
3.7	References.....	127
4.0	In situ Tracking of Domain Growth During the Drying of Solution-cast Block Copolymer Films Using Small Angle X-Ray Scattering, Part I: Ordering Kinetics.....	144
4.1	Abstract.....	145
4.2	Introduction.....	146
4.3	Experimental.....	151
4.3.1	Materials.....	151
4.3.2	Solution Preparation.....	151
4.3.3	Scattering Cell.....	151
4.3.4	In situ SAXS Experiments.....	152
4.4	Results and Discussion.....	153
4.4.1	Phase behavior.....	153
4.4.2	Ordering kinetics during solvent removal under ambient conditions.....	153
4.4.3	Effect of drying temperature on ordering.....	156
4.4.3.1	Drying curves.....	156
4.4.3.2	Ordering Kinetics.....	157
4.4.4	Effect of sweep gas on ordering kinetics.....	160
4.4.4.1	Drying Curves.....	160
4.4.4.2	Ordering Kinetics.....	161

4.5	Conclusions.....	163
4.6	Acknowledgements.....	164
4.7	References.....	164
5.0	In situ Tracking of Domain Growth During the Drying of Solution-cast Block Copolymer Films Using Small Angle X-Ray Scattering, Part II: Domain Dimensions.....	182
5.1	Abstract.....	183
5.2	Introduction.....	184
5.3	Experimental.....	186
5.3.1	Materials.....	186
5.3.2	Solution Preparation.....	186
5.3.3	Scattering Cell.....	187
5.3.4	In situ SAXS Experiments.....	188
5.4	Results and Discussion.....	188
5.4.1	Peak-splitting.....	188
5.4.2	Effect of solvent removal temperature on Bragg spacing.....	190
5.4.3	Effect of drying rate on Bragg spacing.....	194
5.5	Conclusions.....	198
5.6	Acknowledgements.....	199
5.7	References.....	199
6.0	Conclusions & Recommendations.....	211
6.1	Conclusions.....	212
6.2	Recommendations.....	214
6.2.1	Materials Considerations.....	214

6.2.1.1	Synthesis of block copolymers.....	214
6.2.1.2	Selective solvents.....	214
6.2.2	Experimental Considerations.....	217
6.2.2.1	Transmission in situ Small Angle X-ray Scattering (SAXS)	
Experiments.....		217
6.2.2.2	Porous Plate Rheometer.....	217
6.2.2.3	Steady Shear Rheology Experiments.....	220
6.2.2.4	Polarized Optical Microscopy.....	221
6.2.3	References.....	223
Appendix A: Dynamic Mechanical Data.....		225
A.1	Poly(styrene- <i>b</i> -butadiene) in toluene Linear Viscoelasticity.....	226
A.2	Poly(styrene) homopolymer in toluene (25 wt% polymer).....	227
A.3	Dynamic Mechanical Data - Poly(styrene- <i>b</i> -butadiene) in toluene.....	228
A.4	Dynamic Mechanical Data - Poly(styrene- <i>b</i> -isoprene- <i>b</i> -isoprene) in toluene.....	260
Appendix B: Small Angle X-ray Scattering Data.....		263
B.1	SB / toluene Solution Equilibrium Scattering Profiles.....	264
B.2	SIS / toluene Solution Scattering Profiles.....	267
B.3	Lorentz Correction & Integration of Primary Scattering Profile Peaks.....	271
B.4	Iso-concentration SAXS Integrated Intensity vs time data for SB/toluene solution.....	273

B.5 In situ SAXS data – SB in toluene.....	278
Appendix C: Kinetics Data.....	284
C.1 Iso-concentration SB copolymer in toluene Avrami fits from DMR data .....	285
C.2 Iso-concentration SIS copolymer in toluene Avrami fits from DMR data.....	328
C.3 Iso-concentration SB copolymer in toluene Avrami fits from SAXS data .....	334

## List of Figures

### Chapter 1

- Figure 1.1-1 The four classic equilibrium block copolymer melt morphologies (Lamella (L), hexagonally-packed cylinders (C), spheres (S), and gyroid (G)). [Matsen, 1997]. Reprinted with permission from Matsen, M.W.; Bates, F.S. *J. Chem. Phys.* **1997**, *106*, 2436. Copyright 1997, American Institute of Physics.....3
- Figure 1.2-1 Block copolymer melt phase diagram based on mean-field theory [Matsen, 1997]. The microstructures represented are: close-packed spheres ( $S_{CP}$ ), hexagonally-packed cylinders (C), lamella (L), spheres (S) and gyroid (G). Reprinted with permission from Matsen, M.W.; Bates, F.S. *J. Chem. Phys.* **1997**, *106*, 2436. Copyright 1997, American Institute of Physics.....5

### Chapter 2

- Figure 2.1-1 Conventional block copolymer topologies. Reproduced from [Hamley, 2004].....18
- Figure 2.1-2 Stable equilibrium structures for block copolymer melts, Lamellae (L), Gyroid (G), hexagonally-packed cylinders (C), and spheres (S), and metastable complex structure, perforated lamellae (PL). Reprinted with permission from Matsen, M.W.; Bates, F.S. *J. Chem. Phys.* **1997**, *106*, 2436. Copyright 1997, American Institute of Physics.....21
- Figure 2.1-3 Theoretical phase diagram based on self-consistent mean field theory calculations [Matsen, 1997]. Reprinted with permission from Matsen, M.W.; Bates, F.S. *J. Chem. Phys.* **1997**, *106*, 2436. Copyright 1997, American Institute of Physics.....22
- Figure 2.1-4 Concentration profiles (upper panel) and segregation patterns of diblock copolymer melts in the three segregation limits: weak (WSL), intermediate (ISR) and strong (SSL). Reprinted with permission from Rosedale, J.H.; Bates, F.S.; Almdal, K.; Mortensen, K.; Wignall, G.D. *Macromolecules* **1995**, *28*, 1429. Copyright 1995 American Chemical Society.....24
- Figure 2.1-5 Spherical micelle structure comprised of a core of insoluble blocks and a corona of soluble blocks.  $R_c$  is the core radius;  $R_m$  is the micelle radius;  $\xi$  is the blob size. Reprinted with permission from Cogan, K.A.; Gast, A.P.; Capel, M. *Macromolecules* **1991**, *24*, 6512. Copyright 1991 American Chemical Society.....28

Figure 2.1-6	Phase diagram of poly(ethylene oxide) – poly(propylene oxide) (EO <sub>27</sub> -PO <sub>39</sub> -EO <sub>27</sub> ) aqueous solution at dilute, micelle-forming concentrations. Reprinted with permission from Glatter, O.; Scherf, G.; Scillén, K.; Brown, W. <i>Macromolecules</i> <b>1994</b> , 27, 6046. Copyright 1994 American Chemical Society.....29
Figure 2.1-7	Phase diagrams of poly(styrene- <i>b</i> -isoprene) (SI(11-32)) in a) DOP, b) DBP, and c) DEP. Solvent selectivity increases progressing from a to c. DOP is neutral and DBP and DEP are selective for styrene. Reprinted with permission from Lodge, T.P.; Pudil, B.; Hanley, K.J. <i>Macromolecules</i> <b>2002</b> , 35, 4707. Copyright 2002 American Chemical Society.....33
Figure 2.1-8	Phase diagram for Pluronic P65 ((EO) <sub>20</sub> (PO) <sub>30</sub> (EO) <sub>20</sub> ) in water. Reprinted with permission from Wanka, G.; Hoffman, H.; Ulbricht, W. <i>Macromolecules</i> <b>1994</b> , 27, 4145. Copyright 1994 American Chemical Society.....37
Figure 2.2-1	Free energy profiles at various temperatures relative to the order-disorder transition temperature. T <sub>0</sub> is the stable, disordered region, T <sub>1</sub> is the metastable region, and T <sub>2</sub> is the unstable region. Reproduced from [Chaikin, 1995].....47
Figure 2.2-2	Stability regions of the phase diagram as a function of system composition and interaction parameter, $\chi$ . The stable, metastable, and unstable regions correspond to the free energy profiles provided in Figure 2.2-1. Reproduced from [Jones, 2002].....48
Figure 2.2-3	Theoretical crystallization curves based on the Avrami equation for various Avrami exponent values. Reproduced from [Mandelkern, 2002].....55
Figure 2.2-4	Integrated peak intensity obtained by SAXS as a function of time for an ordering block copolymer (poly(styrene- <i>b</i> -isoprene)) melt. Reprinted with permission from Schuler, M.; Stuehn, B. <i>Macromolecules</i> <b>1993</b> , 26, 112. Copyright 1993 American Chemical Society.....62
Figure 2.2-5	Dynamic mechanical response during the ordering of a star copolymer comprised of polystyrene and polyisoprene at various temperatures following temperature quenches. Reprinted with permission from Floudas, G.; Hadjichristidis, N.; Iatrou, H.; Pakula, T.; Fischer, E.W. <i>Macromolecules</i> <b>1994</b> , 27, 7735. Copyright 1994 American Chemical Society.....62
Figure 2.3-1	Schematic of drying of coated film on impermeable substrate by forced convection. Image reproduced from Kim et al. [1998].....72
Figure 2.3-2	Film / substrate system and corresponding mass and energy balance equations assumed by Vrentas and Vrentas [1994] to model polymer film drying using unsteady-state Fickian diffusion.....77

### **Chapter 3**

- Figure 3.1 Schematic of sandwich cell used for SAXS experiments. Inside diameter of well in which the sample is dried is 10 mm.....129
- Figure 3.2 Parallel plate rheometer fixture with solvent trap. The diameters of the top and bottom plates are 25 and 45-mm, respectively.....130
- Figure 3.3 Scattering profiles of SB in toluene at various concentrations. Samples were equilibrated for 12 hours at room temperature. Polymer concentrations are indicated as weight percent polymer in the figure. The inset shows a secondary peak observed at 60 wt% polymer.....131
- Figure 3.4 Dynamic mechanical response,  $|G^*|$ , of SB copolymer in toluene at 30 wt% (o) and 32 wt% (■) polymer as a function of time at a frequency of 0.5 rad/s and 2% strain. The samples were prepared by extracting solvent from a 20 wt% solution at room temperature.....132
- Figure 3.5 Evolution of the complex modulus of 35 (A) and 40 (B) wt% SB copolymer / toluene solutions at room temperature following extraction from a 20 wt% solution. At each concentration, the responses at three different shear rates, all at 2% strain, are studied: 0.1 rad/s (□), 0.5 rad/s (o), 1 rad/s (□).....133
- Figure 3.6 Complex modulus as a function of time during the ordering of the SB block copolymer in a 37 wt% toluene solution at room temperature following extraction from a 20 wt% solution. The curves correspond to a sample that is continually sheared from the time that 37 wt% polymer is reached (□) and a sample that is equilibrated under state conditions for 35 minutes before shearing ensues (◇). Tests were performed at 2% strain at a frequency of 0.5 rad/s.....134
- Figure 3.7 Storage,  $G'$ , (o) and loss,  $G''$ , (■) modulus of a phase separating 32 wt% polymer SB / toluene solution as a function of time at room temperature. Tests were performed at 2% strain at a frequency of 0.5 rad/s.....135
- Figure 3.8 Iso-concentration dynamic mechanical responses of phase separating SB block copolymer in toluene at several concentrations following the removal of solvent from a 20 wt% polymer solution. All samples were prepared and tested at room temperature. Tests were performed at 2% strain at a frequency of 0.5 rad/s. The response of a 32 wt% solution is shown in (A). Concentrations (wt% polymer) shown in (B) are: 35 (▲), 40 (◆), 45 (□), and 50 (●).....136
- Figure 3.9 Integrated intensity of the primary scattering peak during the ordering of the SB

block copolymer in toluene following the removal of solvent from a 20 wt% solution at room temperature. Curves correspond to the following concentrations (wt% polymer): 40 ( $\square$ ), 45 ( $\diamond$ ), 50 ( $\square$ ), 55 (x), and 60 (o). Curves have been arbitrarily shifted for clarity.....137

- Figure 3.10 Half-times of the ordering of SB in toluene at room temperature following extraction of solvent from a 20 wt% solution as a function of concentration. Half-times were determined using the Avrami equation and calculating  $\phi(t)$  from dynamic mechanical data using the parallel (top) and series (bottom) approximations for the complex modulus. At 32 wt%, the total half-time ( $\bullet$ ) and the half-time of the growth period only (o) are shown. At all subsequent concentrations, the half-time corresponds to the single-step growth of  $G^*$  .....138
- Figure 3.11 Half-times of the ordering of SB in toluene following extraction of solvent from a 20 wt% solution at room temperature based on dynamic mechanical (o) and SAXS ( $\blacksquare$ ) data using parallel (top) and series (bottom) approximations to determine  $\phi(t)$ .....139
- Figure 3.12 Avrami exponent during the ordering of SB in toluene following removal of solvent from a 20 wt% solution at room temperature as a function of concentration. Exponent values were calculated using a parallel ( $\blacklozenge$ ) and series ( $\blacksquare$ ) approximations for the complex modulus.....140
- Figure 3.13 Rheology of phase separating SIS copolymer in toluene at room temperature at 37 ( $\blacksquare$ ), 45 ( $\blacklozenge$ ), and 50 ( $\bullet$ ) wt% polymer following extraction of solvent from a 20 wt% solution.....141

## **Chapter 4**

- Figure 4.1 Scattering cell used to simultaneously monitor removal of solvent from block copolymer films and track ordered structure development using SAXS. Sample chamber can be wrapped in heating tape (not shown) to control the solvent removal temperature.....168
- Figure 4.2 SAXS profiles of an SB/toluene solution during solvent removal at 30°C. Peaks positioned at  $n = 1$  and  $3^{1/2}$  are consistent with hexagonally-packed cylinders [Park, 2004].....169
- Figure 4.3 SAXS profiles of an SB/toluene film (60 wt% polymer) during solvent removal at 40°C and 60°C. Peaks positioned at  $n = 1$  and  $3^{1/2}$  are consistent with hexagonally-packed cylinders [Park, 2004].....170
- Figure 4.4 Integrated intensity of the primary SAXS peak ( $n=1$ ) as a function of the polymer weight fraction in a SB/toluene film during solvent removal at 30°C.....171

Figure 4.5	Integrated intensity of the primary SAXS peak ( $n=1$ ) as a function of time collected from a SB film cast in toluene while solvent is simultaneously removed at 30° C.....	172
Figure 4.6	Instantaneous rate of ordering of the SB copolymer into hexagonally-packed cylinders in a neutral solvent, toluene, during continual solvent removal at 30°C.....	173
Figure 4.7	Schematic phase diagram (polymer concentration, $\phi_{\text{polymer}}$ vs. temperature, T) illustrating the solvent removal path (dashed line) of the SB / toluene film at 30°C. $T_{\text{ODT}}$ and $C_{\text{ODT}}$ represent the order-disorder transition temperature and concentration, respectively.....	174
Figure 4.8	Drying curves for SB copolymer films cast from a 20 wt% toluene solution at 30°C (■), 40°C (●) and 60°C (▲).....	175
Figure 4.9	Primary scattering peak integrated intensity as a function of concentration during extraction of toluene from SB copolymer at 30°C (■), 40°C (●), and 60°C (▲).....	176
Figure 4.10	Instantaneous rate of ordering of the SB copolymer into hexagonally-packed cylinders in a neutral solvent, toluene, during continual solvent removal at 30°C (■), 40°C (●) and 60°C (▲).....	177
Figure 4.11	Schematic phase diagram (polymer concentration, $\phi_{\text{polymer}}$ vs. temperature, T) illustrating the solvent removal path (dashed lines) of the SB / toluene film at three different temperatures as indicated in the figure. $T_{\text{ODT}}$ and $C_{\text{ODT}}$ represent the order-disorder transition temperature and concentration, respectively.....	178
Figure 4.12	Drying curves for SB copolymer films cast from a 20 wt% toluene solution at 30°C (A) and 40°C (B). The curves in each figure represent films dried without a sweep gas (filled points) and with a sweep gas (open points).....	179
Figure 4.13	Primary scattering peak integrated intensity as a function of concentration during extraction of toluene from SB copolymer at 30°C (A) and 40°C (B). At both temperatures, films were dried without a sweep gas (closed points) and with a sweep gas (open points).....	180
Figure 4.14	Instantaneous rate of ordering of the SB copolymer into hexagonally-packed cylinders in a neutral solvent, toluene, during continual solvent removal at 30°C (A) and 40°C (B). At both temperatures, films were dried with a sweep gas (open points) and without a sweep gas (closed points).....	181

## **Chapter 5**

- Figure 5.1 Scattering data from SB copolymer film cast from a 20 wt% solution in toluene dried at 40°C. Scattering rings collected at 45 and 72 wt% polymer are shown in (A) and (B), respectively. (C) and (D) show the integrated scattering profiles based on (A) and (B), respectively. The peaks in (C) and (D) are decomposed into the vertical and horizontal film Bragg peaks in (E) and (F), respectively...202
- Figure 5.2 Bragg spacing in horizontal (closed symbols) and vertical (open symbols) film directions of an SB film cast from a 20 wt% (initial concentration) toluene solution as a function of polymer concentration during solvent removal at 30 (A), 40 (B) and 60°C (C).....203
- Figure 5.3 Percent difference ( $\square$ ) in the horizontal and vertical Bragg spacing of an SB film cast from a 20 wt% toluene solution as a function of polymer concentration during solvent removal at 30 ( $\blacksquare$ ), 40 ( $\bullet$ ) and 60°C ( $\blacktriangle$ ).....204
- Figure 5.4 Bragg spacing in horizontal (closed symbols) and vertical (open symbols) film directions of an SB film cast from a 20 wt% toluene solution as a function of polymer concentration during solvent removal with a sweep gas at 30 (A) and 40°C (B).....205
- Figure 5.5 Percent difference ( $\delta$ ) in the horizontal and vertical Bragg spacing of an SB film cast from a toluene solution with an initial concentration of 20 wt% as a function of polymer concentration during solvent removal without a sweep gas (closed symbols) and with a sweep gas (open symbols) at 30 (A) and 40°C (B).....206
- Figure 5.6 Drying curves during the removal of solvent from an SB film cast from a 20 wt% solution at 30°C without a sweep gas ( $\blacksquare$ ), with a sweep gas ( $\square$ ) and in the presence of excess solvent ( $\times$ ).....207
- Figure 5.7 Bragg spacing in horizontal ( $\blacksquare$ ) and vertical ( $\square$ ) film directions of an SB film cast from a 20 wt% toluene solution as a function of polymer concentration during solvent removal in the presence of excess solvent at 30°C.....208
- Figure 5.8 Percent difference ( $\delta$ ) in the horizontal and vertical Bragg spacing of an SB film cast from a 20 wt% toluene solution as a function of polymer concentration during solvent removal at 30°C without a sweep gas ( $\blacksquare$ ), with a sweep gas ( $\square$ ), and in the presence of excess solvent ( $\times$ ).....209
- Figure 5.9 Rate of change of  $\delta$  with respect to polymer concentration during the removal of solvent from an SB film cast from a 20 wt% solution in toluene at 30°C without a sweep gas ( $\blacksquare$ ), with a sweep gas ( $\square$ ), and in the presence of excess solvent ( $\times$ ).....210

## **Chapter 6**

Figure 6.2.2.1	Porous-plate rheometer fixture for extracting solvent from top and bottom of polymer solution. The side walls and bottom of the dish are non-porous metal. The porous-plate is a porous stainless steel substrate.....218
-------------------	---

## List of Tables

### Chapter 2

Table 2.2-1	Diffraction peak positions for classic ordered structures.....	41
Table 2.2-2	Interpretation of Avrami exponent for various modes of nucleation and growth. Reproduced from Mandelkern, 2002.....	56
Table 2.3-1	Film drying parameters describing the boundary conditions for the drying of solution-cast films [Kim, 1998].....	71
Table 2.3-2	Mass and heat transfer parameters used in film drying analysis by Vrentas and Vrentas [Vrentas, 1994].....	78
Table 2.3-3	Vinjamur [2002] non-Fickian film drying model parameters.....	81

### Chapter 3

Table 3.1	Avrami exponents of phase separating SB / toluene solutions at room temperature determined from dynamic mechanical and SAXS data.....	141
Table 3.2	Avrami exponent and half-time of SB and SIS block copolymers.....	143

**Chapter 1**  
**Introduction**

## 1.1. Project Background and Research Objectives

Block copolymer films have found use in a variety of applications in numerous fields. In electronic applications, block copolymers are used to fabricate data storage media, patterned semiconductors, and photonic band-gap materials [Hamley, 2004; Zhang, 2010]. Block copolymer film can also be used in separation processes. Filter media and nano-porous membranes developed using block copolymers are employed as desalination membranes, fuel cell membranes and bio-molecule purification membranes [Fasolka, 2001; Wang, 2002; Hamley, 2004; Zhang, 2010]. This list of applications is not exhaustive. However, it does demonstrate the breadth of uses for this class of copolymers. Regardless of the specific utilization, the main feature of the above materials that makes block copolymers useful for such applications is that the properties of these films are dependent on the film microstructure.

The key features of block copolymers that make them so versatile lie in the fact that they are composed of two or more covalently bonded homopolymer segments. This allows block copolymers to be used to generate a material offering a hybrid of the properties of the constituent blocks. As such, the beneficial properties of each individual block can be incorporated into a block copolymer film, while the drawbacks of each block can be compensated for by the other blocks present [Noshay, 1977]. For instance, thermoplastic elastomers such as poly(styrene-*b*-butadiene) behave as a rubber at low temperatures, but displays properties of a thermoplastic at elevated temperatures [Hamley, 2004]. While polymer blends can also be used to achieve such hybrid properties, block copolymers offer these properties without the occurrence of macrophase separation, which can cause significant gradients in film properties [Lodge, 2003a]. Further, in contrast to blends, block copolymers microphase separate on a nanometer length scale.

The second advantage of block copolymer composition is that it leads to phases which separate into a variety of microstructures, ranging in length scale from 10 – 100 nm [Zhang, 2010]. Four microstructures are shown in Figure 1.1 [Matsen, 1997].

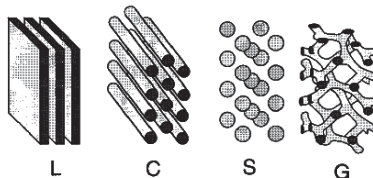


**Figure 1.1-1.** The four classic equilibrium block copolymer melt morphologies (Lamella (L), hexagonally-packed cylinders (C), spheres (S), and gyroid (G)). Reprinted with permission from Matsen, M.W.; Bates, F.S. *J. Chem. Phys.* **1997**, *106*, 2436. Copyright 1997, American Institute of Physics.

While over 30 different morphologies have been identified, the four structures shown in Figure 1.1 are the common, or classic, diblock copolymer microstructures. This includes spheres packed into a face-centered and body-centered lattice (S), hexagonal packed cylinders (C), a lamellae structure (L), and the bicontinuous gyroid phase (G). In general, the minority block will form the microstructure, while the major block forms the matrix [Noshay, 1977]. These structures are what ultimately govern the properties of block copolymer films.

By tailoring the morphology, well-controlled film properties can be obtained [Shibayama, 1983]. For instance, as possible materials for filters, changing structure can be used to control permeability [Yamamura, 2001]. Bicontinuous structures, such as the gyroid phase can be used in solar panels to generate continuous donor and acceptor layers, which improve charge separation and extraction and significantly enhancing solar cell efficiency [Meuler, 2009]. In studying poly(arylene ether sulfone) multiblock copolymers for fuel cell membranes, Lee et al. [2009] found that by changing the morphology in the final film via different processing conditions, the proton conductivity and water uptake of polyelectrolyte membranes for fuel cells

could be improved. The group found that doubling the ionic domain spacing increased the proton conductivity of the membranes by nearly 400%. It is evident from such work that the ability to control film morphology will have a tremendous implications regarding film property enhancement.

While the work performed by Lee et al. [2009] is one of the few studies to quantitatively demonstrate how beneficial control of polymer morphology can be, other studies have considered the influence of processing on block copolymer film morphology [Huang, 2004; van Dijk, 1996; Konrad, 2000; Libera, 1998; Kim, 1998]. For instance, Huang [2004] was able to use variable solvent selectivity and drying rates to obtain both normal and inverted microstructures in solvent-cast poly(styrene-*b*-butadiene) films. Various authors [van Dijk, 1996; Konrad, 2000; Libera, 1998; Kim, 1998] have discussed the ability to manipulate the orientation of certain microstructures in polymer films by changing the film thickness and drying rate. As these works demonstrate, a fundamental understanding of how to control block copolymer structure during processing can be advantageous in enhancing polymer film properties. Unfortunately, these studies fail to provide details on the mechanism by which block copolymers self-assemble during solvent removal. Thus, a need to better understand precisely how these structures form during film processing remains. This includes knowledge of what structures will form and at what rate they will form.

The thermodynamics of the block copolymer system will dictate the accessible and preferred morphologies that evolve during processing. For block copolymer melts, these thermodynamics are a function of temperature and block copolymer composition, including block chemistry and the ratio of the block lengths. Temperature will influence the interaction energy between the two blocks. As temperature decreases, the interaction energy increases,

causing the free energy of the system to increase. When this enthalpic contribution to the free energy exceeds the contribution of the entropic penalty incurred by forming ordered structures, the system phase separates into the microstructures shown in Figure 1.1. The specific structure that forms is determined by the asymmetry of the copolymer. In symmetric copolymers, where the difference in the stretching energy of the two blocks is negligible, lamellae structures form. Asymmetric copolymers develop into curved structures to relieve interfacial tension, packing frustrations, and stretching energies of the blocks.

The phase diagram based on these considerations can be accurately predicted for block copolymer melts. Based on Helfand's [1975; 1976; 1977; 1978] self-consistent field theory, Leibler [1980] predicted phase behavior of diblock copolymers in the weak-segregation limit. A block copolymer melt phase diagram based on mean-field theory is presented in Figure 1.2.

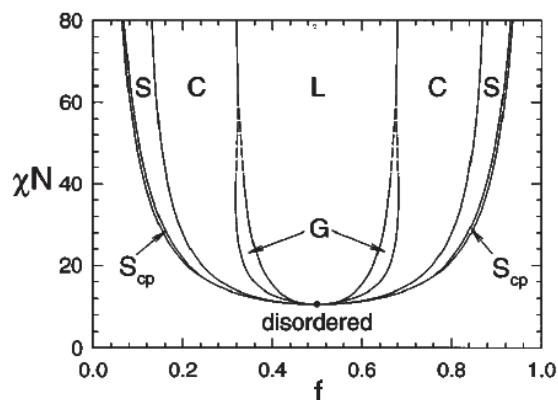


**Figure 1.1-2.** Block copolymer melt phase diagram based on mean-field theory [Matsen, 1997]. The microstructures represented are: close-packed spheres ( $S_{CP}$ ), hexagonally-packed cylinders (C), lamella (L), spheres (S) and gyroid (G). Reprinted with permission from Matsen, M.W.; Bates, F.S. *J. Chem. Phys.* **1997**, *106*, 2436. Copyright 1997, American Institute of Physics.

The four equilibrium structures shown in Figure 1.1 are predicted by this theory. These structures exist below a critical temperature and the preferred microstructure is strictly a function of the polymer composition and the temperature of the melt. It is predicted that the phase diagram in Figure 1.2 will describe most block copolymer melts, regardless of the chemistry of

the blocks. As such, in processing block copolymer melts, the film properties can be easily predicted by the melt composition and temperature. Unfortunately, processing films in the melt state may not be desirable depending on the requirements of the final film.

Solution-casting can offer several benefits over melt-casting. If the order-disorder transition is below the glass transition temperature ( $T_g$ ) of one of the blocks, segmental mobility will be severely limited when trying to process the neat copolymer [Huang, 2003; Huang, 2004]. Solvent can plasticize the copolymer and improve segmental mobility, allowing for sub- $T_g$  processing. Alternatively, if high processing temperatures are necessary to access the desired morphology or suppress phase separation, there is a risk of thermal degradation or unwanted reactions within the film. Solvent can suppress order-disorder transition temperatures [Lodge, 2003a], allowing development to the desired morphologies without necessitating the use of undesirable processing temperatures.

The addition of solvent also improves block segregation [Lodge, 2003a]. Domain dimensions of block copolymer melts are usually confined to 50 nm or less, while solvent allows for domains on the order of 100 nm to develop. As previously alluded to, Lee [2009] found that changing solvent selectivity could increase domain spacing and improve PEM properties. This improved segregation also allows for access to more microstructures for a given block copolymer composition by relaxing interfacial tension and stretching energies associated with curved structures. It has been shown, for instance, that a 25 wt% poly(styrene-*b*-isoprene) block copolymer in a selective solvent, DEP, could develop all four classic morphologies depending on the concentration of the polymer in the solution and the solution temperature [Lodge, 2003b]. However, the advantages offered by solution-casting films come with the consequence of more complex, less predictable phase behavior.

The presence of solvent adds at least three additional degrees of freedom to the determination of the phase behavior: two additional interaction parameters, between the polymer blocks and the solvent, and the polymer concentration in the solution. The interaction parameters between solvents and polymers are difficult to predict as they are highly dependent on the chemistry of each of these components [Lodge, 2002]. This precludes universal predictions of polymer phase behavior in solvents. As a result, when processing novel block copolymer systems, in order to understand the phase behavior and available morphologies, extensive experiments are needed.

The phase behavior of styrenic block copolymers in organic solvents and Pluronics in aqueous solutions have been experimentally studied [Cogan, 1991; Wanka, 1994; Mortensen, 1996; Alexandridis, 1996; Sakurai, 1996; Hajduk, 1998; Svensson, 1998; Hanley, 2000; Mori, 2001; Lai, 2002; Lodge, 2002; Lodge, 2003b; Park, 2008]. One of the more extensive studies on block copolymer behavior in solution was performed by Lodge et al. [2002; 2003b]. Between the two studies, the authors developed phase diagrams for poly(styrene-*b*-isoprene) block copolymers of various compositions in solvents of varying selectivity. While the classic equilibrium structures identified for block copolymer melts were obtained in these solutions, the presence of the structures was a function of not only copolymer composition and solution temperature, but also solvent selectivity, which varies with temperature, and polymer concentration. As anticipated, the phase behavior of block copolymer solutions is complex and the presence of certain microstructures depends heavily on the state of the system. Thus, if a specific structure is desired in a film prepared by solution-casting, it is necessary to understand not only the conditions under which the desired structure will form, but also all other structures that may grow along the processing path. In order to avoid contamination of the final film with

unwanted structures, it must also be understood how the structures present on the processing path develop, how to enhance growth of the desired structure, and suppress growth of undesired structures.

The final structure in a dried solution-cast film is a function of the rate at which a given morphology forms relative to the drying rate. In rapid quenches, the solvent drying rate is typically much faster than the rate of phase separation, causing non-equilibrium structures to be frozen-in [Konrad, 2000]. Extremely slow drying rates become negligible as the phase separation is faster than the drying rate and equilibrium structures, such as those observed by Lodge [2002; Lodge, 2003b] are always achieved. In order to efficiently produce a film with desired properties, the rate of solvent removal must be balanced with the rate of structure formation, requiring an understanding of ordering kinetics.

Phase separation can be tracked by a variety of techniques, including polarized optical microscopy (POM), small angle X-ray scattering (SAXS) or rheology. Though it allows for direct viewing of the developing ordered domain, POM can only track over a limited sample area [Chastek, 2003]. Further, its sensitivity to changes in the degree of ordering in the system is limited to the resolution of the viewing device. SAXS and rheology are very sensitive to changes in the system properties incurred due to the evolving structures. An increase in the concentration of ordered structure in an otherwise disordered polymer system results in an increase in the intensity of the primary scattering peak generated by SAXS. Ordered structure development will also change the complex modulus of the block copolymer melt or solution, allowing phase separation to be monitored with rheology. By tracking changes in either the scattered intensity or modulus over time, information on the rate at which ordered structures form can be acquired.

Studies on the phase separation kinetics of block copolymers include ordering in the melt-phase and in solution [Harkless, 1990; Rosedale, 1990; Amundson, 1992; Schuler, 1993; Winter, 1993; Floudas, 1994a, b; Stuehn, 1994; Floudas, 1995; Hashimoto, 1995; Adams, 1996; Sakamoto, 1997; Balsara, 1998; Hashimoto, 1998; Sakamoto, 1998a, b; Liu, 2004; Yufa, 2009; Patel, 2010; Balsara, 1992; Balsara, 1996; Garetz, 1993; Jian, 1993; Hashimoto, 1996; Soenen, 1997a, b; Nie, 2003; Chastek, 2003; Chastek, 2004; Chastek, 2005]. Both order-disorder and order-order transition kinetics have been considered. These transitions are usually thermally induced through shallow temperatures quenches or jumps to minimize overshoot and, in the case of order-disorder transitions, keep the system in the metastable region where nucleation and growth is known to occur. Because the growth mechanism is known, a number of these authors have compared the phase separation behavior to Avrami kinetics for crystallization and propose the Avrami equation as suitable means for modeling the kinetics. This has allowed for the determination of the type of nucleation (homogeneous or heterogeneous). Further, general conclusions regarding the effect of ordering temperature on the ordering rate can be drawn. Though this work adds to the understanding of how equilibrium block copolymer structures form, this information is unable to anticipate how ordered structures will form under different processing conditions.

The fact that the literature mentioned above only evaluates phase separation kinetics at a single concentration is problematic from a processing standpoint. During solvent removal from a solution-cast film, the polymer concentration is constantly changing. In a selective solvent, multiple morphologies are available at a single temperature, depending on the concentration. Thus, the preferred structure changes over the course of processing, causing the polymers to constantly undergo simultaneous disorder-to-order and order-order transitions as the film dries.

By performing single-condition experiments, the available literature fails to account for these concurrently occurring phase separations. To the author's knowledge, no existing studies have attempted to address how the manner in which solvent is removed from block copolymer solutions influences ordering kinetics at certain concentrations along the processing path.

All the necessary parameters to understand ordering kinetics during film processing have all been individually studied in some capacity. The thermodynamics have been studied and phase diagrams have been produced for block copolymer melts and solution. The ordering kinetics of these equilibrium structures have been studied via temperature quenches at different points of the phase diagrams. It has also been demonstrated that the manner in which solvent is removed from block copolymer films influences the final film properties due to contributions from the thermodynamic factors and ordering kinetics. Yet, disconnect between these three areas of research persists and there has been a failure to bring all three disciplines together to develop a comprehensive understanding of block copolymer ordering during the processing of solution-cast films.

The goal of the current project, *Phase Behavior and Ordering Kinetics of Block Copolymers in Solution During Solvent Removal*, is to determine whether dynamic mechanical measurements can be used to quantify the ordering kinetics of block copolymers during solvent removal in order to improve the processing of solution-cast block copolymer films. This work will provide an improved understanding of the effect of processing conditions on film properties which can be used to better predict and improve final film properties. By using a combination of rheology and SAXS, the intentions of this research are to determine whether dynamic mechanical analysis can be used to identify structures forming at certain points during the drying process and the rate at which they evolve. The effect of processing conditions, such as drying

temperature and drying rate, on the ordering kinetics of block copolymers during film processing will be determined. This research will provide new methods for evaluating block copolymer phase separation in the presence of solvent and during solvent removal.

Based on the goals of this work, the key objectives are:

1. Determine if dynamic mechanical measurements can be used to quantitatively track the ordering of a block copolymer in solution following solvent extraction and determine what the changes in the dynamic mechanical response during phase separation mean in terms of structure development.
2. Use small angle X-ray scattering (SAXS) to provide an improved interpretation of the changes in the dynamic mechanical response (DMR) associated with phase separation. SAXS will be used to determine the phase behavior of a model block copolymer system and identify the developing structures that are being tracked by dynamic mechanical measurements. Experiments to track ordering in block copolymer solution using DMR measurements will be repeated with SAXS so that the DMR measurements can be confirmed and the physical changes in the system that give rise to changes in the DMR can be deduced. It will be determined whether changes in the DMR during ordering arise from changes in ordered domain dimensions, the development of individual structures, or another phenomenon, such as physical cross-linking.
3. Determine if the rules of mixtures can be applied to the DMR data as a function of time to determine the volume fraction of the ordered state in the sample at a given time,  $\phi(t)$ . It will then be determined if the Avrami equation for crystallization can be used in

conjunction with these rules of mixtures to quantify the ordering kinetics obtained from DMR measurements.

4. Determine if a model for quantifying the ordering kinetics, such as the Avrami model, can be coupled with a mass transfer model to predict the extent of ordering in a block copolymer solution at different concentrations along a solvent removal path.

## 1.2 References

1. Adams, J.L.; Quiram, D.J.; Graessley, W.W.; Register, R.A. *Macromolecules* **1996**, *29*, 2929.
2. Alexandridis, P.; Zhou, D.; Khan, A. *Langmuir* **1996**, *12*, 2690.
3. Amundson, K.; Helfand, E.; Patel, S.S.; Quan, X. *Macromolecules* **1992**, *25*, 1935.
4. Balsara, N.P.; Dai, H.J.; Watanabe, H.; Sato, T.; Osaki, K. *Macromolecules* **1996**, *29*, 3507.
5. Balsara, N.P.; Garetz, B.A.; Chang, M.Y.; Dai, H.J.; Newstein, M.C. *Macromolecules* **1998**, *31*, 5309.
6. Balsara, N.P.; Garetz, B.A.; Dai, H.J. *Macromolecules* **1992**, *25*, 6072.
7. Chastek, T.Q.; Lodge, T.P. *Macromolecules* **2003**, *36*, 7672.
8. Chastek, T.Q.; Lodge, T.P. *Macromolecules* **2004**, *37*, 4891.
9. Chastek, T.Q.; Lodge, T.P. *J Polym Sci Pol Phys* **2005**, *43*, 405.
10. Cogan, K.A.; Gast, A.P.; Capel, M. *Macromolecules* **1991**, *24*, 6512.
11. Fasolka, M.J.; Mayes, A.M. *Annu Rev Mater Res* **2001**, *31*, 323.
12. Floudas, G.; Fytas, G.; Hadjichristidis, N.; Pitsikalis, M. *Macromolecules* **1995**, *28*, 2359.
13. Floudas, G.; Hadjichristidis, N.; Iatrou, H.; Pakula, T.; Fischer, E.W. *Macromolecules* **1994**, *27*, 7735.
14. Floudas, G.; Pakula, T.; Fischer, E.W.; Hadjichristidis, N.; Pispas, S. *Acta Polym*, **1994**, *45*, 176.
15. Garetz, B.A.; Newstein, M.C.; Dai, H.J.; Jonnalagadda, S.V.; Balsara, N.P. *Macromolecules* **1993**, *26*, 3151.
16. Hajduk, D.A.; Kossuth, M.B.; Hillmyer, M.A.; Bates, F.S. *J Phys Chem B* **1998**, *102*, 4269.
17. Hamley, I.W. Introduction to Block Copolymers. In *Developments in Block Copolymer Science and Technology*; Hamley, I. W., Ed.; John Wiley & Sons, Ltd.: New York, 2004; p 1.
18. Hanley, K.J.; Lodge, T.P.; Huang, C.I. *Macromolecules* **2000**, *33*, 5918.

19. Harkless, C.R.; Singh, M.A.; Nagler, S.E.; Stephenson, G.B.; Jordansweet, J.L. *Phys Rev Lett* **1990**, *64*, 2285.
20. Hashimoto, T.; Ogawa, T.; Sakamoto, N.; Ichimiya, M.; Kim, J.K.; Han, C.D. *Polymer* **1998**, *39*, 1573.
21. Hashimoto, T.; Sakamoto, N. *Macromolecules* **1995**, *28*, 4779.
22. Hashimoto, T.; Sakamoto, N.; Koga, T. *Phys Rev E* **1996**, *54*, 5832.
23. Helfand, E. *Macromolecules* **1975**, *8*, 295.
24. Helfand, E.; Wasserman, Z.R. *Macromolecules* **1976**, *9*, 879.
25. Helfand, E.; Wasserman, Z.R. *Macromolecules* **1978**, *11*, 961.
26. Helfand, E.; Wasserman, Z.R. *Polym Eng Sci* **1977**, *17*, 582.
27. Huang, H.; Hu, Z.; Chen, Y.; Zhang, F.; Gong, Y.; He, T.; Wu, C. *Macromolecules* **2004**, *37*, 6523.
28. Huang, H.; Zhang, F.; Hu, Z.; Du, B.; He, T.; Lee, F.K.; Wang, Y.; Tsui, O.K.C. *Macromolecules* **2003**, *36*, 4084.
29. Jian, T.; Anastasiadis, S.H.; Fytas, G.; Adachi, K.; Kotaka, T. *Macromolecules* **1993**, *26*, 4706.
30. Kim, G.; Libera, M. *Macromolecules* **1998**, *31* (8), 2670.
31. Konrad, M.; Knoll, A.; Krausch, G.; Magerle, R. *Macromolecules* **2000**, *33* (15), 5518.
32. Lai, C.; Russel, W.B.; Register, R.A. *Macromolecules* **2002**, *35*, 4044.
33. Lee, M.; Park, J.K.; Lee, H.S.; Lane, O.; Moore, R.B.; McGrath, J.E.; Baird, D.G. *Polymer* **2009**, *50*, 6129.
34. Leibler, L. *Macromolecules* **1980**, *13*, 1602.
35. Libera, M.; Kim, G. *Macromolecules* **1998**, *31*, 2569.
36. Liu, Z.; Shaw, M.; Hsiao, B.S. *Macromolecules* **2004**, *37*, 9880.
37. Lodge, T. P. *Macromol Chem Physic* **2003a**, *204*, 265.
38. Lodge, T.P.; Hanley, K.J.; Pudil, B.; Alahapperuma, V. *Macromolecules* **2003b**, *36*, 816.

39. Lodge, T.P.; Pudil, B.; Hanley, K.J. *Macromolecules* **2002**, *35*, 4707.
40. Meuler, A.J.; Hillmyer, M.A.; Bates, F.S. *Macromol Rev* **2009**, *42*, 7221.
41. Mori, K.; Hasegawa, H.; Hashimoto, T. *Polymer* **2001**, *42*, 3009.
42. Mortensen, K. *J Phys-Condens Mat* **1996**, *8*, A103.
43. Nie, H.; Bansil, R.; Ludwig, K.; Steinhart, M.; Konak, C.; Bang, J. *Macromolecules* **2003**, *36*, 8097.
44. Noshay, A.; McGrath, J.E. *Block Copolymers, Overview and Critical Survey*; Academic Press: New York, 1977.
45. Park, S.; Sul, W. *Polymer* **2008**, *49*, 3327.
46. Patel, A.J.; Mochrie, S.; Narayanan, S.; Sandy, A.; Watanabe, H.; Balsara, N.P. *Macromolecules* **2010**, *43*, 1515.
47. Rosedale, J.H.; Bates, F.S. *Macromolecules* **1990**, *23*, 2329.
48. Sakamoto, N.; Hashimoto, T. *Macromolecules* **1998**, *31*, 3292.
49. Sakamoto, N.; Hashimoto, T. *Macromolecules* **1998**, *31*, 3815.
50. Sakamoto, N.; Hashimoto, T.; Han, C.D.; Kim, D.; Vaidya, N.Y. *Macromolecules* **1997**, *30*, 1621.
51. Sakurai, S.; Hashimoto, T.; Fetters, L.J. *Macromolecules* **1996**, *29*, 740.
52. Schuler, M.; Stuehn, B. *Macromolecules* **1993**, *26*, 112.
53. Shibayama, M.; Hashimoto, T.; Kawai, H. *Macromolecules* **1983**, *16*, 1434.
54. Soenen, H.; Berghmans, H.; Winter, H.H.; Overbergh, N. *Polymer* **1997**, *38*, 5653.
55. Soenen, H.; Liskova, A.; Reynders, K.; Berghmans, H.; Winter, H.H.; Overbergh, N. *Polymer* **1997b**, *38*, 5661.
56. Stuehn, B.; Vilesov, A.; Zachmann, H.G. *Macromolecules* **1994**, *27*, 3560.
57. Svensson, B.; Alexandridis, P.; Olsson, U. *J Phys Chem B* **1998**, *102*, 7541.
58. van Dijk, M.A.; van den Berg, R. *Macromolecules* **1996**, *28*, 6773.

59. Wang, F.; Hickner, M.; Kim, Y.S.; Zawodzinski, T.A.; McGrath, J.E. *J Membr Sci* **2002**, *197*, 231.
60. Wanka, G.; Hoffman, H.; Ulbricht, W. *Macromolecules* **1994**, *27*, 4145.
61. Winter, H.H.; Scott, D.B.; Gronski, W.; Okamoto, S.; Hashimoto, T. *Macromolecules* **1993**, *26*, 7236.
62. Yamamura, M.; Nishio, T.; Kajiwara, T.; Adachi, K. *Dry Technol* **2001**, *19*(7), 1397.
63. Yufa, N.A.; Li, J.; Sibener, S.J. *Macromolecules* **2009**, *42*, 2667.
64. Zhang, J.; Yu, X.; Yang, P.; Peng, J.; Luo, C.; Huang, W.; Han, Y. *Macromol Rapid Commun* **2010**, *31*, 591.

## **Chapter 2**

### **Literature Review**

## 2.1 Block Copolymers

Block copolymers are composed of two or more covalently bonded homopolymers [Hamley, 2004]. Common block copolymer topologies are shown in Figure 2.1-1.

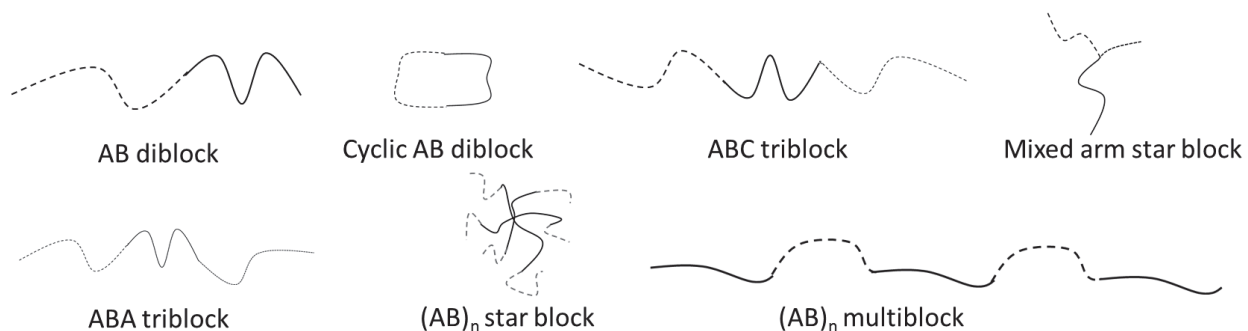


**Figure 2.1-1.** Conventional block copolymer topologies. Reproduced from [Hamley, 2004].

Linear block copolymers include the AB diblock, ABA and ABC triblock, and ABC... multiblock copolymers, where A, B, and C are dissimilar homopolymer blocks. In addition, three non-linear block copolymers are shown. The star block copolymer consists of three or more polymer chains sharing a common junction point. Cyclic block copolymers contain constituents covalently bonded to one another at both chain ends.

Due to dissimilarities in the chemistry of the blocks constituting the above copolymers, significant interaction energies between the blocks provide the driving force for microphase separation [Noshay, 1977]. The blocks will segregate into ordered structures with length scales on the order of nanometers, while macrophase separation is prevented due the covalent bond between the blocks. The degree of the driving force and the preference for certain ordered structures is governed by the chemistry of the chains and the copolymer composition,

particularly the extent of asymmetry of the copolymer as measured by the relative volume fractions of the blocks.

This section will explore the phase separation of block copolymers. Section 2.1.1 will discuss the phase behavior of block copolymer melts. The thermodynamics of block copolymer phase separation, which can be applied to both block copolymer melts and solutions, will be presented in Section 2.1.1.1. An analysis of equilibrium morphologies and details of the phase diagram for block copolymer melts is provided in Section 2.1.1.2. Finally, block copolymer solutions will be considered in Section 2.1.2, where theoretical and experimental phase diagrams will be analyzed.

### **2.1.1 Block Copolymer Melt Phase Behavior**

Leibler [1980] predicted the general phase behavior of block copolymer melts using Landau expansions to provide an improved solution to Helfand's [1975; 1976; 1977; 1978] Self-Consistent Field Theory (SCFT) for block copolymers. While Leibler's [1980] paper explores only the region of the onset of phase separation, the general thermodynamic driving forces for phase separation are applicable to all regions of the phase diagram. This section will begin by describing the thermodynamic principles that give rise to microphase separation. The focus will then be on the currently known block copolymer morphologies in the melt and progress made since Leibler's [1980] paper in understanding the nature of the ordered microdomains in different regions of the phase diagram.

#### **2.1.1.1 Thermodynamics of Phase Separation**

Block copolymer phase separation is driven by fluctuations in the local densities of the constituent blocks,  $\rho_A$  and  $\rho_B$ , and the desire to minimize the free energy of the system through

rearrangement of the blocks [Leibler, 1980]. The Flory-Huggins parameter,  $\chi$ , is central to determining the degree of phase separation and is given as [Hadjichristidis, 2003]:

$$\chi_{AB} = \frac{1}{kT} \left( \varepsilon_{AB} - \frac{(\varepsilon_{AA} + \varepsilon_{BB})}{2} \right) \quad (2.1-1)$$

where  $\varepsilon_{ij}$  is the interaction energy between components  $i$  and  $j$ ,  $k$  is the Boltzmann constant, and  $T$  is the absolute temperature. Because  $\varepsilon_{AB}$ , and therefore  $\chi$ , is positive, unlike monomers will repel one another, leading to microphase separation in order to reduce the number of contacts between unlike species. Such segregation comes at the cost of reduced configurational entropy, thus increasing the free energy of the system. The degree to which this entropy will contribute to the free energy is dictated by  $N$ , the degree of polymerization, and the product of  $\chi$  and  $N$  governs when phase separation will occur [Hadjichristidis, 1003]. At low  $\chi$ , entropic effects dominate, leading to a homogeneous disordered state at high temperatures. Upon decreasing temperature, the enthalpic term,  $\chi$ , begins to become more influential and ordering ensues [Leibler, 1980].

Leibler [1980] determined the critical  $\chi N$  value for phase separation to be 10.5. The temperature at which this condition is met is deemed the order-disorder transition temperature ( $T_{ODT}$ ). At this temperature, the system transforms from a homogeneous mixture to a heterogeneous ordered state [Hamley, 1998]. Typically,  $T_{ODT}$  is higher than the glass transition temperatures of both blocks and is a function of block length, copolymer composition, and molecular weight [Han, 1989]. It has been shown to be thermally reversible, with the disordering process occurring by the gradual diffusion of the minority chains back into the majority chain matrix [Roe, 1981]. At temperatures lower than  $T_{ODT}$  ordered microdomains

form, consisting of various ordered structures, depending on the values of  $\chi_N$  and chain asymmetry.

### 2.1.1.2 Melt Phase Morphologies

Over 30 different morphologies have been identified for diblock and triblock copolymers [Lodge, 2003a]. Due to the breadth of research in this field, this review will focus on diblock copolymers. Four diblock copolymer morphologies are recognized as equilibrium structures: lamellae (L), hexagonal-packed cylinders (C), the bicontinuous gyroid (G), and the body-centered cubic structure of spheres (bcc) [Lodge, 2003a]. In addition, a long-lived metastable complex structure, the perforated lamellae, has been identified [Hamley, 1993]. The structures are illustrated in Figure 2.1-2. In the non-lamellae structures, the component constituting the curved geometry depends on the stretching energy of the blocks. The microstructure is typically formed by the minor bloc [Noshay, 1977]. The structure sizes are determined by the radius of gyration of the polymer blocks [Hamley, 1998] and the interdomain spacing is directly related to the molecular weights of the blocks [Shibayama, 1983b, c].

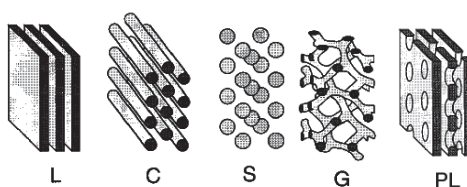


**Figure 2.1-2.** Stable equilibrium structures for block copolymer melts, Lamellae (L), Gyroid (G), hexagonally-packed cylinders (C), and spheres (S), and metastable complex structure, perforated lamellae (PL). Reprinted with permission from Matsen, M.W.; Bates, F.S. *J. Chem. Phys.* **1997**, *106*, 2436. Copyright 1997, American Institute of Physics.

The theoretical phase diagram based on mean field theory is shown in Figure 2.1-3. The PL structure is absent from the phase diagram, although it has been shown to exist at the L/G boundary [Listak, 2008].

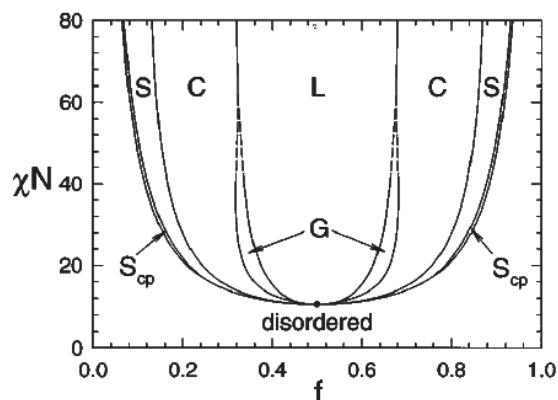


**Figure 2.1-3.** Theoretical phase diagram based on self-consistent mean field theory calculations [Matsen, 1997]. Reprinted with permission from Matsen, M.W.; Bates, F.S. *J. Chem. Phys.* **1997**, *106*, 2436. Copyright 1997, American Institute of Physics.

The lamellae phase is the simplest [Hamley, 1998] and most stable phase with the lowest free energy [Leibler, 1980] as it lacks interfacial curvature. When the ratio of the block volumes is near unity ( $f_A = f_B = 0.5$ ), the lamellae phase exists. However, as the block volumes become increasingly unbalanced, energetic and entropic effects become influential and the system is driven toward structures with a higher mean interfacial curvature [Hadjichristidis, 2003; Hamley, 1998; Matsen, 1996]. Asymmetry causes the difference in degree of stretching of the two blocks to become non-uniform [Matsen, 1996; Matsen, 1997a, b; Hadjichristidis, 2003; Lynd, 2005]. As Hadjichristidis [2003] explained, to compensate, the structures curve toward the block with the lower stretching energy, allowing the other block to relax. In doing so, the system favors surfaces with minimal surface area and constant mean curvature to relieve interfacial tension. The diminished energetic effects due to the minimization of the surface area must in turn be

balanced with the increased packing frustration that results. Decreasing the packing frustration in order to evenly distribute the stretching energy among the chains in the curved domain requires that the domains are of uniform thickness throughout, which will cause deviation ( $\sigma_H$ ) from the constant mean curvature stipulation previously set. Because the interfacial tension contributions to the systems free energy favors  $\sigma_H = 0$ , while packing frustration contributions require positive deviations, a balance is realized at small values of  $\sigma_H$ .

The above argument is sufficient to explain the behavior of the complex structures PL and G in Figure 2.1-3. These phases offer intermediate curvature between the classic L and C equilibrium structures [Matsen, 1997b]. However, as  $\chi N$  increases,  $\sigma_H$  of the complex phases can become quite large, making them unfavorable. Further, it has been determined that  $\sigma_H(\text{PL}) > \sigma_H(\text{G})$ , allowing the bicontinuous gyroid to be an equilibrium structure, but relegating the perforated lamellae to long-lived metastable status [Matsen, 1997b].

The phase diagram based on  $\chi N$  and  $f$  is divided into three regions depending on the value of the free energy term: the weak segregation limit (WSL;  $10.5 \leq \chi N \leq 12$ ), the intermediate segregation regime (ISR;  $12 < \chi N < 100$ ), and the strong segregation limit (SSL;  $\chi N > 100$ ) [Hadjichristidis, 2003; Hamley, 1998]. Within these regions, the extent of ordering and purity of the domains are different. In order to fully understand the phase diagram, the change in phase behavior as one traverses the phase diagram with respect to the order-disorder transition temperature should be understood as well.

### 2.1.1.3 Weak Segregation Limit

The weak segregation limit (WSL) exists near the ODT, between  $\chi N$  values of 10.5 and 12 [Hadjichristidis, 2003]. As the temperature is lowered to the order-disorder transition

temperature, the amplitude of composition fluctuations increases. These fluctuations induce first-order transitions to either the lamellae phase [Bates, 1988] or body-centered cubic structures in asymmetric copolymers, while symmetric copolymers will undergo second-order transitions to the lamellae phase [Leibler, 1980]. When the spinodal curve is reached, second-order, lamellae forming transitions occur at all compositions [Bates, 1985; Hadjichristidis, 2003]. These transitions are reversible, as approaching  $T_{ODT}$  from below will cause minor blocks to become poorly anchored in the microdomain [Matsen, 1996] and to diffuse into the interface [Roe, 1981].

The structures forming in this region are marked by sinusoidal composition profiles, as shown in Figure 2.1-4 [Rosedale, 1995].

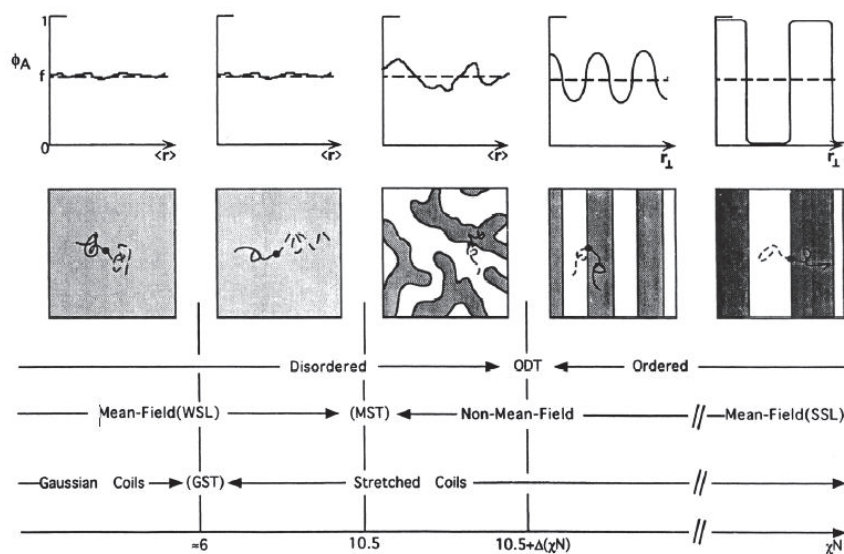


**Figure 2.1-4.** Concentration profiles (upper panel) and segregation patterns of diblock copolymer melts in the three segregation limits: weak (WSL), intermediate (ISR) and strong (SSL). Reprinted with permission from Rosedale, J.H.; Bates, F.S.; Almdal, K.; Mortensen, K.; Wignall, G.D. *Macromolecules* **1995**, *28*, 1429. Copyright 1995 American Chemical Society.

The microdomains consist of an isotropic fluctuation pattern superimposed on the preferred microstructure. There is a lack of long-range order due to the resistance to long-range motion

caused by local excesses of the blocks that result from these compositional fluctuations [Bates, 1990a, b]. The domains that develop are relatively impure and have broad interfaces. These domains are characterized by a domain spacing,  $D$ , that scales as  $N^{1/2}$  [Hadjichristidis, 2003; Bates, 1990a, b]. The spacing in this region is very sensitive to changes in  $f_A$ , as shorter minority blocks are more capable of pulling away from the domain and swelling the interface [Matsen, 1996].

#### **2.1.1.4 Intermediate Segregation Regime**

In the intermediate segregation regime (ISR), fluctuation effects are reduced, as  $N$  increases [Bates, 1988], and complex structures are present [Matsen, 1996; Hadjichristidis, 2003]. Traversing the phase diagram from 0.5 to pure species, the sequence of ordered structures is  $L \rightarrow G \rightarrow C \rightarrow BCC \rightarrow \text{Disorder}$ . The pure component regions of the composition profiles in Figure 2.1-4 have increased and continue to do so with further increases in  $\chi N$ . The composition profile at the interface begins to steepen as narrower interfaces develop. The interfacial width and domain spacing both continue to increase, though the rate of increase with  $\chi N$  is slowed relative to the rate of change in the WSL [Bates, 1988].

#### **2.1.1.5 Strong Segregation Limit**

The SSL was first explored by Meier [1969] and the self-consistent field theory was used by Helfand and Wasserman [1975; 1976; 1977; 1978] to determine the phase diagram in this limit. The predictions of Helfand and Wasserman have been experimentally determined to be within reason by Hashimoto [1983a] and Shibayama [1983b, c]. At large  $\chi N$ , the HPL phase is stable, while the stability region of G is predicted to terminate [Matsen, 1996]. The composition

profile for the SSL is shown in Figure 2.1-4. The microdomains are nearly pure with very narrow interfaces. The nature of the microdomains imposes a high degree of stretching on the copolymer blocks and the entropic contributions to the free energy now consist of entropy loss due to this stretching, in conjunction with confinement entropy resulting from the localization of junction points [Matsen, 1996; Hadjichristidis, 2003]. The dependence of the domain spacing on  $\chi$  is greatly reduced, while the influence of  $N$  has increased with  $D$  increasing following:

$$D \propto \chi^{1/6} N^{2/3} \quad (2.1-2)$$

### 2.1.2 Block Copolymers in Solution

The addition of solvent to a block copolymer system can improve microphase separation and increase the length scales of the ordered domains [Lodge, 2003a]. From a processing stand point, solvents impart mobility to the copolymers without thermal treatment, allowing for a wider processing window and reduce the risk of degrading the polymer [Huang, 2003; Huang, 2004]. Therefore, the understanding of the phase diagram needs to be extended to solutions as well.

While block copolymer melts have been thoroughly studied and the phase diagram can be well predicted, the behavior of the system upon the addition of solvent is difficult to predict due to the extra degrees of freedom available because of solvent-polymer interactions [Hamley, 2004]. In addition to the interaction parameter between unlike blocks (A and B),  $\chi_{AB}$ , there exist parameters between the blocks and solvent (S),  $\chi_{AS}$  and  $\chi_{BS}$  [Young, 1991]. In a neutral solvent, the latter two parameters are nearly equivalent, whereas in an A-selective solvent,  $\chi_{AS} < \chi_{BS}$ . While the preferred ordered structure is still dictated by constant-mean curvature and the relief of interfacial energy, the partitioning of solvent between the blocks plays an important role in

determining how these conditions are satisfied. In a neutral solvent, it was originally proposed that the solvent will partition equally between the blocks, with a slight increase in solvent concentration at the interface to minimize A-B interactions, while a selective solvent will preferentially partition toward the selected block [Helfand, 1982]. The former assumption, which is the basis for the dilution approximation of Helfand and Wasserman [1982] has been shown to be not fully accurate over all concentration ranges [Lodge, 2002]. In addition to these findings, experimental evidence suggesting additional interesting phase behavior not predicted by theory exists [Lodge, 2003b]. This section will begin with a brief analysis of phase behavior in dilute solutions, followed by an analysis of the dilution approximation. A survey of experimental findings of block copolymer phase behavior in solution will then be provided.

#### **2.1.2.1 Dilute Solutions**

The dilute region of the phase diagram extends up to the polymer concentration at which swollen coils overlap [Hamley, 1998]. In selective solvents, above a critical micelle concentration (cmc) and below a critical micelle temperature (cmt), unimers transform into micelles, consisting of a corona, made of the soluble blocks, and a core of insoluble blocks [Wanka, 1994]. Spherical, ellipsoid and rod-like micelles have been observed [Mortensen, 1996; Lodge, 2002]. A model spherical micelle is shown in Figure 2.1-5.

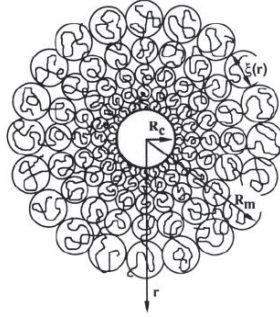


**Figure 2.1-5.** Spherical micelle structure comprised of a core of insoluble blocks and a corona of soluble blocks.  $R_c$  is the core radius;  $R_m$  is the micelle radius;  $\xi$  is the blob size. Reprinted with permission from Cogan, K.A.; Gast, A.P.; Capel, M. *Macromolecules* **1991**, *24*, 6512. Copyright 1991 American Chemical Society.

Such a spherical micelle may either be crew-cut micelles, when the soluble block is shorter than the insoluble block, or hairy micelles, when the opposite is true [Park, 2008]. These structures are characterized by the core radius ( $R_c$ ), blob size ( $\xi$ ), aggregation number ( $N_{agg}$ ), degree of polymerization ( $n$ ), core volume ( $V_{core\_block}$ ), dry polymer volume ( $V_p$ ), saturating polymer concentration ( $\phi_0$ ), and hard sphere interaction radius ( $R_{hs}$ ) [Cogan, 1991; Mortensen, 1996]. The aggregation number is defined as the number of chains forming a single micelle. The star model for micelles treats the corona as being composed of small blobs that grow in size moving away from the micelle core. These quantities are all connected through the following relationships [Cogan, 1991; Mortensen, 1996]:

$$N_{agg} = \frac{4}{3} \frac{1}{n V_{core\_block}} \pi R_c^3 \quad (2.1-3)$$

$$N_{agg} = \frac{4}{3} \frac{c}{V_p \phi_0} \pi R_{hs}^3 \quad (2.1-4)$$

$$\xi = \frac{4r}{\sqrt{N_{agg}}} \quad (2.1-5)$$

The shape and characteristics of the micelle structures are especially sensitive to solvent quality and temperature. The tendency of micelles toward different structures and structure

dimensions is driven by the stretching of core chains, repulsive interactions between corona chains, and surface tension at the core/corona interface [Park, 2008]. Near the cmt, micelle structure is thermotropic [Wanka, 1994]. As temperature increases, polymer chains move from one micelle to another in an effort to obtain the optimal aggregation number such that the interfacial tension is minimized. In general, this results in an increase in  $N_{agg}$ , generating an increase in both  $R_c$  and  $R_{hs}$  [Mortensen, 1996]. This thermotropic behavior has been shown to be limited to within 20°C of the cmt [Wanka, 1994]. The properties have not been shown to be very sensitive to polymer concentration at any dilutions, as the surface tension is independent of concentration above the cmc [Hamley, 2005].

Figure 2.1-6 is a phase diagram of a dilute aqueous solution of poly(ethylene oxide) – poly(propylene oxide) (EO<sub>27</sub>-PO<sub>39</sub>-EO<sub>27</sub>) [Glatter, 1994].

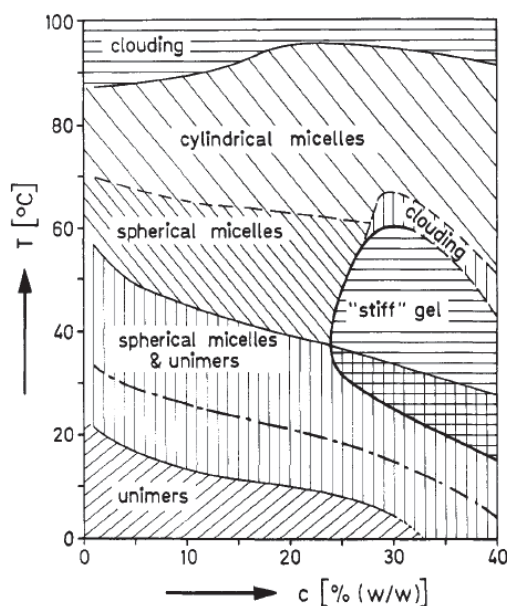


**Figure 2.1-6.** Phase diagram of poly(ethylene oxide) – poly(propylene oxide) (EO<sub>27</sub>-PO<sub>39</sub>-EO<sub>27</sub>) aqueous solution at dilute, micelle-forming concentrations. Reprinted with permission from Glatter, O.; Scherf, G.; Scillén, K.; Brown, W. *Macromolecules* **1994**, 27, 6046. Copyright 1994 American Chemical Society.

The cmt is defined by the line separating the pure unimer and the broad coexistence regions of the phase diagram. Increasing concentration, causes the cmt to decrease. Increasing temperature causes the unimers to disappear as the aggregation number increases. Although the relative fraction of micelles to unimer continually increases, the volume fraction of the micelles decreases as the aggregation number increases [Mortensen, 1996]. Eventually, a transition from spherical to cylindrical micelles occurs.

Above a critical gelation concentration (cgc), defined as the concentration above which the system exhibits a finite yield stress, usually occurring at a volume concentration of  $\phi = 0.68$  [Hamley, 2004], the micelles can pack into ordered cubic structures [Hamley, 1998]. The type of packing is determined by the relative lengths of the soluble and insoluble blocks [Park, 2008]. Due to the short corona length in crew-cut micelles, giving rise to more interactions between the cores upon packing, face-centered cubic packing is favored for crew-cut micelles [Lodge, 2002]. Hairy micelles tend to take on a body-centered cubic structure during gelation.

Micelles account for the dilute region of phase diagrams for block copolymers in selective solvents. Above a certain concentration, the solution will adopt a variety of mesophases similar to those observed for melts. Much like micelles, the structures that the system takes on will be influenced by the solvent-selectivity. Unlike micelles, these structures will be observed in both neutral and selective solvents.

#### **2.1.2.2 The Dilution Approximation and Theoretical Phase Diagrams**

A number of attempts have been made to predict the phase behavior of block copolymer solutions [Helfand, 1972; Hong, 1983; Banaszak, 1992; Huang, 1998; Noolandi, 1996; Yu, 2005; Sun, 2005; Linse, 1993; Fredrickson, 1989a]. Some of the earliest work invoked the dilution

approximation of Helfand and Wasserman [1982]. The dilution approximation assumes that the neutral solvent partitions equally among both blocks. In effect, the melt phase is simply diluted and its behavior is maintained when  $\chi_{AB}$  on the melt phase diagram is replaced by  $\chi_{\text{effective}} = \phi\chi_{AB}$ . Therefore, this theory predicts the classical structures observed for melts. Also like melts, the critical  $\chi_{\text{effective}}$  value for the onset of microphase separation is 10.5. Later work modified the dilution approximation to account for excluded volume and screening effects in the semidilute region of the phase diagram, leading to a new effective interaction parameter,  $\chi_{\text{effective}} = \phi^{\delta}\chi_{AB}$ , where  $\delta$  is predicted to have a value of 1.6. The modified interaction parameter yields lower values of  $T_{\text{ODT}}$  (higher  $\chi N$ ) for a constant polymer concentration, while predicting that the concentration of polymer at the order-disorder transition scales as  $N^{-0.62}$  [Hamley, 1998]. Hamley [1998] notes that in spite of such advances, the self-consistent field theory fails to account for the suppression of the ODT due to fluctuations, the effects of which are amplified by the presence of solvent. Further, as the solution is diluted, chain swelling will generate novel structures not predicted for the melt phase [Lodge, 2002; Lodge, 2003b]. While more recent simulation work has provided vastly improved calculations of phase behavior, including the presence of complex structures and 2-phase regions, factors such as solvent quality and polymer-solvent interactions are difficult to universalize, necessitating experimental studies [Lodge, 2002].

### **2.1.2.3 Experimental Styrenic Block Copolymer Phase Diagrams**

The phase diagrams of block copolymers in solution are not universal. In particular, the phase behavior of Pluronic systems results from entropic effects, while the ordering of styrenic

block copolymers is driven by enthalpic contributions to the free energy [Hamley, 2005]. This section will focus on styrenic block copolymer systems in organic solvents.

The structures developed in block copolymer solutions are dependent on the nature of the solvent. All structures identified for the melt phase have been observed in solutions of styrenic block copolymers in organic solvents of varying selectivity [Hanley, 2000; Lodge, 2002; Lodge, 2003b; Park, 2008] using a combination of small angle X-ray scattering (SAXS), rheology, and microscopy. Depending on solvent selectivity and concentration, the classic packed sphere and cylinder phases can adopt both the normal and the inverted state, in which the blocks comprising the structure and the matrix are switched [Lodge, 2002; Park, 2008]. While the gyroid phase is observed, its stable region is limited to near the order-disorder transition [Sakurai, 1996; Hanley, 2000; Lodge, 2002; Lai, 2002]. Because the bicontinuous phases exist to provide an intermediate curvature between the lamellae and the cylinder phase, these phases are not necessary in the presence of selective solvents, which can swell the blocks, creating an extra degree of freedom to relieve packing frustrations and stabilize the cylinder phase [Lai, 2002; Lodge, 2002]. It has also been reported that the gyroid phase may be replaced entirely by a coexistence phase, incorporating both lamellae and cylinder structures [Lodge, 2002].

Lodge et al. [2002] developed phase diagrams for poly(styrene-*b*-isoprene) in styrene-selective phthalate solvents of varying selectivity. Dioctyl phthalate (DOP) is neutral, while dibutyl phthalate (DBP) and diethyl phthalate (DEP) are selective. The diagrams were developed for SI block copolymers of different molecular weights and compositions. SAXS was used to determine the structure, while SAXS, rheology, and static birefringence were used in conjunction with one another to determine the order-disorder transition and order-order transition

temperatures. Representative phase diagrams of SI(11-32), where the numbers correspond to the respective block molecular weights in kg/mol, in the three solvents are shown Figure 2.1-7.

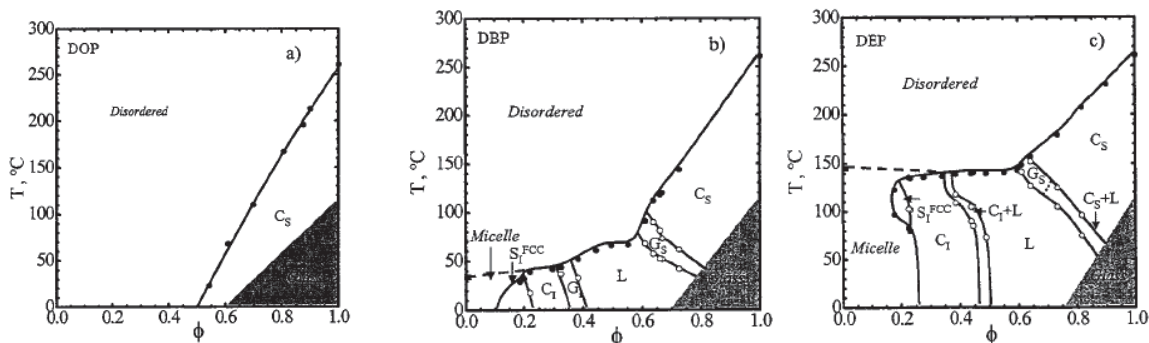


**Figure. 2.1-7.** Phase diagrams of poly(styrene-*b*-isoprene) (SI(11-32)) in a) DOP, b) DBP, and c) DEP. Solvent selectivity increases progressing from a to c. DOP is neutral and DBP and DEP are selective for styrene. Reprinted with permission from Lodge, T.P.; Pudil, B.; Hanley, K.J. *Macromolecules* **2002**, *35*, 4707. Copyright 2002 American Chemical Society.

The phase diagram is a function of temperature and the volume fraction of polymer in solution,  $\phi$ . The order-disorder transition temperatures increase as solvent selectivity increases, while decreasing when progressing from the pure polymer melt state ( $\phi_{\text{Polymer}} = 1$ ) to the dilute region, as the presence of solvent acts to stabilize the disordered state. Further, Lodge and coworkers [2003b] observed that in neutral solvents, the ability of fluctuations to stabilize the disordered state is exacerbated by the presence of the solvent, causing lower order-disorder transition temperatures than the dilution approximation predicts.

The order-order transitions are well predicted by the dilution approximation. In selective solvents, these transitions lean to the left, due to the fact that solvent selectivity decreases with increasing temperature. Hence, as temperature increases and the affinity of the solvent for a particular block diminishes, so too does the swelling of that block, resulting in a loss of stabilization of the more curved phase. As selectivity increases, the dependence of selectivity on

temperature weakens, causing the tilt of the phase boundaries to become less substantial. In highly selective solvents, nearly vertical OOTs have been obtained [Lai, 2002].

In addition to the  $(\phi, T)$  diagrams, Lodge [2002] proposed that the true phase diagram is also composed of  $(\phi, f)$  and  $(T, f)$  diagrams, where  $f$  is the volume fraction of one of the copolymer blocks. In the latter, it was observed that high temperatures, where the selective solvents are nearly neutral, yield a phase diagram that is symmetric about  $f = 0.5$ . The phase behavior is similar to that of the melt phase as predicted by the dilution approximation. Upon cooling, the area of the phase diagram occupied by the ordered phases increases as solvent selectivity sets in and stabilizes the curved structures located at the extremes of the ordered phase region. Eventually, coexistence regions appear at low enough temperatures. The  $(T, f)$  diagram shows similar behavior as the  $(\phi, f)$  diagram. As the system becomes more dilute, the order-disorder transition temperatures become more dependent on solvent-polymer interactions, eventually become constant for all polymer compositions, as polymer-polymer interactions become negligible. In addition to this response of the ODT temperature, the breadth of morphologies observed is reduced.

The structure dimensions scale differently in solutions than in melts because of solvent swelling. As with melts, Shibayama [1983b, c] demonstrated that increasing the molecular weight of the polymer will increase the structure dimensions and the inter-structure distances. However, polymer concentration, along with segregation strength, must also be accounted for.

Whitmore and Noolandi [1990] proposed that the domain spacing,  $d$ , per Kuhn length,  $b$ , in a neutral solvent scales as a function of  $\chi_{AB}$ ,  $N$ , and  $\phi$ :

$$d / a = \chi_{AB}^p N^q \phi^r \quad (2.1-6)$$

It was predicted that in the weak segregation limit,  $p = 1/3$ ,  $q = 0.8$ ,  $r = 0.4$ , while in the strong segregation limit,  $p = 0.2$ ,  $q = 2/3$ ,  $r = 0.22$ . However, the exponent associated with polymer concentration will be influenced by the ability of the solvent to swell the blocks, and is therefore strongly dependent on the ordered structure and solvent selectivity [Hamley, 2005]. In neutral solvents, domain spacing increases with increased polymer concentration and decreases as temperature increases. Mori [2001] experimentally determined the factors in Eq. 2.1-6, with the concentration,  $\phi$ , and temperature,  $T$ , studied as a single parameter,  $\phi/T$ . In the disordered state, the value of  $q$  is 0.5, lower than predicted for either the WSL or the SSL. In the ordered state, the value of  $q$  for the SSL put forth by Whitmore and Noolandi [1990] is recovered. The  $\phi/T$  factor scales by a power of  $1/3$  below the ODT, while the domain spacing is independent of concentration and temperature above the ODT. The latter results had been reported nearly two decades earlier by Shibayama [1983a, b, c], who attributes the decrease in domain spacing with increased temperature or dilution to the fact that these conditions decrease the repulsive nature of the two blocks. Lodge [2002] obtained results for the scaling of  $d$  with  $\phi$  in agreement with his predecessors, as well as found  $\chi$  to scale by an exponent of 0.25, within the estimates of Whitmore and Noolandi [1990]. These values were independent of structure, inconsistent with previous findings of Shibayama [1983a, b, c] who found the domain spacing scaled as  $\phi^{0.5}$  for lamellae, indicating that domain scaling is dependent on structure.

The response of ordered structures in selective solvent is the opposite of that in neutral solvents with regards to the polymer concentration [Hamley, 2005]. The domain spacing still scales inversely with temperature, however, with polymer concentration, the domain spacing is determined as:

$$d \sim \phi_p^{-\beta} \quad (2.1-7)$$

In a selective solvent,  $\beta$  is dependent on structure. Shibayama [1983a, b, c] determined this value to be 1/3 for packed spheres. Lai [2002] extensively studied the domain size scaling in selective solvents. The value of  $\beta$  was found to decrease as the structures traverse from lamellae to cylinders to spheres. The exponent also increases as selectivity increases. Hence, as temperature increases,  $\beta$  will become smaller.

#### **2.1.2.4 Experimental Pluronic Phase Diagrams**

Pluronics are a class of block copolymers composed of poly(ethylene oxide) and poly(propylene oxide) blocks. Pluronics in aqueous solution and aqueous/organic co-solvents are widely studied and general trends in the phase behavior with respect to temperature and copolymer composition are observed. As temperature increases, it has been observed that lower curvature structures are favored and the areas of stability shifts left [Alexandridis, 1996]. As the insoluble block fraction increases, the area of the phase diagram characterized by lamellae structures decreases [Hajduk, 1998]. Increasing the molecular weight of the copolymer stabilizes the ordered structures, resulting in a reduction in the isotropic phase area and a wider range of concentrations producing ordered structures [Hajduk, 1998], accompanied by a greater array of obtainable structures [Alexandridis, 1996].

Exact scaling relationships have not been proposed for Pluronic systems, although details of the changes in structure dimensions with respect to temperature and concentration variations have been reported [Alexandridis, 1996; Alexandridis, 1998; Hajduk, 1998; Svensson, 1998]. Lamellae spacing and interfacial area is found to decrease as the system becomes more concentrated [Alexandridis, 1996; Alexandridis, 1998; Svensson, 1998]. The same trend has been reported for cylinder radius and spacing [Alexandridis, 1998]. Noolandi [1996] predicts a

reduction in the interfacial area of lamellae and cylinders as temperature increases. In the case of cylinders, a rise in temperature causes the hydrophobicity of the corona block to increase, which in turn causes it to try to enter the core, reducing the interfacial area of cylinders. A similar effect of intermixing of the blocks is predicted for lamellae phase.

Despite these general trends, Figure 2.1-8, a phase diagram for an aqueous solution of P65 ((EO)<sub>20</sub>(PO)<sub>30</sub>(EO)<sub>20</sub>), shows how complex the phase behavior of these systems can be [Wanka, 1994].

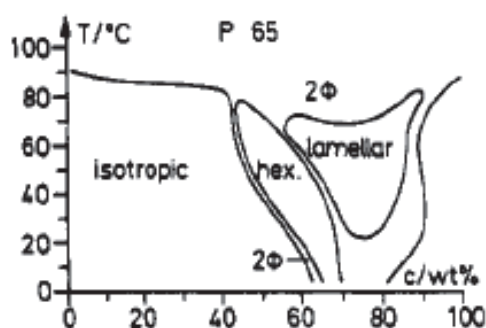


**Figure 2.1-8.** Phase diagram for Pluronic P65 ((EO)<sub>20</sub>(PO)<sub>30</sub>(EO)<sub>20</sub>) in water. Reprinted with permission from Wanka, G.; Hoffman, H.; Ulbricht, W. *Macromolecules* **1994**, *27*, 4145. Copyright 1994 American Chemical Society.

The phase diagram in Figure 2.1-8 shows two of the three classic structures, both of which exist in the normal phase. However, all three classic phases in both the normal and inverted form have been reported for other Pluronic systems [Wanka, 1994; Alexandridis, 1996; Alexandridis 1998; Hajduk, 1998; Svensson, 1998]. Unlike styrenic block copolymers, these systems appear to not generate a gyroid phase [Hajduk, 1998]. Rather, areas of coexisting phases are observed, noted in the above figure by 2φ. This phase diagram exemplifies how complex block copolymer

phase behavior can become in solution in terms of the lyotropic and thermotropic behavior. Multiple coexistence areas with regions of single ordered structures dispersed throughout are present. No definitive trends or criteria for the nature of the boundaries between different ordered regimes on the phase diagram are readily apparent. This would suggest that in such a system, theoretical prediction of the phase behavior becomes increasingly difficult.

## **2.2 Ordering Kinetics**

The phase diagrams discussed in 2.1 represent equilibrium structures. The evolution of these structures from the disordered state occurs over time, ranging from minutes to hours. In order for the phase behavior information to be useful in studying block copolymer solutions during processing, the thermodynamics of the systems as well as the rate at which these structures develop must be understood. The kinetics of phase separation, both order-disorder and order-order transitions, in block copolymer melts have been rigorously studied experimentally [Harkless, 1990; Rosedale, 1990; Amundson, 1992; Schuler, 1993; Winter, 1993; Floudas, 1994a, b; Stuehn, 1994; Floudas, 1995; Hashimoto, 1995; Adams, 1996; Sakamoto, 1997; Balsara, 1998; Hashimoto, 1998; Sakamoto, 1998a, b; Yufa, 2009; Patel, 2010]. Studies concerning ordering kinetics in block copolymer solutions are far less extensive [Balsara, 1992b; Garetz, 1993; Jian, 1993; Balsara, 1996a; Hashimoto, 1996; Soenen, 1997a, b; Chastek, 2003; Nie, 2003; Chastek, 2004; Liu, 2004; Chastek, 2005]. Using rheology, small angle X-ray scattering (SAXS), and static birefringence the ordering mechanism is found to be reminiscent of the nucleation and growth process modeled with Avrami kinetics. This section will begin by detailing the rheological properties and scattering by SAXS of disordered and ordered block copolymers. Subsequently, the discussion will deviate from block copolymers while the possible

mechanisms of phase separation (nucleation and growth and spinodal decomposition) along with Avrami kinetics are introduced. Experimental findings regarding ordering kinetics in block copolymer melts and solutions will then be summarized.

### 2.2.1 Structure factor and small angle X-ray scattering (SAXS)

The structure factor for block copolymers was predicted by Leibler [1980] while studying the phase diagram of melts in the WSL. A Fourier transform of the structure factor in reciprocal space for block copolymer melts is given as:

$$S(q)^{-1} = \frac{F(x, f)}{N} - 2\chi \quad (2.2-1)$$

where  $q$  is the wave vector and  $F(x, f)$  is the free energy of the system. This free energy is a function of the wave vector,  $q$ , and radius of gyration,  $R_g$ , of the copolymer. The structure factor for polymers in neutral solvents was later found by Fredrickson [1989b] to be:

$$S(q)^{-1} = \frac{2\phi}{a^3 N} [F(q) - 2\chi^* N] \quad (2.2-2)$$

In the case of solutions,  $F(q)$  is still a function of the wave vector and  $R_g$ . The structure factor now accounts for concentration,  $\phi$ , and the effective interaction parameter,  $\chi^*$ .

The structure factor can be physically monitored as peaks obtained in small angle X-ray scattering. The wave vector,  $q$ , is related to the scattering angle,  $2\theta$ , and the wavelength,  $\lambda$  [Hamley, 2005]:

$$q = \frac{4\pi \sin 2\theta}{\lambda} \quad (2.2-3)$$

The maximum intensity of the primary peak in a scattering profile corresponds to  $S(q^*)$ . This peak will increase in intensity and become narrower as temperature reduces or the system

becomes more ordered. The position ( $q^*$ ) and intensity ( $I(q^*)$ ) of this peak can provide information about the ordered structure that is developing in a phase separating system. The integrated intensity (area under the primary peak) can be related to the degree of ordering,  $\phi$ , in a sample via the scattering power,  $P$  [Hadjichristidis, 2003]:

$$P = \frac{1}{2\pi^2} \int qI(q) dq \quad (2.2-4)$$

$$P \approx \Delta n^2 \phi(1 - \phi) \quad (2.2-5)$$

The peak intensity will provide information regarding the interfacial area per unit volume ( $S/V$ ) and interfacial width ( $\sigma$ ) of the structure, while the position of the primary peak relates to the interdomain spacing,  $D_{\text{Bragg}}$  [Hamley, 1998]:

$$I(q) \propto \left(\frac{S}{V}\right) q^{-4} \exp(-\sigma^2 q^2) \quad (2.2-6)$$

$$D_{\text{Bragg}} = \frac{2\pi}{q^*} \quad (2.2-7)$$

While the primary peak alone provides quantitative information about the ordered structure, the entire scattering profile can be used to identify what the structure is. The scattering profile consists of secondary diffraction peaks at higher wave vector values. The relative positions of all peaks are unique for given ordered structures, allowing identification of the structure by probing the sample with SAXS [Hamley, 1998; Hamley, 2004; Hamley, 2005]. The primary peak is given the index  $n=1$ . Subsequent peaks are indexed by the ratio of the peak's wave vector to the primary peak wave vector. Table 2.2-1 details the peak positions for the classic ordered structures.

Table 2.2-1. Diffracted peak positions for classic ordered structures

Structure	Relative peak positions
Lamellae*	1: $\sqrt{4}$ : $\sqrt{9}$
BCC**	1: $\sqrt{2}$ : $\sqrt{3}$ : $\sqrt{4}$ : $\sqrt{5}$ : $\sqrt{6}$
FCC**	$\sqrt{3}$ : $\sqrt{4}$ : $\sqrt{8}$ : $\sqrt{11}$ : $\sqrt{12}$ : $\sqrt{16}$ : $\sqrt{19}$ : $\sqrt{20}$
Hexagonal-packed cylinders**	1: $\sqrt{3}$ : $\sqrt{4}$ : $\sqrt{7}$

\*Bendejacq, 2002

\*\*Park, 2004

### 2.2.2 Rheology of Block Copolymers

The rheological properties of block copolymers are strongly influenced by the state of the system. Block copolymers are considered thermoplastic elastomers [Young, 1991]. In the disordered state, the block copolymer behaves as an entangled melt just above  $T_{ODT}$  [Balsara, 1996a], then transitions to Newtonian behavior at sufficiently high temperatures [Hashimoto, 1983b]. The ordered state is effectively cross-linked, causing the polymer to behave as an elastomer. In solution, block copolymers exhibit various types of responses depending on the state of the system, including the degree of ordering and proximity to the microphase separation transition temperature. In studying the ordering and rheology of SB in selective solvents, Watanabe [1982] and Hashimoto [1983b] observed plastic, linear plastic, and viscoelastic, non-Newtonian behavior as temperature increases while below  $T_{ODT}$ . Ordered lattices are characterized by a yield stress that increases with increasing polymer concentration and diminishes as temperature increases [Hashimoto, 1983b; Habas, 2004]. In general, the ordered state has been found to possess a higher complex modulus than the disordered state, sometimes by orders of magnitude [Harkless, 1990; Floudas, 1994a, b; Stuehn, 1994; Floudas, 1995; Hashimoto, 1995; Balsara, 1996a; Jin, 1997; Hashimoto, 1998; Patel, 2010]. However the exact

reason for the change in rheology is debated. Balsara [1996b] claimed that grain growth will not influence the dynamic mechanical response, while Hashimoto [1998] found that prior to the grains filling the entire sample space, grain size does drive the increase in modulus, but whether this is strictly due to an increase in grain volume or surface area or another mechanism such as increased physical cross-linking is not discussed.

Both the ordered and disordered states demonstrate terminal behavior at high frequencies. In the ordered state, Adams [1994] originally reported that the modulus of SI and SIS melts varies as  $\omega^{0.28-0.7}$  at high frequencies. More recently, Cola [2008] has found that for solutions of poly(styrene)-*b*-polybutadiene-*b*-poly(methyl methacrylate) in a neutral solvent  $G' \sim G'' \sim \omega^{0.5}$ . Thus, the rheological response of solutions is comparable to melts. On the other hand, the disordered state terminates as  $G' \sim \omega^2$  and  $G'' \sim \omega$  in both solutions and melts [Watanabe, 1982; Adams, 1994; Balsara, 1996b; Habas, 2004; Cola, 2008].

Because of the differences in the dynamics of ordered and disordered states, rheology has proven an effective tool for locating order-disorder transitions [Han, 1989] and tracking the degree of ordering, as well as the nature of the microstructure [Hadjichristidis, 2003]. Han [1989] proposed using plots of  $\log G'$  vs.  $\log G''$  at various temperatures to locate  $T_{ODT}$ . Below  $T_{ODT}$  the slope of  $\log G'$  vs.  $\log G''$  is temperature sensitive. In the disordered state, the modulus exhibits terminal behavior, which is insensitive to temperature at low frequencies. Hence, when the slope of  $\log G'$  vs.  $\log G''$  ceases to change upon heating, the order-disorder transition has been crossed. This method of deducing  $T_{ODT}$  has proven to be far more effective than plots of modulus as a function of temperature, which rely on a discontinuity in  $G'$  vs.  $T$  to indicate the disordering of the system, as the latter fails for asymmetric copolymers [Han, 1995].

The change in complex modulus upon during phase separation also allows for rheology to be used to determine the degree of ordering based on volume fraction of ordered state in a system,  $\phi$  [Floudas, 1994a, b]. The pure disordered state is characterized by a complex modulus,  $G_{Dis}^*$ , while a fully order block copolymer system has a characteristic modulus,  $G_{Ord}^*$ . It has been proposed that as ordered domains develop in the block copolymer system, the modulus of a partially ordered system can be approximated as a weighted average of  $G_{Dis}^*$  and  $G_{Ord}^*$  using a rule of mixtures [Floudas, 1994a, b]:

$$G^*(t) = \phi(t)G_{ord}^* + (1 - \phi(t))G_{Dis}^* \quad (2.2-7)$$

$$\frac{1}{G^*(t)} = \frac{\phi(t)}{G_{ord}^*} + \frac{1 - \phi(t)}{G_{Dis}^*} \quad (2.2-8)$$

The contributions of the different states to the total modulus of the system can be combined either in series (Eq. 2.2-8) or in parallel (Eq. 2.2-9). These two rules of mixtures correspond to the limits of the properties that can be attained by a composite system consisting of species characterized by distinct, but different physical properties. The series approximation will predict the minimum modulus of a system with an extent of ordering,  $\phi$ , while the parallel approximation provides the upper limit of the modulus of the same system. It has been proposed that by tracking the complex modulus of a phase separating system over time, the rate of ordering can be determined by rearranging either Eq. 2.2-7 or Eq. 2.2-8 to obtain  $\phi(t)$  as a function of modulus [Floudas, 1994a, b]. However, the rule of mixtures only provides estimates of the possible property limits. Such an approach to estimating properties is general and lacks physical meaning as it does not consider what type of system or the properties are being studied.

As previously noted, it is unclear exactly what the rheology is measuring during phase separation and so it is unknown whether or not these mixing rules are giving an accurate

portrayal of how ordered structures are evolving. It remains to be determined what changes in the physical state of the block copolymer system are giving rise to the increase in modulus as ordered structures evolve. Once such information is obtained, the ability for rheology to predict the extent of ordering in a block copolymer system will be improved.

Among the various ordered states, different dynamic mechanical responses are also observed. In micelle and spherical systems, the elasticity of the system varies with the type of packing. Daniel et al. [2001] found that the body-centered cubic packing of poly(oxyethylene)-*b*-poly(oxybutylene) in an aqueous solution is more elastic than face-centered cubic packing. Soenen and coworkers [1997a] extensively studied solutions of poly(styrene)-poly(ethylene, butylene) triblock copolymers in a selective solvent during gelation. The storage and loss modulus of the solutions were continuously probed at different frequencies as the systems gelled. By tracking  $\tan\delta$  over time at various frequencies, the progression of gelation was monitored and gel point was indicated when  $\tan\delta$  exhibited frequency-independent behavior. The group noted that large amplitude oscillatory strain could inhibit lattice formation and break up any lattices formed during gelation. The required strain amplitude increased as the temperature decreased. At 112°C, which is still in the ordered regime, strain in excess of 4% would destroy the lattice, while at room temperature, a minimum strain of 100% was needed to do so. During the gel formation process in the linear viscoelastic regime, where strain did not hinder lattice development, three different regimes were identified, corresponding to liquid-like behavior, a critical gel point, and solid-like behavior. All three are marked by different  $G'$  and  $G''$  responses during frequency sweeps. In the initial stages,  $G'' > G'$ , but crosses over at high frequencies. As the packing improves,  $G'$  exceeds  $G''$  at all frequencies.

Zhao et al. [1996] found that in block copolymer melts of polyethylene-*b*-poly(ethylene) the elasticity increases as the structure dimensionality and connectivity increase. The gyroid structure displays the most elasticity, followed by percolated lamella, and finally cylinders and lamella. The dynamic mechanical responses of the structures are different during frequency sweeps. Spheres, cylinders, the gyroid, and percolated lamella all display a crossover of  $G'$  and  $G''$ . In sphere-forming and gyroid systems,  $G''$  is initially greater than  $G'$ , then crosses over, exhibiting weak frequency dependencies of modulus. At low frequencies,  $G'$  of cylinders and percolated lamella is greater than  $G''$ . Among these four structures, the frequency-dependence of cylinders is the greatest. Lamella structures also show a strong response to frequency, but no crossover, with  $G'' > G'$  for all frequencies studied.

In studying poly(isoprene-*b*-ethyleneoxide) melts, Floudas et al. [1999] observed different behavior of the ordered structures than Zhao et al. [1996] had originally reported. In these systems, the lamella structure exhibits the highest storage modulus, followed by the gyroid phase, then cylinders. Like the work of Zhao et al. [1996] work, Floudas and coworkers [1999] found that the storage modulus of the lamella structure is initially less than the loss modulus. However, unlike their predecessor, Floudas et al. [1999] do observe crossover at high frequencies for lamella, while the cylinder phase does not show crossover. As these studies have shown, the rheological responses of the different ordered structures are not unique, though some generalizations are observed. As such, while rheology can be utilized to determine if ordering has occurred in a system, it is incapable of unambiguously assigning the type of ordered structure [Zhao, 1996].

To use rheology to study the state of block copolymers, care must be taken in choosing suitable experimental conditions. In order for the rheological response to be dominated by the ordered structure, the frequency must be below the inverse of the terminal relaxation time of the

polymer [Daniel, 2001]. This ensures that the properties of the grains and ordered domains are monitored [Hashimoto, 1998]. If the operating frequency exceeds the inverse relaxation time, the properties of individual chains are being measured. Various studies have shown that large amplitude oscillatory strain is also capable of orienting samples, destroying macrolattices, or preventing gel formation in solutions [Adams, 1996; Balsara, 1996a; Soenen, 1997a; Wu, 2005]. It is further known that rheology fails to track grain growth when the grains fill the entire sample space [Balsara, 1996b; Hashimoto, 1998]. Therefore, data regarding early stages of growth are likely more accurate than later stage data for these measurements.

### 2.2.3 Free Energy Diagrams

Phase separation can proceed by either nucleation and growth or spinodal decomposition. The mechanism is determined by the energy state of the system under the conditions of interest. Using the regular solution model, the free energy of separation ( $F_{sep}$ ) for a dual component system is given by [Jones, 2002]:

$$F_{sep} = \frac{\phi_0 - \phi_2}{\phi_1 - \phi_2} F_{mix}(\phi_1) + \frac{\phi_1 - \phi_0}{\phi_1 - \phi_2} F_{mix}(\phi_2) \quad (2.2-8)$$

where the  $\phi_0$  is the initial concentration of component 'A' in the equilibrium mixed state, and  $\phi_1$  and  $\phi_2$  represent the concentration of component 'A' in phase 1 and 2, respectively. Although this solution is found for a binary liquid, a more general form of Eq. 2.2-8 is given by statistical mechanics that can relate to any two-component system [Chaikin, 1995]:

$$\tilde{f} = \frac{a(T - T_c)}{2} (\phi^2 - 2\phi\phi_0) + U\phi(\phi^3 - 4\phi_0^3) \quad (2.2-9)$$

The order parameter is given as  $\phi$ , which is concentration in the case of phase separation copolymers. The parameter  $a$  is a constant,  $T$  is the temperature of the system, and  $T_c$  is the

critical temperature at which the disordered, metastable, and unstable regimes of the phase diagram meet, as will be discussed shortly.

Three solutions for the free energy diagram are possible depending on the system temperature relative to the critical temperature. Theoretical free energy diagrams are shown in Figure 2.2-1. Figure 2.2-2 provides theoretical phase diagrams for any two-component system corresponding to the three solutions provided in Figure 2.2-1. Though Figure 2.2-2 is not specific to block copolymers, the regions of stability are valid for any phase-separating system and can therefore describe phase separating block copolymers.

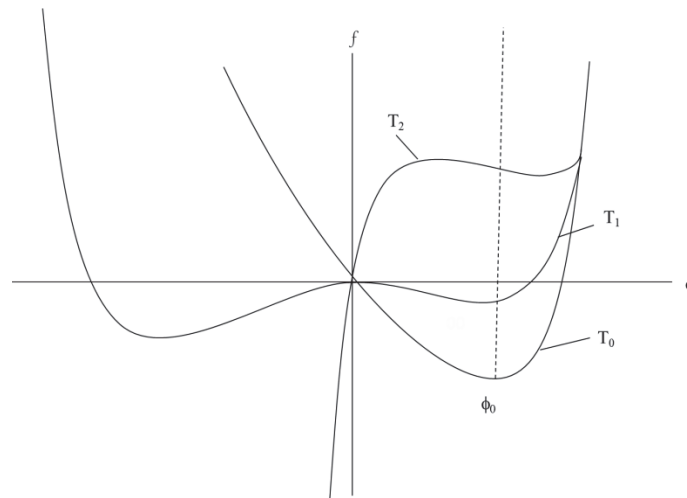


**Figure 2.2-1.** Free energy profiles at various temperatures relative to the order-disorder transition temperature.  $T_0$  is the stable, disordered region,  $T_1$  is the metastable region, and  $T_2$  is the unstable region. Reproduced from [Chaikin, 1995].

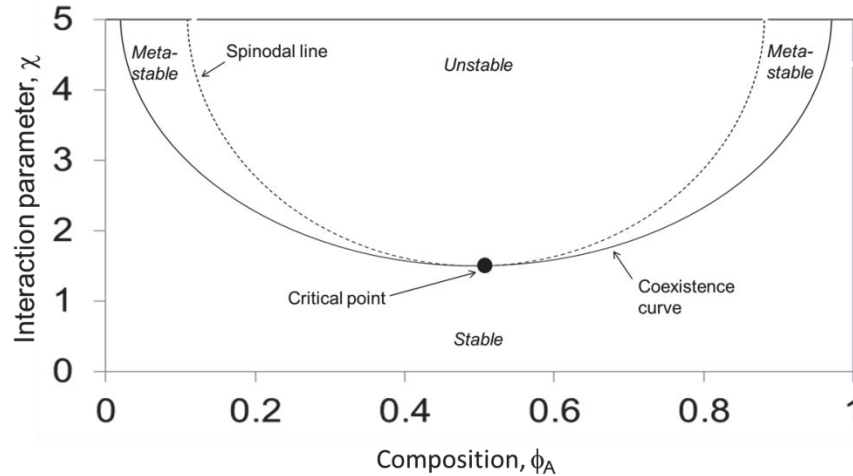


**Figure 2.2-2.** Stability regions of the phase diagram as a function of system composition and interaction parameter,  $\chi$ . The stable, metastable, and unstable regions correspond to the free energy profiles provided in Figure 2.2-1. Reproduced from [Jones, 2002].

The solution to Eq. 2.2-9, as shown in Figure 2.2-1, may be concave up everywhere, display two, non-global minima, or everywhere have a positive slope,  $\partial \tilde{f} / \partial \phi$ . In the first case, denoted by  $T_0$ , the minimum is absolute and located at  $\phi = \phi_0$ . Any perturbations, manifested as concentration fluctuations, result in an increase in the free energy of the system and drive the system back to the initial equilibrium. Hence, the system is stable and remains in the disordered state. The second solution is the metastable state and corresponds to  $T_1$  in Figure 2.2-1. The minimum at  $\phi_0$  is not global, and thus, for certain large concentration fluctuations, the system will tend toward the second minimum present, resulting in a phase separated system. Likewise, for certain values of  $\phi_0$ , a reduction in temperature can result in  $\phi_0$  not being the minimum in free energy, giving rise to a phase separated system. The curve separating the disordered state from this metastable state in Figure 2.2-2 is the coexistence curve. In the final free energy curve ( $T_2$ ), small concentration fluctuations will send the system to a more stable phase separated state. The initial concentration is now located at a local maximum in the free energy diagram and the

system is unstable everywhere. This is the unstable regime, and it is separated from the metastable portion of the phase diagram by the spinodal line. The spinodal curve is characterized by the second derivative of free energy with respect to concentration being zero. The three curves meet when the third derivative of  $\tilde{f}$  with respect to  $\phi$  is zero.

Depending on the region of the phase diagram the system is located, two general modes of the onset of phase separation are possible: nucleation and spinodal decomposition [Chaikin, 1995]. The former occurs in the metastable region, where large concentration fluctuations are required to generate ordering, while the latter is characteristic of the unstable region, in which any small fluctuations are amplified throughout the sample. The following sections will discuss these mechanisms in detail.

#### **2.2.4 Nucleation and Growth**

When the temperature of a system is reduced into the metastable region, a large energy barrier to phase separation persists [Jones, 2002]. The mechanism of phase separation is nucleation and growth, a first order transition [Fredrickson, 1989a]. Nucleation is the process by which a nucleus of ordered phase develops in a homogeneous disordered phase. As the free energy diagram suggests, the net change in free energy must be negative, requiring that concentration fluctuations be quite large. Any nucleus formed by small concentration fluctuations disperses back into the disordered phase. The fluctuations are localized and long-range order will only be achieved through subsequent growth and coarsening of the evolved structures. Nucleation can be either homogeneous, by which the nucleus develops spontaneously due to concentration fluctuations within the sample, or heterogeneous, with nuclei forming on impurities within the sample, including particles or grain boundaries from already formed

structures [Mandelkern, 2002]. In both cases, two contributions to the free energy must be considered: a reduction in free energy within the nucleating volume and the interfacial energy. For a spherical nucleus developed by homogeneous nucleation, with a radius  $r$  composed of small molecules, the free energy is [Jones, 2002]:

$$\Delta F = \frac{4}{3}\pi r^3 \Delta F_v + 4\pi r^2 \gamma \quad (2.2-10)$$

The free energy of the volume is  $\Delta F_v$ , while the interfacial energy is denoted as  $\gamma$ . A critical nucleus radius,  $r^*$ , and critical free energy,  $\Delta F^*$ , are attained by the system when the free energy contributions in Eq. 2.2-10 exactly balance:

$$r^* = \frac{2\gamma}{\Delta F_v} \quad (2.2-11)$$

$$\Delta F^* = \frac{16\pi\gamma^3}{3(\Delta F_v)^3} \quad (2.2-12)$$

The critical free energy given by Eq. 2.2-12 serves as the energy barrier for nucleation while  $r^*$  is the minimum nucleus radius that will result in ordered structure growth. Below the critical radius, the interfacial energy dominates and the free energy increases with increasing nucleus. Any nucleus developing under these conditions will dissolve back into the disordered phase. At the critical radius, the free energy contributions exactly balance, and a larger radius leads to a net decrease in the system's free energy [Chaikin, 1995]. Thus, growth is propagated for a nucleus of radius  $r^*$  or greater. The considerations for heterogeneous nucleation must also include the contact angle of the nucleating material on the nucleation site and surface tension. The contact angle of the nucleus with the host-surface must be less than  $180^\circ$ . Including the contact angle,  $\theta$ , and surface tension,  $\sigma_{\alpha\beta}$  in the free energy equation yields [Mandelkern, 2002]:

$$\Delta G_{het} = \pi r^2 (1 - \cos^2 \theta) (-\sigma_{\alpha\beta} \cos \theta) + 2\pi r^2 (1 - \cos \theta) \sigma_{\alpha\beta} - \frac{\pi r^2}{3} (2 + \cos \theta) (1 - \cos \theta)^2 \Delta G_v$$

(2.2-13)

The critical energy and radius now become:

$$r^* = \frac{2\sigma_{\alpha\beta}}{\Delta G_v} \quad (2.2-14)$$

$$\Delta G_{het} = \frac{4}{3} \pi \frac{\sigma_{\alpha\beta}^2}{\Delta G_v^2} (2 + \cos \theta) (1 - \cos \theta)^2 \quad (2.2-15)$$

In comparing Eq. 2.2-15 to Eq. 2.2-12, the energy barrier for heterogeneous nucleation is lower than that for homogeneous nucleation. Hence, heterogeneous nucleation is typically favored.

Polymers nucleate asymmetrically [Mandelkern, 2002]. The simplest asymmetric nucleus to consider is a cylindrical nucleus having  $\rho$  molecules through the cross section of the cylinder and  $\zeta$  molecules along the length. These molecules are chosen from a polymer chain of  $x$  repeat units. The interfacial energies at the ends of the cylinder and along the cylinder's length are referred to as  $\sigma_{en}$  and  $\sigma_{un}$ , respectively. The free energy associated with nucleation of a cylinder formed by polymer,  $\Delta G_f$ , given by [Mandelkern, 2002]:

$$\frac{\Delta G_f}{xN} = \zeta \rho \Delta G_u - RT \frac{\zeta \rho}{x} + RT \rho \ln \frac{(x - \zeta + 1)}{x} - 2\rho \sigma_{en} \quad (2.2-16)$$

In the nucleation of homopolymers, the entire chain is not part of the nucleus. The portion of the chain that is integrated into the nucleus will affect the free energy of the system.  $\Delta G_f$  dictates how the parts of the chain to nucleate are chosen. The first term in Eq. 2.2-16 contains the free energy of fusion per repeat unit in an infinitely long chain,  $\Delta G_u$ , and describes the gain in free

energy due to the packing of the chains forming the nucleus. The second term represents an changes in entropy due enhanced chain mobility when the ordered domain melts. The third term is an entropy term accounting for the possible ways in which the sequence selected for packing,  $\zeta$ , can be chosen from the chain. The last term is a measure of the interfacial energy at the order-disorder interface. Rather than having a required radius, the nucleating site must now be composed of a minimum number of molecules in the cross section,  $\rho^*$ , and the length,  $\zeta^*$ . The critical cylinder dimensions are reduced as the temperature is reduced [Mandelkern, 2002], consistent with the increased segregation found on descending deeper into the metastable region.

Equation 2.2-16 is a theoretical model for the energy barrier to nucleation derived for large molecules and homopolymers. Its validity for a phase separating block copolymer has not been demonstrated. Fredrickson [1989a] provided an estimate of the energy barrier for nucleation and growth specific to block copolymer melts:

$$\Delta F^* \approx \frac{k_B T}{N^{1/3} \delta^2} \quad (2.2-17)$$

The energy barrier is found to be proportional to the distance between the ordering temperature and the order-disorder transition temperature, denoted as  $\delta$ , and the polymer size as measured by the degree of polymerization,  $N$ . Based on Eq. 2.2-17, Fredrickson [1989a] suggested that the growth completion time scales as:

$$\theta_c \sim N^{1/12} \delta^{3/4} \tau_d e^{\Delta F^* / 4k_B T} \quad (2.2-18)$$

where  $\tau_d$  is the terminal relaxation time of the polymer that is ordering. Analysis of Eq. 2.2-17 and Eq. 2.2-18 revealed that the energy barrier for nucleation of a block copolymer ordered structure is small. It is also found that quenches are limited to  $\delta \sim N^{-1/6}$  before nucleation becomes too rapid to monitor experimentally. Experiments have refuted some of the details of

Fredrickson's [1989a] work, finding discrepancies between the predicted and experimentally determined energy barrier and nucleation rate. Rosedale [1990] claims that heterogeneous, rather than homogeneous, nucleation is the rate-controlling process. Floudas [1994a] determined that the width of the kinetically accessible under-cooling region is over-predicted by Fredrickson [1989a].

### **2.2.5 The Avrami Equation**

The Avrami equation [Avrami, 1939; Avrami, 1940; Avrami, 1941] is a model for the crystallization kinetics of a crystallizing monomer system, and is readily extended to crystallizing polymer melts. The equation provides insight into the rate at which the materials crystallize and the mechanism by which the structure is growing. That is, the equation can predict if a growing nucleus is expanding in one, two, or three dimensions. By analogy, the Avrami equation has been used to describe the rate of phase separation of block copolymers [Floudas, 1994b]. Section 2.2.5.1 will describe the assumptions of the Avrami equation and how it is derived for crystallizing monomers. Details of the information can be ascertained from the model through the Avrami model and the physical meaning of the Avrami parameters, namely the rate constant and Avrami exponent, will be presented. Section 2.2.5.2 will show how the Avrami equation for crystallization can be extended to phase separating polymers.

#### **2.2.5.1. Original Avrami Equation**

The original model for nucleation and growth of monomers is the free growth model, which assumes that growing nuclei do not interfere with one another [Mandelkern, 2002]. While the theoretical basis for the model is sound, the model relies on the assumption that the nucleation rate is either constant or nucleation is instantaneous at time  $t = 0$  [Avrami, 1939;

Avrami, 1940; Avrami, 1941]]. Further, failure to account for impingement is not physically realistic and means that there is no mode of stopping growth, allowing for the fraction of ordered state to exceed unity. In order to overcome these limitations of the free growth model, a modified version of the model to account for impingement was introduced [Avrami, 1939; Avrami, 1940; Avrami, 1941]. Avrami [1939; 1940; 1941] introduced the concept of the phantom nuclei to account for nuclei allowed to develop in an already ordered domain. The fraction of disordered matter in the sample,  $\lambda(t)$ , is taken as the ratio of the change in actual transformed mass fraction,  $(1-\lambda)$ , to the change in transformed mass fraction including phantom nuclei,  $(1-\lambda)'$ . The Avrami relationship takes the form [Avrami, 1941]:

$$1 - \lambda(t) = 1 - \exp \left[ \frac{-\rho_c}{\rho_l} \int_0^t v(t, \tau) N(\tau) d\tau \right] \quad (2.2-20)$$

where  $\rho_c$  is the density of the ordered (crystallized) material,  $\rho_l$  is the density of the untransformed material,  $v(t, \tau)$  is the volume of the growing nucleus at time  $t$ , initiated at time  $\tau$ , and  $N(\tau)$  is the nucleation rate. The growth can be linear, meaning that it is controlled by ordering at the interface of the ordering domain and the growth rate is linear with time. Growth may also be controlled by the diffusion of the crystallizing species through the sample and growth rate is proportional to time to a fractional power. By assuming a constant nucleation rate from time  $t = 0$  onward, and linear, constant-rate crystallite growth, the solution to Eq. 2.2-20 is [Avrami, 1930; Avrami, 1940; Avrami, 1941]:

$$1 - \lambda(t) = 1 - e^{-kt^n} \quad (2.2-21)$$

This model predicts that the degree of ordering in time will be sigmoidal. Characteristic curves for Avrami kinetics at various values of  $n$  are shown in Figure 2.2-3.

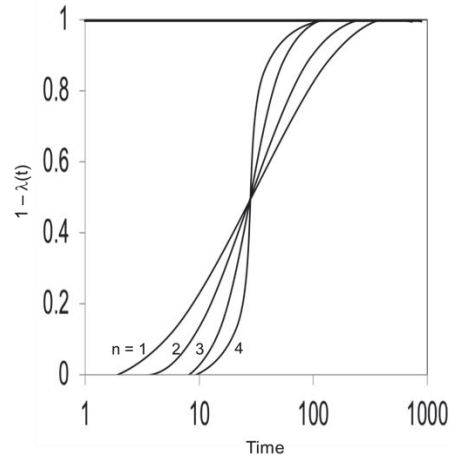


**Figure 2.2-3.** Theoretical crystallization curves based on the Avrami equation for various Avrami exponent values. Reproduced from [Mandelkern, 2002].

The exact shape of the crystallization curve is governed by the rate constant,  $k$ , and the Avrami exponent,  $n$ . As the Avrami exponent increases, the rate of change of  $\lambda(t)$  increases. This illustrates that the Avrami exponent along with the rate constant contain information regarding the ordering rate. As a result, the rate constant alone is not sufficient to compare ordering times among different systems. Both factors can be accounted for by interpreting ordering time based on the ordering half-time [Mandelkern, 2002; Floudas, 1994]:

$$t_{1/2} = \left( \frac{\ln[2]}{k} \right)^{1/n} \quad (2.2-22)$$

When dealing with constant nucleation and growth rates, the Avrami exponent, which varies between one and six, can be correlated to the type of growth and the geometry of the growing ordered phase. Table 2.2-3 shows the types of growth corresponding to values of the Avrami exponent.

Table 2.2-2. Interpretation of Avrami exponent for various modes of nucleation and growth. Reproduced from Mandelkern, 2002.

Growth habit	Homogeneous nucleation				Heterogeneous nucleation
	<u>Linear growth</u>		<u>Diffusion controlled growth</u>		Linear growth
	Steady state	$t = 0^1$	Steady state	$t = 0$	
Sheaf-like	6	5	7/2	5/2	$5 \leq n \leq 6$
Three-dimensional	4	3	5/2	3/2	$3 \leq n \leq 4$
Two-dimensional	3	2	2	1	$2 \leq n \leq 3$
One-dimensional	2	1	3/2	1/2	$1 \leq n \leq 2$

<sup>1</sup>All nuclei activated at  $t = 0$

The Avrami exponent is a combined function of the ordering rate, growth mechanism and the dimensionality of the growing structure. In homogeneous nucleation, linear growth can be distinguished from diffusion controlled growth based as the former is characterized by an integer Avrami exponent, while the latter is defined by fractional values of  $n$ . For a given type of growth mechanism, the dimensionality of the growth of the crystalline domain is prescribed a unique Avrami exponent. One-dimensional growth is growth occurring in a single plane, and is characteristic of lamellar stacking. Two-dimensional growth is usually attributed to the development of a cylindrical structure. Finally, three-dimensional growth correlates to spherulitic growth. Unfortunately, as Table 2.2-3 also illustrates, ambiguity arises when attempting to assign the nucleation and growth mechanism. Within both linear and diffusion controlled growth, different growth dimensionalities can have the same Avrami exponent depending on whether the nucleation is a continually occurring event during crystallization (stead-state) or if all nuclei are initialized at  $t = 0$ . Further, in the case of heterogeneous nucleation, the Avrami exponent may be a non-integer value lying between two extremes. As

such, a given growth dimensionality can be described by an integer value that can also describe a type of homogeneous linear growth, or by a fractional exponent that can also correlate to a type of diffusion controlled growth. It has also been noted that the value of the Avrami exponent can change over the course of crystallization since it is a function of growth rate [Young, 1991]. However, this last limitation can be relaxed by analyzing early stages of the crystallization process. Nonetheless, while the Avrami exponent is partially a property of the growth type, it cannot be solely relied on to determine growth geometry and nucleation type.

### 2.2.5.2. Extension of the Avrami Equation to Polymer Systems

In polymer systems, complete crystallization is rarely realized [Mandelkern, 2002]. In order to account for this, the ratio of the change in actual transformed mass to the change in phantom transformed mass is modified to include the transformed mass fraction at the termination of the process,  $\lambda(\infty)$ . For polymers, Eq. 2.2-20 and Eq. 2.2-21 become Eq. 2.2-24 and Eq. 2.2-25, respectively [Mandelkern, 2002]:

$$\ln \left[ \frac{1 - \lambda(\infty)}{\lambda(t)} \right] = \frac{1}{1 - \lambda(\infty)} \frac{\rho_c}{\rho_l} \int_0^t v(t, \tau) N(\tau) d\tau \quad (2.2-24)$$

$$\ln \left[ \frac{1 - \lambda(\infty)}{\lambda(t)} \right] = \frac{1}{1 - \lambda(\infty)} kt^n \quad (2.2-25)$$

While Eqs. 2.2-20 and 2.2-21 assumed that the system reaches a completely ordered state as  $t$  approaches infinite time, in Eqs. 2.2-24 the extent of ordering will terminate at  $\lambda(\infty)$ . Though these new equations do not assume  $\lambda(t \rightarrow \infty)$ , they cannot predict  $\lambda(\infty)$ . The maximum achievable ordering is an additional model parameter that needs to be estimated from separate experiments. Though the form is different, the interpretation of the Avrami exponent is presumed to be unaltered.

The Avrami parameters (rate constant  $k$  and Avrami exponent  $n$ ) can be determined from experimental data by tracking  $\lambda(t)$  over time and taking the natural logarithm of Eq. 2.2-21 to linearize the equation:

$$\ln[-\ln(\lambda(t))] = \ln(k) + n \ln(t) \quad (2.2-26)$$

As discussed in Section 2.2.2, the degree of ordering in a block copolymer system can be tracked with changes in the dynamic mechanical response or scattering intensity from SAXS experiments. It has been suggested that by analogy,  $\phi(t)$  can be substituted for  $\lambda(t)$  in Eq. 2.2-26 [Floudas, 1994a, b]. Then, by tracking  $\phi(t)$  with rheology or SAXS,  $\lambda(t)$  vs.  $\ln(t)$  can be fit with Eq. 2.2-26 to obtain the Avrami parameters.

Alternatively, Eq. 2.2-25 can be recast in terms of measurable variables. For instance, in terms of the volume of the ordered state,  $V_t$ , Eq. 2.2-25 becomes [Mandelkern, 2002; Young, 1991]:

$$\ln \left[ \frac{V_\infty - V_t}{V_\infty - V_0} \right] = \frac{1}{1 - \lambda(\infty)} k t^n \quad (2.2-27)$$

where  $V_\infty$  is the volume of the ordered state characterized by  $\lambda(\infty)$  and  $V_0$  is the volume of the disordered state. It stands to reason that other values, including complex modulus or scattering peak intensity could also be introduced into Eq. 2.2-26 without changing its physical meaning.

The models provided in this section are derived to describe crystallization of monomer and polymer melt systems. It has been proposed that the phase separation of block copolymers is analogous to the crystallization process and Eqs. 2.2-21 and 2.2-25 can be used to model ordering kinetics of such systems [Floudas, 1994; Floudas, 1999; Liu, 2004]. The ordering of block copolymer melts and solutions has found to proceed over time in a manner similar to Avrami crystallization. Commonly, interpretation of  $n$  has remained the same for ordering melts.

However, the physical meaning of the Avrami parameters in ordering block copolymer solutions has gone unchecked. For instance, it is unclear if the Avrami exponents correspond to the individual microstructures or the dimensionality of the domains within which the ordered structures are forming. An evaluation of what the rate constant and Avrami exponent are indicating about the ordering process in block copolymer solutions is still needed.

### 2.2.6 Spinodal Decomposition

The concepts discussed thus far describe growth in the metastable region of the phase diagram. The mechanism by which growth is initiated in the unstable region is much different, as any small perturbations in the concentration will increase in amplitude [Jones, 2002]. Because the system is globally unstable, the fluctuations are no longer localized [Chaikin, 1995]. Rather, a sinusoidal concentration profile develops throughout the sample, with the wavelength governed by both thermodynamics and chain dynamics [Jones, 2002]. Short wavelength fluctuations are energetically unfavorable, while long wavelength fluctuations are impractical as they would require long distances for the chains to diffuse through. The scales of the fluctuations lie between these two extremes. The fluctuation amplitudes begin small, but gradually increase over time as material diffuses from low polymer block concentration regimes to high polymer block concentration regimes, while maintaining the characteristic wavelengths. The rate at which the amplitude grows,  $R(q)$ , is governed by the effective diffusion coefficient,  $D_{\text{eff}}$ , of the polymer chains through the medium:

$$R(q) = -D_{\text{eff}} q^2 \left( 1 + \frac{2\kappa q^2}{f_0''} \right) \quad (2.2-27)$$

$\kappa$  is the gradient energy coefficient,  $q$  is the wave vector, and  $f_0''$  is the second derivative of the free energy. To the author's knowledge, experimental exploration of spinodal decomposition in block copolymer solutions is limited.

While the modes for the onset of phase separation in the metastable and unstable region are quite different, the subsequent growth processes at later stages are comparable [Chaikin, 1995; Jones, 2002]. At this stage, growth is driven solely by the need to reduce interfacial tension. The interface narrows while the pure domains grow in size. Regardless of the region of the phase diagram in which the growth is occurring, the rate of domain growth scales as  $t^{1/3}$  [Jones, 2002]. In spite of this observation, spinodal decomposition still likely precludes the use of the Avrami model in the unstable region, since the Avrami equation is most valid in the early stages of structure development.

### **2.2.7 Order-Disorder Kinetics**

Beginning with some of the earliest work performed by Hashimoto et al. [1983], the disorder-to-order transition kinetics of block copolymer melts and solutions have been studied extensively [Hashimoto, 1983; Hashimoto, 1986a; Hashimoto, 1986b; Harkless, 1990; Rosedale, 1990; Amundson, 1992; Balsara, 1992a, b; Garetz, 1993; Jian, 1993; Schuler, 1993; Winter, 1993; Floudas, 1994a, b; Stuehn, 1994; Floudas, 1995; Hashimoto, 1995; Adams, 1996; Balsara, 1996a; Hashimoto, 1996; Sakamoto, 1997; Soenen, 1997a, b; Balsara, 1998; Hashimoto, 1998; Sakamoto, 1998a, b; Chastek, 2003; Nie, 2003; Chastek, 2004; Liu, 2004; Chastek, 2005; Yufa, 2009; Patel, 2010]. All of these studies concern ordering following a shallow temperature quench from the disordered state into the metastable regime of the phase diagram. The shallow temperature quench is employed to minimize temperature overshoot and growth is occurring in the metastable region and therefore proceeding by nucleation and growth.

In the above mentioned work, rheology, small angle X-ray scattering (SAXS), dynamic light scattering, static birefringence, polarized optical microscopy, and transmission electron microscopy have all been employed to study ordering kinetics. The microscopy techniques, POM and TEM, are susceptible to error due to the limited sampling area. Chastek [2003; 2004] cited limited view fields and large grains superimposing on one another as the reason for large discrepancies when tracking grain growth rates in a poly(styrene-*b*-isoprene) / DBP solution using POM. While static birefringence is sensitive to grain growth, cubic and bicontinuous phases, as well as defective cylinders, do not birefring, limiting the technique's applicability [Chastek, 2003; Park, 2004; Abuzaina, 2005].

SAXS and rheology, often in combination, are effective in tracking grain growth in both melts and solutions. In SAXS experiments, changes in the shape and intensity of the primary peak are used to determine  $\phi_c$  based on Eq. 2.2-5 and Eq. 2.2-6. Rheological measurements are made under oscillatory shear, as steady shear would induce orientation and could disrupt lattice formation. These experiments have employed both parallel plate and cone-and-plate fixtures, regardless of whether melts or solutions are being monitored. However, parallel plate fixtures are more commonly chosen. Measurements are made under oscillatory shear, as steady shear would induce orientation and could disrupt lattice formation [Balsara, 1992b]. Measurement frequencies are dependent on the system and author's bias, but typically range from on the order of  $10^{-1}$  to  $1 \text{ rad/s}^{-1}$ . The strain amplitude is chosen such that the material remains in the linear viscoelastic regime (LVE), where  $G'$  and  $G''$  are independent of strain. This is done to ensure the accuracy of rheometer calculations, which typically break down in the non-LVE region, and to mitigate any influence shear may have on structure development [Adams, 1996; Daniel, 2001].

In general, the ordering process of block copolymer melts has been found to display a sigmoidal change in the dynamic mechanical response over time, reminiscent of Avrami kinetics for crystallization in semicrystalline materials [Harkless, 1990; Floudas, 1994a, b; Stuehn, 1994; Floudas, 1995; Hashimoto, 1995; Hashimoto, 1998; Patel, 2010]. Representative curves based on scattering and rheology experiments are shown in Figures 2.2-4 and 2.2-5, respectively:

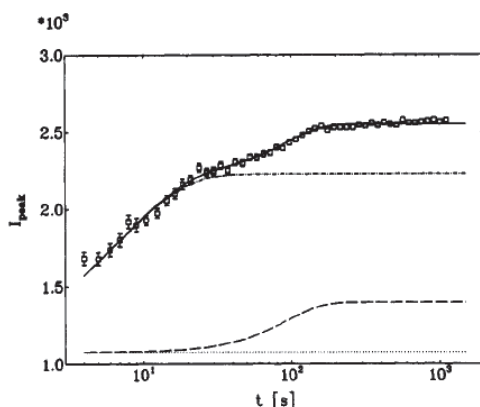


**Figure 2.2-4.** Integrated peak intensity obtained by SAXS as a function of time for an ordering block copolymer (poly(styrene-*b*-isoprene)) melt. Reprinted with permission from Schuler, M.; Stuehn, B. *Macromolecules* **1993**, *26*, 112. Copyright 1993 American Chemical Society.

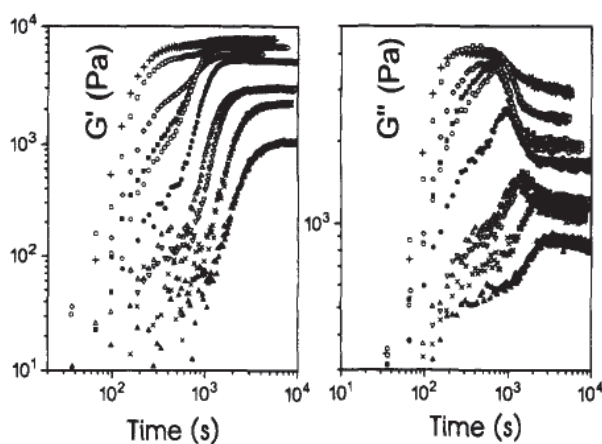


**Figure 2.2-5.** Dynamic mechanical response during the ordering of a star copolymer comprised of polystyrene and polyisoprene at various temperatures following temperature quenches. Reprinted with permission from Floudas, G.; Hadjichristidis, N.; Iatrou, H.; Pakula, T.; Fischer, E.W. *Macromolecules* **1994**, *27*, 7735. Copyright 1994 American Chemical Society.

The total ordering time is on the order of hours. Often, the nucleation and growth is preceded by an incubation period and possibly an initial rise in modulus. These result from undercooling of the disordered state and the evolution of concentration fluctuations, respectively. The first relaxation observed is due to separation of blocks on a local scale, while the development of a macrolattice is a slow process, yielding the second observed rise in modulus [Schuler, 1993; Winter, 1993; Stuehn, 1994]. The first relaxation is reported to be on the order of minutes, while coarsening of the grains occurs over a number of hours. The initial local separation is not always reported [Hashimoto, 1995] and may not be detectable by rheology depending on the temperature at which the experiment is conducted relative to the order-disorder transition temperature [Liu, 2004].

Fits of the data to Avrami's equation have led to both homogeneous and heterogeneous nucleation being reported. The Avrami exponents are typically between 3 and 4 [Floudas, 1994a, b; Sakamoto, 1998a], although values as low as 2 have been reported [Rosedale, 1990]. In order to deduce the nucleation mechanism of a star copolymer composed of polystyrene and polyisoprene, Floudas [1994a] analyzed  $t_{1/2}$  as a function of quench depth,  $\delta$ . If the ordering time is linear with  $\delta^{-1}$ , the nucleation is heterogeneous, whereas homogeneous nucleation will result in a linear relationship between  $t_{1/2}$  and  $\delta^{-2}$ . Based on this criteria, the author concludes that for the cases in which  $n = 3$ , the growth mechanism is heterogeneous nucleation. It is further suggested that when  $n = 4$ , phase separation is most likely proceeding via spinodal decomposition, though no proof is offered. Sakamoto [1998a] interpret Avrami exponents between 3 and 4 differently for a poly(styrene-*b*-isoprene) melt. The authors claim that these exponents correspond to homogeneous nucleation and growth. It can be seen, that ambiguity still arises in interpreting the Avrami exponent for block copolymer ordering.

The dependence of the ordering rate on ordering temperature is well understood. Growth is quite slow near the microphase separation transition temperature. The ordering time is parabolic with temperature, as the driving force for phase separation increases as the temperature is moved away from  $T_{ODT}$ , until a critical point at which kinetic effects take over, severely limiting chain mobility [Liu, 2004; Patel, 2010].

In addition to ordering time, Floudas [1994b] found that for the diblock copolymer SI, the Avrami exponent is parabolic with quench depth. In this case, as the quench depth increases,  $n$  increases from 2.8 to 4.3, then decreases. The initial rise can be attributed to a transition from nucleation and growth to spinodal decomposition as the quench depth increases. .

In solution, measurements are made at constant concentration. Similar trends in the ordering process to those of melts have been reported using polarized light intensity measurements, SAXS, and rheology [Balsara, 1996a; Nie, 2003; Liu, 2004]. Again, a competition between thermodynamic and kinetic factors governs the ordering rate. Chastek [2004] reported Avrami exponents of 2.6 to 2.8 for cylinders forming in SI solutions. Using POM, it was confirmed that heterogeneous nucleation was occurring. The Avrami exponents are reported to be slightly lower than the expected value of 3 due to grain anisotropy. Liu [2004] also tracked changes in the Avrami exponent as a function of ordering temperature in a solution of poly(styrene-*b*-ethylene-*alt*-propylene) in squalane. As the ordering temperature increases, the Avrami exponent increases from 3.8 to 6, then decreases to 1. Some of the extreme exponent values are ascribed to the nucleation process being too rapid for measurement, nucleation finishing before temperature fluctuations settled, or nuclei being too small to detect during the initial ordering process.

In addition to temperature effects, Liu [2004] also studied the influence of concentration on ordering time, but found no discernable trend. Rather, the influence of concentration on ordering time depended on temperature. However, these studies were limited to three concentrations in the semidilute region. Soenen [1997a, b] looked at the gel time of polymer solutions as a function of temperature and concentration by tracking  $\tan\delta$ . While more definitive trends with respect to polymer concentration are found, again only three concentrations were considered. Thus, while the ordering in solutions have been studied, albeit far less intensely than melt-phase ordering, the work is far from providing a full understanding of ordering during processing.

### **2.2.8 Order-Order Kinetics**

Order-order transitions must also be considered for film processing, particularly when selective solvents that give way to rich phase diagrams are used. Though the mechanisms of the transitions have been reported and appear to be well understood in both the melt and in solution, few studies on the kinetics are available [Matsen, 1998; Floudas, 1999; Floudas, 2000; Wang, 2002; Bang, 2003; Park, 2004; Honda, 2006]. Among the transitions considered are the fcc to bcc packing of spheres, the evolution of cylinders from spheres, transitions between cylinders and the gyroid structure, and between cylinders and lamella [Matsen, 1998; Floudas, 1999; Floudas, 2000; Wang, 2002; Bang, 2003; Park, 2004]. These transitions may take between a few seconds to hours. The transition again results in a sigmoidal response in  $G^*$ , with two rises developing depending on the transition type and experiment conditions, indicating a nucleation and growth process [Floudas, 1999; Floudas, 2000; Wang, 2002]. Floudas [1999] reported Avrami exponents for the transition from cylinders to lamellae and from cylinders to a gyroid

structure. The exponents are found to be 3 and 2, respectively. The authors determine that in the transition from one ordered state to another, heterogeneous nucleation is observed.

The work presented in this section provides beneficial information regarding the fundamentals of the phase separation kinetics of block copolymers. However, the studies suffer a variety of shortcomings that prohibits the application of this information in order to improve film processing. All transitions are thermally induced through either temperature quenches or jumps. These temperature changes are generally shallow to prevent significant overshoot. Shallow temperature quenches also guarantee that structures evolve via nucleation and growth. Though it may be the mode of phase separation in an industrial practice, spinodal decomposition of block copolymers has not garnered much attention. Further, in film processing, structures evolve as polymer films dry and pass through various ODTs and OOTs. Therefore, drying-induced transitions still need consideration in order for a full understanding of block copolymer behavior during processing to be achieved.

### 2.3 Solution-cast Block Copolymer Films

Polymer films can be melt-cast or solution-cast. Depending on the application and requirements for the film properties, solution-casting offers several advantages over melt-processing. If the order-disorder transition temperature of the melt is below the  $T_g$  of one or both of the blocks, segmental mobility will be limited in the ordered region while excessively high order-disorder transition temperatures may require heating the polymer to a temperature at which it is susceptible to thermal degradation [Huang, 2003]. This issue can be alleviated by processing the block copolymers in solution [Huang, 2003]. Solvents impart mobility to the copolymers without thermal treatment [Huang, 2004], broadening the processing window without risking polymer degradation. Solution-casting also allows for thinner films to be generated, typically in the range of 4 – 20  $\mu\text{m}$  [Benkreira, 1993b].

In processing solution-cast films, the morphology and properties of the films are strongly influenced by the drying process, polymer composition and solvent selectivity [Noshay, 1977; Kim, 2001; Lodge, 2003a; Huang, 2004]. Poor drying can lead to internal gradients, which diminish the mechanical integrity of the film [Kim, 2001]. Interactions between unlike polymer blocks and between the solvent and polymer directly control the phase behavior of the polymer-solvent system [Kim, 2001]. The strength, stiffness, toughness, transparency, and permeability of the cast film can all be controlled by varying the polymer and system composition in order to control the nature of the interface between polymers [Adhikar, 2003]. In addition, shear during casting, film thickness, and substrate type are of importance. Shear induces orientation and stabilizes the ordered phases as well as increasing the ODT temperature, allowing for higher processing temperatures [Hamley, 2004]. Typically in thick films, the morphologies near the free surface and in the bulk are different [Konrad, 2000]. In thin films, substrate surface effects

will determine whether or not the morphology in the bulk is similar to or distinctly different from surface morphologies [Libera, 1998].

Of particular interest for controlling film properties is the drying process. Drying temperature, air velocity (when dried by forced convection), drying time, drying rate, and the presence of solvent in the drying environment all determine the formation of ordered structures in the film [Kim, 2001; Yamamura, 2001; Huang, 2003]. Morphology formation and equilibrium structures can be controlled by balancing the rate of phase separation with the diffusion rate of solvent [Yamamura, 2001]. In rapid quenches, the solvent drying rate is typically much faster than the rate of phase separation, causing non-equilibrium structures to be frozen-in, while extremely slow drying rates allow equilibrium structures predicted by the phase diagram to form [Yamamura, 2001]. A post-processing procedure, such as thermal and solvent annealing, also influences microstructure and has been studied as a potential means for reaching equilibrium structures in films [Libera, 1998]. Annealing minimizes surface-thermodynamics effects, which can lead to more uniform observed morphologies between the interfaces and the bulk. Annealing time will dictate whether equilibrium structures or intermediate, metastable structures form [Shibayama, 1983c; Kim, 1998; Libera, 1998; Guo, 2008].

This section will discuss the processing of solution-cast films, in particular, the drying stage. A discussion on the work done in modeling the drying process will be provided, followed by an in depth analysis of experimental work that studies the influence of the aforementioned processing factors on film morphology.

### **2.3.1 Solution-casting**

In general, four coating processes exist [Benkreira, 1993a]. In a free withdrawal coating method, a substrate is plunged into a bath of liquid at a certain speed. In metering coating, a

solution is metered onto a surface using different flow geometries. The die coating technique utilizes flow geometries to deliver exact amounts of liquid onto a substrate. The fourth commonly used method is gravure coating. An exact amount of solution is deposited onto a substrate using a knurled steel roller, engraved with cells that are flooded with the solution to be cast. Liquid is either directly deposited onto a substrate or applied to a second roll that deposits the coating. This method allows for very thin films to be fabricated (typically 4 – 20  $\mu\text{m}$ ) at relatively high speeds ( $> 1 \text{ m/s}$ ). Either direct or reverse roll coating is possible. In direct roll coating, the stock is passed between the applicator and backup roller, which rotate in opposite directions. The thickness of the film is controlled by the clearance between the applicator and feed as well as the solution viscosity. The shear rate on the coating is dependent on the casting speed and gap distance, but usually ranges from  $10^4$  to  $10^5 \text{ s}^{-1}$ . During reverse roll coating, the material being coated is passed between two rollers rotating in the same direction. Typically, reverse roll coating yields smoother films, but the range of applicability is limited.

After coating the film, solvent is removed. The drying step is one of the most important parts of the casting process as it is the final point at which chemical and physical properties of the film can be affected [Guttoff, 2006]. Well-controlled drying is crucial to the integrity of the film. While residual solvent will always be present in the coating after drying, if the film leaves the dryer too wet, future product may be contaminated or the film may fuse to the take-up roll. Drying too rapidly can generate significant concentration profiles in the film [Kheshgi, 1997] and result in the coating being exposed to heat for long periods of time, bringing about the risk of physical damage, polymer degradation, or unwanted chemical reactions [Guttoff, 2006]. Drying can be achieved by any combination of three methods: convection, in which heated air flows over the coating and/or below the substrate; conduction, achieved by heating the sample by

direct contact of the bottom of the substrate with a heated surface; or radiation, by which heat is transferred to the sample by electric heaters [Guttoff, 2006]. Convection is most commonly used in industry as it offers numerous benefits over the other two processes. The flowing air will not only heat the sample, but also removes excess solvent that has evaporated, improving the flux of solvent across the film/air interface. Further, the flowing air has a high heat transfer coefficient, which allows for lower-temperature air to be used and prevent overheating the film. In addition, agitating the sweep gas can increase the mass transfer coefficient, which also enhances the flux of solvent at the interface [Kheshgi, 1997]. Due to its prevalence, the remainder of this section will concern convective drying of films.

Film drying proceeds by mass transfer from the film surface into the gas above the film and is a function of solvent volatility, and diffusion of volatiles through the film [Kheshgi, 1997]. In considering these factors, the drying process can be divided into three zones: the pre-dryer zone, the constant rate period (CDRP), and the falling rate period (FDRP) [Guttoff, 2006]. The pre-dryer zone is generally neglected when considering the drying process. It is the short-lived period after the film has been coated and before it enters the dryer.

In the second zone, the CDRP, the solution is fully wetted and solvent evaporation proceeds as if no polymer were present [Kim, 2001]. Solvent evaporation from the film surface is slower than the rate of diffusion of solvent through the film, making the former the rate-limiting process in this stage [Guttoff, 2006]. The film is void of temperature gradients and the evaporation is controlled only by mass transfer resistance at the film / air interface [Kim, 2001]. The equations governing the boundary condition at the film surface, which controls the drying rate, are given in Eq. 2.3-1 and Eq. 2.3-2:

$$\rho_i b_c \frac{dz_i}{dt} = k_m (C_i^{sat} - C_i^\infty) \quad (2.3-1)$$

$$C_i^{sat} = \gamma_i z_i \frac{P_i^{sat}}{RT(z_i)} \quad (2.3-2)$$

Table 2.3-1. Film drying parameters describing the boundary conditions for the drying of solution-cast films [Kim, 2001]

Parameter	Definition	Units
$\rho$	Molar density	mol / m <sup>3</sup>
$b_c$	Film thickness	m
$z_i$	Volume fraction of $i$	No units
$t$	Time	s
$k_m$	Mass transfer coefficient	m/s
$C_i^{sat}$	Saturation solvent concentration	mol / m <sup>3</sup>
$C^\infty$	Solvent concentration in bulk air	mol / m <sup>3</sup>
$\gamma_i$	Activity coefficient of $i$	No units
$P_i^{sat}$	Saturated vapor pressure of $i$	Pa
$R$	Gas constant	m <sup>3</sup> *Pa /K*mol
$T(z_i)$	Film temperature as a function of concentration	K

Table 2.3-1 provides the parameter definitions. Since the polymer will not evaporate, the only species considered in these equations and denoted by the subscript,  $i$ , is the solvent. When a sweep gas is present,  $C^\infty$  is zero. The saturation pressure is calculated from the Antoine equation. The mass balance at the surface must be coupled with the energy balance to determine the film temperature due to evaporative cooling. As these equations show, drying is controlled by solely surface evaporation in the CDRP and the rate of solvent loss with time is constant.

When a substantial amount of solvent has been removed, the film enters the falling rate period (FDRP). The surface is nearly dry at this point and diffusion of solvent through the film becomes rate limiting [Kim, 2001; Gutoff, 2006]. Whereas in the previous zone all heat supplied to the coating went into solvent evaporation, in this stage, the film begins to be heated. A substantial rise in the coating temperature is observed, along with a decline in drying rate, which persists until the end of the drying process.

While the drying process can be experimentally monitored using gravimetric techniques, in a casting process, high web speeds make such measurements difficult [Kim, 2001]. However, an accurate understanding of how a film will dry during processing is necessary for efficient dryer design. Hence, considerable efforts have gone into modeling the film drying process. In particular, it is desirable to be able to predict drying profiles based solely on neat polymer and pure solvent properties.

### 2.3.2 Modeling Film Drying

A schematic of the film drying process is provided in Figure 2.3-2:

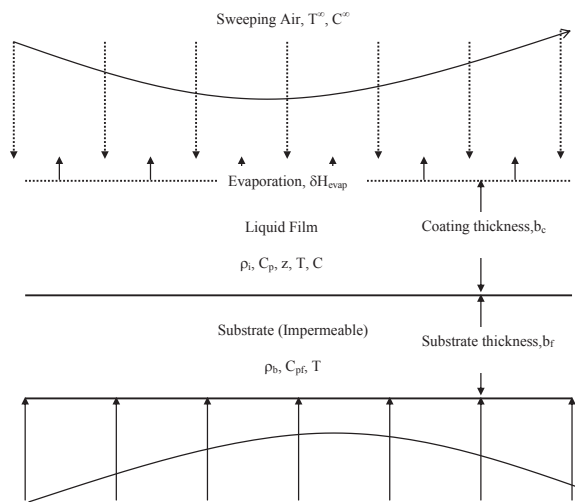


**Figure 2.3-1.** Schematic of drying of coated film on impermeable substrate by forced convection. Image reproduced from Kim et al. [2001]

The liquid film is characterized by a density,  $\rho_f$ , a heat capacity,  $C_p$ , and a temperature  $T$ . The volume fraction of polymer in the film is  $z$  in Figure 2.3-1 and the saturation concentration at the film/air interface is  $C$ . The impermeable substrate is assumed to be at the same temperature as the film. The substrate is also characterized by a density,  $\rho_b$ , and a heat capacity,  $C_{pf}$ .

At the film/air interface, mass transfer of the solvent into the boundary layer is the major drying process. This boundary condition is described by Eq. 2.3-1. Kim et al. [2001] suggested using Eq. 2.3-1 as a lumped parameter model for modeling film drying and were able to demonstrate reasonable success doing so when simulation results were compared to experimental drying data. More sophisticated models will be presented later in this section.

Heat transfer through the boundary layer and to the film surface must be accounted for, as it will contribute the mass transfer rate by providing the heat of evaporation of the liquid solvent. The heat transfer coefficient,  $h$ , can be predicted by Martin's correlation [Kim, 2001], which relates the heat transfer coefficient to the conditions of the sweep gas, including temperature, velocity, and the geometry through which the sweep gas is introduced. The correlation is given in Eq. 2.3-3, where  $K$  and  $n$  are constants that depend on the air temperature and impingement nozzle geometry:

$$\bar{h} = Kw^n \quad (2.3-3)$$

In addition to heat transfer, mass transfer at the interface provides the boundary condition for film drying at the free surface. The mass transfer coefficient,  $k$ , in conjunction with the vapor pressure of the solvent under the drying conditions and the concentration of solvent in the gas above the film surface, will dictate the rate of solvent evaporation. Through the Chilton-Colburn analogy, the heat transfer coefficient is correlated to the mass transfer coefficient [Kim, 2001]:

$$k_m = \frac{h}{k_a} (Le)^{0.42} \quad (2.3-4)$$

$$\frac{Sh}{Nu} = (Le)^{0.42} \quad (2.3-5)$$

Within the film, diffusion of solvent through the film must be modeled. Diffusion is dependent on both self-diffusion (solvent through solvent) and mutual diffusion (solvent through polymer). These processes are governed by the self- and mutual-diffusion coefficients,  $D_1$  and  $D^P$ , respectively. These diffusion coefficients can be predicted by invoking the free volume theory of Vrentas and Duda [1985a, b]. The mutual and self-diffusion constants are given as

$$D^P = D_1(1 - \phi_1)^2(1 - 2\chi\phi_1) \quad (2.3-6)$$

$$D_1 = D_0 \exp\left[\frac{-E}{RT}\right] \exp\left[\frac{-\gamma(\omega_1\hat{V}_1^* + \omega_2\xi\hat{V}_2^*)}{\left(\frac{K_{11}}{\gamma}\right)\omega_1(K_{21} + T - T_{g1}) + \left(\frac{K_{12}}{\gamma}\right)\omega_2(K_{22} + T - T_{g2})}\right] \quad (2.3-7)$$

The parameters in Eq. 2.3-6 and Eq. 2.3-7 are identified as follows:

$\phi_1$ : solvent volume fraction

$\chi$ : solvent-polymer interaction parameter

$D_0$ : pre-exponential constant

$E$ : energy required for molecule to overcome interactions

$\gamma$ : overlap parameter

$\hat{V}_i^*$ : critical hole free volume of component  $i$ , required for species to jump from current position to free volume

$\omega_i$ : mass fraction of component  $i$

$T_{gi}$ : glass transition temperature of component  $i$

$\hat{V}_{FH}^*$ : average hole free volume per gram of mixture

$\xi$ : ratio of the critical molar volume of solvent jumping unit to the critical molar volume of the polymer jumping unit

$K_{11}, K_{21}$ : free volume parameters for the solvent

$K_{22}, K_{12}$ : free volume parameters for the polymer

When the model was originally introduced, the authors [Vrentas & Duda, 1985a; 1985b] predicted the parameters both fully empirically and semi-empirically.  $D_0$ ,  $K_{11} / \gamma$ , and  $K_{21} - T_{g1}$

can be predicted from solvent viscosity data if the activation energy,  $E$ , is assumed to be zero.  $\xi$  can only be determined from experimentally obtained information on the polymer-solvent system. In order for the predictions of these parameters to be valid, data over a wide temperature range should be available. The polymer free volume parameters can be predicted either empirically or from the WLF parameters. While this method for predicting the diffusion coefficients is still widely accepted, it must be noted that in testing the model predictions against systems of toluene / polystyrene, ethylbenzene / polystyrene, and toluene / poly(vinyl alcohol), as high as 500% error was incurred. Hence, care must be taken in applying the Vrentas-Duda theory.

Zielinski et al. [1992] attempted to predict all the parameters of the Vrentas-Duda theory based on neat polymer and pure solvent properties. The critical hole volume,  $\hat{V}_i^*$ , of each component is predicted based on the specific volume of the solvent and polymer at absolute zero, which can be determined by group contributions. The free volume parameters of the polymer can be ascertained from viscosity data (Eq. 2.3-8) or WLF parameters,  $C_{12}$  and  $C_{22}$  (Eq. 2.3-9a, b).

$$\ln \eta_2 = \ln A_2 + \left( \frac{\gamma \hat{V}_2^*}{K_{12} [(K_{22} - T_{g2}) + T]} \right) \quad (2.3-8)$$

$$\frac{\gamma \hat{V}_2^*}{K_{12}} = 2.303 C_{12} C_{22} \quad (2.3-9a)$$

$$K_{22} = C_{22} \quad (2.3-9b)$$

Similarly, the solvent free volume parameters can be determined from the WLF parameters,  $C_{11}$  and  $C_{21}$ .

$$\frac{\gamma \hat{V}_1^*}{K_{11}} = 2.303 C_{11} C_{21} \quad (2.3-10a)$$

$$K_{21} = C_{21} \quad (2.3-10b)$$

The only parameter that Vrentas and Duda [1985a, b] could not determine from pure component data is  $\xi$ . Zielinski [1992] notes that this parameter can be determined from the following relationship

$$\xi = \frac{\tilde{V}_1^o(0)}{\tilde{V}_{2j}} \quad (2.3-11)$$

The numerator is the specific volume of the solvent at absolute zero and is again predicted by group contributions. The denominator can be determined from the glass transition temperature of the polymer and can therefore be obtained from pure polymer data. By using the fully predictive model, the authors find that the theoretical diffusion coefficients agree well with literature data. However, the use of the model should be limited to within 150°C above the system glass transition temperature. The accuracy of the model also diminishes as the polymer concentration increases.

Early approaches to modeling film drying [Blandin, 1987; Waggoner, 1989] utilized Fickian diffusion to predict concentration profiles within the film and drying rates under unsteady-state conditions. However, these studies fail to account for temperature profiles in the film, assume the diffusion coefficient is constant, and do not consider film shrinkage. The work of Vrentas and Vrentas [1994] accounted for all these factors. Like Blandin [1987] and Waggoner [1989], the authors model the drying process by unsteady-state Fickian diffusion. However, they now include terms to account for changes in film thickness and the temperature profile through the film. Figure 2.3-3 shows the system assumed by the authors. The corresponding equations for heat and mass transfer are also provided. The properties denoted by

$G$  or  $g$  are defined for the gas phases above the film and below the substrate, respectively. Any parameters labeled  $S$  or  $P$  respectively correspond to the solvent and polymer phases.

The diagram shows a cross-section of a film/substrate system. The vertical axis is labeled  $x$  and the horizontal axis is labeled  $y$ . The system is divided into three regions: Gas (top), Polymer Layer (middle), and Substrate (bottom). The boundaries are at  $x = X(y)$ ,  $x = 0$ , and  $x = -H$ .

**Gas (top):**

- Equation:  $p_{1i}^G = f(\rho_1^P)$
- Equation:  $-D^P \frac{\partial \rho_1^P}{\partial x} - \rho_1^P \frac{dX}{dt} = k_1^G [p_{1i}^G - p_{1b}^G] - k^P \frac{\partial T^P}{\partial x} = \Delta H_{vap} \rho^P \frac{\partial X}{\partial t} + h^G (T^G - T^P)$
- Equation:  $\rho^P \hat{C}_p^P \frac{\partial T^P}{\partial t} = k^s \frac{\partial^2 T^P}{\partial x^2}$

**Polymer Layer (middle):**

- Equation:  $\frac{\partial \rho_1^P}{\partial t} = \frac{\partial}{\partial x} \left( D^P \frac{\partial \rho_1^P}{\partial x} \right)$
- Equation:  $\frac{\partial \rho_1^P}{\partial x} = 0$
- Equation:  $k^P \frac{\partial T^P}{\partial x} = k^s \frac{\partial T^s}{\partial x} \quad T^P = T^s$
- Equation:  $\rho^s \hat{C}_p^s \frac{\partial T^s}{\partial t} = k^s \frac{\partial^2 T^s}{\partial x^2}$

**Substrate (bottom):**

- Equation:  $k^s \frac{\partial T^s}{\partial x} = h^g (T^s - T^g)$

**Gas (bottom):**

- Equation:  $T^g \quad h^g$

$$\frac{\partial X}{\partial t} = \left[ \frac{D^P \hat{V}_1^P}{1 - \rho_1^P \hat{V}_1^P} \frac{\partial \rho_1^P}{\partial x} \right]_{x=X}$$

**Figure 2.3-2.** Film / substrate system and corresponding mass and energy balance equations assumed by Vrentas and Vrentas [1994] to model polymer film drying using unsteady-state Fickian diffusion.

Table 2.3-2. Mass and heat transfer parameters used in film drying analysis by Vrentas and Vrentas [Vrentas, 1994]

Parameter	Definition
$p_{1i}^G$	Partial pressure of component 1 in the gas phase
$p_{1b}^G$	Partial pressure of component 1 in the bulk phase
$\rho_i^j$	Density of component $i$ in the $j$ phase
$\rho^i$	Density of component $i$
$D^p$	Mutual diffusion coefficient in the polymer phase
$k_i^j$	Mass transfer coefficient of component $i$ in the $j$ phase
$k^j$	Thermal conductivity of the $j$ phase
$\Delta H_{vap}$	Heat of vaporization of solvent
$h^j$	Heat transfer coefficient of the $j$ phase
$\hat{C}_p^j$	Heat capacity of the $j$ phase
$T^j$	Temperature of the $j$ phase

In the equations presented in Fig. 2.3-3, the mass flux and energy balance in the film are being solved in a region of time-dependent thickness. To simplify the solution of these equations, the authors propose transforming the equations to a dimensionless form in order to immobilize the phase transformation. In order to do so, the following dimensionless variables are introduced:

Length variable:  $\eta = \frac{x}{X(t)}$  (2.3-12)

$$\text{Mass density: } c = \frac{\rho_1^P}{\rho_{10}^P} \quad (2.3-13)$$

$$\text{Temperature: } T^* = \frac{T - T_0}{T^G - T_0} \quad (2.3-14)$$

$$\text{Time: } t^* = \frac{D_0^P t}{L^2} \quad (2.3-15)$$

$$\text{Thickness: } X^* = \frac{X}{L} \quad (2.3-16)$$

Implementing the dimensionless variables yields the following governing equations:

$$\text{Energy Balance: } \frac{dT^*}{dt^*} = \frac{\frac{L(h^G + h^s)}{D_0^P \rho^P \hat{C}_p^P} [1 - T^*] + \frac{h^s (T^s - T^G) L}{D_0^P \rho^P \hat{C}_p^P (T^G - T_0)} + \frac{\Delta H_{vap}}{\hat{C}_p^P (T^G - T_0)} \frac{dX^*}{dt^*}}{\frac{\rho^s \hat{C}_p^s H}{\rho^P \hat{C}_p^P L} + X^*} \quad (2.3-17)$$

$$\text{Solvent continuity: } \frac{\partial c}{\partial t^*} - \frac{\eta}{X^*} \frac{dX^*}{dt^*} \frac{\partial c}{\partial \eta} = \frac{1}{(X^*)^2} \frac{\partial}{\partial \eta} \left( \frac{D^P}{D_0^P} \frac{\partial c}{\partial \eta} \right) \quad (2.3-18)$$

$$\text{Thickness variation: } X^* \frac{dX^*}{dt^*} = \left[ \frac{\hat{V}_1^P \rho_{10}^P \left( \frac{D^P}{D_0^P} \right) \frac{\partial c}{\partial \eta}}{1 - \rho_{10}^P \hat{V}_1^P c} \right]_{\eta=1} \quad (2.3-19)$$

Boundary conditions:

$$\frac{\partial c}{\partial \eta} = 0 \text{ at } \eta = 0 \quad (2.3-20a)$$

$$-\frac{D^P}{D_0^P} \left( \frac{\partial c}{\partial \eta} \right)_{\eta=1} - c(\eta=1) X^* \frac{dX^*}{dt^*} = \frac{k_1^G [p_{1i}^G - p_{1b}^G] L X^*}{D_0^P \rho_{10}^P} \quad (2.3-20b)$$

$$c(0,\eta)=1 \quad (2.3-20c)$$

$$X^*(0)=1 \quad (2.3-20d)$$

Though the authors provide a scheme for solving the coupled equations, they offer no actual solution. Other groups have used this approach and results are in agreement with literature [Alsoy, 1998]. The method was expanded to multi-component systems by Alsoy [1999]. While the authors are for the most part consistent with Vrentas and Vrentas [1994], they neglect temperature gradients in the film, assuming that heat transfer in the gas phase is greater than that through the polymer or substrate. In spite of this assumption, using a model system of polystyrene / THF / toluene, the model yields results consistent with literature.

Since the original paper by Vrentas and Vrentas [1994], more sophisticated models have been developed. Wong [2004] utilizes Fickian diffusion to consider a semicrystalline polymer that crystallizes during the drying process. Crystallization will influence the drying by limiting diffusion as a more tortuous path is generated by the crystalline domains. The Vrentas-Duda free volume theory is used to deduce the diffusion coefficients. Despite presenting a novel approach to the drying process, the authors assume isothermal drying. Evaporative cooling and temperature profiles will undoubtedly influence crystallization kinetics. Further, a simple model for crystallization is used. The authors assume crystallization rate can be described by Eq. 2.3-21.

$$\frac{\partial v}{\partial t} = \sum_{i=1}^{n-2} k_i w_i \quad (2.3-21)$$

where  $v$  is the volume fraction of crystalline material in the system,  $k_i$  is the folding rate and  $w_i$  is the weight fraction of component  $i$ . Prior to this work, Cairncross et al. [1996] considered the

drying of a system that is co-currently cross-linking. The estimation of the reaction kinetics are sound and effective for reacting systems. In spite of these advances, modeling of a phase separating block copolymer system with non-simplified kinetics models has yet to be proposed.

The models presented so far have assumed Fickian diffusion under all conditions. Vinjamur et al. [2002] consider non-Fickian diffusion by accounting for polymer relaxation, the generation of stress gradients, and the phenomenon of skinning during drying. During film shrinkage, stress gradients develop, which influence the transport of solvent through the film. Near the surface of the film, stress relaxations are quick and give rise to non-Fickian solvent diffusion. If the sweep gas velocity and temperature are sufficiently high, a thin layer of low-solvent concentration forms in a process known as skinning. The group uses the Vrentas-Duda model for the diffusion coefficient, but proposes an altered form of the solvent flux equation, which incorporates stress relaxations. In the new model, the mass transport equation is given below with the parameter definitions provided in Table 2.3-3.

$$j = -D \frac{\partial C}{\partial \xi} - E \frac{\partial \pi}{\partial \xi} \quad (2.3-21)$$

$$E = D \frac{\hat{V}_s^2 M_{ws} G_o}{RT} \frac{1}{\left(1 + C \hat{V}_s\right) \left(\frac{\partial f(C)}{\partial C}\right)} \quad (2.3-21)$$

Table 2.3-3. Vinjamur [2002] non-Fickian film drying model parameters

Parameter	Definition
j	Mass flux
D	Mutual diffusion coefficient
C	Solvent concentration per unit volume of polymer
$\xi$	Distance in polymer material coordinates
E	Diffusion coefficient for the stress
$\pi$	Microscopic in-plane stress in the polymer due to film shrinkage

$\hat{V}_s$	Partial specific volume of the solvent
$M_{ws}$	Molecular weight of solvent
$G_o$	Shear modulus of the pure polymer
$R$	Gas constant
$T$	Coating temperature
$f(c)$	Local equilibrium fugacity of the solution

The stress experienced by the polymer in the film is described by Maxwell's model, assuming a single relaxation time,  $\tau_{relax}$ .

$$g(C)\frac{\partial C}{\partial t} = \frac{\partial \pi}{\partial t} + \frac{\pi}{\tau_{relax}} \quad (2.3-22)$$

The coefficient,  $g(C)$ , is the ratio of the instantaneous shear modulus to the shear modulus of the pure polymer. The relaxation time of the polymer is determined as the ratio of the neat polymer self-diffusion coefficient to the self-diffusion coefficient of the polymer at the concentration of interest. Thus, the relaxation time can be predicted from the Vrentas-Duda free volume parameters. The energy balances are presumed to be unaffected by stress and polymer relaxation. As such, they are of the same form presented previously in the Vrentas and Vrentas [1994] analysis.

The new model is tested on a PMMA/acetone system due to availability of experimental data for comparison. The authors compared model predictions to experimental data in the context of the three drying periods. The new model predicts a sigmoidal concentration profile in the warmup period with a flat profile near the surface, as opposed to the sharply decreasing profile predicted by Fickian diffusion. Vinjamur [2002] anticipates the ability of stresses near the surface to draw solvent to the surface, diminishing the severity of the concentration gradient. In the constant-rate period, Fickian diffusion takes over near the surface. As one moves from the free surface to the substrate, a transition back to non-Fickian diffusion is observed, before

Fickian diffusion is recovered closer to the substrate. As time increases during the constant drying rate period, the width of the Fickian diffusion zone increases toward the substrate. In the falling rate period, significant concentration gradients develop as non-Fickian diffusion again takes over. Further, a thin, low-concentration layer evolves near the surface of the film. The simulation agrees well with results the group obtains experimentally. By incorporating polymer chain dynamics, this model is one of the more sophisticated and complete models for predicting polymer film drying.

All of the models reviewed thus far presume the ratio of the friction factors of the components is constant in order to simplify the calculations. Verros and Malamataris [2005] have presented an approach to predicting film drying behavior of multi-component systems using Fickian diffusion in concert with the Gibbs-Duhem theorem for diffusing systems, and considered friction coefficients whose ratios change during drying. To modify the original Vrentas-Duda theory for the diffusion coefficient, the authors solve the following relationships for the friction factor,  $\zeta_{ij}$ .

$$\sum_{k=1}^3 c_k \zeta_{ik} = 0 \quad (2.3-23a)$$

$$\zeta_{12} = \sqrt{\zeta_{11}\zeta_{22}} \quad (2.3-23b)$$

$$\zeta_{13} = \frac{v_3}{u_3} \left( \frac{RT}{N_A^2 D_{T1}} - \frac{u_2}{v_2} \zeta_{12} \right) \quad (2.3-23c)$$

$$\zeta_{23} = \frac{v_3}{u_3} \left( \frac{RT}{N_A^2 D_{T2}} - \frac{u_1}{v_1} \zeta_{12} \right) \quad (2.3-23d)$$

$$D_{Ti} = \frac{D_i^*}{1 - \frac{D_i^*}{D_i^0}} \quad (2.3-23e)$$

$$D_i^0 = \frac{RTM_i v_i}{u_i \zeta_{i^*} N_A^2} \quad (2.3-23f)$$

The solution of these equations, along with the equations to model the mass flux and moving boundary layer, proved to be labor intensive. Nonetheless, the drying behavior of a model system of formamide-acetone-cellulose acetate is shown to be in good agreement with literature data. This approach provides a means to extend analysis to a variety of multi-component systems.

Since the work of Vrentas and Vrentas [1994], significant improvements have been made in predicting film drying. Individually, authors have explored the drying behavior as the system crystallizes or cross-links, considered the influences of chain dynamics during drying, and accounted for multiple components. Unfortunately, a unification of these works has yet to be realized, making true film properties difficult to predict purely through modeling.

### 2.3.3 Processing Conditions Affecting Film Morphology

The ability of drying rate to govern the microstructures attained during the processing of block copolymer films has been widely studied. The drying rate not only determines the morphologies formed, but the size of and distance between microdomains and the orientation of the morphologies [Pedemonte, 1974; Shibayama, 1983c; Miyake, 1993; Libera, 1998; Yamamura, 2001; Huang, 2003]. Miyake [1993] studied the formation of percolated structures in thin films. The group obtained bicontinuous structures of cylinders upon rapid drying. Huang [2003] studied the influence of drying rate on structure formation of poly(styrene-*b*-butadiene) and poly(styrene-*b*-butadiene-*b*-styrene) during the drying of solution-cast films using the neutral solvent toluene. At high drying rates and below a critical molecular weight,  $MW^*$ , inverted

phases form, with polybutadiene (PB) cylinders in a polystyrene (PS) matrix. The formation can be understood in terms of enthalpy effects, which increase directly with molecular weight. Using the equations for free energy supplied by Helfand and Wasserman [1982], the authors plotted the difference in free energy between the inverted and normal phases against the number of polymer chains per unit volume. They found that the inverted phase free energy is always higher than the normal phase free energy. The inverted phase is a metastable structure formed during drying. When the film composition reaches the semidilute region, chains overlap, resulting in repulsion between unlike blocks and the formation of aggregates. Within the aggregates, momentary compressions form and relax. Swifter blocks will relax faster and diffuse into the corona. The PB block is faster than PS due to its lower molecular weight in the polymers used. Hence, it forms the cylinder while PS forms the matrix. This mechanism is accurate at low molecular weights, when the PB is faster than PS and the difference in free energy between the inverted and normal phases is minimal. As molecular weight increases, PB becomes entangled whereas PS is not. This allows PS to diffuse more rapidly and fill the corona. Further, the difference in free energies increases with molecular weight, making inverted phases very unstable. Given ample time, achieved by slowing the drying rate, the system relaxes to normal cylinders.

As was discussed in section 2.1, the size of the ordered structures and domains is a function of the thermodynamics of the system. Since growth occurs over time, kinetic factors must also be considered to predict the structure size during film drying. Shibayama et al. [1983c] explained the domain growth phenomenon based on thermodynamic considerations. In their work, the authors observed lamellae, cylinders, and spheres. As the fraction of polymer in the film increases, the blocks stretch and align perpendicular to the interface. In doing so, the end-to-end distances of the blocks increase and the thickness of the lamella or radii of the

cylinders or spheres increase. This growth is favored as the decreased interfacial energy is more significant than the loss of conformational entropy. Changing structure size will increase the number of chains per unit area,  $N/S$ . In the case of lamellae and cylinders, this increase in  $N/S$  displaces the chemical junction points along the interface. The relaxation time from this displacement increases as the polymer concentration in the film increases. If the drying rate is fast relative to the relaxation time, the microstructures are frozen in. They may be further reduced in size by deswelling as solvent leaves the structure. In spheres, the change in radius is governed by the transport of the PS chains through the PB matrix. This gives rise to thermodynamic and frictional enthalpies, making the potential barrier for the growth of spheres higher than that for lamellae and cylinders. The resulting increase in relaxation time hinders the growth of spheres and sphere growth is less drastic during drying.

Orientation of the microstructures has garnered attention, particularly in the case of cylinders, which may align perpendicular to the film surface or in-plane [Gattiglia, 1995; Kim, 1998; Konrad, 2000]. It is generally agreed that the in-plane orientation is more stable and that, given enough time, cylinders will align parallel to the film surface. Kim [1998] explains the thermodynamic stability of the parallel orientation based on energy effects:

$$G_I = 2\pi r t N_v \gamma_{PB/PS} + 2A \gamma_{PB/Air} \quad (2.3-24)$$

$$G_v = [2\pi r t N_v + 2\pi r^2 N_v] \gamma_{PB/PS} + 2A \gamma_{PB/air} \quad (2.3-25)$$

$$\Delta G = G_v - G_I = 2\pi r^2 N_v \gamma_{PB/PS} = 2\phi_{PS} \gamma_{PB/PS} t \quad (2.3-26)$$

$G_I$  is the free energy of the in-plane structures,  $G_v$  is that of the vertical structures,  $N_v$  is the number of chains per volume,  $r$  is the cylinder radius,  $A$  is the film surface area,  $\gamma$  is the interfacial energy, and  $t$  is the film thickness. As thickness decreases, the free energy difference

decreases. It is concluded that the driving force toward in-plane structures is increased in thick films.

Konrad [2000] reports that in thick films, a mixture of vertical and in-plane structures are observed regardless of drying conditions. The vertical structures are predominant near the free-surface, but upon etching, only in-plane structures are found. The authors ascribe this behavior to surface energy effects. It is reasonable to suggest that since solvent evaporation is faster near the surface, vertical structures form at the air-film interface [Libera, 1998]. It has also been proposed that the orientation is due to the repeat distance between cylinders [van Dijk, 1996]. Thick films can form complete in-plane orientation because there are no restrictions on the spacing. In thin films, which have a thickness equivalent to only a few repeat equilibrium distances, the top and bottom surface impose an in-plane orientation to allow more degrees of orientation freedom. In very thin films which are on the order of one or fewer repeat distances in thickness, the parallel orientation costs too much configurational freedom and equilibrium distances cannot be maintained. Vertical orientations form to allow equilibrium repeat distances to exist between cylinders.

Vertical cylinders are observed throughout films at high drying rates [Kim, 1998; Libera, 1998]. As drying rate is decreased in the experiments performed by Libera [1998], the cylinders transition from strictly vertical to a mixture of vertical and in-plane, to strictly in-plane. This is because the ability for the system to reach equilibrium is time dependent, which directly correlates to drying rate. The initial formation of vertical cylinders can be explained in terms of solvent diffusion [Libera, 1998]. At high drying rates, the structures must align perpendicular to minimize the tortuosity of the path taken by the solvent out of the film. The condition is not as stringent when dealing with cylinders as vertical and in-plane structures can be diffused through.

This gives rise to a mixture of orientations, but vertical cylinders dominate. When the drying rate is slow enough that fast diffusion is not vital, the cylinders can align in-plane.

The effects of drying conditions cannot be wholly decoupled from the effects of solvent type. Factors such as vapor pressure [Kim, 1998] and solvent selectivity [Nishioka, 1969; Wilkes, 1969; Saam, 1970; Pillai, 1972; Pedemonte, 1974; Huang, 2004; Guo, 2008] will dictate the behavior of the solvent as it relates to the drying rate and affect the morphology. Huang and coworkers [2004] studied the effect of solvent selectivity on the formation of inverted structures in SB and SBS films using two PS-selective solvents (toluene and benzene) and a PB-selective solvent (cyclohexane). In the former two solvents, the copolymer was capable of forming inverted structures, while in cyclohexane, only normal phases appear. The authors conclude that the swelling of the polystyrene domain by the PS-selective solvent causes the curvature of the domain interface toward PB. If the increase in PS volume fraction is high, inverted phases form. However, increasing the volume fractions also increases the effective volume, in turn increasing surface energy. When the interaction parameters of the solvent with each individual block is only slightly different, the driving force for curvature of the interface is small relative to the thermodynamic effects and the system will tend back toward the normal phase.

The employment of solvent selectivity to control microstructure is not restricted to the casting solution. Annealing is typically performed by holding samples at elevated temperatures for long period of time. This will cause structures to change size, transition to new ordered structures [Kim, 1998; Libera, 1998] or increase interdomain spacing [Shibayama, 1983c; Libera, 1998]. The drawback to thermal treatment is that it is incapable of causing ordering from disordered phases. The introduction of solvent into a system imparts mobility to the polymer chains without thermal treatment. During solvent annealing, the solvent diffuses in and out of

the film. This process will equilibrate in time. Therefore, solvent is always present and segmental motion never stops. However, the solvent is also constantly diffusing through the chains, thereby controlling how the blocks approach equilibrium structures. Kim et al. [2004] have shown that using solvents to anneal films in the absence of thermal treatment is sufficient for generating uniform, void-free films. Guo [2008] extended the studies to account for solvent selectivity. The group annealed SB films in either cyclohexane (PB-selective), benzene (PB-selective), or heptane (PS-selective) over the course of eight hours. The structures formed upon annealing include both normal and inverted structures and are dependent on solvent selectivity and annealing time. Depending on the annealing conditions, the group was able to obtain single structure films and switch from inverted to normal structures. Interestingly, the selectivity of the solvent did not dictate which block formed the ordered phase. In the PB-selective solvent, cyclohexane, PS forms a sphere-between-cylinder structures, while annealing with the other PB-selective solvent, benzene, produces PB spheres.

Guo [2008] details the mechanism by which the structures evolve during solvent annealing. Heptane will segregate toward the PB domain, affording the PB block the opportunity to relax and stretch to form the matrix. PS blocks aggregate into cylinders to minimize contact with heptane to reduce the interfacial energy. Benzene, on the other hand, is a good solvent for PB and PS. Both blocks are given mobility in the film. The slight preference for PS causes the benzene to diffuse more slowly through the PS blocks. Therefore, while PB is free to move, it is likely frozen in prior to reaching an equilibrium state. Like PB in heptane, PS is now provided ample time to relax and form the matrix. In cyclohexane, the PS again forms the ordered structures and PB forms the matrix. In this case, the PS forms spheres packed between cylinders, as opposed to only cylinders as formed by PB in benzene. This is because

cyclohexane has a higher viscosity than benzene which slows the diffusion of solvent. In doing so, the PS is given time to relax so that the kinetics are eliminated from the determination of film morphology.

The kinetic effects can be enhanced by controlling the vapor pressure of either the casting or annealing solvent. As the vapor pressure of the solvent decreases, the drying rate also decreases, allowing more time for the formation of stable structures [Miyake, 1993]. In solvent annealing under different vapor pressures, increasing the vapor pressure decreases the volume fraction of polymer in the film due to more solvent diffusing into the film [Guo, 2008]. This allows more mobility of the polymer. Balancing vapor pressure with annealing time allows control of how far the system proceeds toward equilibrium.

This section presented past attempts to understand film drying. Drying models have predominately been aimed at predicting necessary drying conditions to minimize residual solvent. An understanding of structure development during drying has primarily been pursued experimentally. These studies have brought to light the importance of film processing on film properties. Despite all the progress made in these areas, a unification of these two aspects of polymer solution processing (drying modeling and structure evolution) has not been fully realized. Attempts to account for crystallization during film drying were severely simplified and the kinetics were not well represented. A need to bring together the current understanding of phase separation kinetics and film drying exists to improve film processing.

## 2.4 References

1. Abuzaina, F.M.; Patel, A.J.; Mochrie, S.; Narayanan, S.; Sandy, A.; Garetz, B.A.; Balsara, N.P. *Macromolecules* **2005**, *38*, 7090.
2. Adams, J.L.; Graessley, W.W.; Register, R.A. *Macromolecules* **1994**, *27*, 6026.
3. Adams, J.L.; Quiram, D.J.; Graessley, W.W.; Register, R.A. *Macromolecules* **1996**, *29*, 2929.
4. Adhikar, R.; Michler, G. H.; Huy, T. A.; Ivan'kova, E.; Godehardt, R.; Lebek, W.; Knoll, K. *Macromol Chem Phys* **2003**, *204*, 488 .
5. Alexandridis, P.; Zhou, D.; Khan, A. *Langmuir* **1996**, *12*, 2690.
6. Alexandridis, P.; Olsson, U.; Lindman, B. *Langmuir* **1998**, *14*, 2627.
7. Alsoy, S.; Duda, J.L. *Dry Technol* **1998**, *16*, 15.
8. Alsoy, S.; Duda, J.L. *AICHE J* **1999**, *45*, 896.
9. Amundson, K.; Helfand, E.; Patel, S.S.; Quan, X. *Macromolecules* **1992**, *25*, 1935.
10. Avrami, M. *J Chem Phys* **1939**, *7*, 1103.
11. Avrami, M. *J Chem Phys* **1940**, *8*, 212.
12. Avrami, M. *J Chem Phys* **1941**, *9*, 177.
13. Balsara, N.P.; Perahia, D.; Safinya, C.R.; Tirrell, M.; Lodge, T.P. *Macromolecules* **1992**, *25*, 3896.
14. Balsara, N.P.; Dai, H.J. *J Chem Phys* **1996**, *105*, 2942.
15. Balsara, N.P.; Dai, H.J.; Watanabe, H.; Sato, T.; Osaki, K. *Macromolecules* **1996**, *29*, 3507.
16. Balsara, N.P.; Garetz, B.A.; Chang, M.Y.; Dai, H.J.; Newstein, M.C. *Macromolecules* **1998**, *31*, 5309.
17. Balsara, N.P.; Garetz, B.A.; Dai, H.J. *Macromolecules* **1992**, *25*, 6072.
18. Banaszak, M.; Whitmore, M.D. *Macromolecules* **1992**, *25*, 3406.

19. Bang, J.; Lodge, T.P. *J Phys Chem B*, **2003**, *107*, 12071.
20. Barton, A.F.M. *Chem Rev* **1975**, *75*, 731.
21. Bates, F.S.; Hartney, M.A. *Macromolecules* **1985**, *18*, 2478
22. Bates, F.S.; Fredrickson, G.H. *Annu Rev Phys Chem* **1990**, *41*, 525.
23. Bates, F.S.; Rosedale, J.H.; Fredrickson, G.H. *J Chem Phys* **1990**, *92*, 6255.
24. Bates, F.S.; Rosedale, J.H.; Fredrickson, G.H. *Phys Rev Lett* **1988**, *61*, 2229.
25. Bendejacq, D.; Ponsinet, V.; Joanicot, M.; Loo, Y.; Register, R.A. *Macromolecules* **2002**, *35*, 6645.
26. Benkreira, H. Classification of Coating Flows. In *Thin Film Coatings*; Benkreira, H., Ed.; The Royal Society of Chemistry: Cambridge, 1993a.
27. Benkreira, H. Thin Films With Direct Gravure Coating. In *Thin Film Coatings*; Benkreira, H., Ed.; The Royal Society of Chemistry: Cambridge, 1993b.
28. Blandin, H.P.; David, J.C.; Vergnaud, J.M.; Illien, J.P.; Malizewicz, M. *J Coating Technol* **1987**, *59*, 27.
29. Cairncross, R.A.; Francis, L.F.; Scriven, L.E. *AICHE J* **1996**, *42*, 55.
30. Chaikin, P.M. *Principles of Condensed Matter Physics*; Cambridge University Press: New York, 1995.
31. Chastek, T.Q.; Lodge, T.P. *Macromolecules* **2003**, *36*, 7672.
32. Chastek, T.Q.; Lodge, T.P. *Macromolecules* **2004**, *37*, 4891.
33. Chastek, T.Q.; Lodge, T.P. *J Polym Sci Pol Phys* **2005**, *43*, 405.
34. Cogan, K.A.; Gast, A.P.; Capel, M. *Macromolecules* **1991**, *24*, 6512.
35. Cola, E.D.; Fleury, C.; Panine, P.; Cloitre, M. *Macromolecules* **2008**, *41*, 3627.
36. Daniel, C.; Hamley, I.W.; Wilhelm, M.; Mingvanish, W. *Rheol Acta* **2001**, *40*, 39.
37. Floudas, G.; Fytas, G.; Hadjichristidis, N.; Pitsikalis, M. *Macromolecules* **1995**, *28*, 2359.
38. Floudas, G.; Hadjichristidis, N.; Iatrou, H.; Pakula, T.; Fischer, E.W. *Macromolecules* **1994**, *27*, 7735.

39. Floudas, G.; Pakula, T.; Fischer, E.W.; Hadjichristidis, N.; Pispas, S. *Acta Polym*, **1994**, *45*, 176.
40. Floudas, G.; Ulrich, R.; Wiesner, U. *J Chem Phys* **1999**, *110*, 652.
41. Floudas, G.; Ulrich, R.; Wiesner, U.; Chu, B. *Europhys Lett* **2000**, *50*, 182.
42. Fredrickson, G.H.; Bates, F.S. *Annu Rev Mater Sci* **1996**, *26*, 501.
43. Fredrickson, G.H.; Binder, K. *J Chem Phys* **1989**, *91*, 7265.
44. Fredrickson, G.H.; Leibler, L. *Macromolecules* **1989**, *22*, 1238.
45. Garetz, B.A.; Newstein, M.C.; Dai, H.J.; Jonnalagadda, S.V.; Balsara, N.P. *Macromolecules* **1993**, *26*, 3151.
46. Glatter, O.; Scherf, G.; Scillén, K.; Brown, W. *Macromolecules* **1994**, *27*, 6046.
47. Guo, R.; Huang, H.; Chen, Y.; Gong, Y.; Du, B.; He, T. *Macromolecules* **2008**, *41*, 890.
48. Guttoff, E.B.; Cohen, E.D. *Coating and Drying Defects: Troubleshooting Operating Problems*, 2<sup>nd</sup> ed.; Wiley-Interscience: Hoboken, 2006.
49. Habas, J.; Pavie, E.; Lapp, A.; Peyrelasse, J. *J Rheol* **2004**, *48*, 1.
50. Hadjichristidis, N.; Pispas, S.; Floudas, G. *Block Copolymers: Synthetic Strategies, Physical Properties, and Applications*; Wiley-Interscience: New York, 2003.
51. Hajduk, D.A.; Kossuth, M.B.; Hillmyer, M.A.; Bates, F.S. *J Phys Chem B* **1998**, *102*, 4269.
52. Hamley, I.W. Introduction to Block Copolymers. In *Developments in Block Copolymer Science and Technology*; Hamley, I. W., Ed.; John Wiley & Sons, Ltd.: New York, 2004; p 1.
53. Hamley, I.W. *Block Copolymers in Solution: Fundamentals and Applications*; John Wiley & Sons: Hoboken, 2005.
54. Hamley, I.W. *The Physics of Block Copolymers*; Oxford University Press: Oxford, 1998.
55. Hamley, I.W.; Koppi, K.A.; Rosedale, J.H.; Bates F.S.; Almdal K.; Mortensen, K. *Macromolecules* **1993**, *26*, 5959.
56. Han, C.D.; Baek, D.M.; Kim, J.K.; Ogawa, T.; Sakamoto, N.; Hashimoto, T. *Macromolecules* **1995**, *28*, 5043.

57. Han, C.D.; Kim, J.; Kim, J.K. *Macromolecules* **1989**, *22*, 383.
58. Hanley, K.J.; Lodge, T.P. *Macromolecules* **2000**, *33*, 5918.
59. Harkless, C.R.; Singh, M.A.; Nagler, S.E.; Stephenson, G.B.; Jordansweet, J.L. *Phys Rev Lett* **1990**, *64*, 2285.
60. Hashimoto, T.; Sakamoto, N. *Macromolecules* **1995**, *28*, 4779.
61. Hashimoto, T.; Shibayama, M.; Kawai, H. *Macromolecules* **1983**, *16*, 1093.
62. Hashimoto, T.; Shibayama, M.; Kawai, H.; Watanabe, H.; Kotaka, T. *Macromolecules* **1983**, *16*, 361.
63. Hashimoto, T.; Sakamoto, N.; Koga, T. *Phys Rev E* **1996**, *54*, 5832.
64. Hashimoto, T.; Kowsaka, K.; Shibayama, M.; Kawai, H. *Macromolecules* **1986a**, *19*, 754.
65. Hashimoto, T.; Kowsaka, K.; Shibayama, M.; Kawai, H. *Polymer Preprints* **1983**, *24*, 224.
66. Hashimoto, T.; Kowsaka, K.; Shibayama, M.; Suehiro, S. *Macromolecules* **1986b**, *19*, 754.
67. Hashimoto, T.; Ogawa, T.; Sakamoto, N.; Ichimiya, M.; Kim, J.K.; Han, C.D. *Polymer* **1998**, *39*, 1573.
68. Helfand, E. *Macromolecules* **1975**, *8*, 295.
69. Helfand, E.; Tagami, Y. *J Chem Phys* **1972**, *56*, 3592.
70. Helfand, E.; Wasserman, Z.R. Microdomain Structure and the Interface in Block Copolymers. In *Developments in Block Copolymers I*; Goodman, I., Ed. Applied Science: London, 1982; p 99.
71. Helfand, E.; Wasserman, Z.R. *Macromolecules* **1976**, *9*, 879.
72. Helfand, E.; Wasserman, Z.R. *Macromolecules* **1978**, *11*, 961.
73. Helfand, E.; Wasserman, Z.R. *Polym Eng Sci* **1977**, *17*, 582.
74. Honda, T.; Kawakatsu, T. *Macromolecules* **2006**, *39* (6), 2340.

75. Hong, K.M.; Noolandi, J. *Macromolecules* **1983**, *16*, 1083.
76. Huang, H.; Hu, Z.; Chen, Y.; Zhang, F.; Gong, Y.; He, T.; Wu, C. *Macromolecules* **2004**, *37*, 6523.
77. Huang, C.; Lodge, T.P. *Macromolecules* **1998**, *31*, 3556.
78. Huang, H.; Zhang, F.; Hu, Z.; Du, B.; He, T.; Lee, F.K.; Wang, Y.; Tsui, O.K.C. *Macromolecules* **2003**, *36*, 4084.
79. Jian, T.; Anastasiadis, S.H.; Fytas, G.; Adachi, K.; Kotaka, T. *Macromolecules* **1993**, *26*, 4706.
80. Jin, X.; Lodge, T.P. *Rheol Acta* **1997**, *36*, 229.
81. Jones, R.A.L. *Soft Condensed Matter*; Oxford University Press: New York, 2002.
82. Khesghi, H.S. The fate of thin liquid films after coating. In *Liquid Film Coating: Scientific principles and their technological implications*; Kistler, S.F. & Schweizer, P.M., Ed.; Chapman & Hall: New York, 1997; p 183.
83. Kim, G.; Libera, M. *Macromolecules* **1998**, *31*, 2670.
84. Kim, S. H.; Misner, M. J.; Russel, T. P. **2004**, *16*, 2119.
85. Kim, S.S.; Hyun, J.C. *Drying of Coated Film*; Wypych, G. Ed.; ChemTec Publishing: Ontario, 2001.
86. Konrad, M.; Knoll, A.; Krausch, G.; Magerle, R. *Macromolecules* **2000**, *33*, 5518.
87. Lai, C.; Russel, W.B.; Register, R.A. *Macromolecules* **2002**, *35*, 4044.
88. Leibler, L. *Macromolecules* **1980**, *13*, 1602.
89. Libera, M.; Kim, G. *Macromolecules* **1998**, *31*, 2569.
90. Linse, P. *J Phys Chem* **1993**, *97*, 13896.
91. Listak, J.; Jakubowski, W.; Mueller, L.; Plichta, A.; Matyjaszewski, K.; Bockstaller, M.R. *Macromolecules* **2008**, *41*, 5919.
92. Liu, Z.; Shaw, M.; Hsiao, B.S. *Macromolecules* **2004**, *37*, 9880.
93. Lodge, T. P. *Macromol Chem Physic* **2003**, *204*, 265.

94. Lodge, T.P.; Hanley, K.J.; Pudil, B.; Alahapperuma, V. *Macromolecules* **2003**, *36*, 816.
95. Lodge, T.P.; Pudil, B.; Hanley, K.J. *Macromolecules* **2002**, *35*, 4707.
96. Lynd, N.A.; Hillmyer, M.A. *Macromolecules* **2005**, *38*, 8803.
97. Mandelkern, L. *Crystallization of Polymers* Cambridge University Press: New York, 2002; Vol. 2.
98. Matsen, M.W. *Phys Rev Lett* **1998**, *80*, 4470.
99. Matsen, M.W.; Bates, F.S. *J Polym Sci Pol Sci* **1997**, *35*, 945.
100. Matsen, M.W.; Bates, F.S. *J Chem Phys* **1997**, *106*, 2436.
101. Matsen, M.W.; Bates, F.S. *Macromolecules* **1996**, *29*, 7641.
102. Meier, D.J. *J Polym Sci* **1969**, *26*, 81.
103. Miyake, Y.; Sekiguchi, Y.; Kohjiya, S. *J Chem Eng Jpn* **1993**, *26*, 543.
104. Mori, K.; Hasegawa, H.; Hashimoto, T. *Polymer* **2001**, *42*, 3009.
105. Mortensen, K. *J Phys-Condens Mat* **1996**, *8*, A103.
106. Nie, H.; Bansil, R.; Ludwig, K.; Steinhart, M.; Konak, C.; Bang, J. *Macromolecules* **2003**, *36*, 8097.
107. Nishioka, A.; Furukawa, J.; Yamashita, S. *Kogyo Kagaku Zasshi* **1969**, *72*, 2440.
108. Noolandi, J.; Shi, A.; Linse, P. *Macromolecules* **1996**, *29*, 5907.
109. Noshay, A.; McGrath, J.E. *Block Copolymers, Overview and Critical Survey*; Academic Press: New York, 1977.
110. Park, M.J.; Bang, J.; Harada, T.; Char, K.; Lodge, T.P. *Macromolecules* **2004**, *37*, 9064.
111. Park, S.; Sul, W. *Polymer* **2008**, *49*, 3327.
112. Patel, A.J.; Mochrie, S.; Narayanan, S.; Sandy, A.; Watanabe, H.; Balsara, N.P. *Macromolecules* **2010**, *43*, 1515.
113. Pedemonte, E.; Cartasegna, S.; Turturro, A. *Chimica e l'Industria* **1974**, *56*, 3.

114. Pillai, P.S.; Livingston, D.I.; Strang, J.D. *Rubber Chem. Technol.* **1972**, *45*, 241.
115. Roe, R.; Fishkis, M.; Chang, J.C. *Macromolecules* **1981**, *14*, 1091.
116. Rosedale, J.H.; Bates, F.S. *Macromolecules* **1990**, *23*, 2329.
117. Rosedale, J.H.; Bates, F.S.; Almdal, K.; Mortensen, K.; Wignall, G.D.  
*Macromolecules* **1995**, *28*, 1429
118. Saam, J.C.; Gordon, D.J.; Lindsey, S. *Macromolecules* **1970**, *3*, 1.
119. Sadtler. *Infrared Spectra Handbook of Common Organic Solvents*; Sadtler Research Laboratories: Philadelphia, 1983.
120. Sakamoto, N.; Hashimoto, T. *Macromolecules* **1998**, *31*, 3292.
121. Sakamoto, N.; Hashimoto, T. *Macromolecules* **1998**, *31*, 3815.
122. Sakamoto, N.; Hashimoto, T.; Han, C.D.; Kim, D.; Vaidya, N.Y. *Macromolecules* **1997**, *30*, 1621.
123. Sakurai, S.; Hashimoto, T.; Fetters, L.J. *Macromolecules* **1996**, *29*, 740.
124. Schuler, M.; Stuehn, B. *Macromolecules* **1993**, *26*, 112.
125. Shibayama, M.; Hashimoto, T.; Kawai, H. *Macromolecules* **1983a**, *16*, 16.
126. Shibayama, M.; Hashimoto, T.; Kawai, H. *Macromolecules* **1983b**, *16*, 1427.
127. Shibayama, M.; Hashimoto, T.; Kawai, H. *Macromolecules* **1983c**, *16*, 1434.
128. Smallwood, I.M. *Handbook of Organic Solvent Properties*; Halsted Press: New York, 1996.
129. Soenen, H.; Berghmans, H.; Winter, H.H.; Overbergh, N. *Polymer* **1997a**, *38*, 5653.
130. Soenen, H.; Liskova, A.; Reynders, K.; Berghmans, H.; Winter, H.H.; Overbergh, N. *Polymer* **1997b**, *38*, 5661.
131. Stuehn, B.; Vilesov, A.; Zachmann, H.G. *Macromolecules* **1994**, *27*, 3560.
132. Sun, P.; Yin, Y.; Li, B.; Chen, T.; Jin, Q.; Ding, D.; Shi, A. *Phys Rev E* **2005**, *72*, 061408-1.

133. Svensson, B.; Alexandridis, P.; Olsson, U. *J Phys Chem B* **1998**, *102*, 7541.
134. van Dijk, M.A.; van den Berg, R. *Macromolecules* **1996**, *28*, 6773.
135. Verros, G.D.; Malamataris, N.A. *Polymer* **2005**, *46*, 12626.
136. Vinjamur, M.; Cairncross, R.A. *AIChE J* **2002**, *48*, 2444.
137. Vrentas, J.S.; Duda, J.L.; Ling, H.C. *J Polym Phys Pol Sci* **1985a**, *23*, 275.
138. Vrentas, J.S.; Duda, J.L.; Ling, H.C.; Hou, A.C. *J Polym Phys Pol Sci* **1985b**, *23*, 289.
139. Vrentas, J.S.; Vrentas, C.M. *J Polym Phys Pol Sci* **1994**, *32*, 187.
140. Waggoner, R.A.; Blum, F.D. *J Coating Technol* **1989**, *61*, 51.
141. Wang, C.; Lodge, T.P. *Macromol Rapid Commun* **2002**, *23*, 49.
142. Wanka, G.; Hoffman, H.; Ulbricht, W. *Macromolecules* **1994**, *27*, 4145.
143. Watanabe, H.; Kotaka, T.; Hashimoto, T.; Shibayama, M.; Kawai, H. *J Rheol* **1982**, *26*, 153.
144. Whitmore, M.D.; Noolandi, J. *J Chem Phys* **1990**, *93*, 2946.
145. Wilkes, G.L.; Stein, R.S. *J. Polym. Sci., Polym. Phys. Ed.* **1969**, *7*, 1525.
146. Winter, H.H.; Scott, D.B.; Gronski, W.; Okamoto, S.; Hashimoto, T. *Macromolecules* **1993**, *26*, 7236.
147. Wong, S.; Altinkaya, S.A.; Mallapragada, S.K. *Polymer* **2004**, *45*, 5151.
148. Wu, L.; Lodge, T.P.; Bates, F.S. *J Rheol* **2005**, *49*, 1231.
149. Yamamura, M.; Nishio, T.; Kajiwara, T.; Adachi, K. *Dry Technol* **2001**, *19*, 1397.
150. Young, R.J.; Lovell, P.A. *Introduction To Polymers*, 2<sup>nd</sup> ed.; CRC Press: Boca Raton, 1991.
151. Yu, B.; Li, B.; Sun, P.; Chen, T.; Jin, Q.; Ding, D.; Shi, A. *J Chem Phys* **2005**, *123*, 234902-1.
152. Yufa, N.A.; Li, J.; Sibener, S.J. *Macromolecules* **2009**, *42*, 2667.
153. Zhang, J.; Yu X.; Yang, P.; Peng, J.; Luo, C.; Huang, W.; Han, Y. *Macromol.*

*Rapid Commun.* **2010**, *31*, 591.

154. Zhao, J.; Majumdar, B.; Schulz, M.F.; Bates, F.S.; Almdal, K.; Mortensen, K.; Hajduk, D.A.; Gruner, S.M. *Macromolecules* **1996**, *29*, 1204.
155. Zielinski, J.M.; Duda, J.L. *AICHE J* **1992**, *38*, 405.

## Chapter 3

### **Iso-concentration Ordering Kinetics Of Block Copolymers In Solution During Solvent Extraction Using Dynamic Oscillatory Measurements**

# Iso-concentration Ordering Kinetics Of Block Copolymers In Solution During Solvent Extraction Using Dynamic Oscillatory Measurements

M. J. Heinzler<sup>1</sup>, S. Han<sup>1</sup>, J.A. Pople<sup>2</sup>, S. M. Martin<sup>1</sup>, and D. G. Baird<sup>1</sup>

<sup>1</sup>Department of Chemical Engineering, Virginia Tech, Blacksburg, VA 24060

<sup>2</sup>Stanford Synchrotron Radiation Lightsource, SLAC National Accelerator Laboratory, Menlo Park, CA 94025

## 3.1 Abstract

The iso-concentration ordering kinetics of poly(styrene-*b*-butadiene) in a neutral solvent, toluene, at several concentrations along the solvent extraction path at room temperature were studied using dynamic mechanical rheological measurements and SAXS. These experiments are in contrast to more common studies of the ordering kinetics of block copolymers, which consider phase separation following temperature quenches. Poly(styrene-*b*-butadiene) in toluene was found to order into hexagonally-packed cylinders beginning at a polymer concentration of 30 wt%. Below a concentration of 42 wt% polymer, the half-times as a function of concentration displayed behavior similar to the predictions of Binder and Fredrickson for homogeneous nucleation phase separation following temperature quenches through the order-disorder transition temperature. The half-time was found to initially decrease, then increase, due to a competition between thermodynamic and kinetic effects. At higher concentrations, the half-time decreased once more, which was believed to be the result of a change in the ordering mechanism. An Avrami exponent of 1 was obtained at all concentrations and was correlated to two-dimensional diffusion-controlled growth at concentrations below 42 wt% polymer, and heterogeneous nucleation and linear growth at higher concentrations. A comparison of the rheological and SAXS data suggested that changes in the dynamic mechanical response during ordering were induced by the development of individual microstructures acting as physical

crosslinks. However, a correlation between microstructure and the Avrami exponent was not found.

### 3.2 Introduction

In the presence of solvent, the phase behavior of block copolymers becomes complex compared to the neat polymer melt phase behavior. Whereas in a block copolymer melt the phase separated microstructure is dictated by the molecular weights of the blocks and the interaction parameter between the blocks, which is a function of temperature, in solution the phase behavior is also a function of the interactions of the blocks with the solvent and the polymer concentration. As such, for a given copolymer composition, many different temperature and concentration-dependent equilibrium structures are observed. For instance, Lodge and coworkers [2002] extensively studied the phase behavior of poly(styrene-*b*-isoprene) block copolymers in solvents of various selectivities. The authors demonstrated that while the addition of a neutral solvent only gives rise to a single structure, cylinders, over all temperatures and concentrations for which growth was observed, changing to a selective solvent made it possible to obtain all four classic phases (cylinders, lamellae, spheres and gyroids) for the same copolymer composition. Additionally, by changing the solvent content, the structure-forming block can be switched. In a separate study, Lodge et al. [2003] showed that by changing the block copolymer composition, even in a neutral solvent several lyotropic and thermotropic microstructures could be obtained, including metastable structures such as the perforated layer structure. Hence, a wider range of microstructures are possible for a polymer in solution than in the melt state.

The rate of formation of the equilibrium structures discussed above is dependent on the temperature and concentration of the solution, which causes the structure development during the

processing of block copolymer solutions to depend on processing conditions such as drying temperature and drying rate. For instance, by drying solution-cast poly(styrene-ethylene/butylene-styrene) films at high temperatures, Wang et al. [2001] obtained films consisting of a combination of branched cylinders and spheres. Lowering the drying temperature caused a transformation to non-branched cylinders and spheres. Finally, at low enough temperatures, the resultant morphology of the film was cylinders mixed with disordered regions. Zhang and coworkers [2000] showed that by rapidly removing a neutral solvent from a poly(styrene-*b*-butadiene-*b*-styrene) copolymer ordering could be impeded and a fully disordered film results. Moderate drying rates led to the presence of metastable inverted phases, with polybutadiene forming the ordered structure in a polystyrene matrix, due to kinetic trapping of these structures during solvent removal. In this regime, either cylinders or spheres were obtained depending on the rate of solvent extraction. Slow drying rates provided ample time for the transition from metastable to equilibrium structures during the solvent removal, yielding polystyrene cylinders in a polybutadiene matrix in the dried film. Additionally, Kim and Libera [1998] showed that rapid solvent removal inhibits the development of long-range order.

Several groups have sought to understand the kinetics governing the formation of these structures in solution. Soenen et al. [1997] tracked the formation of a physical gel in poly(styrene)-poly(ethylene, butylene) / hydrocarbon oil solution at several temperatures and concentrations by monitoring changes in  $\tan\delta$  curves over time. The ordering kinetics of the solution were compared across the different temperatures and concentrations in terms of critical gelation time. Nie et al. [2003] used small angle X-ray scattering to monitor the ordering of a triblock copolymer in a selective solvent from a disordered state following a quench to a temperature at which ordered structures form. Changes in the intensity of the primary scattering

peak as a function of time could be fit to an Avrami-like model to determine the ordering time at a number of temperatures below the order-disorder transition temperature. Liu and coworkers [2004] used rheology to understand the effect of temperature and concentration on the development of ordered structures in a disordered solution. The dynamic mechanical response of the solution increased over time as the solution ordered, from which changes in the extent of ordering in the material could be determined. The authors also used small angle X-ray scattering to confirm their results. Finally, Chastek and Lodge [2003, 2004] directly monitored the growth of grains containing ordering microstructures from a disordered state using polarized optical microscopy. The ordering kinetics could be compared based on differences in the rate of change of the grain dimensions.

Others have given consideration to the kinetics of order-order transitions. Liu and coworkers [2006] used the Avrami model for nucleation and growth to quantify the transition of a triblock copolymer from body-centered cubic packed spheres (BCC) to face-centered cubic packed spheres (FCC). Wang and Lodge [2002] studied the cylinder-to-gyroid transition and cylinder-to-hexagonally perforated layer structure-to-gyroid transitions of a block copolymer in solution. Li et al. [2007] have analyzed the kinetics of the hexagonally-packed cylinder to BCC transition of a block copolymer in a selective solvent as a function of temperature. Finally, Park et al. [2004] studied a more extensive series of transitions in a poly(styrene-*b*-isoprene) block copolymer in a selective solvent. They tracked the system as the BCC structures in a mixed state with hexagonal close-packed structures transitioned to FCC, then to a homogeneous sample of hexagonal close-packed structures, and finally to hexagonally packed cylinders. All these studies have used SAXS to monitor the transitions. Further, in all cases, like with the disorder-

order transitions previously discussed, structural changes are induced by quenching or ramping temperature.

In the literature reviewed above, the analysis of the ordering kinetics of block copolymers in solution is inadequate for fully understanding how ordered structures develop during solvent extraction. The disorder-to-order and order-to-order transitions were induced by thermal quenches. That is, samples were equilibrated at one state and subsequently heated or cooled to induce a phase transition. In processing solution-cast films, ordering is induced by progressing through different concentrations. Further, the literature considered only a few, relatively low concentrations, spanning narrow concentration ranges, when studying the influence of concentration on ordering kinetics. For instance, Liu et al. [2004] only analyzed three concentrations from 10 to 20 wt% polymer. Likewise, Soenen et al. [1997] only used three concentrations in their work, this time ranging from 15 to 30 wt% polymer. However, Chastek and Lodge [2003] showed that under suitable conditions, the development of ordered structures can still occur at concentrations as high as 70 wt% polymer. Therefore, when processing block copolymer solutions, if the solvent removal rate is fast enough such that concentrated films are attained prior to the ordering process being completed, the ordering kinetics at high concentrations are not trivial and must also be understood.

In this work, changes in the dynamic mechanical response (DMR) of a phase separating block copolymer, poly(styrene-*b*-butadiene) in a neutral solvent, toluene, were used to track iso-concentration ordering kinetics during the extraction of solvent from a block copolymer solution at several concentrations ranging from the dilute to concentrated regime. Because it will be of interest to analyze how the kinetics change as the solution concentration progresses away from the order-disorder transition concentration, the equilibrium phase behavior at ambient conditions

was first determined by small angle X-ray scattering (SAXS). The ordering kinetics at several concentrations along the phase diagram following solvent removal were then studied using rheology. It will first be shown that the ordering process being monitored is not influenced by the introduction of external stresses imposed through shear flow. The rheology of the phase separating block copolymer at several concentrations during the solvent removal process will then be presented. Similar data obtained by SAXS is then used to confirm the rheology and provide insight into the cause of the change in the dynamic mechanical response during ordering (development of individual microstructures versus changes in ordered grain dimensions). The ordering kinetics are subsequently quantified using the Avrami model for crystallization. This will allow direct comparison of the ordering kinetics as a function of concentration. Further, it will provide a basis on which to directly compare the rheology and scattering results. Finally, the rheological experiments are repeated with poly(styrene-*b*-isoprene-*b*-styrene), which gives a different equilibrium microstructure in toluene, to determine if the method provides any information on the microstructure.

### **3.3 Experimental**

#### **3.3.1 Materials**

Poly(styrene-*b*-butadiene) (SB) block copolymer was purchased from Sigma-Aldrich and used as received. Size exclusion chromatography was used to determine  $M_w$  to be 119.3 kg/mol with a PDI of 1.01. The polymer is 33 wt% polystyrene. A second block copolymer, poly(styrene-*b*-isoprene-*b*-styrene) was also used to study the effect of microstructure on the Avrami parameters. This copolymer had a molecular weight of 90 kg/mol and was 21 wt%

polystyrene. The solvent used was toluene (> 99.5% pure), which was also used as received from Sigma-Aldrich. Toluene is a neutral solvent for both copolymers.

### **3.3.2 Solution Preparation**

Twenty weight-percent block copolymer solutions were prepared by dissolving an appropriate amount of copolymer, determined gravimetrically, in toluene. In a sealed vial, solutions were sonicated at room temperature until a clear solution was obtained. Solutions were used within 24 hours of preparation and re-sonicated prior to each use to ensure uniformity.

### **3.3.3 Equilibrium SAXS Measurements**

All SAXS experiments were performed at the Stanford Synchrotron Radiation Lightsource at SLAC National Accelerator Laboratory (Menlo Park, CA). A schematic of the sandwich cell used for SAXS experiments is shown in Fig. 3.1. The inner diameter of the well is 10-mm. A half of a gram of 20 wt% polymer solution was deposited dropwise into the well and subsequently dried at room temperature to the desired concentration. The cell was then sealed and equilibrated at room temperature for 12 hours before obtaining scattering patterns. Later experiments on the kinetics of the structure development would show that changes in the scattering profile ceased around four to six hours, making the 12 hours sufficient for obtaining equilibrium structures. However, the experiments described here were performed prior to the kinetics experiments, hence the excessive equilibration time.

### **3.3.4 Iso-concentration Rheology Measurements**

Iso-concentration rheology measurements were performed on a Rheometrics RMS-800 using a modified parallel plate fixture shown in Fig. 3.2. The top fixture is a 25-mm parallel plate fitted with a solvent-trap. The bottom fixture is a 45-mm (I.D.) dish.

Precisely 2.5 g of the 20 wt% polymer solution are transferred drop-wise to the bottom dish. Solvent is removed from the sample at room temperature in a hood while the concentration is monitored gravimetrically. Measurements are made at concentrations between 32 wt% and 50 wt% polymer. Drying times range from 30 to 45 minutes, depending on the desired concentration. Solution thicknesses at these concentrations range from 0.7-mm to 0.5-mm, respectively. When the desired concentration is reached, the dish is transferred to the rheometer. Approximately 60 seconds elapses between reaching the concentration and the start of rheology measurements. This time has proven negligible relative to the total ordering time.

To ensure that the concentration is constant during the experiment, the solvent trap is filled with a hydrocarbon oil, Paraffin Oil, purchased from Sigma-Aldrich to act as a barrier to the toluene. Two cover slips rest on the edges of the bottom dish and are partially submerged in the solvent trap as shown in Fig. 3.2 to seal the sample without interfering with measurements. Prior to placing the cover slips on the bottom plate, a fresh 20 wt% solution is deposited drop-wise around the rim of the dish. This helps to saturate the headspace over the sample and to create a seal to prevent the loss of solvent at the edges of the cover slips.

Changes in the dynamic mechanical response were tracked over time until a constant complex modulus is observed. Oscillatory shear experiments were performed at 2% strain and a frequency of 0.5 rad/s. The 2% strain condition satisfies the requirement of linear viscoelasticity over the concentrations studied [Heinzer, 2011].

### **3.3.5 Iso-concentration SAXS Measurements**

Kinetics experiments using SAXS were performed using the sandwich cell shown in Fig. 3.1. To account for the difference in the diameters of the well of the sandwich cell and the rheometer cup, only 0.6 g of solution were used for SAXS experiments. By appropriately changing the

initial amount of material, the same final film thickness obtained in the rheology experiments was obtained in SAXS experiments. It was assumed that drying was unidirectional and as such, samples used for rheology and SAXS experiments were comparable. Further, the times required for the rheology and SAXS samples to reach the concentrations of interest were the same.

When the desired concentration was reached, the cell was sealed and placed in the beam path. Scattering profiles were obtained approximately every 60 seconds using an exposure time of 30 seconds to enhance the signal-to-noise ratio. Scattering patterns were integrated to obtain two-dimensional scattering profiles using custom software developed at SLAC.

### **3.4 Results and Discussion**

#### **3.4.1 Phase behavior**

SAXS was used to determine the phase behavior of the SB copolymer in toluene at room temperature and locate the order-disorder transition concentration. The two-dimensional scattering profiles at three concentrations are shown in Fig. 3.3. An inset shows the scattering peak at higher wave-vectors. At 25 wt% polymer, no primary peak evolves in the equilibrated sample indicating no measurable ordering. At a polymer concentration of 30 wt%, a primary peak appears. This indicates the onset of ordering in the sample, identifying 30 wt% polymer as the order-disorder concentration at room temperature.

At 60 wt% polymer, a secondary peak can be resolved. This peak is positioned at a wave-vector that is  $3^{1/2}$  times the primary peak wave-vector. This scattering profile is consistent with hexagonally-packed cylinders. Though not shown in Fig. 3.3 for clarity, this secondary peak first appears around 40 wt% polymer. The position relative to the primary peak is still at  $q=3^{1/2}$ , indicating that at this temperature the structure is not concentration-dependent.

Rheology was used to confirm the order-disorder concentration. The dynamic mechanical response (DMR) of SB / toluene solutions at 30 wt% and 32 wt% polymer following the removal of solvent from a 20 wt% solution as a function of time under constant shear are shown in Fig. 3.4. The complex modulus of the 30 wt% polymer solution remains constant over a four hour period, while the modulus of the 32 wt% polymer solution increases. The data suggests that at 30 wt% no ordering is occurring, while at 32 wt% the SB copolymer is ordering. Although the 30 wt% sample in Fig. 3.3 was given a lengthy equilibration time, it is noted that a diffuse ring was present within five minutes of starting the experiment and an increase in the intensity during a five minute period was observed. As such, the data indicates that at this concentration, changes in the mechanical properties of the solution due to phase separation are too minute to influence the rheology. It is also possible that concentration gradients contribute to the disagreement in the exact location of  $C_{ODT}$ . Nonetheless, the concentration predicted by rheology to be  $C_{ODT}$ , 32 wt%, is considered to be in good agreement with the order-disorder transition concentration identified using SAXS. Further, ordering at shallow concentration-quenches across  $C_{ODT}$  are measurable using rheology.

### **3.4.2 Rheology of ordering SB / toluene solutions**

In order to use changes in the dynamic mechanical response over time to monitor the development of ordered structures in the SB / toluene solution following solvent extraction, it must first be established that the introduction of shear stresses is not manipulating the growth of the ordered structures. Two separate experiments were performed to explore the influence of shear on the evolution of  $|G^*|$ . First, the time-dependent behavior of  $|G^*|$  at three different shear rates was checked to confirm that the same response was obtained regardless of shear rate. In the second experiment, a sample was equilibrated for some time in the absence of shear. Shear flow

is then started and the progression of the modulus is compared to changes in the modulus of a sample that was continually sheared.

Figs. 3.5a and b show the complex modulus as a function of time of two polymer solutions (35 and 40 wt%). In each case, the dynamic mechanical response is shown under three different shear rates: 0.1, 0.5, 1.0 rad/s. While it appears that differences in the time-dependence of  $|G^*|$  exist among the different shear rates, it must be noted that over multiple trials as high as 20% variability in the rheology data was observed. The error is exacerbated at longer times. This explains the deviation in the data commonly seen at long times. With the exception of data collected at 1 rad/s for a 35 wt% solution, the data at early times ( $< 5000$  s) agrees well over all frequencies at all concentrations. Further, all discrepancies in the data are within the 20% error observed over multiple trials at a given frequency. As such, the data appears to be in good agreement with negligible frequency-dependence.

To further verify that the presence of shear was not promoting growth, a sample at 37 wt% polymer following solvent removal was allowed to equilibrate under static conditions prior to monitoring the complex modulus. This sample is denoted as sample 'A'. When the desired concentration was reached, an initial point at zero seconds was collected to ensure consistency between sample A and a sample that is continually sheared from zero seconds, sample 'B'. The initial point required the sample be subjected to 2% strain at a frequency of 0.5 rad/s for approximately 30 seconds. After this point was collected, the shearing was ceased and the sample equilibrated for 35 minutes. After the equilibration time elapses, shear was re-introduced.

The complex moduli of samples A and B are shown in Fig. 3.6. The initial modulus at zero seconds is the same for both samples. Upon the startup of shear flow for sample A at 35

minutes, the moduli of both samples are still comparable. The modulus of sample A (346 Pa) is 8.5% greater than the modulus of sample B (319 Pa), which is well below the 20% variability previously noted. The continued growth of the modulus of sample A is nearly parallel to the trend observed from this point on for sample B. Considering these results concurrently with the data presented in Figs. 3.5A and 5B, the presence of shear below 1 rad/s does not appear to be inducing or affecting the ordering process. In all subsequent rheology experiments to track the order of the SB block copolymer in toluene, 2% strain and an angular frequency of 0.5 rad/s were used.

In Fig. 3.7, the storage and loss modulus versus time of a 32 wt% SB / toluene solution are presented. Details of the particular shapes of the curves are reserved for later in the discussion. Rather, these curves are intended to illustrate the liquid-to-solid transition of the ordering block copolymer solutions. At 32 wt% polymer, which is approximately  $C_{ODT}$ , the solution initially displays liquid-like behavior with  $G''$  (18.4 Pa) greater than  $G'$  (12.4 Pa). Such behavior indicates that a physical gel has not formed at the beginning of the experiment. The moduli eventually cross one another at 1030 s, indicating the formation of a physical gel, which is attributed to the development of ordered microstructures.

It was observed that as the concentration increased, the crossover occurs at shorter times. At 37 wt% polymer, not shown here, the crossover is observed at 140 s. The shorter time to crossover is believed to be the result of more rapid formation of ordered structures at concentrations away from  $C_{ODT}$ . Though it is plausible that the behavior at 37 wt % is an artifact of the time elapsed while drying a sample from 32 wt%, when ordering starts, to 37 wt%, this drying time is not long enough to justify the difference in the crossover time. Drying from 32 wt% polymer to 37 wt% polymer takes approximately 300 s. The crossover at 37 wt% polymer

is observed about 140 s into the experiment, meaning that a critical gel would be formed in 440 s. However, at 32 wt% polymer, it takes 1030 s to form the gel. The difference in the cross-over time is, therefore, a consequence of different ordering rate. At higher concentrations, beginning with 40 wt% polymer, a gel has already formed when the rheological experiment is started. However, an increase in the modulus is still observed as the sample continues to order. Similar behavior is observed at higher concentrations.

Figs. 3.8A and B show the rheology of the phase separating SB / toluene solution at concentrations between 32 and 50 wt% polymer. For simplicity, the data is now presented as  $G^*$ , the complex modulus. The 32 wt% solution data is plotted on its own in Fig. 3.8A as the scale of the modulus data in Fig. 3.8B masks several important features of this data. As previously discussed, ordering is first detected at 32 wt% polymer. Two distinct steps in the modulus are observed. The first step continues for one hour. The second step is slightly longer, with the modulus increasing for 4500 s before leveling at 194 Pa. After maintaining a constant modulus for another 2000 s, the sample does display a slight yield. Such yielding is only witnessed at 32 wt% polymer.

The two-step increase in the complex modulus has been reported by other groups and conflicting views regarding the cause of this behavior exist. Schuler and Stuehn [1993] attribute the first step to the localized segregation of the blocks of a polymer and the second step to the diffusion of the segregated polymers onto a microlattice. Liu et al. [2004] also observed a two-step increase in the modulus near the order-disorder transition temperature. However, the first step was ascribed to the formation of ordered phase nuclei, while the second step is a consequence of the subsequent growth. These results were based on the fact that a ring in the scattering pattern was present at early times, which corresponded to the first step in the modulus.

Thus, the rheology is responding to nucleation rather than localized chain segregation. As previously discussed, a diffuse ring was observed in the scattering pattern almost immediately at 30 wt% polymer. Thus, the combination of scattering and rheology results in this work are consistent with Liu et al. [2004] and the first step in the rheology data is assigned to the nucleation event.

Ordering in the SB copolymer solution is observed until a polymer concentration of 50 wt%. At 52 wt% polymer, not shown here, the solution showed an initial decrease in the modulus upon the startup of flow before reaching a constant modulus value of 520 Pa. As such, ordering at concentrations greater than 50 wt% polymer were not detectable using rheology.

The sudden cessation of ordering at 52 wt% polymer can be explained by several events: either the ordering process has completed, the ordering kinetics are so slow that appreciable changes in the modulus are not witnessed over the time scale measured, or rheology is not sensitive to any structural changes at this concentration. The first explanation is not believed to be the case because the drying time required to reach a 52 wt% solution is only around 45 minutes, while ordering at all preceding concentrations is on the order of four hours. Both of the latter proposed explanations are, however, plausible. It would be expected that at a certain concentration the solution becomes kinetically trapped. In studying the phase behavior of poly(styrene-*b*-isoprene) copolymers of significantly lower molecular weights than the polymer used in this study, Lodge et al. [2002] found that at room temperature, between concentrations of 60 and 80 vol% polymer, samples became kinetically trapped and equilibrium structures do not form. In the work presented here, above 50 wt% polymer, the polymer lacks sufficient mobility to continue ordering and diffusion is impeded.

Alternatively, at 52 wt% polymer, rheology may not be capable of detecting any further changes in the structure of the ordering block copolymer. Sakamoto [1998] found that when the grains containing the ordered structures occupy the entire sample space, rheology is no longer sensitive to structural changes in the sample. That is, while re-packing and alleviation of grain-boundary defects may be ongoing, a lack of newly formed structures results in no measurable change in the dynamic mechanical response of the solution. Further commentary on the cause of this upper-limit will be provided later when SAXS measurements are used to study the kinetics and confirm the rheology data.

At all intermediate concentrations, a single increase in the modulus is seen. This is again consistent with what is seen during temperature quenches. The nucleation event is now too rapid to be measured on the allotted time-scale. This single step is believed to correspond to the second step observed at 32 wt% polymer.

The modulus initially shows a sharp increase followed by a slower growth over time before eventually leveling off. Based on the curves, it is believed that the growth rate changes as the extent of ordering in the sample increases, with the later stages of the growth being slower than the initial growth. The time to reach a constant complex modulus varies with concentration and ranges from approximately ninety minutes to five hours. In general, the completion time increases with concentration. However, considering the shape of the curves, this does not preclude the possibility of the ordering rates at higher concentrations being faster.

### **3.4.3 Small Angle X-ray Scattering Measurements**

Like the dynamic mechanical response, the integrated intensity of the primary SAXS peak will increase as the ordered microstructure concentration in a solution increases. As such, changes in the scattered intensity can be used in a manner comparable to the complex modulus to

study the ordering kinetics of block copolymers. SAXS data collected during the ordering of the SB block copolymer is presented here to confirm the rheology data and lend insight into the cause of the change in the dynamic mechanical response during ordering.

A parallel set of experiments was performed using SAXS to monitor structure growth following solvent removal. The resulting intensity versus time data at several concentrations is shown in Fig. 3.9. Because intensity is an arbitrary value, the curves in Fig. 3.9 have been shifted for clarity. Changes in the scattered intensity are observed from 40 wt% to 60 wt%, while lower concentrations were not studied due to time constraints. The data indicates that ordering is still occurring at higher concentrations than were measurable using rheology. The extended range of concentrations for which ordering is observed may be due to the fact that scattering may be more sensitive to later stages of domain growth and structure packing. Changes in the scattering intensity are incurred by the development of new ordered structures as well as improved packing and long-range ordering of already existing structures. As discussed earlier, rheology may not be sensitive to these later stages of growth. The data, therefore, suggest that beyond 50 wt% polymer solution, packing and development of long-range order are continuing, but the grains have likely impinged on one another.

For concentrations that were measured by both rheology and SAXS, the data are qualitatively the same in that a single rise in the intensity is seen, but quantitatively, disparities between the ordering times exist. The ordering times of the 40 wt% solution measured by rheology is around two to three hours, while it is closer to four hours using SAXS. A similar difference in the ordering time occurs for the 50 wt% solution. Such discrepancies in the total ordering times determined by rheology and by SAXS have been reported by Hashimoto et al. [1998]. Again, this is believed to be a consequence of grain impingement. Considering this,

along with the fact that the ordering times are on the same order of magnitude, the ordering times based on SAXS and rheology appear to agree with one another within reason.

### 3.4.4 Avrami fitting

Under the conditions when the ordering is believed to be a nucleation and growth process, it is proposed that the Avrami model, given in Eq. 3-1, can be used to quantify the kinetics of phase separation [Floudas, 1994].

$$\frac{\phi}{\phi_{\infty}} = 1 - e^{-zt^n} \quad (3-1)$$

In this model,  $\phi$  is the volume fraction of the sample in the ordered phase at any time  $t$ , while  $\phi_{\infty}$  is the final achievable volume fraction of the ordered phase in the sample. The parameters  $z$  and  $n$  represent a rate constant and the Avrami exponent, respectively. The Avrami exponent provides insight into the rate of the growth of the ordered phase as well as information regarding the dimensionality of the growing crystalline domain.

Using the parameters of the Avrami equation, the half-time of the ordering process can be calculated by means of Eq. 3-2.

$$t_{0.5} = \left(\frac{\ln 2}{z}\right)^{\frac{1}{n}} \quad (3-2)$$

The half-time indicates the time necessary for  $\phi$  to reach a value of  $0.5\phi_{\infty}$ . By incorporating both the rate constant and the Avrami exponent, both of which contain information regarding the ordering rate, the half-time provides a basis for comparing ordering kinetics of different samples.

It has further been proposed that the volume fraction of the ordered state during the phase separation can be extracted from DMR data [Floudas, 1994]. It is assumed that the complex modulus at a given time is the average of the modulus of the disordered state,  $G_0^*$ , and the ordered state,  $G_{\infty}^*$ , weighted by the volume fractions of the ordered ( $\phi$ ) and disordered ( $1-\phi$ )

states. These moduli can be combined by either the parallel or series approximations given in Eq. 3-3a and b, respectively.

$$G^* = \varphi G_{\infty}^* + (1 - \varphi)G_0^* \quad (3-3a)$$

$$\frac{1}{G^*} = \frac{\varphi}{G_{\infty}^*} + \frac{1-\varphi}{G_0^*} \quad (3-3b)$$

In terms of dynamic mechanical analysis, the parallel combination represents the case when the strain is equally distributed among the ordered and disordered phases while in the series approximation it is assumed that the stress is equal among the phases [Floudas, 1994]. These rules of mixtures represent the limiting values of the composite modulus. The parallel mode provides the minimum  $\phi(t)$  while the series approximation provides the maximum estimated  $\phi(t)$ . In a similar manner, the integrated intensity from SAXS data can be substituted for the modulus and  $\phi(t)$  can be determined from SAXS.

As discussed in Section 3.4.2, the rheological data collected from the SB / toluene system indicates a nucleation event and subsequent growth stage occurring during the solvent removal process. The kinetics of the ordering of SB block copolymer in toluene were, therefore, quantitatively studied with the Avrami model, using the rheology and scattering data to determine  $\phi(t)$ , respectively. Because the series and parallel modes provide estimates of the maximum and minimum values for  $\phi(t)$ , the data was analyzed based on both approximations. In this analysis,  $G_0^*$  is taken as the modulus at zero seconds and  $G_{\infty}^*$  is the modulus of the final plateau.

The ordering kinetics as a function of concentration are analyzed by comparing the half-times determined by the parallel and series approximations. The results based on DMR data are shown in Fig. 3.10. Before analyzing the data in full, a comment on the data at 32 wt% polymer is necessary. Two points are shown at this concentration, which is a consequence of the double-

step behavior of the 32 wt% data. The first step has been ascribed to the formation of nuclei and the second step to growth. Because data at subsequent concentrations only show the second step, to effectively normalize the data at 32 wt%, the half-time of the second step only is determined by shifting the time to zero at the end of the first step. This data is represented by the open points in Fig. 3.10. The total time to reach this stage in the development, however, is this half-time in addition to the nucleation time. This is represented by the filled point. By presenting the data in this manner, comparisons of only the growth periods and the total ordering times as a function of concentration can be made. All other data is reported taking  $t = 0$  s as the start of the single step in the modulus versus time data.

At all concentrations, the half-time predicted by the parallel approximation is greater than the half-time predicted by the series approximation. The difference between the two methods increases with concentration and can be as high as 280% (4132 s) at 42 wt% polymer. However, it is also noted that the error in the half-times for a given method also increases with concentration and is believed to contribute to the discrepancy.

The half-time based on the series and parallel approximations display similar trends with concentration, though it is noted that the data determined by the series approximation displays more significant error, particularly up to a concentration of 42 wt% polymer. The half-times of both the growth period and the overall ordering at 32 wt% polymer are significantly greater than the half-time of the 35 wt% polymer solution. Thus, initially moving away from the order-disorder concentration causes the ordering rate to increase. As the sample is concentrated further, to 37 wt% polymer, the half-time is unaffected by the loss of solvent. Though the average half-times at 35 and 37 wt% do differ, the overlap of the confidence intervals of the data indicates the data are not statistically different.

The half-time then increases with concentration, goes through a maximum at 42 wt% polymer, then decreases once more. At 40 wt% polymer, the half-time based on the parallel approximation increases to 1971 s, then to 5612 s at 42 wt% polymer, while the series approximation predicts an increase from 762 s to 1480 s. The half-time decreases at 45 wt% polymer to 3571 s or 953 s based on the parallel and series approximations, respectively. According to the parallel approximation data, the error associated with this half-time shows minimal overlap with the confidence interval of the 40 wt% data. It is believed, therefore, that the ordering time is still longer than that observed at 40 wt% polymer, but shorter than the ordering time at 42 wt% polymer. Finally, at 50 wt% polymer, both methods exhibit an increase in the average half-time, though there is substantial overlap in the range of data with the data gathered at 45 wt% polymer. It is, therefore, likely that ordering times have begun to level-off.

Between 32 and 42 wt% polymer, the trend in the ordering time can be explained by the competition between changes in the thermodynamic and kinetic effects as the film becomes more concentrated. Near the order-disorder transition concentration the ordering is very slow. This finding is consistent with reports of the kinetics near the order-disorder transition temperature following temperature quenches. The disordered state at this point is metastable and the energy barrier for nucleation is high. Thus, the driving force for phase separation is low and the kinetics are slow. Progressing to a higher concentration, 35 wt% polymer in this case, causes the disordered phase to become unstable and phase separation is thermodynamically favorable. This results in faster kinetics as indicated by the reduction in the half-time. Continuing to increase the polymer concentration will increase the driving force for phase separation while reducing the mobility of the polymer chains, which will slow the kinetics. Between 35 and 37 wt% polymer, the ordering time remains nearly constant, indicating relatively little change in the

thermodynamic and kinetic effects between these concentrations. At higher concentrations, chain mobility becomes the rate-determining factor. As the concentration of polymer continues to increase, the diffusion of the chains is continually impeded, causing the half-time to increase with concentration.

Fredrickson and Binder [1989] predict that following a temperature quench across the order-disorder transition temperature,  $T_{ODT}$ , the half-time of diblock copolymer ordering via homogeneous nucleation and growth is proportional to the square of the quench depth,  $T_{ODT} - T$ . A similar trend is observed in this work with respect to concentration quench depth between 32 and 42 wt% polymer. Although Fredrickson and Binder's theory describes the response of the phase separation process to temperature, the analogous behavior observed here strongly suggests a similar phenomenon and ordering mechanism proceeding as solvent is extracted. It is therefore concluded that during the concentration quench, the SB copolymer undergoes homogeneous nucleation and growth.

At higher concentrations, the decrease in ordering times may be evidence that the mechanism of ordering has changed. Concentration gradients and a substantial level of ordering may be present by the time these higher concentrations are reached. The advancing fronts of the grain boundaries of the ordered domains may serve as nucleation sites for subsequent growth, changing the ordering mechanism to heterogeneous nucleation and linear growth. The energy barrier for such growth will be lower and could result in faster ordering rates. It is also plausible that the phase separation is no longer a nucleation and growth event. Though the nucleation and growth event will have already started at lower concentrations, the remaining disordered state may undergo another ordering mechanism such as spinodal decomposition.

The half-times determined from SAXS data using parallel and series combinations to calculate the composite scattering intensity are shown in Fig. 3.11. The trends predicted by SAXS using the different approximations for the intensity do not agree with one another. Using the parallel approximation, the half-time increases slightly between 40 and 45 wt% polymer, as predicted by the DMR data. The half-time then appears to continually decrease until 55 wt% polymer is reached, which is not predicted by the DMR data. The half-time then increases once more at 60 wt% polymer. When the series approximation is applied to the SAXS data, a rise in half-time between 40 and 45 wt% polymer is predicted followed by relatively constant ordering times. Nearly constant half-times are also observed over this concentration range using the DMR data. The discrepancy at 40 wt% may be due to the associated error of the measurement.

The ordering times predicted by the scattering data deviate significantly from the ordering times predicted by the DMR data at certain concentrations. Good agreement is seen between the two sets of data using either approximation for  $\phi(t)$  at 50 wt%. At 40 wt%, the series approximation also yields comparable half-times based on SAXS and DMR, while SAXS over-predicts the half-time based on the parallel approximation. At 45 wt% polymer, the scattering data predicts much longer half-times than the DMR data regardless of the rule of mixtures applied. One possible reason for this behavior has already been discussed and the discrepancy is justified on the basis that scattering is more sensitive to later stages of the ordering process. It is also noted that the methods used to calculate the composite properties (modulus or intensity) represent the extremes of the range of possible values. Recognizing this, it can be seen that the ranges of the scattering data and the rheology data overlap substantially and are on the same order of magnitude. The actual ordering times may be somewhere in between and it is,

therefore, plausible that the scattering and rheology data are in better agreement than the data suggests.

The Avrami exponents as determined by the series and parallel approximations are shown in Fig. 3.12. The Avrami exponents calculated by the two methods are in agreement with one another. The average Avrami exponent based on the parallel approximation over all concentrations, except 37 wt% polymer, is  $0.75 \pm 0.06$ . Using the series approximation the average exponent value is  $0.66 \pm 0.06$ . At 37 wt%, the Avrami exponent is approximately  $1.1 \pm 0.08$ . The exact cause of this deviation is unclear.

The Avrami exponent can be correlated to the mechanism and dimensionality of the growth occurring during the ordering process. For example, an Avrami exponent of 0.5 indicates homogeneous nucleation followed by one-dimensional, diffusion-controlled growth, while a value of 1 represents homogeneous nucleation and two-dimensional, diffusion-controlled growth or heterogeneous nucleation and one-dimensional, linear growth. Unfortunately, at most concentrations, none of the Avrami exponents obtained by rheology exactly agree with these correlated values. However, at 37 wt% polymer, the exponent attains a value of approximately 1.0, which is consistent with correlations to the growth mechanism. It is not sensible that the mechanism would change progressing from 35 to 37 wt% and then return to the mechanism at 35 wt% polymer. It is believed, therefore, that the other Avrami exponents are representative of the same growth mechanism correlated to an Avrami exponent of 1.0. The deviation is attributed to the fact that the Avrami exponent is also a function of ordering rate, which may be shifting the Avrami exponent to a lower value than expected.

In order to better interpret the Avrami exponent, the values obtained by rheology are compared to those determined by SAXS in Table 3.1. In most cases, the Avrami exponents

determined by SAXS are higher than the values determined by rheology. Though some discrepancy exists, in a majority of cases, the Avrami exponents determined by SAXS and rheology are within 0.1 of one another when the error associated with the DMR data is considered. As such, it is believed that the Avrami exponents obtained by the two measurements are in fairly good agreement.

The data collected by SAXS provide insight into the nature of the growth mechanism. The Avrami exponents determined by SAXS are close to 1.0, providing more support to the argument made above regarding the actual value of the Avrami exponent. It is, therefore, concluded that the Avrami exponent is indicative of behavior associated with an exponent of 1.0 rather than 0.5. As discussed, this suggests either homogeneous nucleation and two-dimensional diffusion-controlled growth or heterogeneous nucleation and one-dimensional, linear growth. The trend in the half-time prior to 45 wt% polymer leads to the conclusion that the ordering is proceeding by homogeneous nucleation. Thus, between 32 and 42 wt%, two-dimensional diffusion-controlled growth is occurring. At higher concentrations, as has been discussed, the mechanism of phase separation appears to change. The Avrami exponent remains one, which could be interpreted as heterogeneous nucleation and linear growth, with the advancing fronts of the already formed ordered grains serving as nucleation sites.

#### **3.4.5 Effect of microstructure on Avrami exponent**

Because the rheology was found to be sensitive to the development of microstructures, based on the Avrami exponent, the effect of microstructure on the Avrami exponent is investigated using poly(styrene-*b*-isoprene-*b*-styrene), which exhibits spheres as equilibrium microstructure in toluene at room temperature [Heinzer, 2011]. The DMR at three different concentrations are shown in Fig. 3.13. At all three concentrations, a single step in the modulus is

observed. The modulus increases in a sigmoidal manner before plateauing at long times. The final modulus is reached between 10,000 and 20,000 seconds, depending on the concentration.

These curves were again fit to the Avrami model. Because the parallel model gave less significant error when analyzing the kinetics of the SB copolymer, only Avrami fits based on the parallel approximation are presented here. The Avrami exponents and ordering times of the SIS and SB copolymers are shown in Table 3.2. Interestingly, at 45 and 50 wt% polymer, the ordering times of the two polymers are comparable. This indicates that the ordering rates are similar and at these two concentrations should not convolute any interpretation of the Avrami exponent data. At 37 wt% polymer, the ordering times are, however, substantially different. This could help to also determine the influence of ordering rate on the Avrami exponent.

The data at the higher concentrations (45 and 50 wt% polymer) will first be considered since the ordering rates are nearly identical. The Avrami exponents of the SIS copolymer are slightly higher than those of the SB copolymer at both concentrations. However, they are still very close, being within 0.1 of one another. Both sets of Avrami exponents are nearly 1.0. This suggests that the type of microstructure is not strongly influencing the Avrami exponent even though the rheology is sensitive to an increase in the number of physical crosslinks.

At 37 wt% polymer, the ordering of the SIS copolymer is much slower than that of the SB. The Avrami exponent of the SIS is now appreciably higher (1.33 versus 1.04). This deviation, not seen when the ordering rates were the same, leads to the conclusion that the Avrami exponent is a strong function of the ordering rate for an ordering block copolymer in solution.

### **3.5 Conclusions**

The iso-concentration ordering kinetics of poly(styrene-*b*-butadiene) in a neutral solvent following solvent removal have been studied using rheology and small angle X-ray scattering.

The order-disorder concentration at room temperature is located around 30 wt% polymer, beyond which the SB copolymer orders into hexagonally packed cylinders. The dynamic mechanical response could be used to track the iso-concentration ordering between a polymer concentration just beyond  $C_{ODT}$  (32 wt%) and 50 wt% polymer, while SAXS indicated the ordering process continues at concentrations as high as 60 wt% polymer. The discrepancy is believed to be due to a lack of sensitivity of rheology to packing of ordered structures in impinged grains.

Near the order-disorder transition concentration, the nucleation event is relatively slow and was, therefore, measurable by rheology as indicated by a two-step increase in the modulus. Away from  $C_{ODT}$ , the nucleation event is too rapid to be detected in these experiments. Up to a critical concentration of 42 wt% polymer, the half-time as the concentration progresses away from  $C_{ODT}$  follows a similar trend to that predicted by Binder and Fredrickson for homogeneous nucleation and growth following temperature quenches. The half-time initially decreases, then increases with concentration as kinetic effects become rate-limiting. Above 42 wt% polymer, a second decrease in the ordering time is believed to be the consequence of a change in the ordering mechanism from homogeneous nucleation to either heterogeneous nucleation or spinodal decomposition.

Avrami exponents close to 1 were found at all concentrations based on the rheology and scattering data. Below 42 wt% polymer, the Avrami exponent is interpreted as being indicative of homogeneous nucleation and two-dimensional diffusion-controlled growth, while above 42 wt%, the Avrami exponent corresponds to heterogeneous nucleation and one-dimensional linear growth. The agreement between the rheology and scattering data suggest that the two measurements are responding to the same changes in the system (development of individual

microstructures). As such, the effect of microstructure on the Avrami parameter was investigated. It was found that the Avrami exponent was relatively insensitive to the particular microstructure, but was influenced by changes in the ordering rate.

### 3.6 Acknowledgements

Partial funding for this work was provided by the Institute for Critical Technology and Applied Science at Virginia Tech. The authors acknowledge Eastman Chemical Company for providing funding through the Eastman Fellowship in Polymer Science. Portions of this research were carried out at the Stanford Synchrotron Radiation Laboratory, a national user facility operated by Stanford University on behalf of the U.S. Department of Energy, Office of Basic Energy Sciences. The SSRL Structural Molecular Biology Program is supported by the Department of Energy, Office of Biological and Environmental Research, and by the National Institutes of Health, National Center for Research Resources, Biomedical Technology Program, and the National Institute of General Medical Sciences.

### 3.7 References

1. Chastek, T.Q.; Lodge, T.P. *Macromolecules* **2003**, *36*, 7672.
2. Chastek, T.Q.; Lodge, T.P. *Macromolecules* **2004**, *37*, 4891.
3. Floudas, G.; Hadjichristidis, N.; Iatrou, H.; Pakula, T.; Fischer, E.W. *Macromolecules* **1994**, *27*, 7735.
4. Fredrickson, G.H.; Binder, K. *J. Chem. Phys.* **1989**, *91*, 7265.
5. Hashimoto, T.; Ogawa, T.; Sakamoto, N.; Ichimiya, M.; Kim, J.K.; Han, C.D. *Polymer* **1998**, *39*, 1573.
6. Kim, G.; Libera, M. *Macromolecules* **1998**, *31*, 2569.

7. Li, M.; Liu, Y.; Nie, H.; Bansil, R.; Steinhart, M. *Macromolecules* **2007**, *40*, 9491.
8. Liu, Y.S.; Li, M.H.; Bansil, R.; Steinhart, M. *Macromolecules* **2007**, *40*, 9482.
9. Liu, Y.S.; Nie, H.F.; Bansil, R.; Steinhart, M.; Bang, J.; Lodge, T.P. *Phys. Rev. E* **2006**, *73*, 061803.
10. Liu, Z.; Shaw, M.; Hsiao, B.S. *Macromolecules* **2004**, *37*, 9880.
11. Liu, Z.; Shaw, M.; Hsiao, B.S. *J. Rheol.* **2004**, *48*, 1389.
12. Lodge, T.P.; Pudil, B.; Hanley, K.J. *Macromolecules* **2002**, *35*, 4707.
13. Lodge, T.P.; Hanley, K.J.; Pudil, B.; Alahapperuma, V. *Macromolecules* **2003**, *36*, 816.
14. Nie, H.F.; Bansil, R.; Ludwig, K.; Steinhart, M.; Konak, C.; Bang, J. *Macromolecules* **2003**, *36*, 8097.
15. Park, M.J.; Bang, J.; Harada, T.; Char, K.; Lodge, T.P. *Macromolecules* **2004**, *37*, 9064.
16. Schuler, M.; Stuehn, B. *Macromolecules* **1993**, *26*, 112.
17. Soenen, H.; Berghmans, H.; Winter, H.H.; Overbergh, N. *Polymer* **1997**, *38*, 5653.
18. Wang, C.Y.; Lodge, T.P. *Macromol. Rapid Commun.* **2002**, *23*, 49.
19. Wang, Y.; Shen, J.S.; Long, C.F. *Polymer* **2001**, *42*, 8443.
20. Zhang, Q.L.; Tsui, O.K.C.; Du, B.Y.; Zhang, F.J.; Tang, T.; He, T.B. *Macromolecules* **2000**, *33*, 9561.

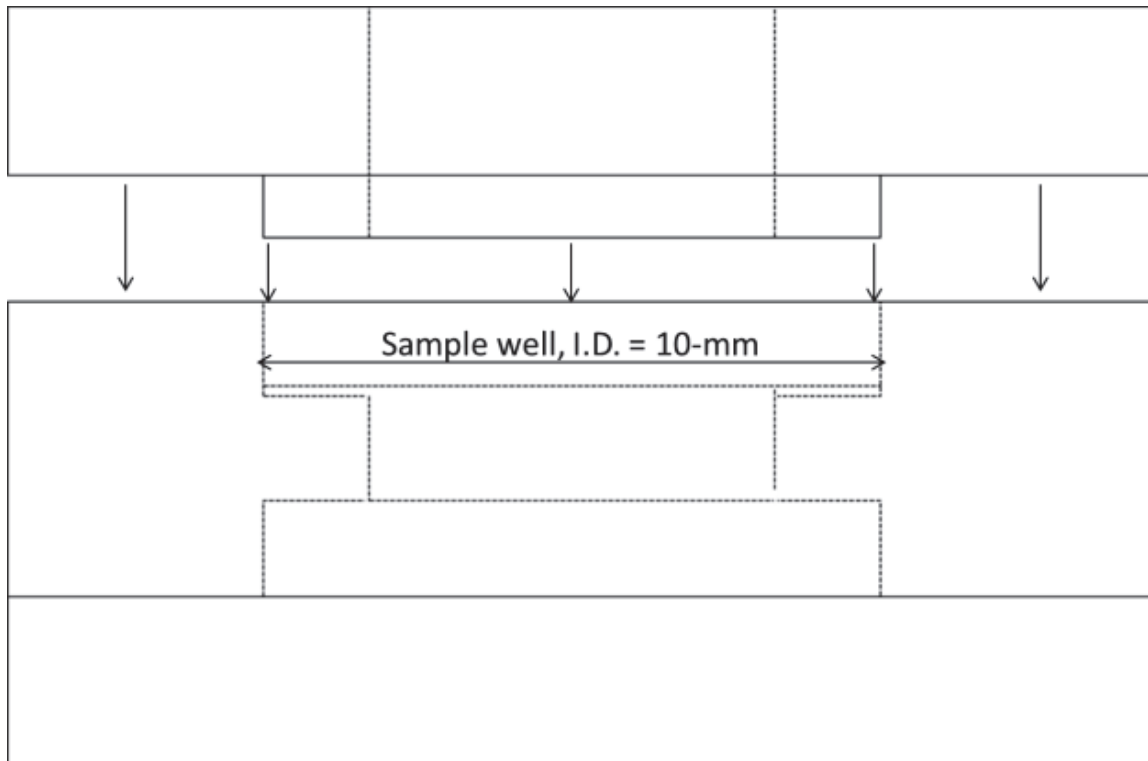


**Figure 3.1.** Schematic of sandwich cell used for SAXS experiments. Inside diameter of well in which the sample is dried is 10 mm.

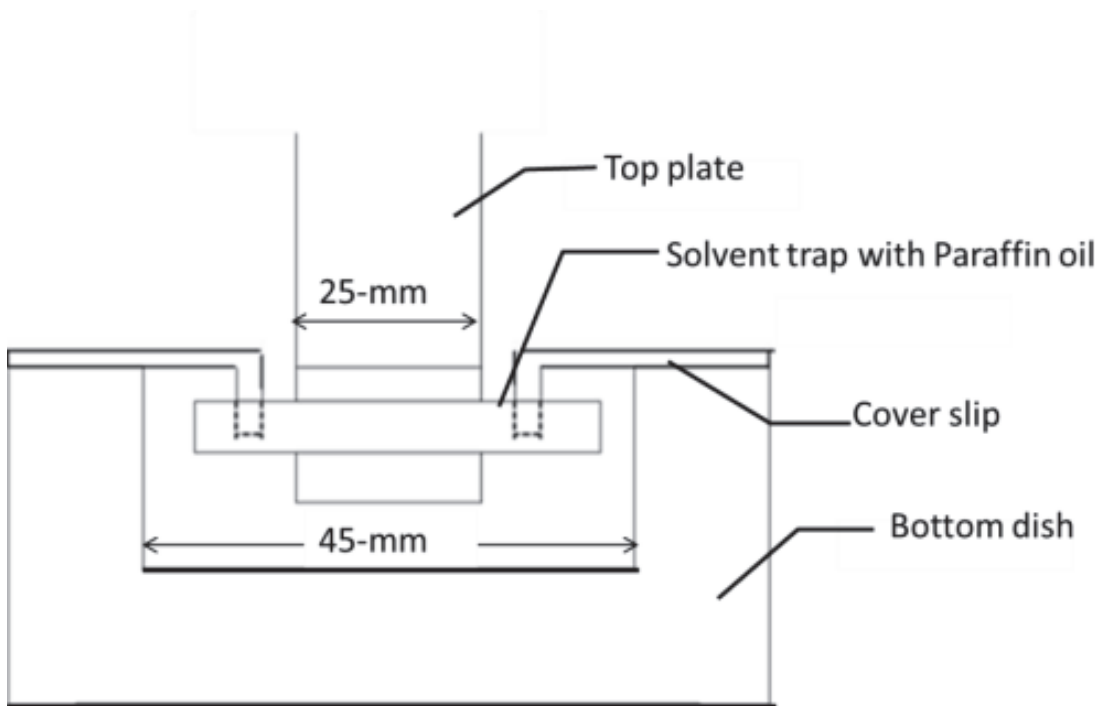


**Figure 3.2.** Parallel plate rheometer fixture with solvent trap. The diameters of the top and bottom plates are 25 and 45-mm, respectively.

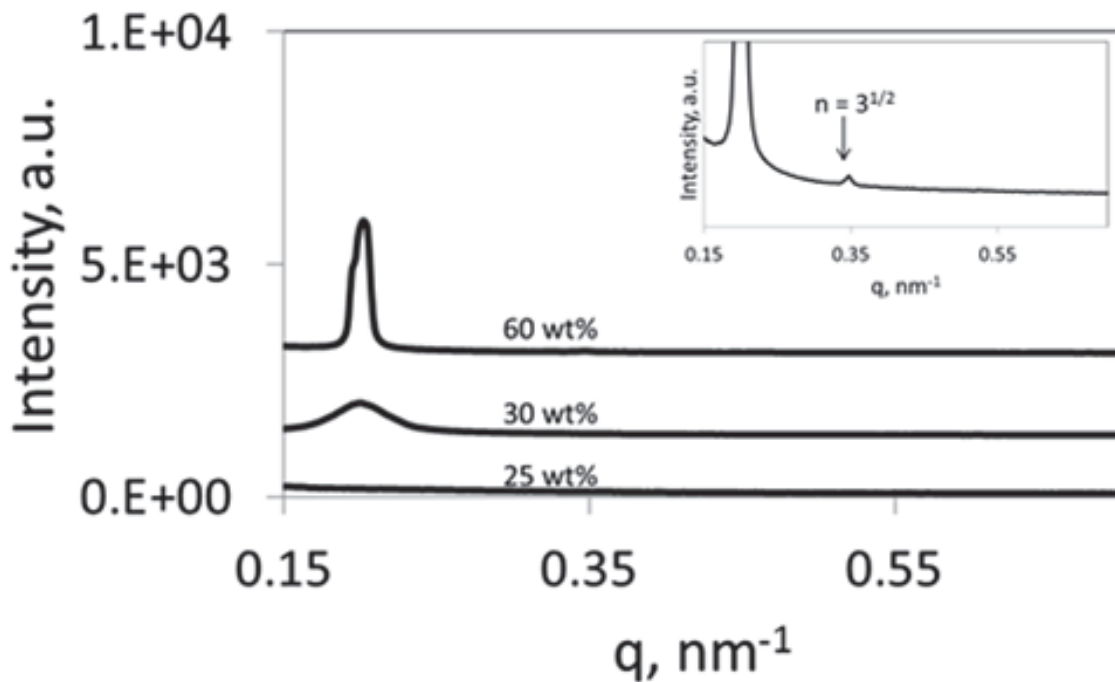


**Figure 3.3.** Scattering profiles of SB in toluene at various concentrations. Samples were equilibrated for 12 hours at room temperature. Polymer concentrations are indicated as weight percent polymer in the figure. The inset shows a secondary peak observed at 60 wt% polymer.

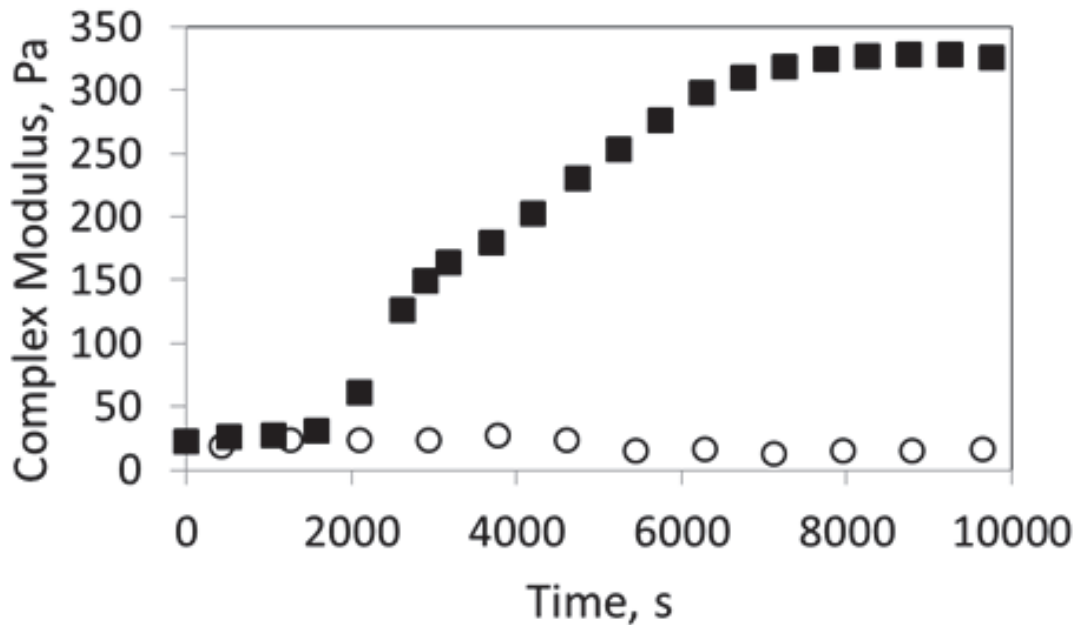


**Figure 3.4.** Dynamic mechanical response,  $|G^*|$ , of SB copolymer in toluene at 30 wt% (o) and 32 wt% (■) polymer as a function of time at a frequency of 0.5 rad/s and 2% strain. The samples were prepared by extracting solvent from a 20 wt% solution at room temperature.

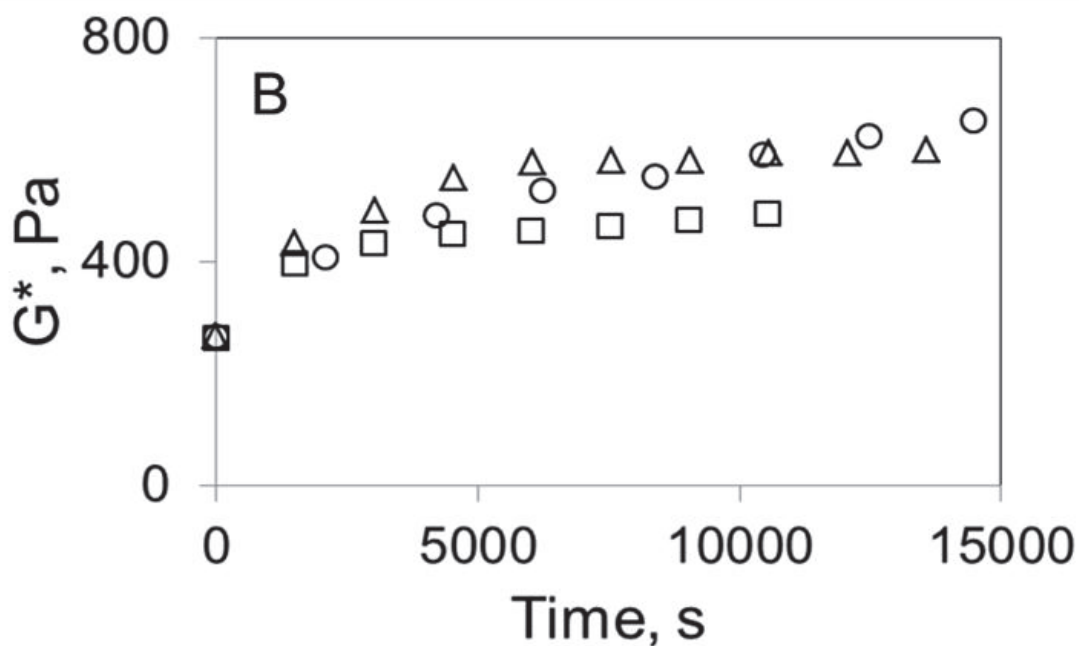
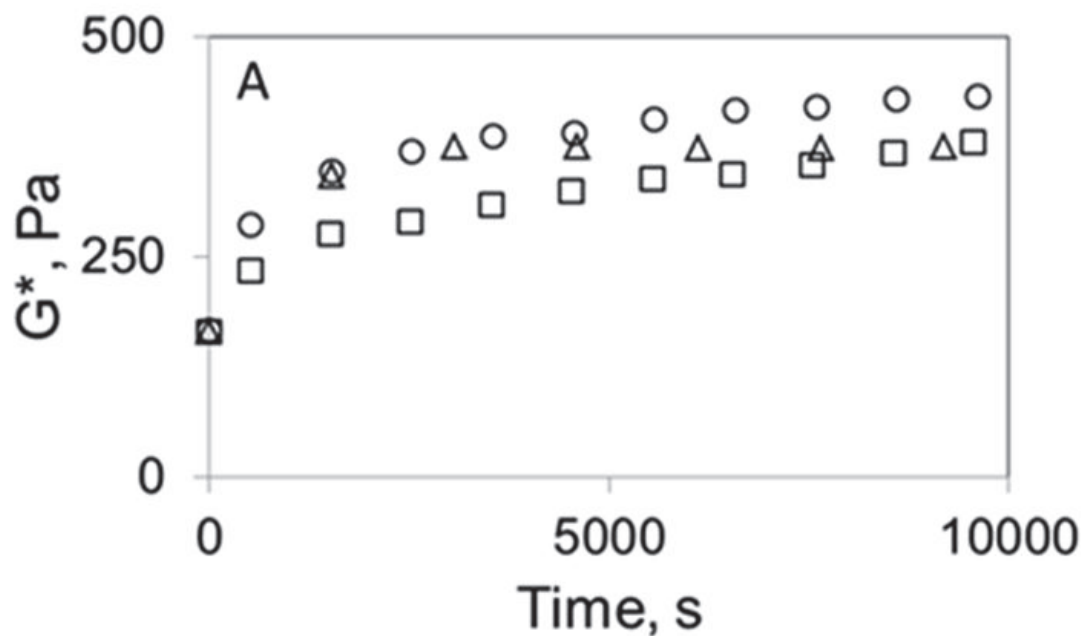


**Figure 3.5.** Evolution of the complex modulus of 35 (A) and 40 (B) wt% SB copolymer / toluene solutions at room temperature following extraction from a 20 wt% solution. At each concentration, the responses at three different shear rates, all at 2% strain, are studied: 0.1 rad/s ( $\Delta$ ), 0.5 rad/s ( $\circ$ ), 1 rad/s ( $\square$ ).



**Figure 3.6.** Complex modulus as a function of time during the ordering of the SB block copolymer in a 37 wt% toluene solution at room temperature following extraction from a 20 wt% solution. The curves correspond to a sample that is continually sheared from the time that 37 wt% polymer is reached (□) and a sample that is equilibrated under state conditions for 35 minutes before shearing ensues (◇). Tests were performed at 2% strain at a frequency of 0.5 rad/s.

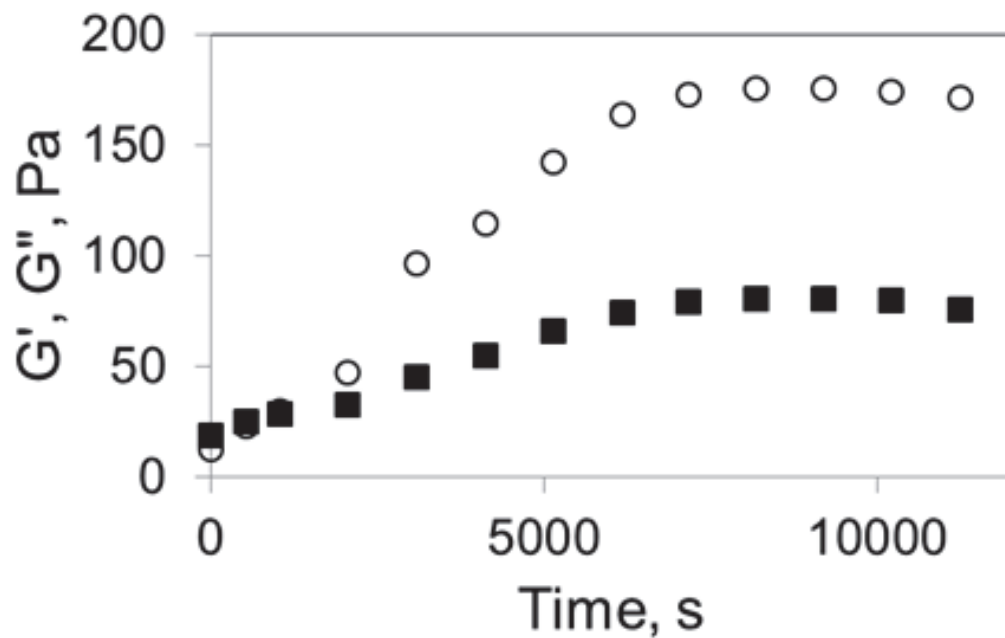


**Figure 3.7.** Storage,  $G'$ , (o) and loss,  $G''$ , (■) modulus of a phase separating 32 wt% polymer SB / toluene solution as a function of time at room temperature. Tests were performed at 2% strain at a frequency of 0.5 rad/s.

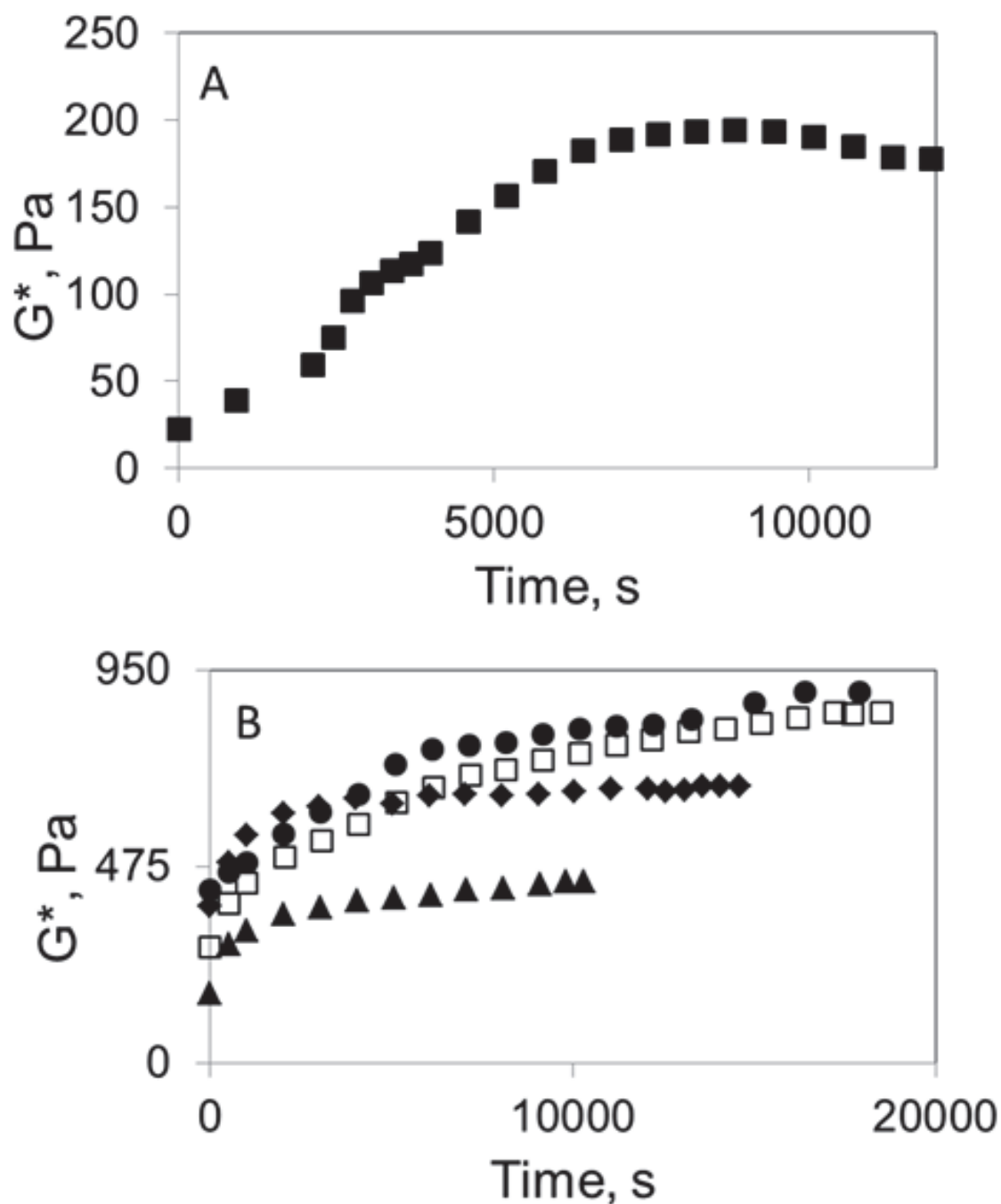


**Figure 3.8.** Iso-concentration dynamic mechanical responses of phase separating SB block copolymer in toluene at several concentrations following the removal of solvent from a 20 wt% polymer solution. All samples were prepared and tested at room temperature. Tests were performed at 2% strain at a frequency of 0.5 rad/s. The response of a 32 wt% solution is shown in (A). Concentrations (wt% polymer) shown in (B) are: 35 ( $\blacktriangle$ ), 40 ( $\blacklozenge$ ), 45 ( $\square$ ), and 50 ( $\bullet$ ).

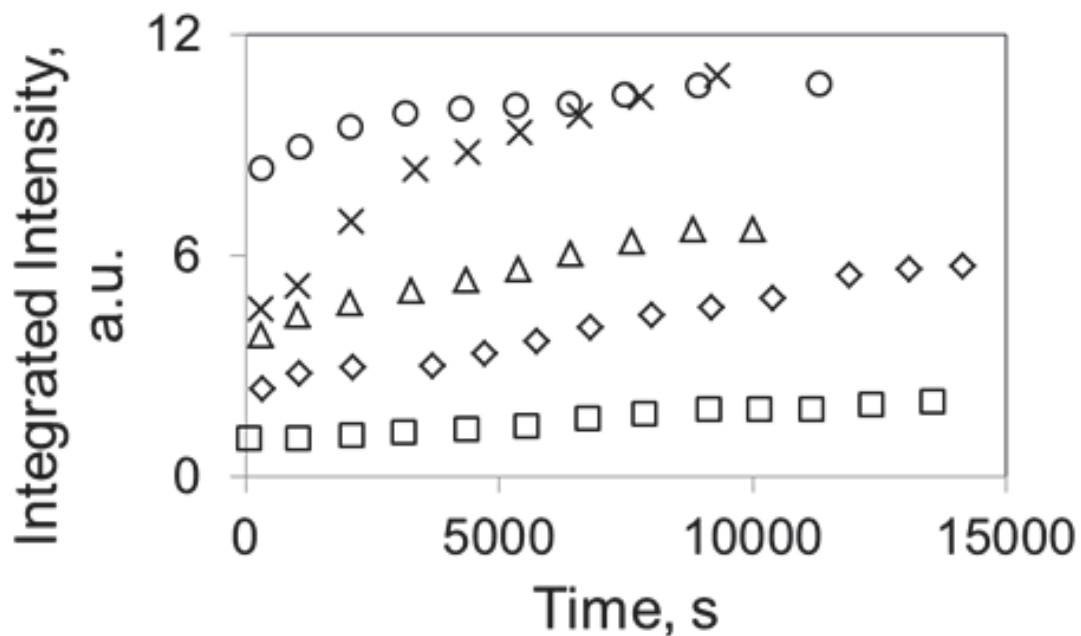


**Figure 3.9.** Integrated intensity of the primary scattering peak during the ordering of the SB block copolymer in toluene following the removal of solvent from a 20 wt% solution at room temperature. Curves correspond to the following concentrations (wt% polymer): 40 (□), 45 (◇), 50 (Δ), 55 (x), and 60 (o). Curves have been arbitrarily shifted for clarity.

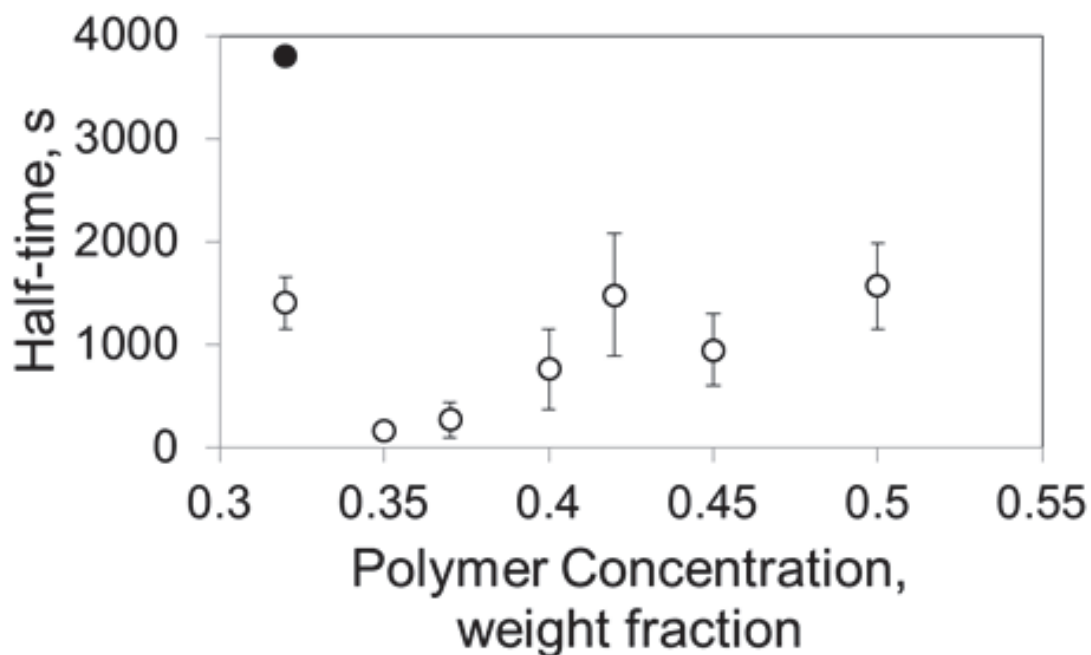
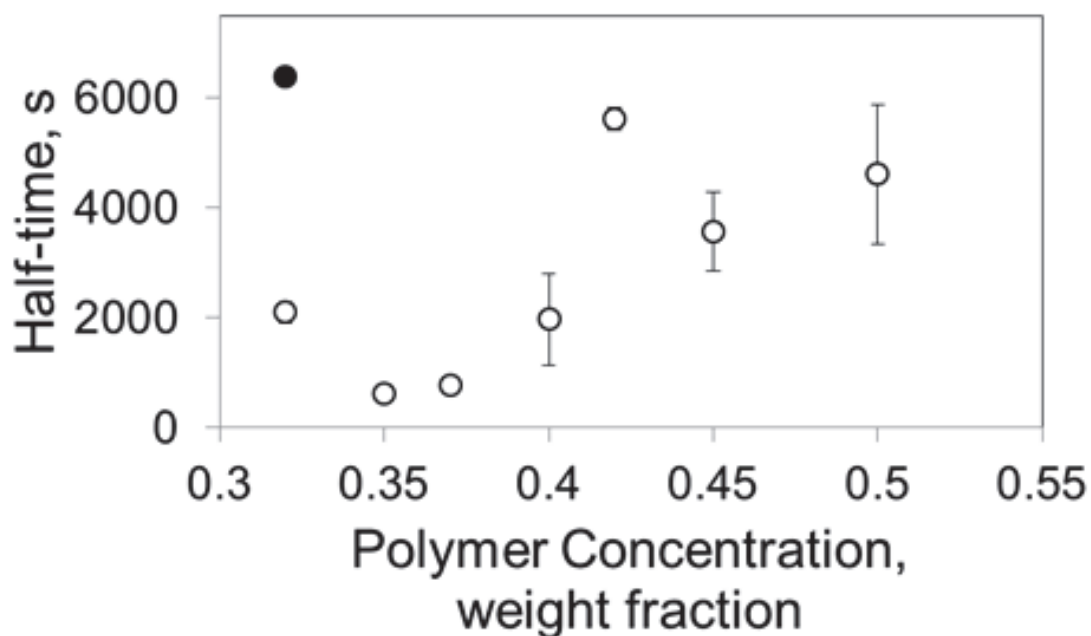


**Figure 3.10.** Half-times of the ordering of SB in toluene at room temperature following extraction of solvent from a 20 wt% solution as a function of concentration. Half-times were determined using the Avrami equation and calculating  $\phi(t)$  from dynamic mechanical data using the parallel (top) and series (bottom) approximations for the complex modulus. At 32 wt%, the total half-time ( $\bullet$ ) and the half-time of the growth period only (o) are shown. At all subsequent concentrations, the half-time corresponds to the single-step growth of  $G^*$ .

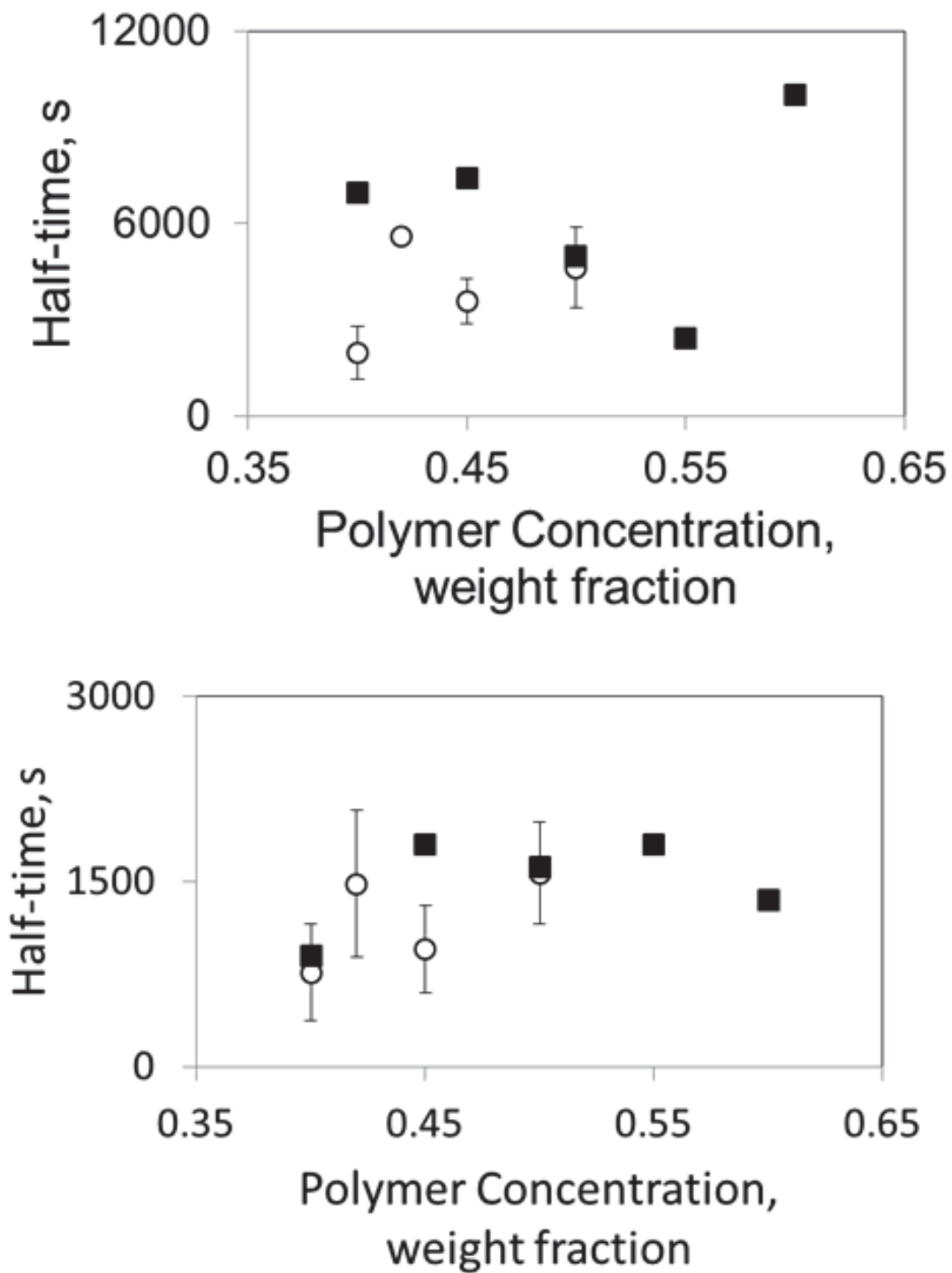


**Figure 3.11.** Half-times of the ordering of SB in toluene following extraction of solvent from a 20 wt% solution at room temperature based on dynamic mechanical (o) and SAXS (■) data using parallel (top) and series (bottom) approximations to determine  $\phi(t)$ .

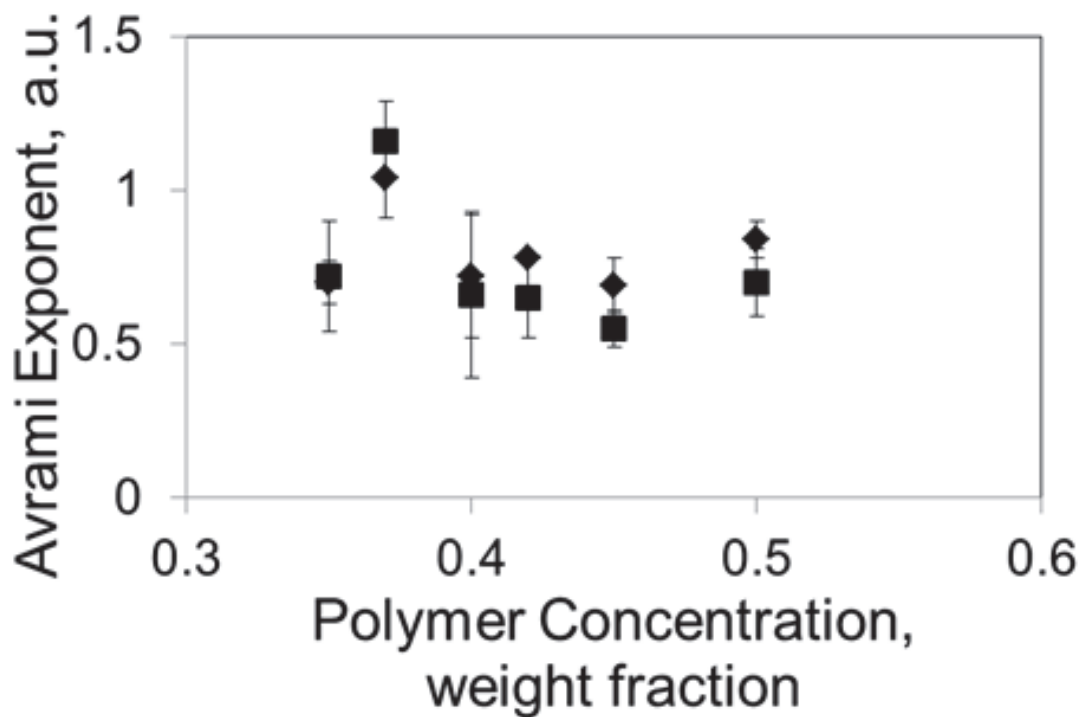


**Figure 3.12.** Avrami exponent during the ordering of SB in toluene following removal of solvent from a 20 wt% solution at room temperature as a function of concentration. Exponent values were calculated using a parallel (◆) and series (■) approximations for the complex modulus.

**Table 3.1.** Avrami exponents of phase separating SB / toluene solutions at room temperature determined from dynamic mechanical and SAXS data

Polymer Concentration (wt %)	Parallel		Series	
	Rheology	SAXS	Rheology	SAXS
40	$0.72 \pm 0.3$	1.1	$0.66 \pm 0.27$	0.7
45	$0.69 \pm 0.09$	0.79	$0.55 \pm 0.06$	0.79
50	$0.84 \pm 0.06$	1.0	$0.7 \pm 0.11$	0.85

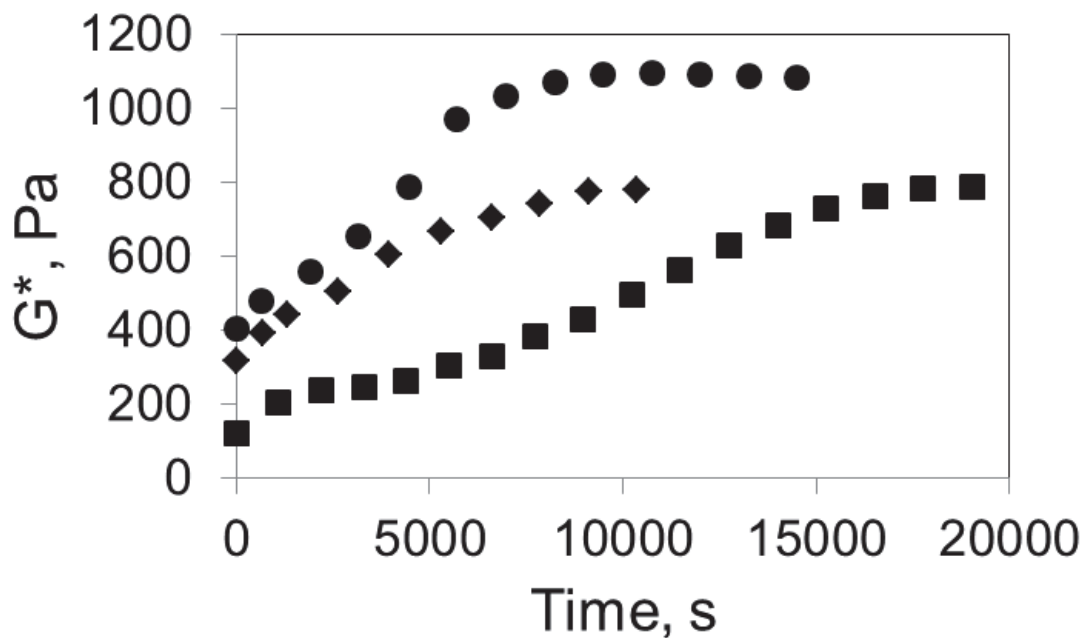


**Figure 3.13.** Rheology of phase separating SIS copolymer in toluene at room temperature at 37 (■), 45 (◆), and 50 (●) wt% polymer following extraction of solvent from a 20 wt% solution.

**Table 3.2.** Avrami exponent and half-time of SB and SIS block copolymers

	Polymer Concentration	n	$t_{0.5}$
SB	37	1.04	776.15
	45	0.69	3394.00
	50	0.84	4617.00
SIS	37	1.33	9722.60
	45	0.79	3733.00
	50	0.90	4943.80

## **Chapter 4**

### **In situ Tracking of Domain Growth During the Drying of Solution-cast Block Copolymer Films Using Small Angle X-Ray Scattering, Part I: Ordering Kinetics**

# **In situ Tracking of Domain Growth During the Drying of Solution-cast Block Copolymer Films Using Small Angle X-Ray Scattering, Part I: Ordering Kinetics**

Michael J. Heinzer<sup>1</sup>, Sangil Han<sup>1</sup>, J. A. Pople<sup>2</sup>, Donald G. Baird<sup>1</sup>, Stephen M. Martin<sup>1</sup>

<sup>1</sup>Department of Chemical Engineering, Virginia Polytechnic Institute and State University, Blacksburg, VA 24061-0211

<sup>2</sup> Stanford Synchrotron Radiation Lightsource, SLAC National Accelerator Laboratory, Menlo Park, CA 94025

## **4.1 Abstract**

The ordering of a poly(styrene-*b*-butadiene) block copolymer solution into hexagonally-packed cylinders during the extraction of a neutral solvent from a solution-cast film was studied in real-time using *in situ* small angle X-ray scattering. By tracking changes in the scattering intensity as solvent is continually removed from the film, information on the ordering rate was obtained as the film progresses from the dilute to the concentrated regime. At room temperature, the ordering rate was found to be controlled by thermodynamics below a critical concentration and by limited chain mobility at higher concentrations. The effect of drying temperature on the ordering kinetics was investigated by extracting solvent at three different temperatures: 30, 40, and 60°C. The net effect of drying temperature on the ordering rate was found to depend on a competition between the- thermodynamics of the drying film and the mobility of the copolymer chains. An intermediate temperature, 40°C, provided a balance between these competing phenomena, resulting in improved overall ordering in the films during solvent extraction. Finally, the effect of drying rate was considered by drying films in the presence of a sweep gas. The introduction of a sweep gas to remove solvent resulted in appreciable concentration gradients that hindered ordering in the films.

## 4.2 Introduction

Block copolymers are versatile candidates for numerous applications. In electronics, block copolymers are used to fabricate data storage media, patterned semiconductors, and photonic band-gap materials [Hamley, 2004; Zhang, 2010]. Block copolymer films can also be used in separation processes. Filter media and nano-porous membranes developed using block copolymers are employed as desalination membranes and bio-molecule purification membranes [Fasolka, 2001; Hamley, 2004; Wang, 2002; Zhang, 2010]. They have also been explored for fuel cell membranes as possible alternatives to Nafion® [Lee, 2009].

Central to making block copolymers such attractive materials is the ability to promote the development of specified microstructures on a nanometer length-scale which in turn govern material properties [Lodge, 2003]. For instance, block copolymers forming a bicontinuous structure have proven useful in creating efficient solar panels [Meuler, 2009]. Lee et al. [2009] demonstrated that changes in the dimensions of the lamella microstructure in block copolymer fuel cell membranes are a suitable means for improving proton flux. In other applications, including porous membranes [Jackson, 2010; Kang, 2009; Pai, 2004; Uehara, 2009], photonics [Backstaller, 2001], and sensors [Wirnsberger, 2001], hexagonally-packed cylinders have been utilized. As such, it is desirable to be able to control the final microstructure in order to optimize material properties for various applications.

The presence of a solvent allows access to a wider range of microstructures for a given block copolymer composition than can be attained in the melt state. Further, the breadth of structures that can be obtained by the addition of solvent is strongly dependent on the nature of the solvent [Alexandridis, 1998; Alexandridis, 1997; Alexandridis, 1996; Forster, 2001; Hanley, 2000; Lai, 2002; Lodge, 2002; Svensson, 1998]. Lodge [2002] extensively studied the phase

behavior of poly(styrene-*b*-isoprene) in solution, showing that by changing the solvent selectivity, a block copolymer developing only cylinders in a neutral solvent, could form lamella, gyroid, and spheres in selective solvents. Not only was the selective solvent effective in creating new microstructures, but both normal and inverted versions of these structures could be obtained.

The equilibrium microstructures obtained by Lodge [2002] were shown to be a function of the solvent selectivity, solution temperature and solution composition. This dependence of microstructure on the nature of the solvent provides an additional degree of freedom to controlling morphology during the processing of block copolymer films.

Because of the complexity of the phase behavior of block copolymers in solution, the structure development during the processing of solution-cast films is dependent on the manner in which the solvent is removed. For instance, Wang et al. [2001] showed that because of the thermotropic nature of block copolymer phase behavior in solution, changing the temperature at which a block copolymer film was dried changed the microstructure in the final film. Further, Huang et al. [2004] and Gong and coworkers [2006] demonstrated that the ordered structures developing at a given point during solvent removal is dependent on the concentration of polymer in the film. As the film becomes more concentrated, a block copolymer may go through many metastable states and order-order transitions. As a consequence of this, it has been shown that the film morphology is also a function of the drying rate [Gong, 2005; Huang, 2002; Kim, 1998; Zhang, 2000]. It is evident from such studies that— an understanding of the ordering kinetics during solvent removal is imperative.

Tremendous efforts have been made to understand the mechanism of ordered structure growth in block copolymer films during solution-casting. Consideration has been given to the influence of drying temperature [Lee, 2009], drying rate [Gong, 2005; Kim, 1998], solvent

selectivity [Huang, 2004; Lee, 2009; Leolukman, 2008; Li, 2010] and solvent annealing [Guo, 2008; Kim, 1998; Leolukman, 2008; Li, 2010; Luo, 2010; Paik, 2010; Peng, 2006; Peng, 2004] on structure development. However, these studies typically only look at the final morphology following prescribed processing conditions. While many authors attempt to deduce an ordering mechanism, rarely is kinetic data collected during the solvent extraction process itself.

In some instances, groups have monitored structure evolution at certain points during solvent removal. At several concentrations during film drying Gong and coworkers [2006] freeze-dried samples and analyzed the morphology using microscopy. The authors were able to show the progression of the morphology from polystyrene spheres in a poly(methyl methacrylate) matrix to polystyrene cylinders to lamellae, and finally to PMMA cylinders. Similarly, Huang [2004] froze in structures during the removal of a neutral solvent, toluene, from styrenic block copolymer films, observing transitions between inverted and normal spheres and cylinders while moving from dilute to concentrated films. While these studies were capable of demonstrating the lyotropic nature of the drying film, the work did not quantify the kinetics of such transitions.

Recently, Paik et al. [2010] demonstrated the ability to track order-disorder and order-order transitions through in situ GISAXS measurements. This work, however, was primarily concerned with structure changes during solvent annealing as the films swell or deswell. Though the work did comment on structure development during the addition and removal of solvent, the kinetics of the structure formation and the drying process itself was not the focal point of the work.

Numerous other authors have studied the ordering kinetics of block copolymers in solution [Bang, 2003; Chastek, 2003; Chastek, 2004; Liu, 2004; Nie, 2003; Park, 2004; Soenen,

1997]. These works have tracked growth from a disordered state [Chastek, 2003; Chastek, 2004; Liu, 2004; Nie, 2003; Soenen, 1997] and transitions between two ordered states [Bang, 2003; Park, 2004]. Rheology, SAXS, or a combination of these methods is used to determine the degree of ordering in the solution as a function of time. The ordering kinetics are then quantitatively analyzed using a suitable model, particularly the Avrami model for crystallization, to obtain information regarding the ordering rate and growth mechanism. Others [Chastek, 2003; Chastek, 2004] have used polarized optical microscopy to directly monitor the growth of ordered domains by measuring the growth front velocity of the grains.

The studies mentioned above fail to fully explain the ordering kinetics during solvent removal. The transitions being explored are thermally induced. That is, the growth of a new state is initiated by heating or cooling through a thermal transition. They also fail to account for the ordering kinetics over a full range of concentrations that will be encountered during film drying, concerning themselves primarily with temperature effects. In multiple cases, only a single concentration is considered for a given block copolymer solution [Chastek, 2003; Nie, 2003; Park, 2004]. When multiple concentrations have been considered, only a few concentrations in semi-dilute solutions are given attention [Liu, 2004; Soenen, 1997]. In solvent extraction, one is concerned with changes induced because of the lyotropic nature of the solution. It is important to understand how the ordering process changes as one proceeds through order-disorder transition concentrations and subsequent order-order transitions into the concentrated region of the film.

In the work presented here, *in situ* small angle X-ray scattering (SAXS) measurements were used to track, in real-time, the evolution of ordered structures in a block copolymer film during solvent removal. SAXS is a powerful tool for studying the phase separation process of a

block copolymer. Quantitative information regarding the ordered domain can be obtained by analyzing the primary scattering peak. The Bragg spacing is a function of the wave-vector of the primary peak,  $q^*$  :

$$d_{Bragg} = \frac{2\pi}{q^*} \quad (4-1)$$

The extent of ordering in the sample,  $\phi$ , is related to the integrated intensity of the primary peak through the scattering power,  $P$ :

$$P = \frac{1}{2\pi} \int I(q)q dq \quad (4-2)$$

where,  $I(q)$  is the relative intensity at a wave-vector,  $q$ . The scattering power can then be related to the volume fraction of the ordered phase in the material,  $\phi$ , by Eq. 4-3:

$$P = \Delta n^2 \phi (1 - \phi) \quad (4-3)$$

In Eq. 4-3,  $\Delta n$  is the difference in the electron densities of the two phases. This relation holds for a binary system. Thus, by monitoring changes in the scattering power as a function of time and polymer concentration during solvent removal, the ordering kinetics can be tracked in real-time.

In the current study the development of ordered structures as solvent is continually removed from a block copolymer film was monitored by tracking changes in the scattering power. The kinetics of the ordering process were quantified at concentrations ranging from the dilute to the concentrated regimes during the drying process. Changes in the ordering kinetics with concentration during solvent removal at room temperature are first discussed. The effect of drying temperature on the ordering kinetics during solvent removal is then described. Finally, the effect of changing the drying rate by drying films in the presence and absence of a sweep gas is discussed.

## **4.3 Experimental**

### **4.3.1 Materials**

A block copolymer, poly(styrene-*b*-butadiene) (SB), was purchased from Sigma-Aldrich and used as received. Based on SEC, the weight-average molecular weight of the diblock copolymer was determined by SEC to be 119.3 kg/mol and the PDI is 1.01. The polymer is reported to be 33% polystyrene. A neutral solvent, toluene (> 99.5% pure), was purchased from Sigma-Aldrich and used as received.

### **4.3.2 Solution Preparation**

Solutions were prepared by dissolving an appropriate amount of copolymer in toluene to yield a 20 wt% polymer solution. Solutions were made in a sealed vial and sonicated at room temperature overnight (> 12 hours) or until a clear solution was obtained prior to use. Solutions were used within 24 hours of preparation.

### **4.3.3 Scattering Cell**

The apparatus for SAXS measurements during solvent removal was designed and fabricated in our lab and is shown in Fig. 4.1. The apparatus consists of an aluminum cell attached to an aluminum harness. Two Kapton® windows are present on the side of the cell. On the back of the cell are two ports that serve as inlet and outlets for a nitrogen sweep gas. Nitrogen gas enters through the bottom port and exits through the top port.

The cell is covered by an aluminum lid to create a closed environment within the cell, with the exception of the inlet and outlet gas. A thermocouple (Type K, purchased from Omega®) is inserted through a hole in the center of the lid to monitor the temperature inside the cell.

Insulated fiberglass Omegalux<sup>TM</sup> heating tape (FGS051-020) purchased from Omega® was used to heat the environment surrounding the sample. The tape was wrapped around the unit, extending from lid down the cell to just above the Kapton® windows. The heating tape allowed temperature control from ambient to approximately 200°C, which was sufficient for achieving the temperatures desired in these experiments. The heating tape is powered by a variable transformer. During experiments, the temperature fluctuated no more than +/- 1°C.

The cell is capable of simultaneously monitoring solvent loss from a polymer solution and continuously obtaining scattering profiles during the solvent removal process. An aluminum stage is attached to a telescopic post that can be adjusted manually. The post runs through the bottom of the cell and attaches to a balance that sits in the harness. The harness attaches to a motorized stage so that the cell, stage, and balance can be moved in the beam line as a single unit. The balance is connected to computer to register the weight of the sample on the stage during experiments.

#### **4.3.4 In situ SAXS Experiments**

A 0.15 g sample of polymer solution was transferred drop-wise by pipette from the solution vial onto a 25-mm x 25-mm silica wafer on the stage in the sample cell. The final polymer films had a thickness of 50-µm. The samples were dried in the cell while the weight was recorded every five seconds. As solvent was removed, they were exposed to an incident X-ray beam for 30-seconds every 60-seconds. The beam entered through the Kapton® window at an angle parallel to the film surface at 0°. A portion of the beam was occluded by the polymer solution. For consistency, the sample was positioned such that the same amount of beam was occluded to begin each experiment. The sample position relative to the beam path was not adjusted during the experiment. In total, five different drying conditions were examined. The

samples were dried at three different temperatures (30, 40, 60°C) without a nitrogen sweep gas and at 30°C and 40°C, samples were also dried in the presence of a nitrogen sweep gas.

## **4.4 Results and Discussion**

### **4.4.1 Phase behavior**

Small angle X-ray scattering (SAXS) profiles for the SB block copolymer/toluene film recorded during solvent removal at 30°C are depicted in Fig. 4.2 for polymer weight fractions between 0.22 and 0.8. The primary peak at a wave-vector of  $0.2 \text{ nm}^{-1}$  first appears at 30 wt% polymer. Beginning around a polymer weight fraction of 0.5, secondary peaks appear. The intensity of these secondary peaks is relatively low. Insets in Fig. 4.2 show these secondary peaks more clearly. The secondary peak is located at a  $q / q_{\text{max}}$  value of  $3^{1/2}$ . Based on the relative positions of the peaks in the scattering profiles and the position of the primary peak, the microstructure is hexagonally-packed cylinders [Park, 2004] with a Bragg spacing of approximately 30 nm. The relative positions of the peaks are constant over all solvent concentrations, indicating that the structure does not depend on solvent content.

Scattering profiles at a concentration of 60 wt% SB for films dried at 40°C and 60°C are shown in Fig. 4.3. Insets are again included to more clearly show the secondary peaks. These peaks have been shifted for clarity. Secondary peaks also appear at a wave-vector ( $0.33 \text{ nm}^{-1}$ ) that is  $3^{1/2}$  times the primary peak position, indicating hexagonally-packed cylinders at 40°C and 60°C.

### **4.4.2 Ordering kinetics during solvent removal under ambient conditions**

The degree of ordering in the block copolymer film is related to the integrated intensity of the primary peak ( $n=1$ ) in the SAXS profile. Prior to integration, all profiles are normalized to

account for changes in concentration and film thickness. Fig. 4.4 contains a plot of the integrated intensity as a function of concentration for solvent removal from an SB/toluene film at 30 °C. Below the order-disorder transition (ODT), there is no discernible ordering and the integrated intensity is equal to zero. The onset of ordering is signaled by an increase in the integrated intensity beginning at approximately 30 wt% polymer, which we identify as the order-disorder concentration. The integrated intensity increases in a sigmoidal manner above the ODT concentration. The fluctuations observed in the semi-dilute region are due to interference caused by reflections off the film surface.

The integrated intensity increases as the solvent is removed before leveling off at approximately 80 wt% polymer, indicating that the ordered phase has stopped growing. Growth is still observed at relatively high polymer concentrations ( $> 60$  wt% polymer) where chain mobility is expected to be limited, but it must be recognized that the concentrations in Fig. 4.4 are average concentrations for a relatively thick film ( $> 50$   $\mu\text{m}$ ). The existence of concentration gradients results in regions in the film where the local concentration is below the average concentration. The continued growth likely occurs in the more dilute regions of the film where chain movement is still possible.

The sigmoidal shape of the integrated intensity indicates that the ordering rate varies with polymer concentration. The ordering rate during the solvent removal can be quantified by plotting the integrated intensity as a function of time, shown in Fig. 4.5. The data is fit with a third-order polynomial to smooth out the noise due to reflections from the film surface. The derivative at a given time is defined as the instantaneous ordering rate at the corresponding polymer concentration.

The instantaneous ordering rates as a function of polymer concentration are shown in Fig. 4.6. The ordering rate is concave down with respect to concentration. Initially, the instantaneous ordering rate increases as the polymer concentration increases above the ODT concentration (~30 wt% polymer). A broad maximum is reached between approximately 42 and 50 wt% polymer, followed by a decrease as the sample becomes more concentrated.

The trend depicted in Fig. 4.6 is the result of competition between thermodynamic and kinetic factors. Fig. 4.7 is a schematic phase diagram for a block copolymer in solution showing the order-disorder transition (ODT – solid line) and a constant temperature drying path (dashed line) for solvent removal from the copolymer film. Near the order-disorder transition the disordered state is metastable and the energy barrier for nucleation is large. Moving away from order-disorder transitions makes the disordered state unstable. It has been reported that the half-time for ordering decreases as the inverse of the square of the quench depth ( $\delta = T_{\text{ODT}} - T$ ) for shallow temperature quenches below the ODT temperature. Thus, the ordering is slow near the ODT and increases farther away from it. Similar behavior is responsible for the increase in ordering rate as polymer concentration increases beyond the ODT concentration. Fig. 4.7 shows that as the solvent is removed from the film, the film moves farther from the order-disorder transition concentration and  $\delta$  increases. The combination of these effects causes the net thermodynamic driving force for phase separation to increase as the film initially becomes more concentrated. This results in an increased ordering rate.

Increasing the polymer concentration also results in a reduction in chain mobility, so that as the driving force for ordering increases, chain mobility is continually decreasing. At high polymer concentrations the chain mobility decreases to the point that the kinetic factors begin to dominate the thermodynamic factors in dictating the ordering rate. Thus, a continual decrease in

the ordering rate is observed as the polymer concentration increases into the concentrated regime. The ordering rate approaches zero at high polymer concentrations when the chains become kinetically trapped.

### **4.4.3 Effect of drying temperature on ordering**

#### **4.4.3.1 Drying curves**

Toluene was removed from poly(styrene-*b*-butadiene) (SB) block copolymer films at three different temperatures (30°C, 40°C, 60°C.) Fig. 4.8 contains drying curves (polymer wt% vs. time). The drying rate is primarily controlled by evaporation of solvent at the film/air interface at short times, referred to as the constant drying regime, and the rate of solvent removal increases with increasing temperature. At longer times, the solvent removal is diffusion-controlled, resulting in a decreased drying rate. The onset of diffusion-controlled solvent removal occurs at shorter times and higher residual solvent content as temperature is increased. This is attributed to the formation of a “skin” – a thin region of high polymer concentration – at the film surface due to rapid solvent removal at the air/film interface relative to the rate of solvent diffusion through the film. Upon the formation of the skin layer, the solvent removal becomes extremely slow. Increasing the drying temperature increases skin formation and the degree of solvent trapping below the skin layer. A consequence of this phenomenon is the development of substantial concentration gradients in the film. While techniques such as vacuum drying exist for removing residual solvent, they are not compatible with the experiments currently being performed. Therefore, these studies are limited to the final concentrations observed in Fig. 4.8.

#### 4.4.3.2 Ordering Kinetics

The integrated intensities of the primary SAXS peaks recorded during solvent removal from an SB/toluene film at 30°C, 40°C and 60°C are plotted as a function of polymer concentration in Fig. 4.9. The integrated intensities are normalized to account for temperature, solvent content, and film thickness differences. Beyond the concentrations shown in Fig. 4.9, reflections off the surface interfere with the scattering signal, producing unreliable data. Only concentrations for which interference is not present are analyzed.

Increasing the temperature from 30°C to 40°C resulted in higher integrated intensities for a given concentration despite shorter ordering times due to the higher drying rate. The final integrated intensity at 40°C, obtained at 66 wt% polymer, is around 12 a.u. while the final integrated intensity obtained at 30°C at 90 wt% polymer is only 7 a.u. This indicates that the ordering is more rapid at 40°C than at 30°C.

Further increasing the temperature to 60°C also results in more rapid ordering than observed at 30°C. At 53 wt% polymer, the integrated intensity from the film dried at 60°C is 5 a.u., as opposed to a value of 3 a.u. for the film dried at 30°C. The film dried at 60°C has a lower integrated intensity for a given polymer concentration than the film dried at 40°C; however, the drying rate at 60°C is faster than the drying rate at 40°C.

The instantaneous ordering rates for SB-toluene films dried at 30°C, 40°C, and 60°C are shown in Fig. 4.10. At the two elevated temperatures, 40°C and 60°C, the ordering rates are significantly higher than the rates measured at 30°C for all concentrations. At 40°C and 60°C, the ordering rates continue to increase at concentrations for which the film dried at 30°C begins to show a decrease in the ordering rate. The data taken at 40°C shows a slowing of the rate of increase of the ordering rate with concentration, which may indicate it is approaching a

maximum. This maximum does not occur in the range of measurable data, but would be at a higher concentration than the maximum obtained at 30°C. At 60°C, the ordering rates do not appear to be approaching a maximum.

The ordering rates at 40°C and 60°C show a crossover at around 55 wt% polymer. At low concentrations, the ordering rates at 40°C are nearly double the ordering rates at 60°C. After the cross-over, the ordering rate at 60°C is approximately 10% higher than the ordering rate at 40°C at 53 wt% polymer, the final point for which ordering data was obtained at 60°C.

The trends in ordering rate with temperature and concentration in Fig. 4.10 can be explained by considering two effects: the changes in the thermodynamic driving force with temperature, and the changes in chain mobility with temperature and concentration. The kinetics at a given temperature and concentration are the result of a combination of these effects. To help explain these concepts, Fig. 4.11 depicts a schematic block copolymer/solvent phase diagram, showing the ODT and drying paths for films dried at three different temperatures. As temperature decreases (moving vertically in the phase diagram) the interaction parameter between the styrene and butadiene blocks increases, increasing the driving force for phase separation. As discussed in Section 4.4.2, the ordering time is expected to decrease as the square of the quench depth,  $\delta$ . Films dried at 60°C will always be closest to the disordering temperature, and will have the lowest driving force for ordering at all concentrations. Disregarding the effect of chain mobility, the ordering rate should increase as temperature decreases. However, decreasing the temperature also decreases chain mobility, so if structure growth is diffusion-driven, decreasing the chain mobility should decrease the ordering rate. The changes in thermodynamics and chain mobility with temperature cannot be decoupled. If the increase in the interaction parameter with lowered temperature is substantial enough to offset the

loss of thermal mobility, the net result is an increase in the ordering rate. Alternatively, if the diminished chain mobility cannot be overcome by improved thermodynamics, the ordering rate is slowed.

The ordering rate at 30°C is lower than at 40°C or 60°C. At 30°C the driving force for chain segregation is the greatest, but is offset by the decreased chain mobility, as shown in Fig. 4.11. This results in lower ordering rates at 30°C than at the higher temperatures.

The ordering rate of the film dried at 40°C is higher than that of the film dried at 60°C for low polymer concentrations. As shown in Fig. 4.11, the film dried at 40°C will have a higher thermodynamic driving force for phase separation, but lower chain mobility. In this case, the difference in the chain mobility at these two temperatures appears to be small relative to the difference in the thermodynamic driving forces.

The crossover in the ordering rates at 40°C and 60°C suggests that chain mobility decreases more rapidly with concentration at 40°C than at 60°C. As shown in Fig. 4.11, as the film becomes more concentrated, the relative difference in  $\delta$  decreases. That is, differences in the thermodynamic driving force become less substantial moving deeper into the phase diagram. Eventually, the difference in thermodynamic driving force is negligible relative to the difference in the chain mobility. The ordering rate cross-over observed in Fig. 4.10 is attributed to the increased influence of chain mobility at lower temperatures as polymer concentration increases. At higher concentrations, higher temperatures result in higher ordering rates because of improved chain mobility; however, the improved mobility comes at the cost of shorter ordering times, which results in a lower degree of ordering at a given concentration, as seen in Fig. 4.9.

In addition to having different ordering rates, the instantaneous ordering rate curves display different shapes. This results from changes in the thermodynamic driving force as the

concentration changes. Increasing the polymer concentration in the film by removing solvent results in an increase in the thermodynamic driving force for phase separation and a reduction in chain mobility. At 30°C, this was manifested as a maximum in the ordering rate as a function of concentration. The higher ordering rates and lack of an observable maximum at 40°C and 60°C suggests that the increased temperature results in a significant increase in chain mobility.

#### **4.4.4 Effect of sweep gas on ordering kinetics**

The data presented in Section 3.2 is sufficient to investigate how ordering kinetics change with drying temperature. However, changing the temperature inherently changes the dry rate which will alter certain characteristics of the system, such as the development of concentration gradients in the film, which can affect ordering in the film. Unfortunately, such factors cannot be independently analyzed based on Section 4.4.3. To better understand how drying rate influences ordering, films dried at 30°C and 40°C were dried in the presence and absence of a sweep gas.

##### **4.4.4.1 Drying Curves**

The solvent removal rates at 30°C and 40°C were altered by introducing a sweep gas. Films prepared with a sweep gas still exhibited the same cylindrical structure as those formed in the absence of sweep gas. Figures 4.12a and b show the drying curves for films dried with and without a sweep gas at 30°C and 40°C, respectively. At both temperatures, the sweep gas results in a slower drying rate. The presence of a sweep gas should improve mass transfer at the film/air interface, but the slower drying rates indicate that the rapid solvent evaporation at the surface causes the development of a skin layer. The skin layer creates a diffusion barrier for residual solvent in the film and slows the solvent removal rate. Nonetheless, drying with a sweep gas allowed for two different drying rates to be studied at a single drying temperature.

#### 4.4.4.2 Ordering Kinetics

Plots of the integrated intensity as a function of concentration for films dried with and without a sweep gas at 30°C and 40°C are shown in Figures 4.13a and b, respectively. At 30°C, the range of concentrations over which ordering was observed is different for the two different solvent removal rates. The onset of ordering occurs at a lower concentration with sweep gas than without. This is attributed to the fact that introducing a sweep gas results in significant concentration gradients. As such, at lower average concentrations, the concentration near the film's free surface is expected to be higher than the order-disorder transition concentration. This results in ordered phase growth at concentrations below the expected ODT. Reflection from the surface of the films dried with a sweep gas prevented data analysis at high polymer concentrations.

At 30°C and concentrations below 35 wt% polymer, the rate of change of the integrated intensity with concentration for a film dried in the presence of a sweep gas is comparable to the trend observed for a film dried without a sweep gas. Beyond approximately 35 wt% polymer, the integrated intensities of the two films deviate from one another, with the film dried without a sweep gas ordering more rapidly with respect to concentration. This is observed despite the film having a faster solvent removal rate and a shorter time to order.

At 40°C, no difference in the onset of ordering is discernible. It appears that under both solvent removal conditions, the rise in the integrated intensity begins at nearly the same concentration. However, the film dried in the presence of a sweep gas shows a significant degree of scatter in the data at low polymer concentrations. Prior to 35 wt% polymer, the intensities of the films dried under both conditions are comparable as concentration changes. The intensities with respect to concentration diverge at approximately 35 wt% polymer. At approximately 50

wt% polymer, which is the maximum concentration that reliable data was obtained using a sweep gas, the intensities are comparable once more. Thus, the apparent differences in changes in intensity with concentration may be due to scatter in the data collected from the film dried with a sweep gas.

Figs. 4.14a and b show the instantaneous ordering rates for the films dried at 30°C and 40°C, respectively. At both temperatures, films dried without a sweep gas have higher ordering rates than films dried with a sweep gas. This is attributed to the fact that the films dried with a sweep gas have more significant concentration gradients. This results in the formation of a skin with a high polymer concentration at the surface with concentration decreasing rapidly away from the surface. Conditions are unfavorable for ordering due to limited chain mobility in the concentrated skin and a low driving force for ordering in the dilute region of the film. The concentrations in the films dried without a sweep gas are more uniform, resulting in faster ordering throughout the film. Despite these difference, the decreased ordering rates observed in the films dried with a sweep gas are offset by increased ordering times resulting in a similar degree of ordering for a given concentration, as shown in Figure 4.13.

Changing the drying rate at 30°C affects the shape of the ordering rate versus concentration curve. The ordering rate of the film dried with a sweep gas increases with concentration for all measured concentrations. Therefore it can be inferred that the maximum ordering rate occurs at a higher concentration when removing solvent with a sweep gas than without a sweep gas. This can be attributed to steep concentration gradients in the film dried with a sweep gas resulting in regions with low polymer concentration (i.e. below the average film concentration) where the ordering rate is still high. Further study is necessary to confirm the presence of gradients in the film and their effect on the maximum ordering rate. However, it is

clear that the presence of a sweep gas, and resultant change in drying rate, significantly affect the ordering in the film.

#### **4.5 Conclusions**

*In situ* small angle X-ray scattering (SAXS) has been used to quantify the kinetics of the development of ordered structures in a block copolymer film during solvent removal in real-time. The technique allows the simultaneous determination of the type of ordered structure (e.g. cylinders, lamellae) and the extent of ordering as a function of the film concentration. Ordering was studied as a function of temperature and in the presence and absence of a sweep gas. The ordering kinetics at a given concentration and temperature are the result of a competition between changes in the thermodynamic driving force for phase separation and chain mobility. In general, the ordering rate increases as the concentration initially progresses beyond the order-disorder transition due to an increased thermodynamic driving force. At high concentrations, chain mobility decreases and the ordering rate decreases until the film becomes kinetically trapped.

Drying the film at elevated temperatures (40°C and 60°C) serves to decrease the effect of lowered chain mobility at high concentrations and improves ordered phase formation during the solvent removal process. The ordering kinetics also become more complex due to the competition between thermodynamics and chain mobility. The intermediate drying temperature, 40°C, resulted in the highest initial ordering kinetics and final degree of ordering due to the balance between thermodynamic and kinetic effects. The high temperature, 60°C, exhibited lower initial ordering rates due to the formation of a high polymer concentration 'skin' that acted as a diffusion barrier, and the final degree of ordering was limited by the short drying time.

The addition of a sweep gas resulted in a decreased drying rate due to the formation of a high polymer concentration ‘skin’ that limited solvent diffusion. The skin formation results in steep concentration gradients at the surface of the film, which decreases the instantaneous ordering rates. At a low temperature, 30°C, the difference in ordering rates resulted in slight differences in the extent of ordering in the film at a given concentration. At an elevated temperature, 40°C, there is no net effect on the extent of ordering in the film because the reduction in ordering rate is balanced by longer ordering times due to the slower drying rate.

#### **4.6 Acknowledgements**

Partial funding for this work was provided by the Institute for Critical Technology and Applied Science at Virginia Tech. The authors acknowledge Eastman Chemical Company for providing funding through the Eastman Fellowship in Polymer Science. Portions of this research were carried out at the Stanford Synchrotron Radiation Laboratory, a national user facility operated by Stanford University on behalf of the U.S. Department of Energy, Office of Basic Energy Sciences. The SSRL Structural Molecular Biology Program is supported by the Department of Energy, Office of Biological and Environmental Research, and by the National Institutes of Health, National Center for Research Resources, Biomedical Technology Program, and the National Institute of General Medical Sciences.

#### **4.7 References**

1. Alexandridis, P.; Olsson, U.; Lindman, B. *Langmuir* **1998**, *14*, 2627.
2. Alexandridis, P.; Olsson, U.; Lindman, B. *Langmuir* **1997**, *13*, 23.
3. Alexandridis, P.; Zhou, D.; Khan, A. *Langmuir* **1996**, *12*, 2690.
4. Bang, J.; Lodge, T.P. *J. Phys. Chem. B* **2003**, *107*, 12071.
5. Bockstaller, M.; Kolb, R.; Thomas, E.L. *Adv. Mater.* **2001**, *13*, 1783.
6. Chastek, T.Q.; Lodge, T.P. *Macromolecules* **2004**, *37*, 4891.

7. Chastek, T.Q.; Lodge, T.P. *Macromolecules* **2003**, *36*, 7672.
8. Fasolka, M.J.; Mayes, A.M. *Annu. Rev. Mater. Res.* **2001**, *31*, 323.
9. Forster, S.; Berton, B.; Hentze, H.P.; Kramer, E.; Antonietti, M.; Lindner, P.  
*Macromolecules* **2001**, *34*, 4610.
10. Fredrickson, G.H.; Binder, K. *J. Chem. Phys.* **1989**, *91*, 7265.
11. Gong, Y.M.; Hu, Z.J.; Chen, Y.Z.; Huang, H.Y.; He, T.B. *Langmuir* **2005**, *21*, 11870.
12. Gong, Y.M.; Huang, H.Y.; Hu, Z.J.; Chen, Y.Z.; Chen, D.J.; Wang, Z.B.; He, T.B.  
*Macromolecules* **2006**, *39*, 3369.
13. Guo, R.; Huang, H.; Chen, Y.; Gong, Y.; Du, B.; He, T. *Macromolecules* **2008**, *41*, 890.
14. Hamley, I.W. Introduction to Block Copolymers. In *Developments in Block Copolymer Science and Technology*; Hamley, I. W., Ed.; John Wiley & Sons, Ltd.: New York, 2004; p 1.
15. Hanley, K.J.; Lodge, T.P.; Huang, C.I. *Macromolecules* **2000**, *33*, 5918.
16. Huang, H.; Hu, Z.; Chen, Y.; Zhang, F.; Gong, Y.; He, T.; Wu, C. *Macromolecules* **2004**, *37*, 6523.
17. Huang, H.; Zhang, F.; Hu, Z.; Du, B.; He, T.; Lee, F.K.; Wang, Y.; Tsui, O.K.C.  
*Macromolecules* **2002**, *36*, 4084.
18. Jackson, E.A.; Hillmyer, M.A. *ACS Nano* **2010**, *4*, 3548.
19. Kang, M.; Moon, B. *Macromolecules* **2009**, *42*, 455.
20. Kim, G.; Libera, M. *Macromolecules* **1998**, *31*, 2569.
21. Lee, M.; Park, J.K.; Lee, H.S.; Lane, O.; Moore, R.B.; McGrath, J.E.; Baird, D.G.  
*Polymer* **2009**,

50, 6129.

22. Lai, C.J.; Russel, W.B.; Register, R.A. *Macromolecules* **2002**, *35*, 841.
23. Leolukman, M.; La, Y.H.; Li, X.; Gopalan, P. *Polym. J.* **2008**, *40*, 825.
24. Li, Y.; Huang, H.; He, T.; Gong, Y. *J. Phys. Chem. B* **2010**, *114*, 1264.
25. Liu, Z.; Shaw, M.; Hsiao, B.S. *Macromolecules* **2004**, *37*, 9880.
26. Lodge, T. P. *Macromol. Chem. Physic.* **2003**, *204*, 265.
27. Lodge, T.P.; Pudil, B.; Hanley, K.J. *Macromolecules* **2002**, *35*, 4707.
28. Luo, C.; Huang, W.; Han, Y. *Macromol. Rapid Commun.* **2009**, *30*, 1917.
29. Meuler, A.J.; Hillmyer, M.A.; Bates, F.S. *Macromolecules* **2009**, *42*, 7221.
30. Nie, H.F.; Bansil, R.; Ludwig, K.; Steinhart, M.; Konak, C.; Bang, J. *Macromolecules* **2003**, *36*, 8097.
31. Pai, R.A.; Humayun, R.; Schulberg, M.T.; Sengupta, A.; Sun, J.N.; Watkins, J.J. *Science* **2004**, *303*, 507.
32. Paik, M.Y.; Bosworth, J.K.; Smilges, D.M.; Schwartz, E.L.; Andre, X.; Ober, C.K. *Macromolecules* **2010**, *43*, 4253.
33. Park, M.J.; Bang, J.; Harada, T.; Char, K.; Lodge, T.P. *Macromolecules* **2004**, *37*, 9064.
34. Peng, J.; Kim, D.H.; Knoll, W.; Xuan, Y.; Li, B.Y.; Han, Y.C. *J. Chem. Phys.* **2006**, *125*, 064702.
35. Peng, J.; Xuan, Y.; Wang, H.F.; Yang, Y.M.; Li, B.Y.; Han, Y.C. *J. Chem. Phys.* **2004**, *120*, 11163.
36. Soenen, H.; Berghmans, H.; Winter, H.H.; Overbergh, N. *Polymer* **1997**, *38*, 5653.
37. Svensson, B.; Alexandridis, P.; Olsson, U. *J. Phys. Chem. B* **1998**, *102*, 7541.
38. Uehara, H.; Kakiage, M.; Sekiya, M.; Sakuma, D.; Yamonobe, T.; Takano, N.; Barraud,

- A.; Meurville, E.; Ryser, P. *ACS Nano* **2009**, *3*, 924.
39. Wang, F.; Hickner, M.; Kim, Y.S.; Zawodzinski, T.A.; McGrath, J.E. *J. Membr. Sci.* **2002**, *197*, 231.
40. Wang, Y.; Shen, J.S.; Long, C.F. *Polymer*, **2001**, *42*, 8443.
41. Wirnsberger, G.; Scott, B.J.; Stucky, G.D. *Chem. Commun.* **2001**, *01*, 119.
42. Zhang, J.; Yu X.; Yang, P.; Peng, J.; Luo, C.; Huang, W.; Han, Y. *Macromol. Rapid Commun.* **2010**, *31*, 591.
43. Zhang, Q.L.; Tsui, O.K.C.; Du, B.Y.; Zhang, F.J.; Tang, T.; He, T.B. *Macromolecules* **2000**, *33*, 9561.

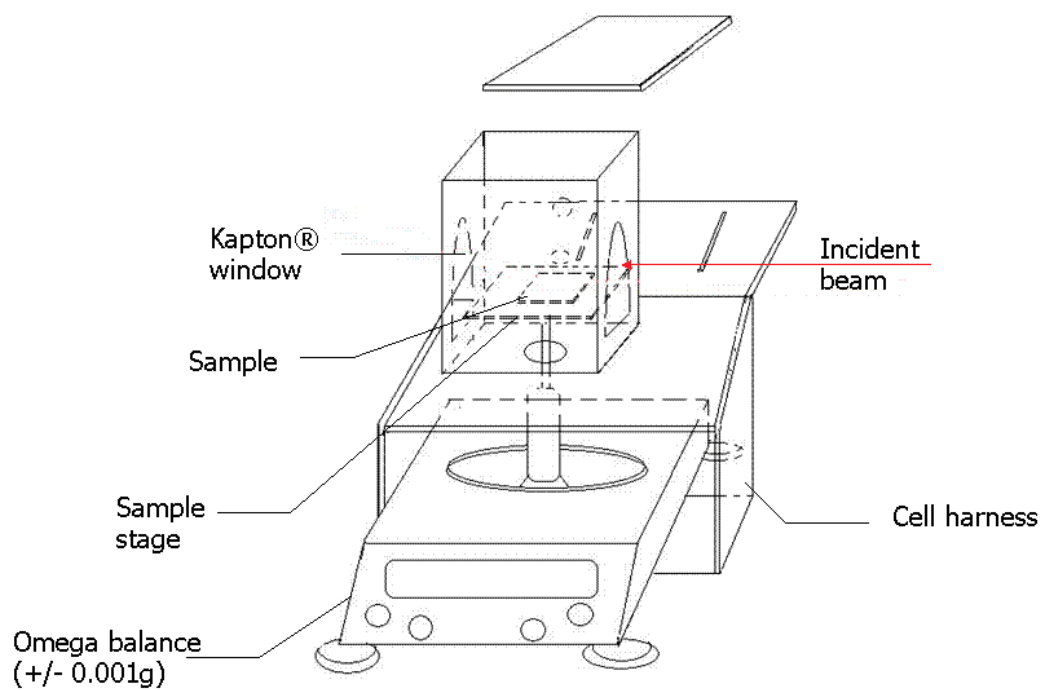


**Figure 4.1.** Scattering cell used to simultaneously monitor removal of solvent from block copolymer films and track ordered structure development using SAXS. Sample chamber can be wrapped in heating tape (not shown) to control the solvent removal temperature.

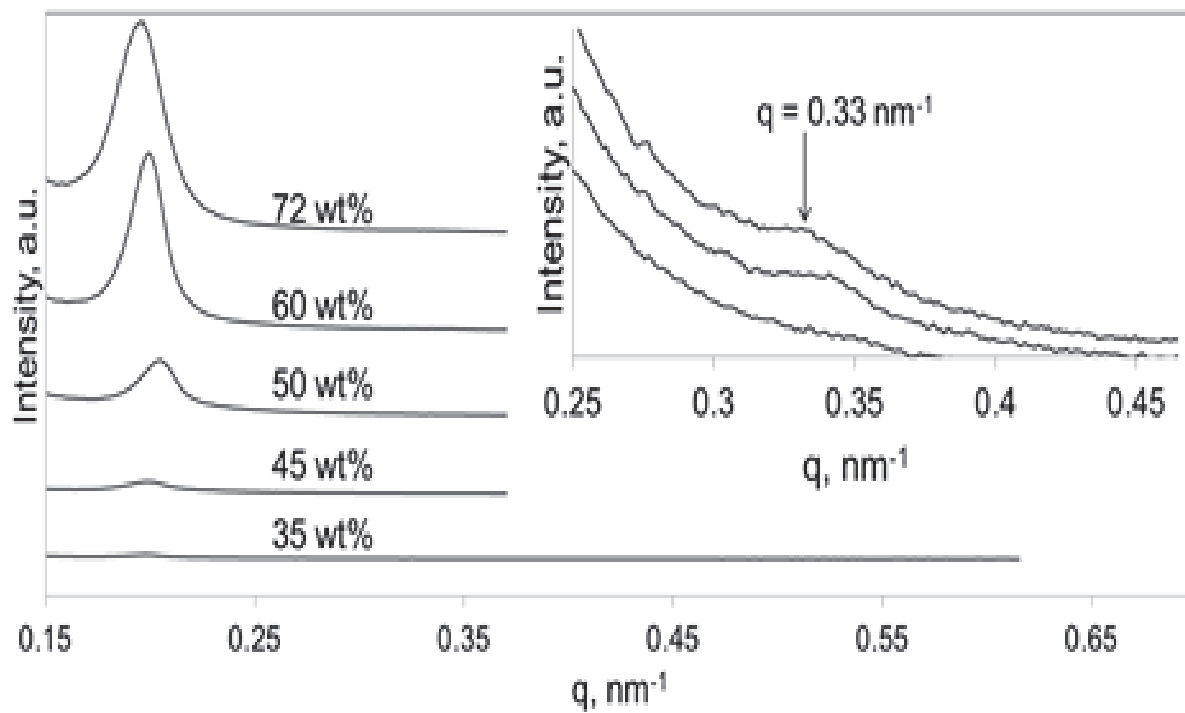


**Figure 4.2.** SAXS profiles of an SB/toluene solution during solvent removal at 30°C. Peaks positioned at  $n = 1$  and  $3^{1/2}$  are consistent with hexagonally-packed cylinders [Park, 2004].

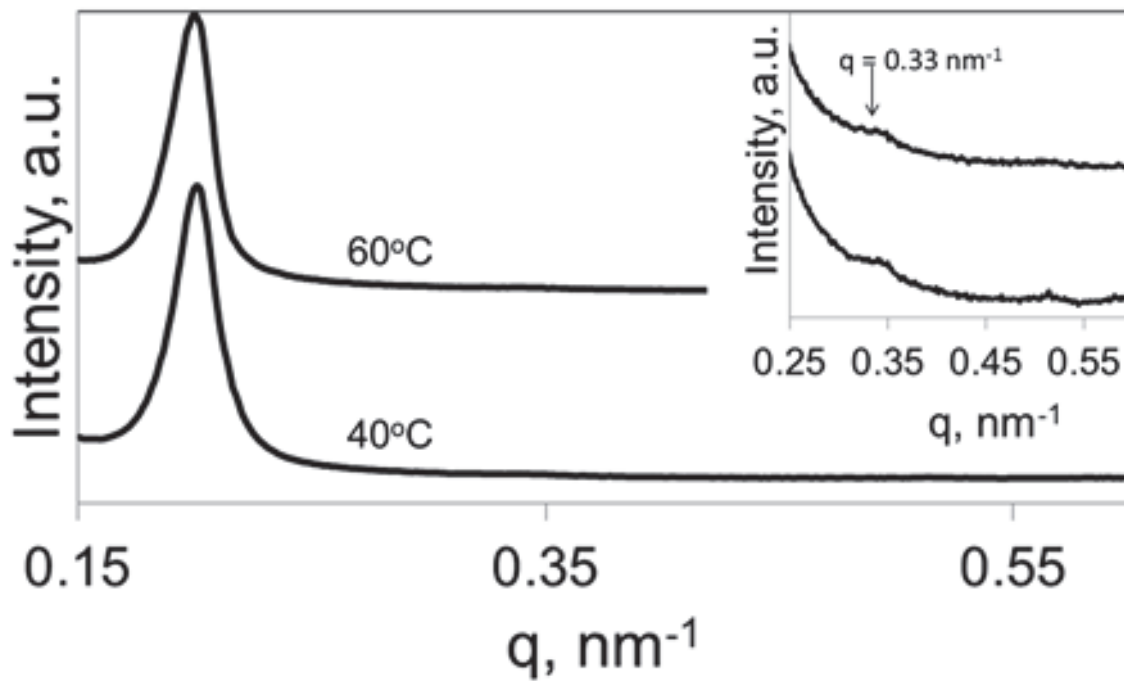


**Figure 4.3.** SAXS profiles of an SB/toluene film (60 wt% polymer) during solvent removal at 40°C and 60°C. Peaks positioned at  $n = 1$  and  $3^{1/2}$  are consistent with hexagonally-packed cylinders [Park, 2004].

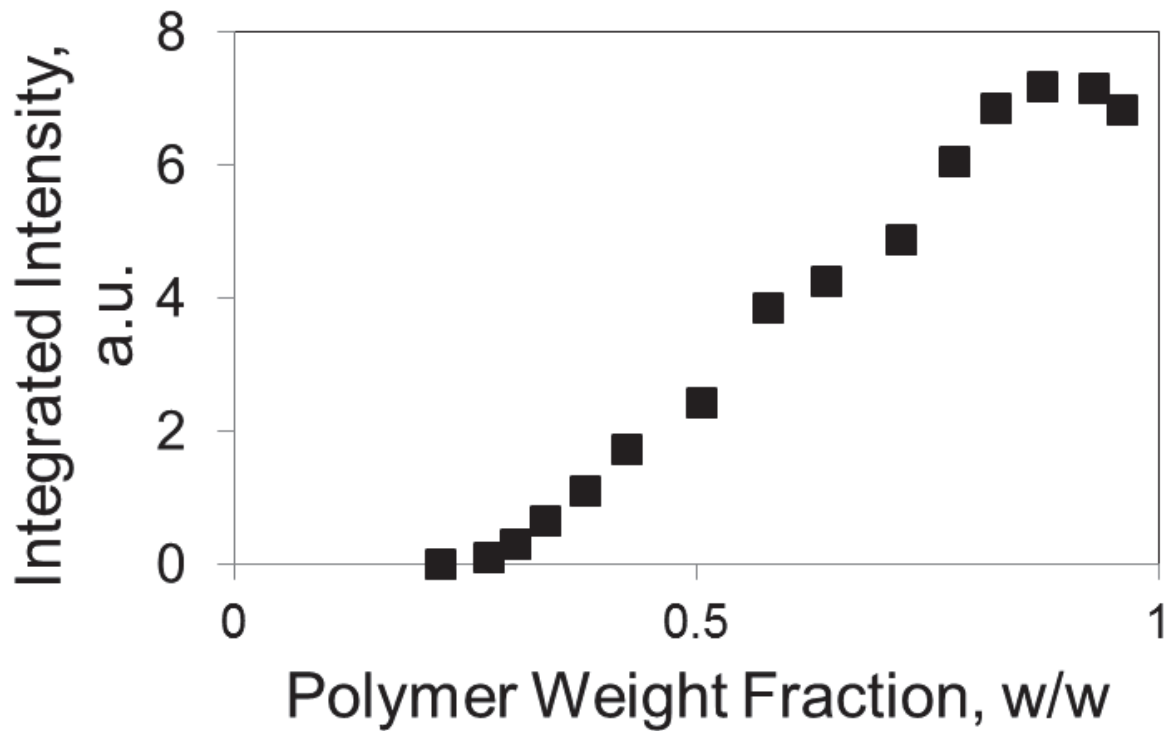


**Figure 4.4.** Integrated intensity of the primary SAXS peak ( $n=1$ ) as a function of the polymer weight fraction in a SB/toluene film during solvent removal at 30° C.

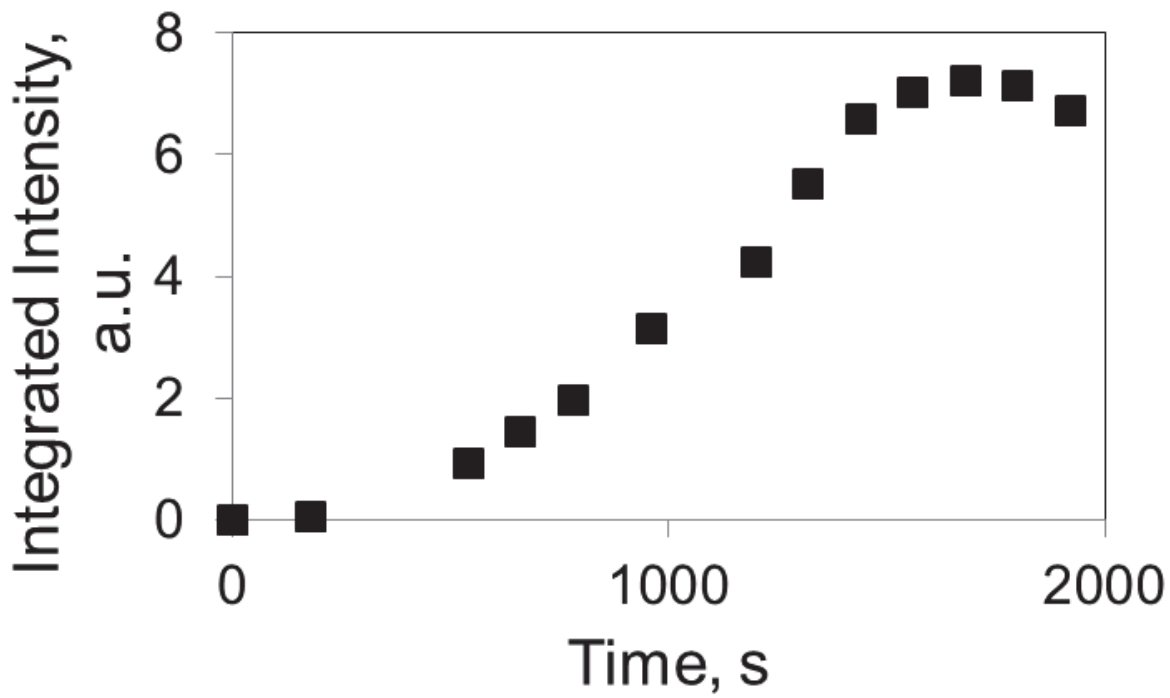


**Figure 4.5.** Integrated intensity of the primary SAXS peak ( $n=1$ ) as a function of time collected from a SB film cast in toluene while solvent is simultaneously removed at 30° C.

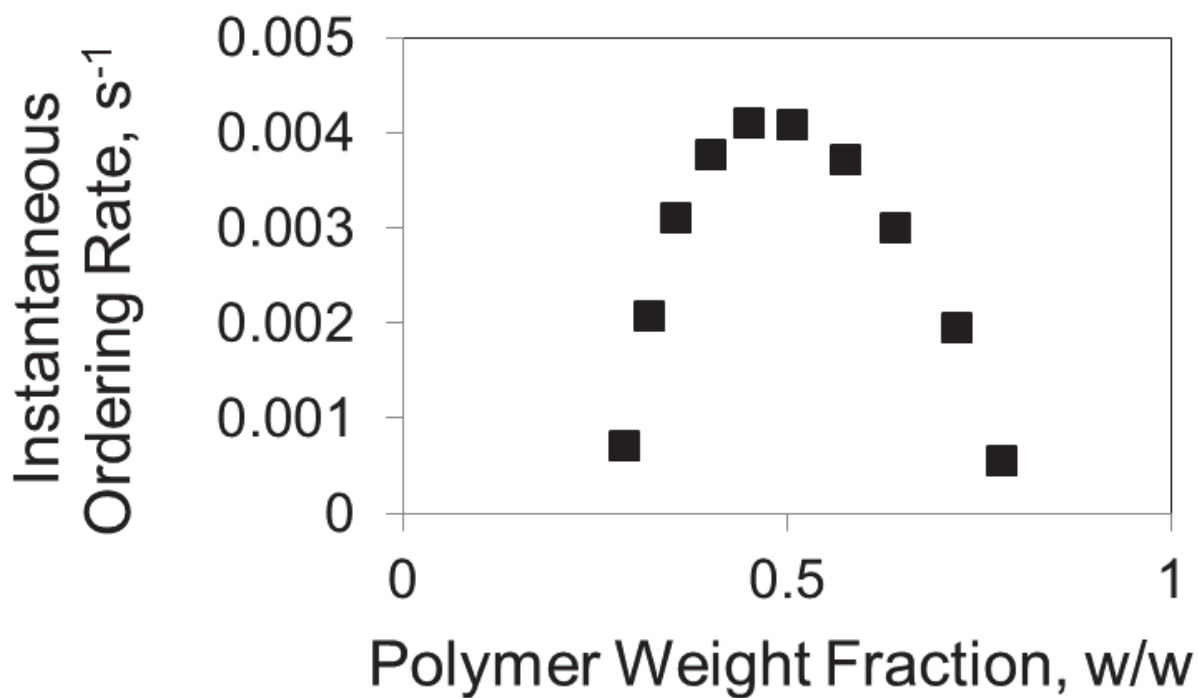


**Figure 4.6.** Instantaneous rate of ordering of the SB copolymer into hexagonally-packed cylinders in a neutral solvent, toluene, during continual solvent removal at 30°C.

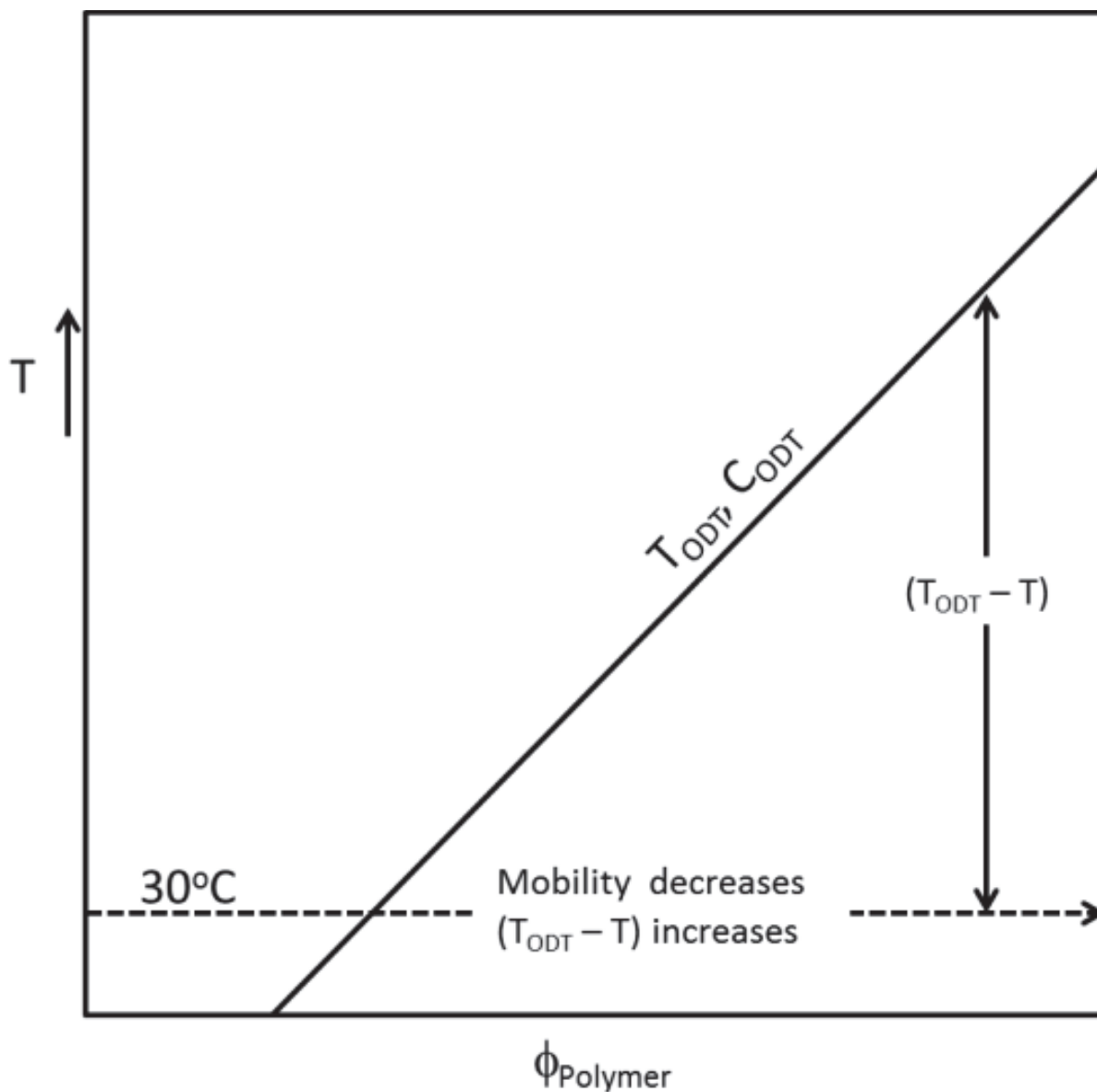


**Figure 4.7.** Schematic phase diagram (polymer concentration,  $\phi_{\text{Polymer}}$  vs. temperature,  $T$ ) illustrating the solvent removal path (dashed line) of the SB / toluene film at  $30^{\circ}\text{C}$ .  $T_{\text{ODT}}$  and  $C_{\text{ODT}}$  represent the order-disorder transition temperature and concentration, respectively.

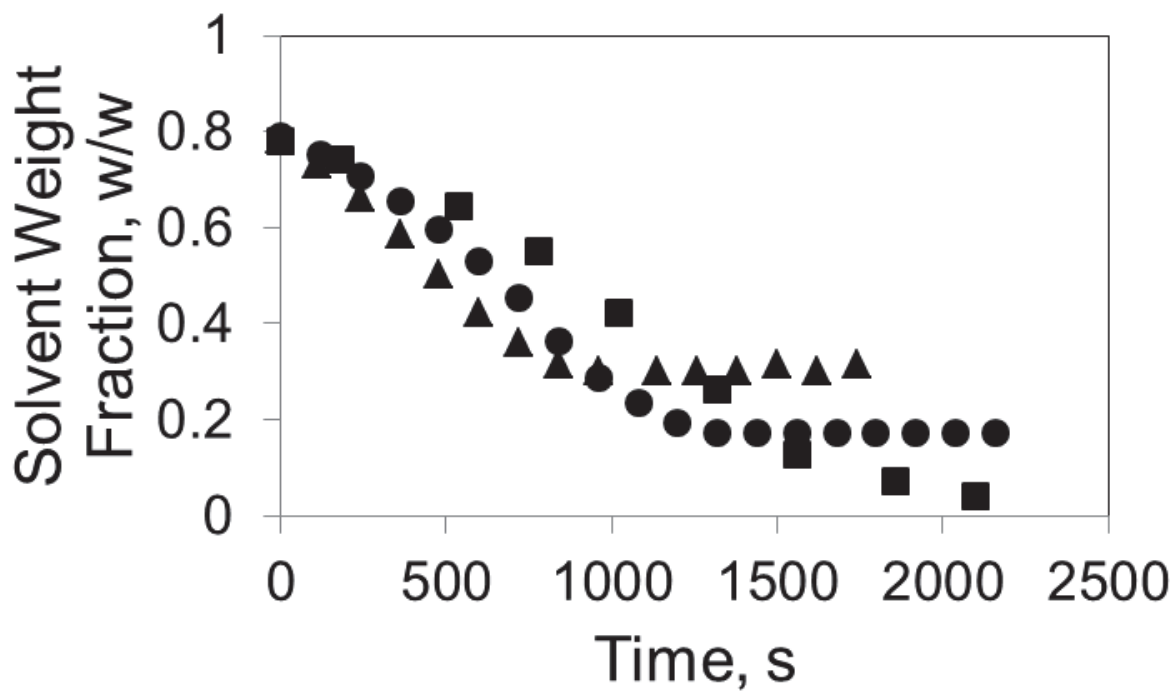


**Figure 4.8.** Drying curves for SB copolymer films cast from a 20 wt% toluene solution at 30°C (■), 40°C (●) and 60°C (▲).

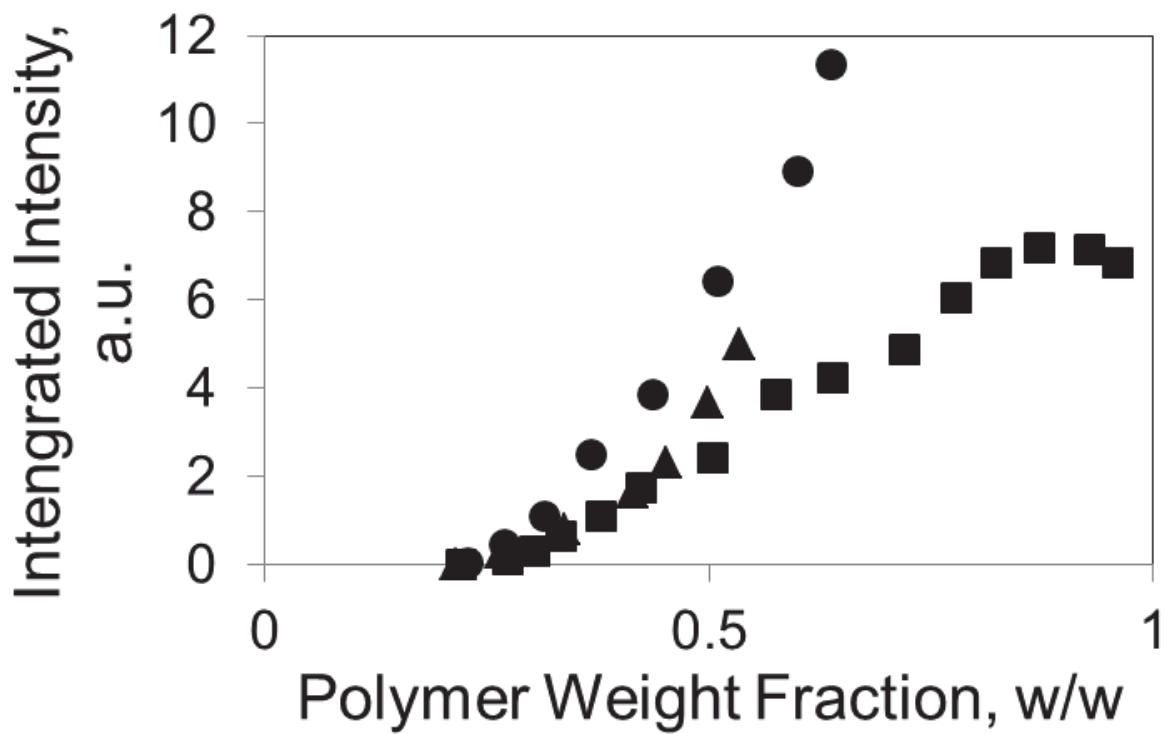


**Figure 4.9.** Primary scattering peak integrated intensity as a function of concentration during extraction of toluene from SB copolymer at 30°C (■), 40°C (●), and 60°C (▲).

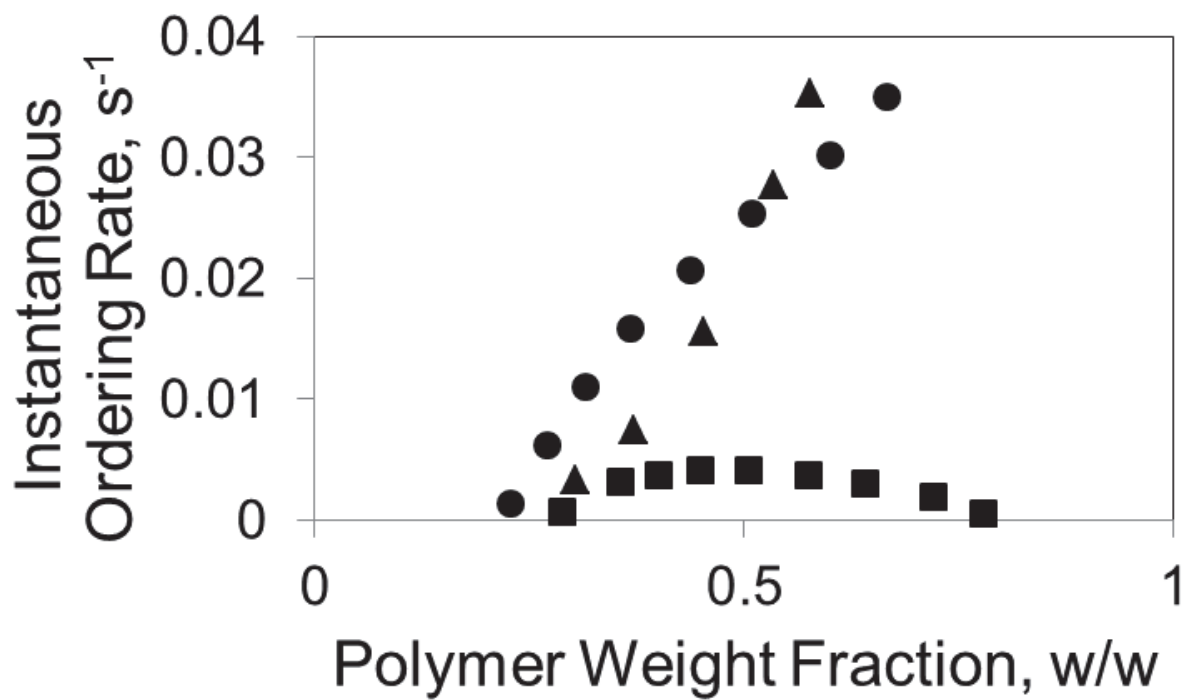


**Figure 4.10.** Instantaneous rate of ordering of the SB copolymer into hexagonally-packed cylinders in a neutral solvent, toluene, during continual solvent removal at 30°C (■), 40°C (●) and 60°C (▲).

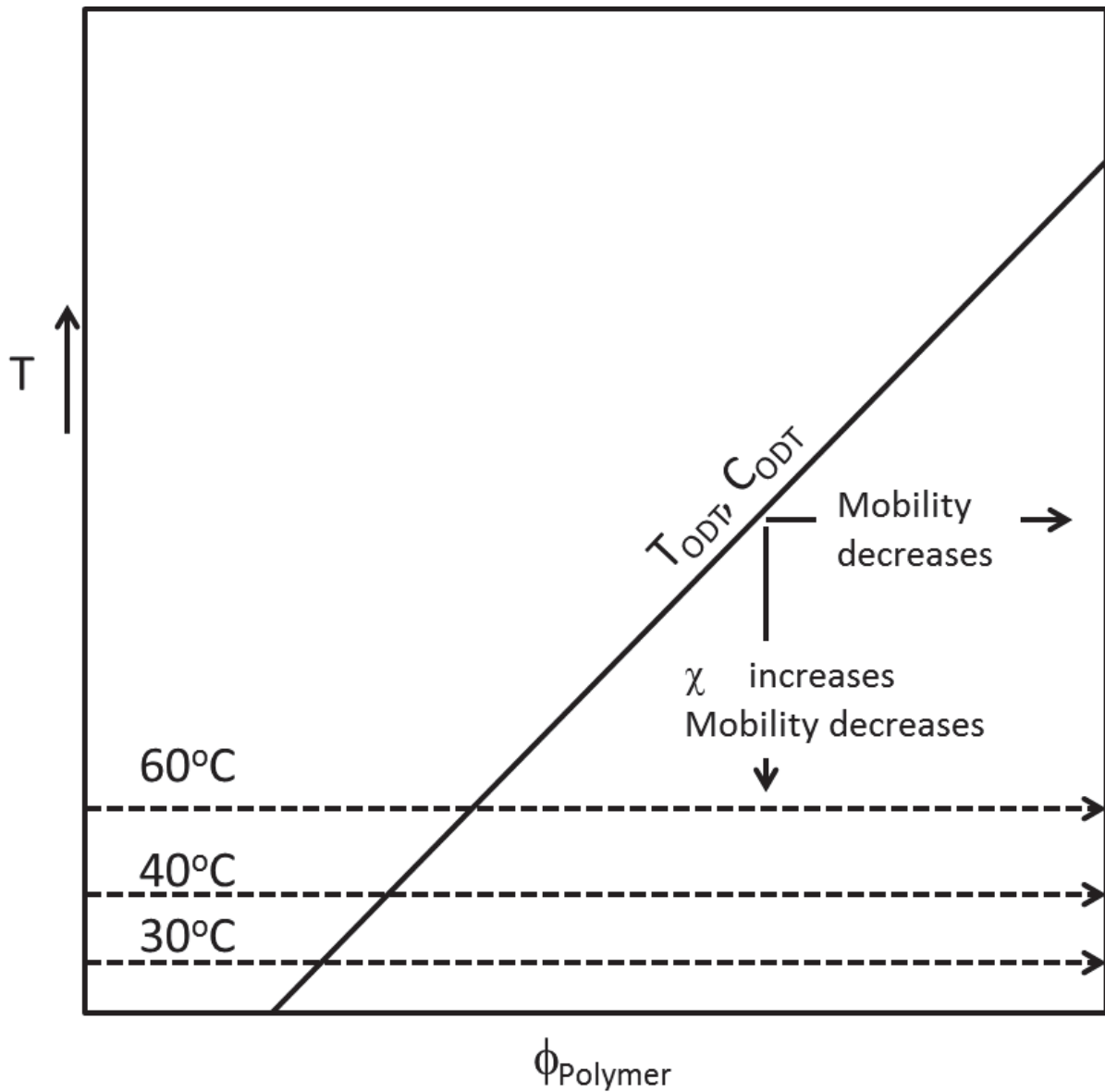


**Figure 4.11.** Schematic phase diagram (polymer concentration,  $\phi_{\text{Polymer}}$  vs. temperature, T) illustrating the solvent removal path (dashed lines) of the SB / toluene film at three different temperatures as indicated in the figure.  $T_{\text{ODT}}$  and  $C_{\text{ODT}}$  represent the order-disorder transition temperature and concentration, respectively.

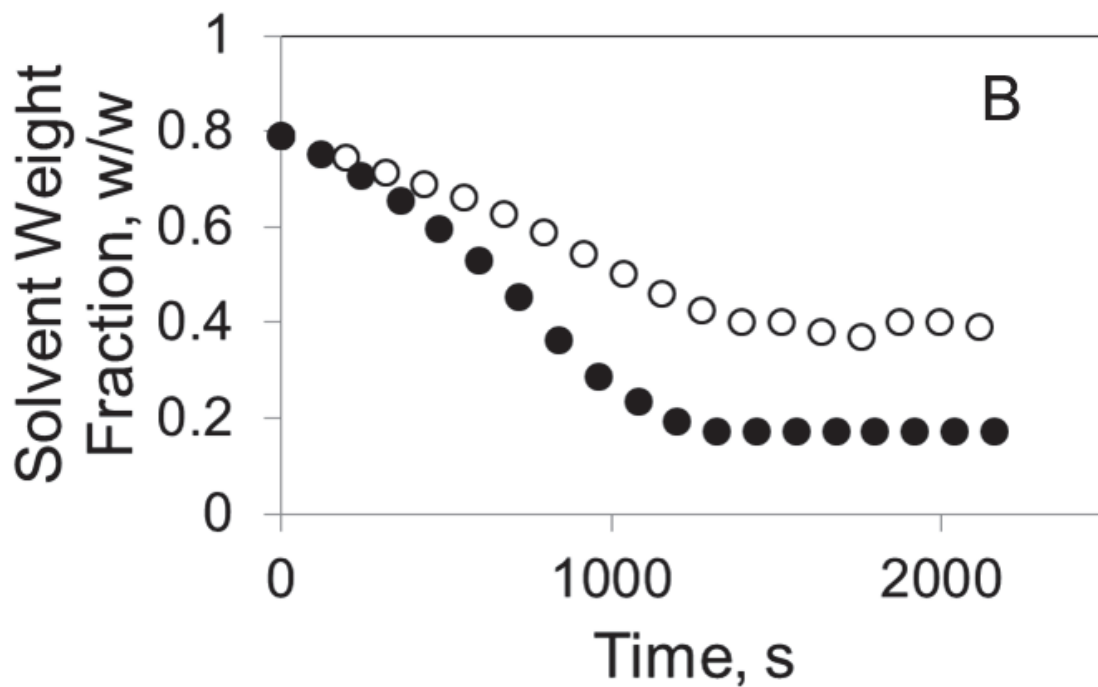
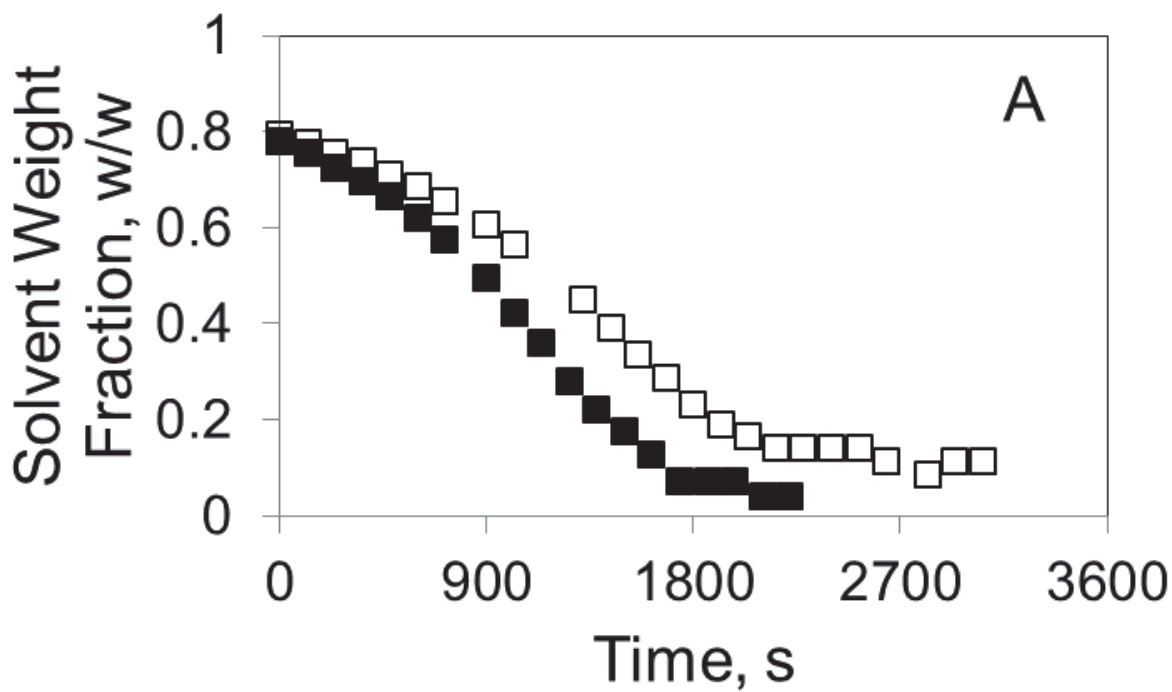


**Figure 4.12.** Drying curves for SB copolymer films cast from a 20 wt% toluene solution at 30°C (A) and 40°C (B). The curves in each figure represent films dried without a sweep gas (filled points) and with a sweep gas (open points).

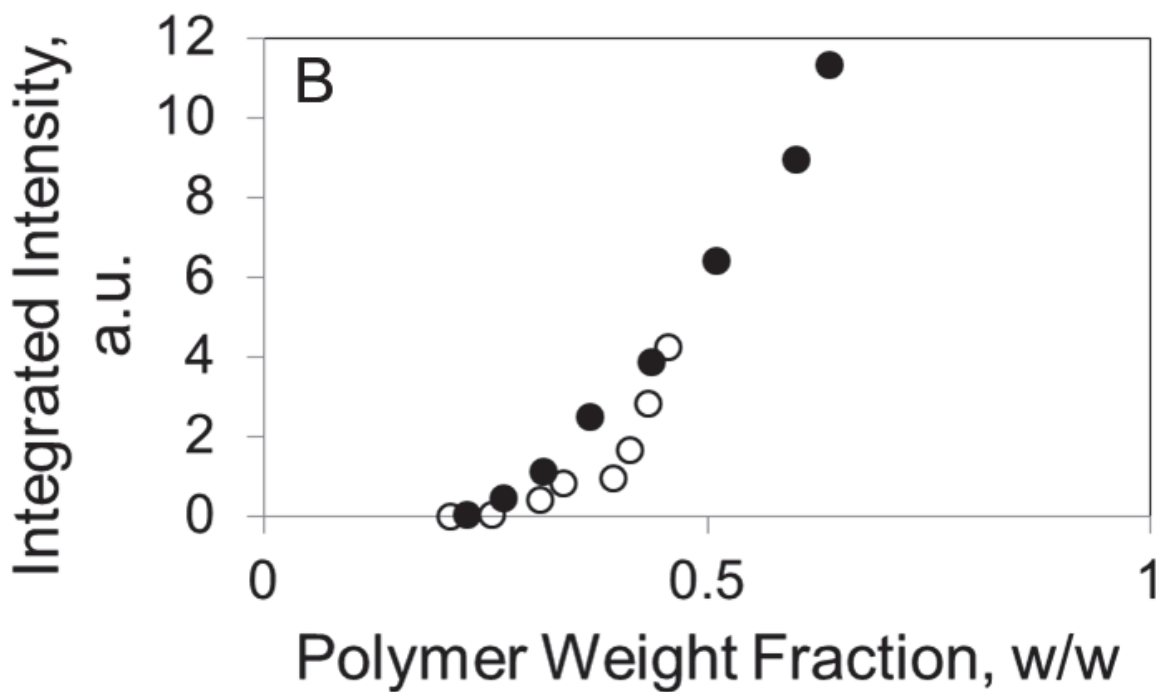
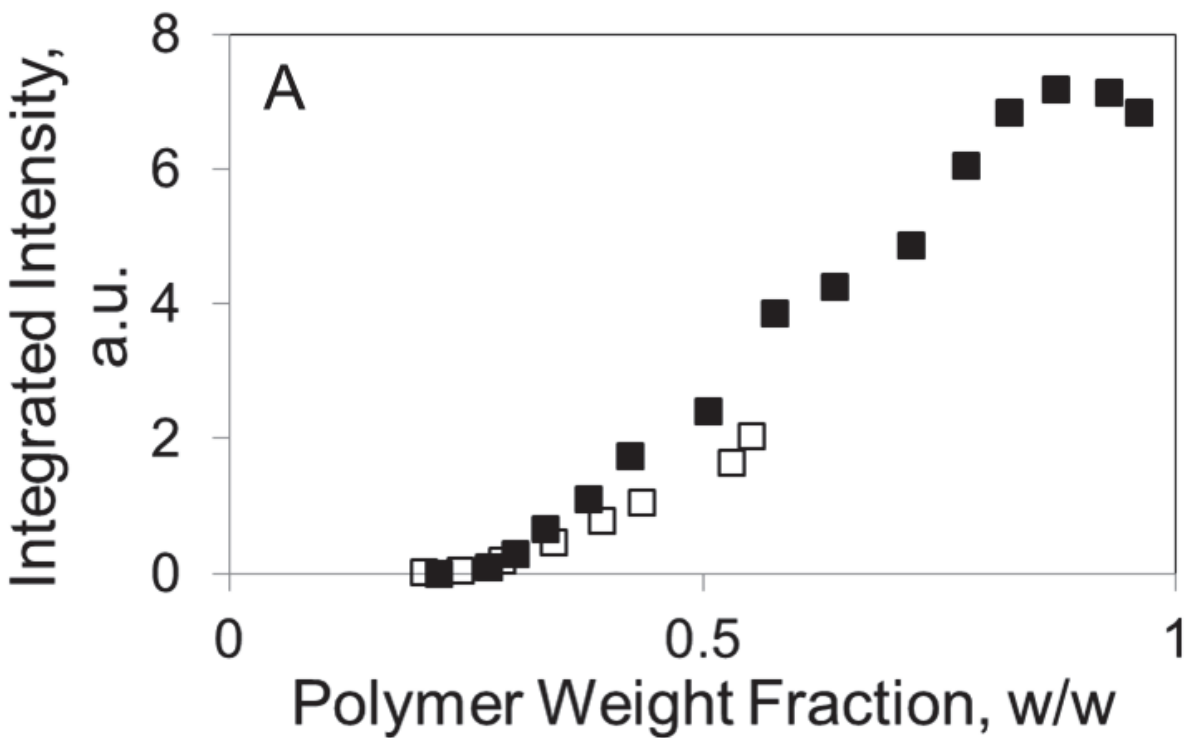


**Figure 4.13.** Primary scattering peak integrated intensity as a function of concentration during extraction of toluene from SB copolymer at 30°C (A) and 40°C (B). At both temperatures, films were dried without a sweep gas (closed points) and with a sweep gas (open points).

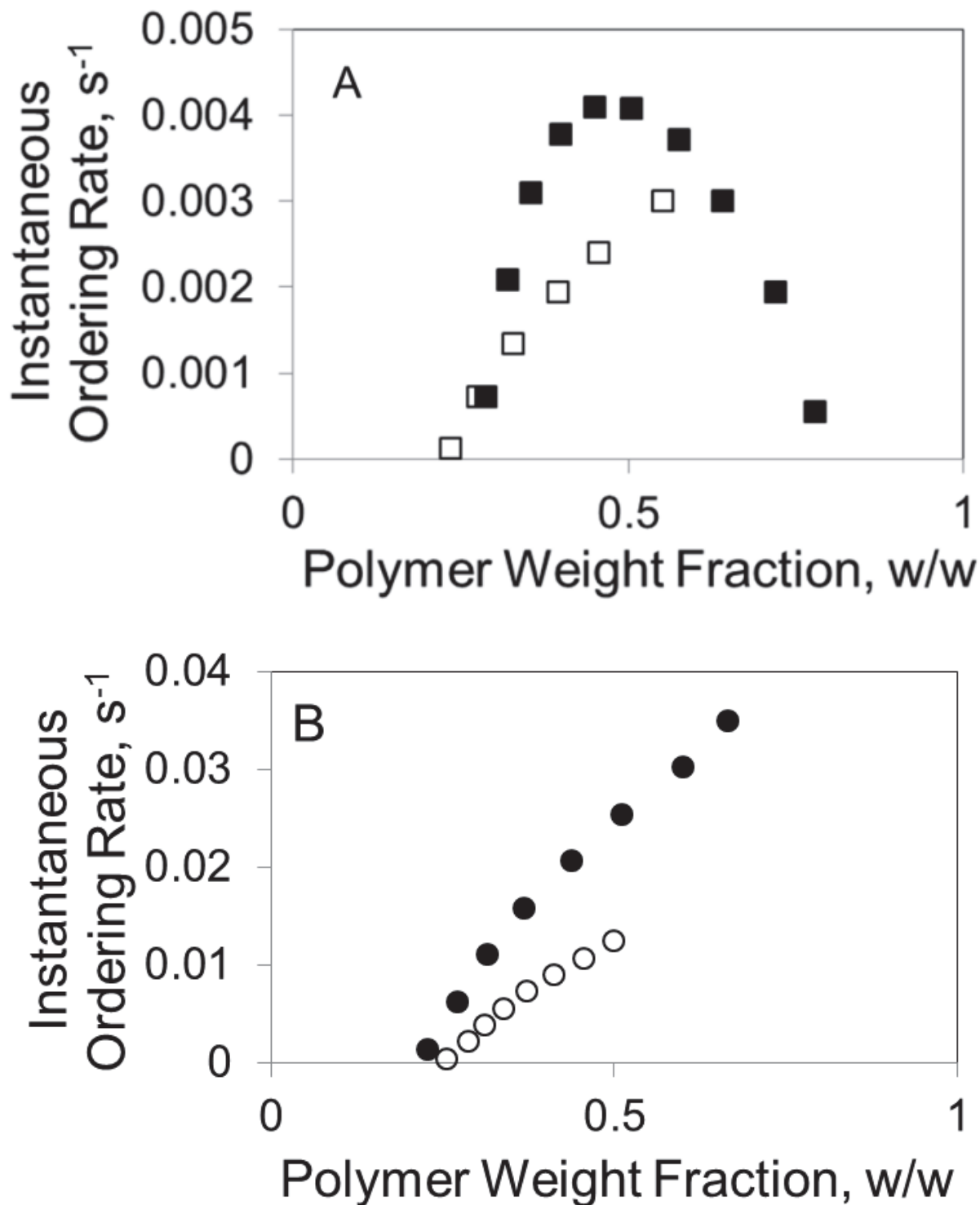


**Figure 4.14.** Instantaneous rate of ordering of the SB copolymer into hexagonally-packed cylinders in a neutral solvent, toluene, during continual solvent removal at 30°C (A) and 40°C (B). At both temperatures, films were dried with a sweep gas (open points) and without a sweep gas (closed points).

## **Chapter 5**

### **In situ Tracking of Domain Growth During the Drying of Solution-cast Block Copolymer Films Using Small Angle X-Ray Scattering, Part II: Domain Dimensions**

# **In situ Tracking of Domain Growth During the Drying of Solution-cast Block Copolymer Films Using Small Angle X-Ray Scattering, Part II: Domain Dimensions**

Michael J. Heinzer<sup>1</sup>, Sangil Han<sup>1</sup>, John A. Pople<sup>2</sup>, Donald G. Baird<sup>1</sup>, Stephen M. Martin<sup>1</sup>

<sup>1</sup>Department of Chemical Engineering, Virginia Polytechnic Institute and State University, Blacksburg, VA 24061-0211

<sup>2</sup>Stanford Synchrotron Radiation Lightsource, SLAC National Accelerator Laboratory, Menlo Park, CA 94025

## **5.1 Abstract**

Changes in the spacing of hexagonally-packed cylinders in a poly(styrene-*b*-butadiene) copolymer film during the continual extraction of toluene under different solvent removal conditions were studied by in situ small angle X-ray scattering (SAXS) measurements. As the solvent is removed from the film, the Bragg spacing in both the vertical and horizontal film direction increase due to increasing segregation power. Eventually, the polymer chains become kinetically trapped and Bragg spacing in both the vertical and horizontal direction decrease due to deswelling of the domains. These findings are consistent with previous observations of block copolymers in a neutral solvent. It was also observed that the Bragg spacing in the vertical direction decreases due to compression of the domains as the film thickness decreases. The degree of compression increased with increased polymer concentration due to an increase in the chain relaxation time. Increasing the drying temperature resulted in more severe domain compression, which is likely due to faster solvent removal. Removing solvent in the presence of a sweep gas further increased the domain compression. This was ascribed to the formation of a skin at the film surface, which leads to rapid kinetic trapping. When the solvent removal rate was decreased and skinning was avoided by saturating the sample chamber with the casting solvent, the resultant domain compression was impeded.

## 5.2 Introduction

Due primarily to their ability to phase separate into ordered structures on a nanometer length-scale, block copolymers are valuable materials in a number of applications. The gyroid [Meuler, 2009] and lamella [Lee, 2009] microstructures have been used to fabricate conductive materials. Hexagonally-packed cylinders are favored in other applications, such as porous membranes [Pai, 2004; Kang, 2009; Nuxoll, 2009; Jackson, 2010; Uehara, 2009], photonics [Bockstaller, 2001], and sensors [Wirnsberger, 2001]. Block copolymers have also received a great deal of attention as candidates for templates for patterned surfaces [Segalman, 2008; Bitá, 2008] for which other microstructures may be desirable, depending on the surface features necessitated by the end application.

While the specific microstructure is of considerable importance, equally as important in controlling material properties are the orientation and dimensions of these microstructures. For instance, cylinders oriented through the plane of the film are targeted for porous membranes and filters [Jackson, 2010]. Similar orientation is necessary in order for cylinders to effectively serve as templates for aligned nanowires [Zhang, 2002; Jung, 2008]. By changing the cylinder dimensions, including diameter and length, in membranes for drug delivery, the rate transport of species through a membrane can be controlled [Uehara, 2009; Yang, 2010]. This has also been shown to effectively improve membrane selectivity via size-exclusion [Nuxoll, 2009]. Both of these properties prove useful in fabricating drug-delivery devices. Similarly, changes in domain dimensions have been found to improve conductivity of fuel cell membranes prepared from block copolymers [Lee, 2009]. It is, therefore, advantageous to understand how microstructure dimensions and orientation evolve during the preparation of block copolymer films.

This paper is the second part of a two-part series on the study of block copolymer ordering during the extraction of solvent from a solution-cast film [Heinzer, 2011]. As such, while it is recognized that several methods, such as shear alignment [Jain, 2005; Marencic, 2010; Wu, 2005], electric fields [Olszowka, 2009], and graphoepitaxy [Bita, 2008; Segalman, 2001; Xiao, 2011], have been demonstrated to successfully control microstructure dimensions and orientation in block copolymer films, the work presented here focuses on the effect of solvent evaporation rate and temperature. Both temperature and drying rate have been shown to dictate the orientation of resultant thin film microstructures. For instance, Kim and Libera [1998] were able to switch the orientation of polystyrene cylinders in a poly(styrene-*b*-butadiene-*b*-styrene) film from perpendicular to in-plane by decreasing the drying rate. Liang et al. [2007] showed that at low temperatures, cylinders of a solution-cast block copolymer film orient parallel to the substrate, while subjecting the film to elevated temperatures yields vertical cylinder. The current work explores the evolution of the orientation of hexagonally-packed cylinders in a block copolymer film as solvent is continually extracted.

In Part 1 of this series [Heinzer, 2011], a set of small angle X-ray scattering experiments that allowed ordering of a block copolymer in the presence of solvent to be monitored in real time as solvent was extracted from a solvent-cast film were first introduced. The ability to quantitatively monitor structure development via changes in the scattering profile with concentration and time was demonstrated. The kinetics of the ordering process were reported in terms of the instantaneous ordering rates at several concentrations along the drying path starting at 20 wt% polymer.

In addition to providing information about the extent of ordering in the film, the in situ SAXS experiments were also capable of exposing details regarding the ordered domain

dimensions and microstructure orientation as the film contracts during solvent removal. Specifically, as solvent is removed, changes in the Bragg spacing in the vertical film direction were observed. This paper presents experimental results from real-time tracking of the dimensions and orientation of ordered structures during the removal of solvent from a block copolymer film. Details regarding the analysis of the scattering profiles to extract information about the horizontal and vertical Bragg spacing will be described. Based on this analysis, the effect of solvent removal temperature on the compression and resulting spacing of ordered microstructures during extraction of solvent from a block copolymer film is presented. Finally, the effect of drying rate on domain compression is discussed. The information presented is part of a larger effort to quantitatively analyze phase separation in block copolymer films during solvent removal.

## **5.3 Experimental**

### **5.3.1 Materials**

A block copolymer, poly(styrene-*b*-butadiene) (SB), was purchased from Sigma-Aldrich and used as received. Based on SEC, the weight-average molecular weight of the diblock copolymer was determined by SEC to be 119.3 kg/mol and the PDI is 1.01. The polymer is reported to be 33% polystyrene. A neutral solvent, toluene (> 99.5% pure), was purchased from Sigma-Aldrich and used as received.

### **5.3.2 Solution Preparation**

Solutions were prepared by dissolving an appropriate amount of copolymer in toluene to yield a 20 wt% polymer solution. Solutions were made in a sealed vial and sonicated at room

temperature overnight (> 12 hours) or until a clear solution was obtained prior to use. Solutions were used within 24 hours of preparation.

### 5.3.3 Scattering Cell

The apparatus for SAXS measurements during solvent removal was designed and fabricated in our lab and is shown in Fig. 4.1. The apparatus consists of an aluminum cell attached to an aluminum harness. Two Kapton® windows are present on the side of the cell. On the back of the cell are two ports that serve as inlet and outlets for a nitrogen sweep gas. Nitrogen gas enters through the bottom port and exits through the top port.

The cell is covered by an aluminum lid to create a closed environment within the cell, with the exception of the inlet and outlet gas. A thermocouple (Type K, purchased from Omega®) is inserted through a hole in the center of the lid to monitor the temperature inside the cell.

Insulated fiberglass Omegalux™ heating tape (FGS051-020) purchased from Omega® was used to heat the environment surrounding the sample. The tape was wrapped around the unit, extending from lid down the cell to just above the Kapton® windows. The heating tape allowed temperature control from ambient to approximately 200°C, which was sufficient for achieving the temperatures desired in these experiments. The heating tape is powered by a variable transformer. During experiments, the temperature fluctuated no more than +/- 1°C.

The cell is capable of simultaneously monitoring solvent loss from a polymer solution and continuously obtaining scattering profiles during the solvent removal process. An aluminum stage is attached to a telescopic post that can be adjusted manually. The post runs through the bottom of the cell and attaches to a balance that sits in the harness. The harness attaches to a motorized stage so that the cell, stage, and balance can be moved in the beam line as

a single unit. The balance is connected to computer to register the weight of the sample on the stage during experiments.

#### **5.3.4 In situ SAXS Experiments**

A 0.15 g sample of polymer solution was transferred drop-wise by pipette from the solution vial onto a 25-mm x 25-mm silica wafer on the stage in the sample cell. The final polymer films had a thickness of 50- $\mu\text{m}$ . The samples were dried in the cell while the weight was recorded every five seconds. As solvent was removed, they were exposed to an incident X-ray beam for 30-seconds every 60-seconds. The beam entered through the Kapton® window at an angle parallel to the film surface at 0°. A portion of the beam was occluded by the polymer solution. For consistency, the sample was positioned such that the same amount of beam was occluded to begin each experiment. The sample position relative to the beam path was not adjusted during the experiment. In total, five different drying conditions were examined. The samples were dried at three different temperatures (30, 40, 60°C) without a nitrogen sweep gas and at 30°C and 40°C, samples were also dried in the presence of a nitrogen sweep gas.

### **5.4 Results and Discussion**

#### **5.4.1 Peak-splitting**

This section describes the analysis of the scattering patterns to obtain information regarding spacing of ordered structures in the vertical and horizontal film directions. Data collected at two concentrations during the removal of solvent at 40°C will be used for illustrative purposes to facilitate the discussion. Details regarding the cause of the behavior will be discussed in later sections of the paper.

The scattering patterns produced by an SB copolymer film at 45 and 72 wt% polymer during the extraction of toluene at 40°C are shown in Figs. 5.1a and b, respectively. The radial position from the center of the pattern corresponds to different wave vectors,  $q$ . The wave-vector of the inner-most ring,  $q^*$ , can be used to determine the distance between microstructures, or Bragg spacing ( $D_{\text{Bragg}}$ ), as shown in Eq. 5-1:

$$D_{\text{Bragg}} = \frac{2\pi}{q^*} \quad (5-1)$$

The angular position,  $\theta$ , along the ring relates to orientation in the film. The angle is taken to increase clockwise from zero at the abscissa of the left quadrants. The radial position of the ring at  $\theta = 0^\circ$  provides information regarding the horizontal Bragg spacing, while the position of the ring at  $\theta = 90^\circ$  gives the vertical Bragg spacing. Thus, the pattern at 45 wt%, which is a nearly perfect circle indicates that the ordered domains in the film at this concentration are randomly oriented and the Bragg spacing in both the horizontal and vertical film directions are identical. At the elevated concentration (72 wt%) the scattering pattern now forms an ellipse with the major axis along the vertical direction. Based on this pattern, the wave vector of the primary peak in the vertical film direction is higher than the wave vector of the primary peak in the horizontal direction. As such, the Bragg spacing in the vertical direction is smaller than the horizontal Bragg spacing.

The scattering profiles resulting from integrating around the scattering patterns in Figs. 5.1a and b are shown in Figs. 5.1c and d, respectively. The primary peak obtained from the nearly perfect circle at 45 wt% polymer is sharper than the primary peak based on the ellipse at 72 wt% polymer. The sharp peak is due to the consistency of Bragg spacing at all angular positions in Fig. 5.1a. The broad peak in Fig 5.1d represents the distribution of Bragg spacings

due to the ellipse in Fig. 5.1b. As such, the peak in Fig. 5.1d can be considered to be comprised of multiple Bragg peaks corresponding to the horizontal and vertical film directions.

In order to determine the horizontal and vertical Bragg spacings, the peaks in Figs. 5.1c and d are decomposed into their constitutive Bragg peaks by integrating the scattering pattern over incremental angular positions. The results are shown in Figs. 5.1e and 5.1f. The solid line is the Bragg peak based on integrating from  $\theta = 5^\circ$  to  $15^\circ$ . This represents the Bragg spacing in the horizontal film direction. The Bragg peak shown by the dashed line is determined by integrating from  $\theta = 75^\circ$  to  $85^\circ$ . This peak indicates the Bragg spacing of microstructures in the vertical film direction. By decomposing the scattering patterns obtained at several concentrations during the removal of solvent from the SB / toluene film, the compression of the ordered domain can be quantitatively analyzed by comparing the vertical and horizontal Bragg spacings.

#### **5.4.2 Effect of solvent removal temperature on Bragg spacing**

Details regarding the solvent removal rate and phase behavior of the SB copolymer in toluene during solvent extraction can be found in Part I of this two part series of papers. At all three solvent removal temperatures (30, 40,  $60^\circ\text{C}$ ), the SB copolymer begins to form hexagonally-packed cylinders in toluene between 25 and 30 wt% polymer. Further, the solvent removal rate increased as temperature increased, while the final attainable concentration decreased due to skin formation at the film surface.

The horizontal (filled symbols) and vertical (open symbols) Bragg spacings obtained during the extraction of toluene from the SB film at three different temperatures are shown in Figs. 5.2a – c. Before proceeding with the discussion, it will be useful to define terminology to be used in the subsequent discussion. *Deswelling* refers to shrinkage of the individual ordered

domains due to the diffusion of solvent from said ordered domains as the film dries. *Compression*, on the other hand, arises from changes in the film thickness as solvent is extracted from the film. As the film thickness decreases, both individual microstructures and ordered domains are physically pressed closer to one another in the vertical direction as the film surface advances down. Based on these definitions, deswelling will occur in both the horizontal and vertical film direction. Alternatively, assuming the film is pinned in the horizontal direction, compression will affect only the vertical Bragg spacing. The effects of these two phenomenon will be considered individually. Because the bottom surface of the film is believed to be pinned, which makes the horizontal film Bragg spacing insensitive to compression, changes in the horizontal Bragg spacing during solvent extraction will be used to study the effect of deswelling on the Bragg spacing. Differences in the vertical and horizontal Bragg spacings will then be used to study compression during solvent removal.

The Bragg spacing at all three temperatures is initially the same (~32 nm). It has been shown that in a neutral solvent, increasing the temperature can decrease the Bragg spacing [Shibayama, 1983a]. This result is not confirmed here, but the severity of the temperature-dependence of the Bragg spacing is variable among different molecular weights and polymer compositions. Thus, for the particular copolymer used in this work, the temperature range studied may not be large enough to yield significant differences in the Bragg spacing. Further, the samples were not given time to equilibrate as solvent is constantly being removed, which may also contribute to the lack of temperature-dependent Bragg spacing.

The Bragg spacing changes with polymer concentration, increasing up to a critical concentration,  $C_{\text{crit}}$ , then decreasing.  $C_{\text{crit}}$  is typically between 70 and 80 wt% polymer. The increase in the Bragg spacing is about 2 nm. The trends are observed in both the vertical and

horizontal direction and are, therefore, believed to be due to changes in solvent content in the ordered domains. Shibayama et al. [1983b] observed a similar trend while tracking the Bragg spacing of poly(styrene-*b*-isoprene) in toluene. The authors note that the increase in Bragg spacing is observed even as deswelling occurs, as is observed in this work. The authors attribute the increasing Bragg spacing to increased segregation power between the blocks as the polymer concentration increases. Above  $C_{\text{crit}}$ , it was proposed that the reduction in Bragg spacing is due to deswelling of the domains and slow chain relaxation. The arguments put forth by Shibayama et al. [1983b] are pertinent to the data presented here and justify the trends in Figs. 5.2a – c.

The vertical and horizontal Bragg spacings are initially in agreement at all three temperatures. Thus, the microstructures are oriented randomly with the same Bragg spacing in all directions. At a certain concentration,  $\phi^*$ , the vertical and horizontal Bragg spacings deviate from one another.  $\phi^*$  is around 60 wt% at all temperatures, though it is difficult to distinguish the exact value from the data in Fig. 5.2.

Prior to  $C_{\text{crit}}$ , the horizontal Bragg spacing increases more rapidly than the vertical Bragg spacing. After  $C_{\text{crit}}$ , the vertical Bragg spacing decreases more drastically than the horizontal Bragg spacing. It is speculated that both effects are the consequence of compression the domains in the vertical direction as the film thickness decreases. Below  $C_{\text{crit}}$ , the continual compression of the domains in the vertical direction diminishes the effect of the increase in segregation power as concentration increases. Above  $C_{\text{crit}}$ , the compression of the domains in the vertical direction exacerbates the effect of deswelling as solvent exits the domains.

The severity of the compression during solvent extraction is quantified by the percent difference between the horizontal and vertical Bragg spacings,  $\sigma$ . Fig. 5.3 shows  $\sigma$  as a function of concentration at the three temperatures presented above. Around 50 wt% polymer,  $\sigma$  begins

to increase at all three temperatures, indicating disparities between the horizontal and vertical Bragg spacings. Between 65 and 70 wt% polymer, discrepancies in the rate of increase of  $\sigma$  with concentration at the three temperatures are observed. The rate of increase of  $\sigma$  with concentration increases with temperature and at a given concentration above 65 wt% polymer,  $\sigma$  is most severe at the highest solvent removal temperature.

The following discussion presents a proposed explanation for the trends observed in Fig. 5.3. For the purposes of this discussion, it is assumed that the solvent partitions equally between the ordered and disordered phases in the film, which is reasonable given that the solvent, toluene, is neutral for the SB copolymer. It is recognized that under the conditions that the solvent preferentially swells one of the blocks, these arguments may be invalid. As such, the subsequent section is not proposed as a generalization that can be extended to selective solvents.

The value of  $\sigma$  is believed to be strongly dependent on the relaxation time of the polymer relative to the rate of compression of the film at a given concentration. As the film is compressed, the polymer chains attempt to repack such that the equilibrium spacing is attained once more. The rate at which the re-packing process occurs depends on chain mobility and relaxation times. The presence of solvent facilitates this relaxation process. Enough residual solvent remains in the film at low concentrations, in this case below 50 wt% polymer, to make the relaxation process quicker than rate of compression of the domains, as dictated by the rate of decrease of the film thickness. Above 50 wt% polymer, the lack of solvent leads to a loss of chain mobility, slowing the relaxation process. Therefore, when the domains are compressed and the equilibrium spacing is lost, the films do not have enough time to reorder as the film thickness decreases.

The differences in the rate at which  $\sigma$  increases with increasing concentration data among the different temperatures is due differences in solvent removal rates, which results in different film compression rates. Because the solvent removal rate increases with temperature, the time between compressions and, therefore, time to relax back to the equilibrium spacing, decreases as temperature increases. Though the relaxation time should increase with temperature, this effect appears to be insignificant relative to the differences in the film compression rates. As a result, the film dried at 60°C displays the most severe compression of the ordered domains in the vertical direction for a given concentration, followed by the film prepared at 40°C.

### 5.4.3 Effect of drying rate on Bragg spacing

Solvent was removed at 30 and 40°C at two different rates per temperature by removing solvent in the presence and absence of a sweep gas. Based on the drying curves provided in Part I of this series, the presence of a sweep gas slows the solvent removal rate at both temperatures. The slower solvent removal was attributed to the rapid formation of a skin at the surface of the film, which also introduced steep concentration gradients in the film. Thus, the presence of a sweep gas affords the opportunity to study domain compression as a function of solvent removal rate.

The horizontal (filled symbols) and vertical (open symbols) Bragg spacings as a function of concentration in films dried in the presence of sweep gas at 30 and 40°C are shown in Figs. 5.4a and b, respectively. Comparing the data in Fig. 5.4 to the corresponding data without a sweep gas in Fig. 5.2, it does not appear that changing the drying rate changes the Bragg spacing at low concentrations. Further, a similar trend in the Bragg spacing with concentration is seen when a sweep gas is present. However, the presence of a sweep gas shifts  $C_{\text{crit}}$  to a lower

concentration.  $C_{\text{crit}}$  in Fig. 5.4 is now closer to 60 wt% polymer than 70 wt% polymer. It is postulated that the lower  $C_{\text{crit}}$  value observed when removing solvent with a sweep gas results from the development of the skin layer near the film surface. Assuming that a steep concentration gradient exists due to skin formation, the solvent content near the film surface is much lower than in the bulk film. Kinetic trapping of the polymer chains near the surface occurs at a lower average polymer concentration, lowering  $C_{\text{crit}}$ .

The domain compression is again analyzed by considering  $\sigma$  as a function of polymer concentration. In Fig. 5.5a and b are compared the  $\sigma$  values during the removal of solvent with and without a sweep gas at 30 and 40°C, respectively. At both temperatures, the presence of a sweep gas intensifies the domain compression. The effect at 40°C is substantially more pronounced than at 30°C. For instance, the maximum difference in the  $\sigma$  values between the samples dried at 30°C is 5.5% at a polymer concentration of 88 wt%. At 40°C, the maximum difference in  $\delta$  values is approximately 10% at 63 wt% polymer.

The concentration-dependence of  $\sigma$  observed using a sweep gas is contradictory to the expected behavior based on the arguments proposed in Section 5.4.2. In Section 5.4.2 rapid solvent removal was the likely cause of the increased domain compression at elevated temperatures. However, it is seen that the presence of a sweep gas yields more severe domain compression despite a slower solvent removal rate. The results observed in Fig. 5.4 are believed to be a consequence of the formation of the skin layer and steep concentration gradients, which are interfering with the effect of the change in the solvent removal rate. As previously discussed, the formation of a skin layer kinetically traps the SB copolymer near the film surface. Thus, while the rate of change of the average concentration is slower when a sweep gas is used, the solvent extraction near the surface is rapid and domain compression near the surface is high.

It was desirable to examine the effect of drying rate on domain compression without the development of a skin layer interfering with the results. In order to achieve this, an additional solvent removal condition was implemented at 30°C. A reservoir of the solvent, toluene, was placed in the chamber beneath the sample, effectively saturating the chamber in which the film is dried. The drying curves during the removal of solvent at room temperature under three different conditions are shown in Fig. 5.5. The filled and open squares correspond to the removal of solvent with and without a sweep gas previously discussed. The curve denoted with the cross-marks represents solvent removal when the chamber was saturated. Saturating the sample chamber decreases the drying rate. It is speculated that under the slow solvent evaporation, significant skinning is avoided, thereby making the only substantial difference between the film dried without a sweep gas and the film dried in the presence of solvent the solvent removal rate.

The concentration-dependence of the horizontal and vertical Bragg spacings of a film dried in the presence of solvent is shown in Fig. 5.6. The horizontal Bragg spacing again shows the expected trend with concentration. However,  $C_{\text{crit}}$  is now at a substantially higher concentration than in all previous experiments. The continual presence of solvent at the film surface may be limiting the formation of concentration gradients and imparting appreciable mobility to the polymer in the film, thus allowing resistance to kinetic trapping. This mitigates the effect of deswelling until a higher concentration is reached.

It is also seen in Fig. 5.5 that  $\phi^*$  is at a higher concentration ( $> 70$  wt%) than observed in any other sample. As such, the microstructures can resist a net decrease in Bragg spacing due to compression at higher concentrations than achievable under the previously discussed solvent removal conditions.

The  $\sigma$  versus concentration curves for the three films dried at 30°C are shown in Fig. 5.8. As discussed in the preceding paragraph, the presence of solvent is delaying  $\phi^*$ . Therefore, while the  $\delta$  of the two films dried in the absence of solvent begin to increase at approximately the same polymer concentration (60 wt%), the film dried in the presence of solvent does not show appreciable  $\delta$  values until 70 wt%. Above 70 wt% polymer,  $\sigma$  of the film dried in the presence of solvent is lower than the  $\delta$  values of the films dried without a solvent reservoir.

In order to ensure that the lower  $\sigma$  value at a given concentration obtained by removing solvent in a saturated chamber is not simply an artifact of the delayed onset of residual compression, the rate of change of  $\sigma$  with respect to concentration under the three solvent removal conditions are compared in Fig. 5.9. At all concentrations, the rate of compression with concentration is lowest when a solvent is present. The difference between the film dried in the presence of solvent and the film dried with a sweep gas in an unsaturated chamber ranges from 350% at 70 wt% polymer to 160% at 90 wt% polymer. This illustrates that the discrepancy in  $\sigma$  observed in Fig. 5.8 is not just a result of the delayed onset of peak-splitting and the slower drying rate reduces the effect of film shrinkage on Bragg spacing. These results also support the arguments made in Section 5.4.2 that the net domain compression is a strong function of the relaxation time of the polymer chains relative to the rate of domain compression, which is controlled by the solvent removal rate. Thus, when the solvent removal is slowed by saturating the chamber with solvent, the ratio of relaxation time to domain compression rate decreases and chains are given longer times to relax. It is also noted, however, that the presence of solvent at the film / air interface may be assisting the relaxation process during the extraction of solvent.

## 5.5 Conclusions

In situ small angle X-ray scattering measurements were made as solvent was removed under various conditions from a poly(styrene-*b*-butadiene) copolymer film. These measurements revealed information regarding changes in the microstructure spacing as a function of solvent concentration in real-time. The Bragg spacing was found to follow a similar trend with respect to concentration as has previously been reported for block copolymers in a neutral solvent. Increasing the polymer concentration in the film initially led to increased segregation of the blocks and larger Bragg spacings. Above a critical concentration, the polymers were kinetically trapped and the Bragg spacing decreased as the domains deswelled due to the loss of solvent.

In addition to deswelling effects, it was observed that the vertical spacing of the microstructure decreased due to compression of the ordered domains as the film thickness decreased during solvent extraction. At low concentrations, the polymer chains were able to relax back to their equilibrium spacing between subsequent compressions of the domains and the Bragg spacing in the vertical direction was essentially unaffected. At a certain concentration, the rate of domain compression was too rapid for the chains to relax as the film thickness decreased. As such, the Bragg spacing in the vertical direction continually decreased with concentration.

The compression of the domains was found to increase as the solvent removal temperature increases. It was determined that over the temperature range utilized in this work, the severity of domain compression was primarily governed by the rate of solvent removal, which dictates the rate of domain compression. Thus, while increasing the temperature will reduce the relaxation time, this was not sufficient to overcome the increased rate of compression upon faster solvent removal. In spite of this finding, decreasing the solvent removal rate at a given temperature by introducing a sweep gas resulted in an increase in the domain compression.

This was ultimately attributed to the formation of the skin at the film surface, which masked the effect of solvent removal rate. This limitation was overcome by drying a film in the presence of excess solvent to slow the solvent removal rate without forming a skin. The reduced solvent removal rate delayed the onset of peak-splitting and reduced the rate of domain compression with concentration.

## 5.6 Acknowledgements

Partial funding for this work was provided by the Institute for Critical Technology and Applied Science at Virginia Tech. The authors acknowledge Eastman Chemical Company for providing funding through the Eastman Fellowship in Polymer Science. Portions of this research were carried out at the Stanford Synchrotron Radiation Laboratory, a national user facility operated by Stanford University on behalf of the U.S. Department of Energy, Office of Basic Energy Sciences. The SSRL Structural Molecular Biology Program is supported by the Department of Energy, Office of Biological and Environmental Research, and by the National Institutes of Health, National Center for Research Resources, Biomedical Technology Program, and the National Institute of General Medical Sciences.

## 5.7 References

1. Bitai, I.; Yang, J.K.W.; Jung, Y.S.; Ross, C.A.; Thomas, E.L.; Berggren, K.K. *Science* **2008**, *321*, 939.
2. Bockstaller, M.; Kolb, R.; Thomas, E.L. *Adv. Mater.* **2001**, *13*, 1783.
3. Heinzer, M.J.; Han, S.; Pople, J.A.; Baird, D.G.; Martin, S.M. **2011**, Manuscript in Submission
4. Jackson, E.A.; Hillmyer, M.A. *ACS Nano* **2010**, *4*, 3548.
5. Jain, A.; Hall, L.M.; Garcia, C.B.W.; Gruner, S.M.; Wiesner, U. *Macromolecules* **2005**, *38*, 10095.

6. Jung, Y.S.; Jung, W.; Tuller, H.L.; Ross, C.A. *Nano Lett.* **2008**, *8*, 3776.
7. Kang, M.; Moon, B. *Macromolecules* **2009**, *42*, 455.
8. Kim, G.; Libera, M. *Macromolecules* **1998**, *31*, 2569.
9. Lee, M.; Park, J.K.; Lee, H.S.; Lane, O.; Moore, R.B.; McGrath, J.E.; Baird, D.G. *Polymer* **2009**, *50*, 6129.
10. Liang, G.D.; Xu, J.T.; fan, Z.Q. *J. Phys. Chem. B* **2007**, *111*, 11921.
11. Marcencic, A.P.; Adamson, D.H.; Chaikin, P.M.; Register, R.A. *Phys. Rev. E* **2010**, *81*, 011503.
12. Meuler, A.J.; Hillmyer, M.A.; Bates, F.S. *Macromolecules* **2009**, *42*, 7221.
13. Nuxoll, E.E.; Hillmyer, M.A.; Wang, R.F.; Leighton, C.; Siegel, R.A. *ACS Appl. Mater. Interfaces* **2009**, *1*, 888.
14. Olszowka, V.; Hund, M.; Kuntermann, V.; Scherdel, S.; Tsarkova, L.; Boker, A. *ACS Nano* **2009**, *3*, 11091.
15. Pai, R.A.; Humayun, R.; Schulberg, M.T.; Sengupta, A.; Sun, J.N.; Watkins, J.J. *Science* **2004**, *303*, 507.
16. Phillip, W.A.; O'Neill, B.; Rodwogin, M.; Hillmyer, M.A.; Cussler, E.L. *ACS Appl. Mater. Interfaces* **2010**, *2*, 847.
17. Segalman, R.A. *Science* **2008**, *321*, 919.
18. Shibayama, M.; Hashimoto, T.; Kawai, H. *Macromolecules* **1983a**, *16*, 16.
19. Shibayama, M.; Hashimoto, T.; Hasegawa, H.; Kawai, H. *Macromolecules* **1983b**, *16*, 1427.
20. Uehara, H.; Kakiage, M.; Sekiya, M.; Sakuma, D.; Yamonobe, T.; Takano, N.; Barraud, A.; Meurville, E.; Ryser, P. *ACS Nano* **2009**, *3*, 924.

21. Wirnsberger, G.; Scott, B.J.; Stucky, G.D. *Chem. Commun.* **2001**, *01*, 119.
22. Wu, L.; Lodge, T.P.; Bates, F.S. *J. Rheol.* **2005**, *49*, 1231.
  
23. Xiao, S.; Yang, X.M.; Lee, K.Y.; ver der Veerdonk, R.J.M.; Kuo, D.; Russell, T.P.  
*Nanotechnology* **2011**, *22*, 305302.
24. Yang, S.Y.; Yang, J.A.; Kim, E.S.; Jeon, G.; Oh, E.J.; Choi, K.Y.; Hahn, S.K.; Kim, J.K.  
*ACS Nano* **2010**, *4*, 3817.
  
25. Zhang, Z.T.; Dai, S.; Blom, D.A.; Shen, J. *Chem. Mater.* **2002**, *14*, 965.

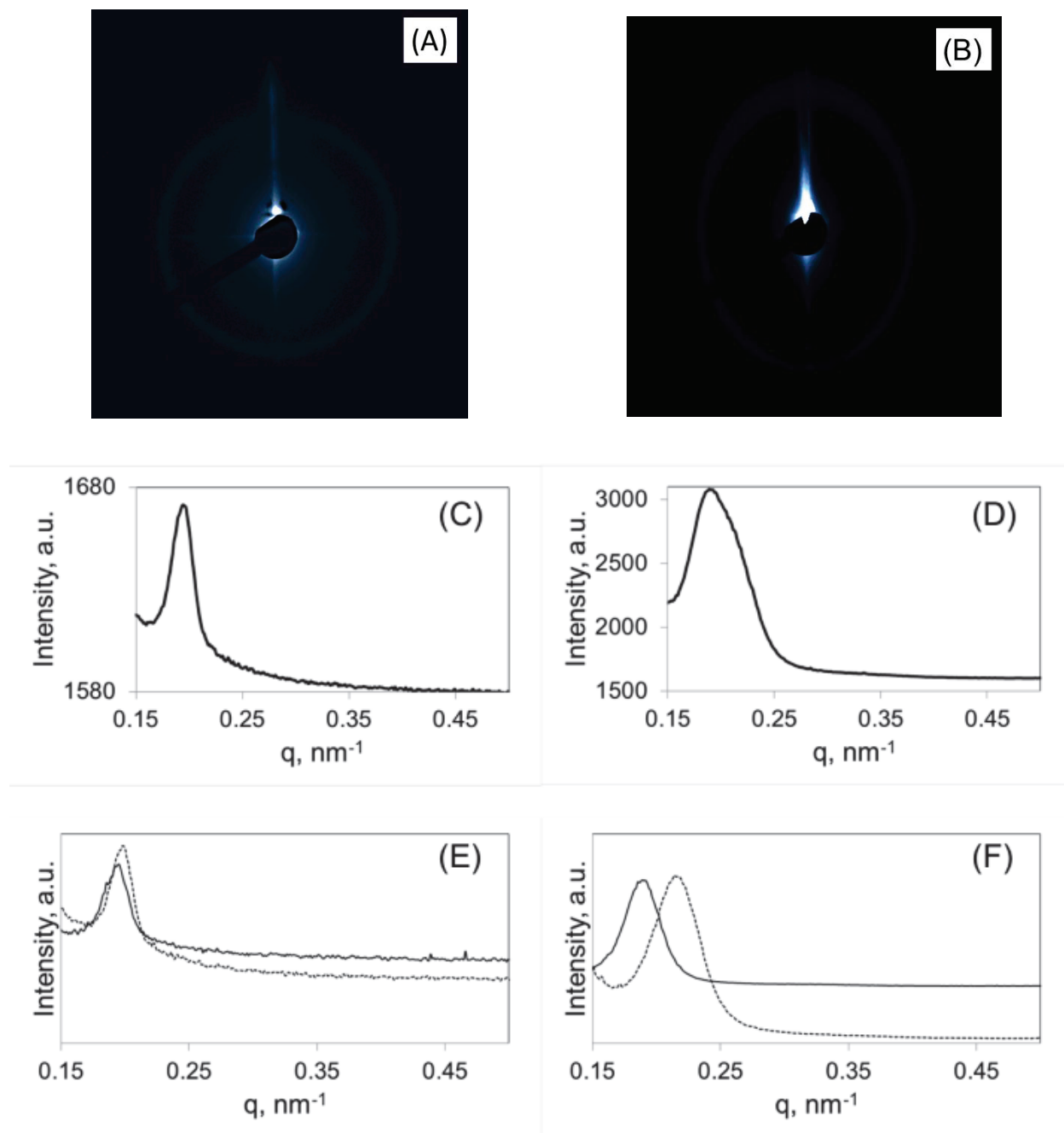


**Figure 5.1.** Scattering data from SB copolymer film cast from a 20 wt% solution in toluene dried at 40°C. Scattering rings collected at 45 and 72 wt% polymer are shown in (A) and (B), respectively. (C) and (D) show the integrated scattering profiles based on (A) and (B), respectively. The peaks in (C) and (D) are decomposed into the vertical and horizontal film Bragg peaks in (E) and (F), respectively.

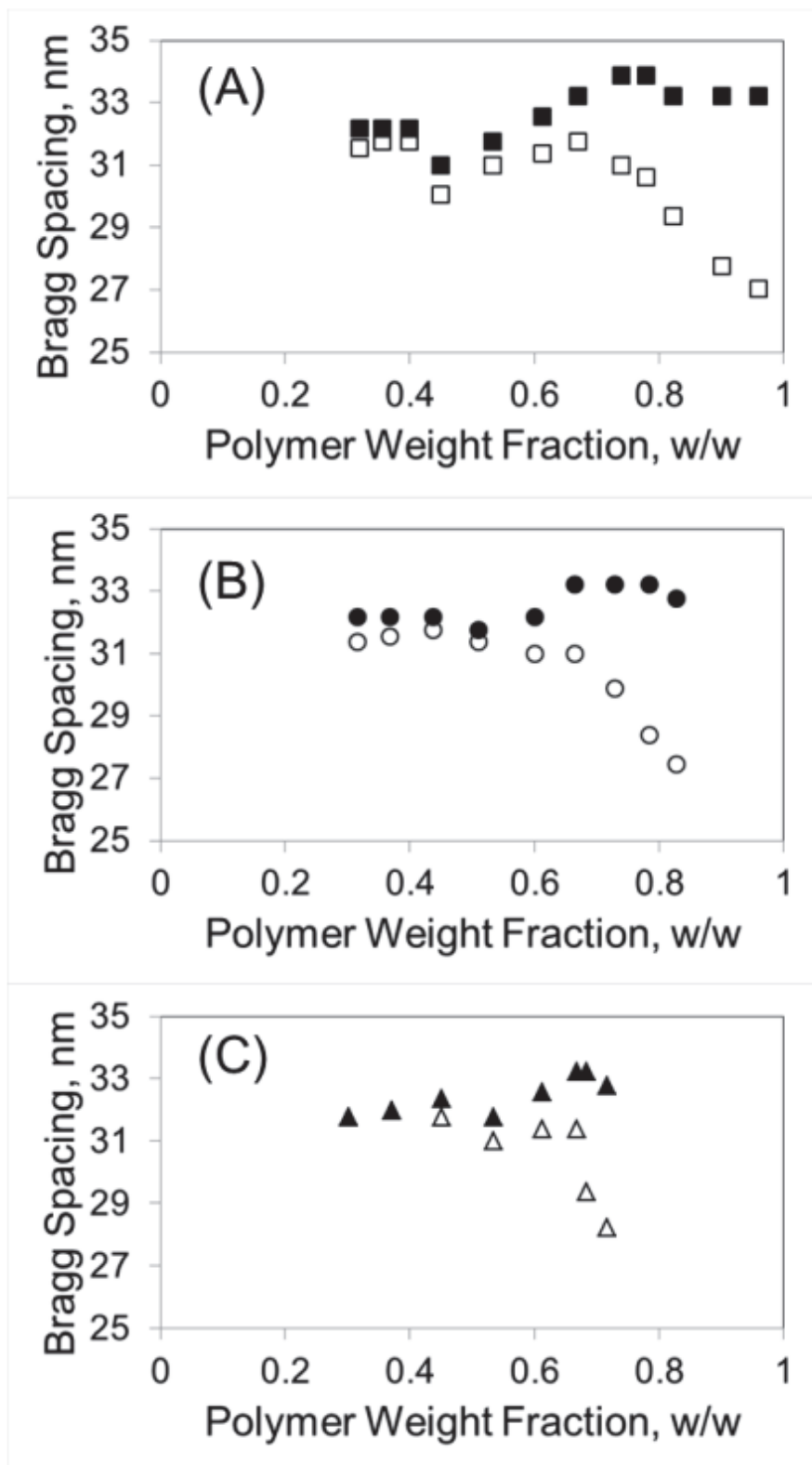


**Figure 5.2.** Bragg spacings in horizontal (closed symbols) and vertical (open symbols) film directions of an SB film cast from a 20 wt% (initial concentration) toluene solution as a function of polymer concentration during solvent removal at 30 (A), 40 (B) and 60°C (C).

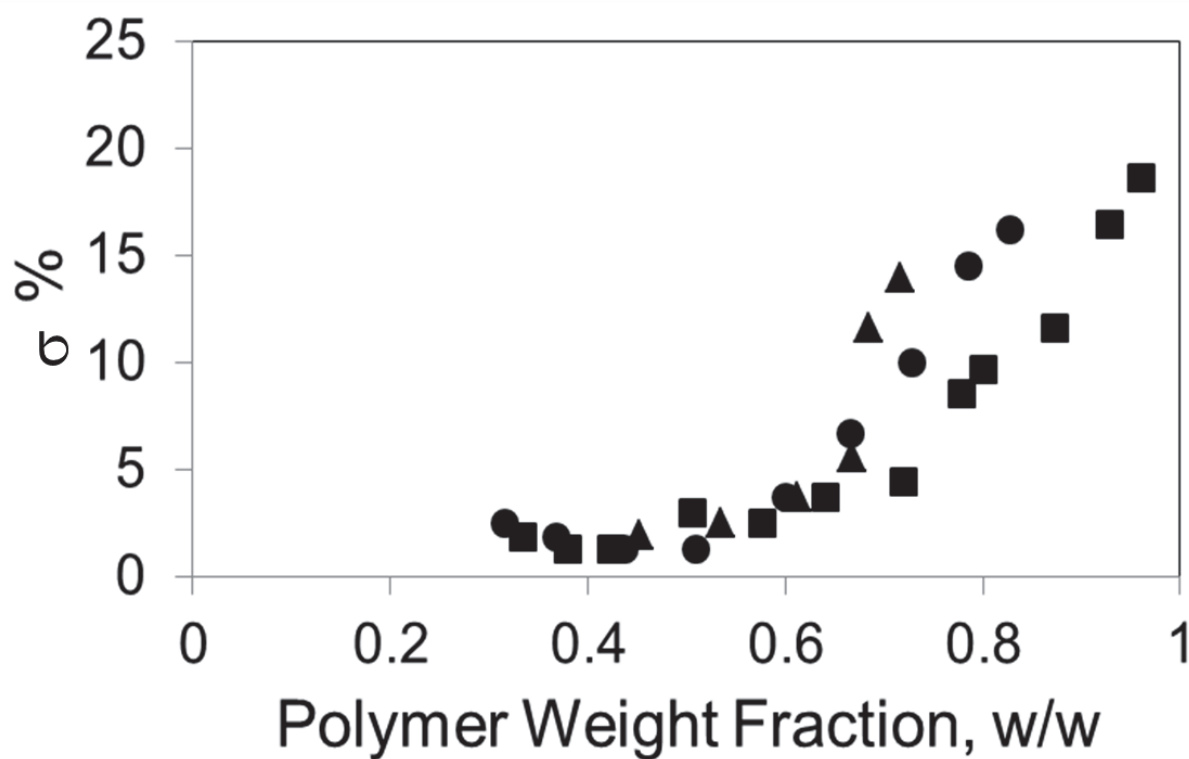


**Figure 5.3.** Percent difference ( $\sigma$ ) in the horizontal and vertical Bragg spacings of an SB film cast from a 20 wt% toluene solution as a function of polymer concentration during solvent removal at 30 (■), 40 (●) and 60°C (▲).

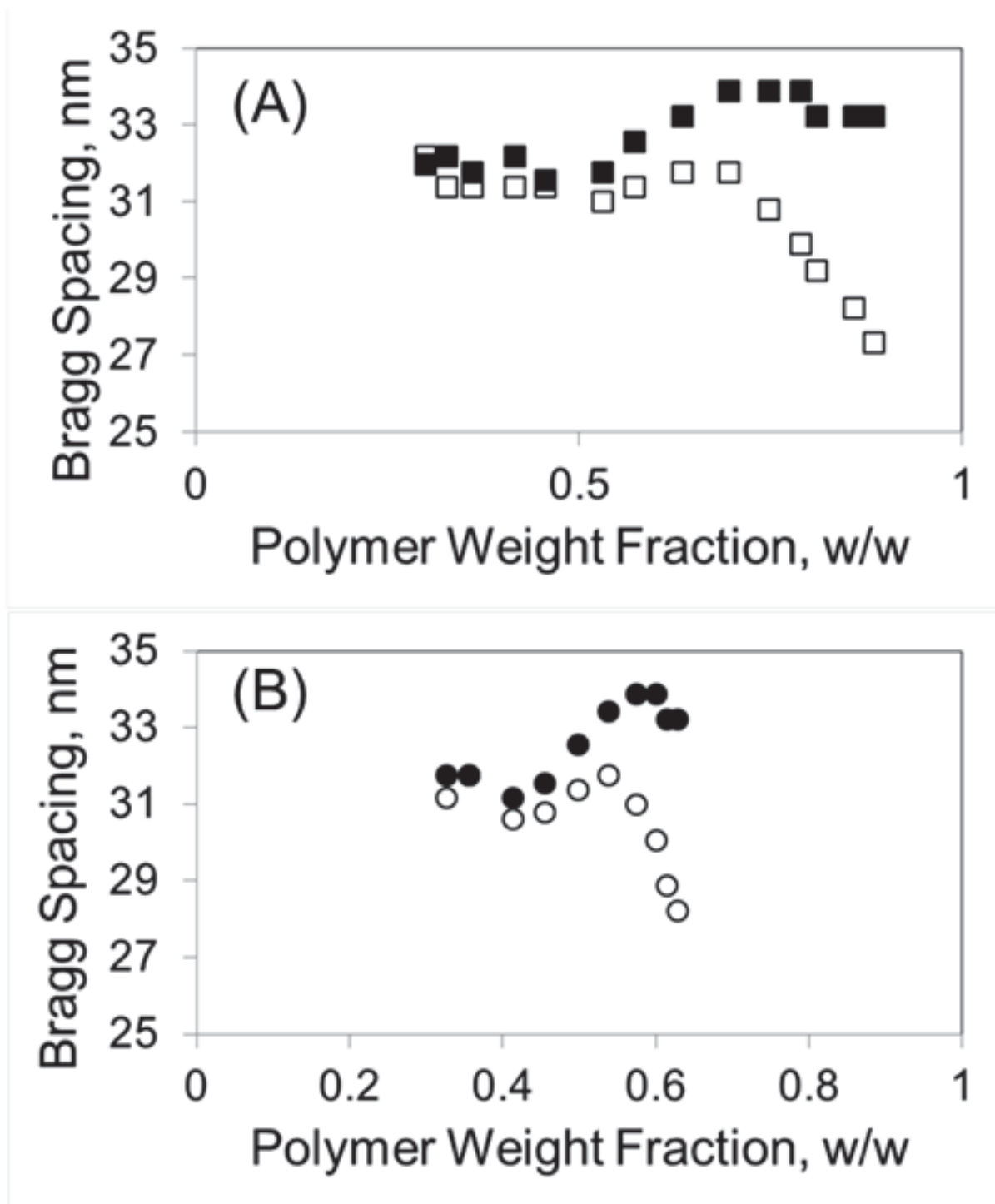


**Figure 5.4.** Bragg spacings in horizontal (closed symbols) and vertical (open symbols) film directions of an SB film cast from a 20 wt% toluene solution as a function of polymer concentration during solvent removal with a sweep gas at 30 (A) and 40°C (B).

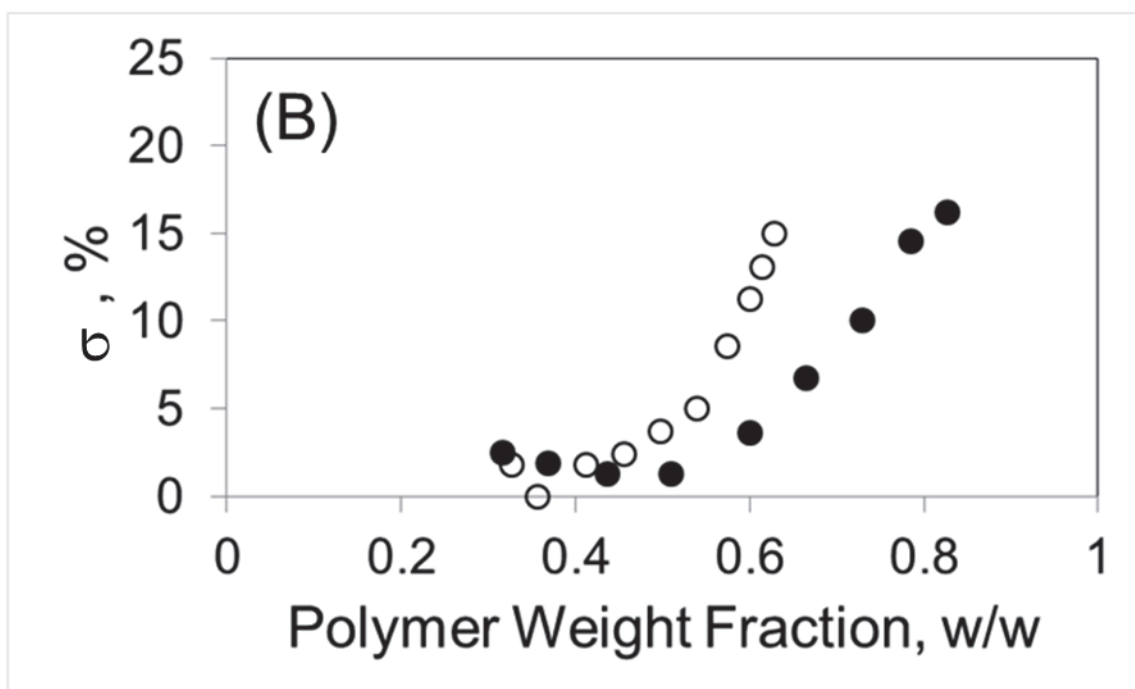
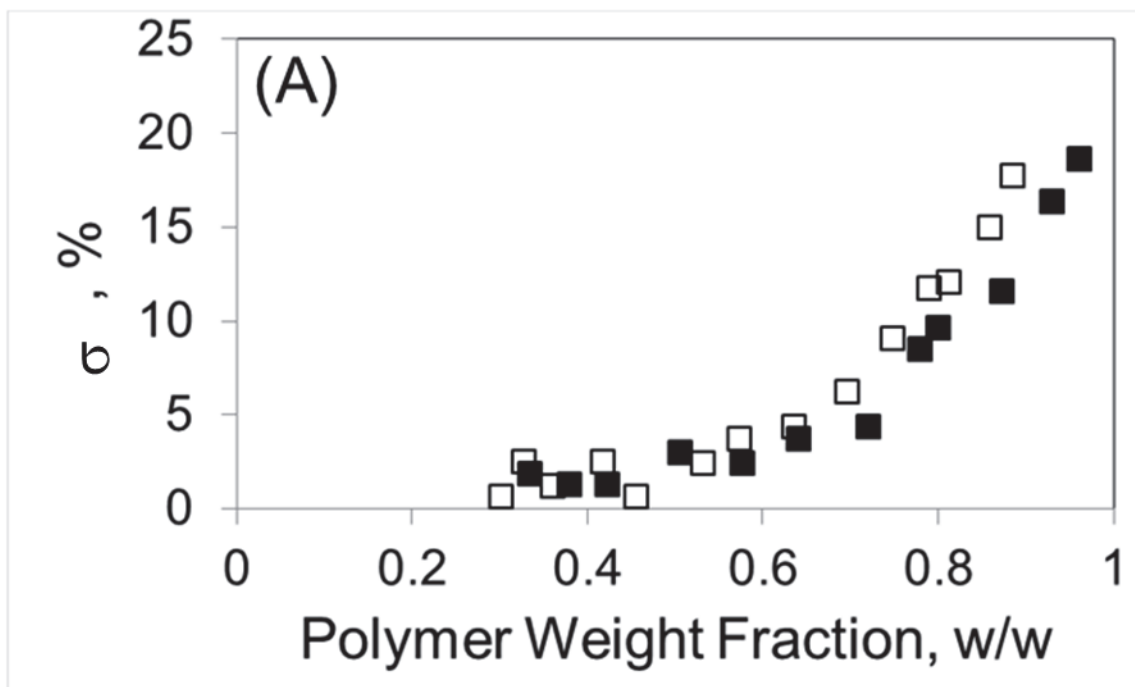


**Figure 5.5.** Percent difference ( $\sigma$ ) in the horizontal and vertical Bragg spacings of an SB film cast from a toluene solution with an initial concentration of 20 wt% as a function of polymer concentration during solvent removal without a sweep gas (closed symbols) and with a sweep gas (open symbols) at 30 (A) and 40°C (B).

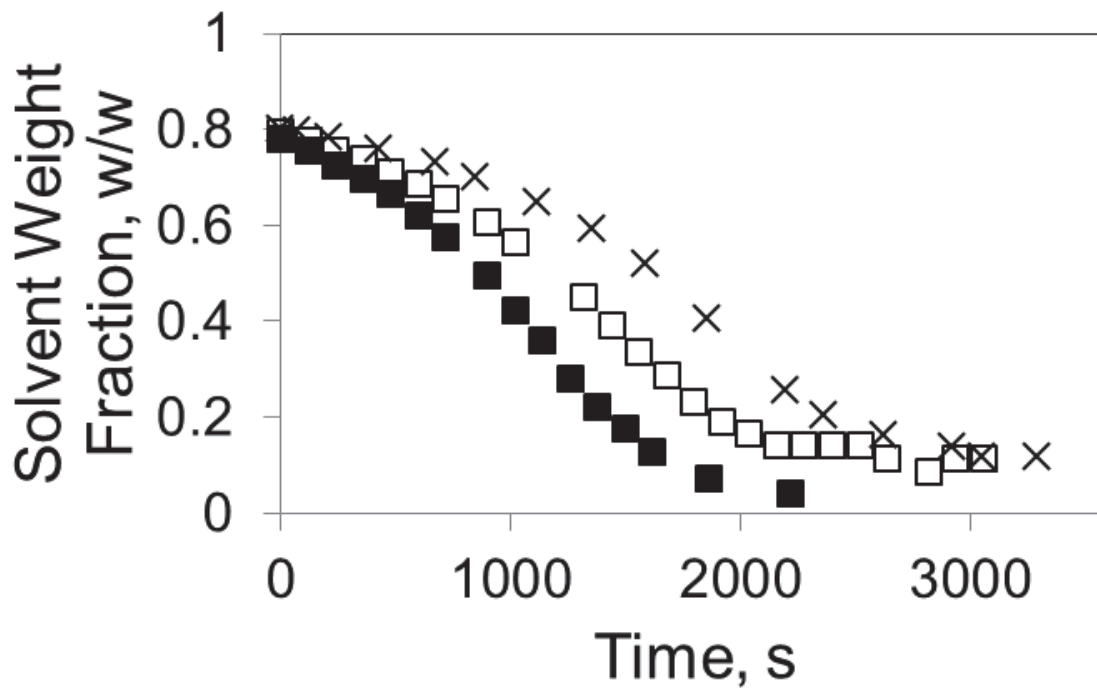


**Figure 5.6.** Drying curves during the removal of solvent from an SB film cast from a 20 wt% solution at 30°C without a sweep gas (■), with a sweep gas (□) and in the presence of excess solvent (x).

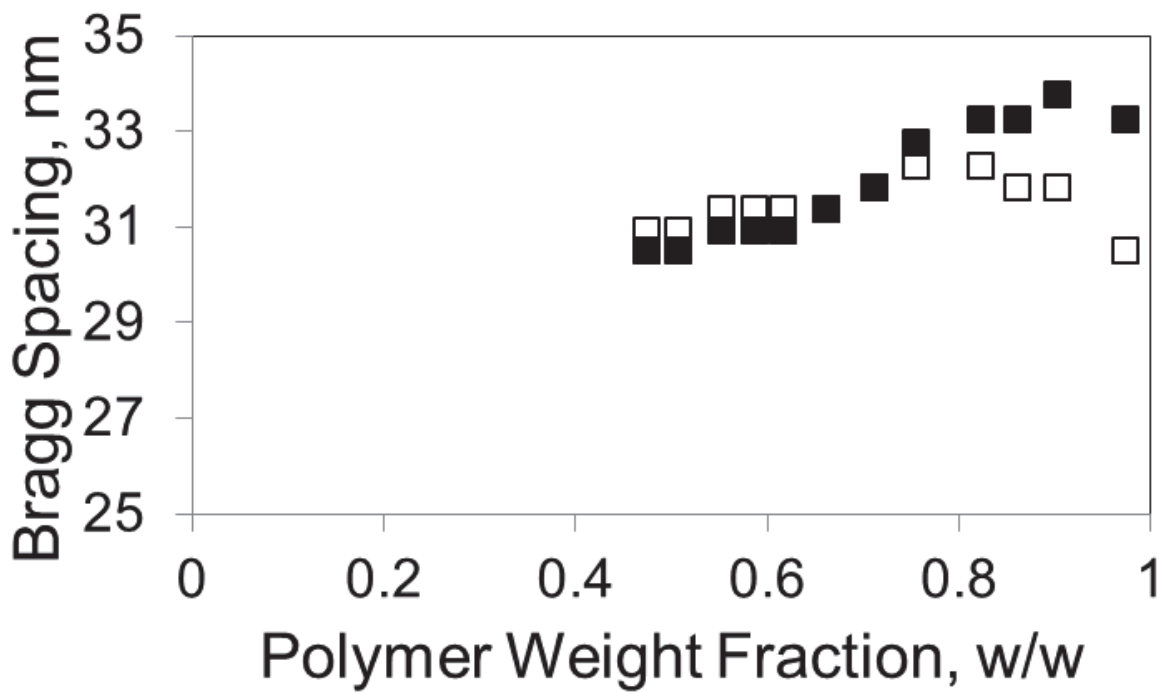


**Figure 5.7.** Bragg spacings in horizontal (■) and vertical (□) film directions of an SB film cast from a 20 wt% toluene solution as a function of polymer concentration during solvent removal in the presence of excess solvent at 30°C.

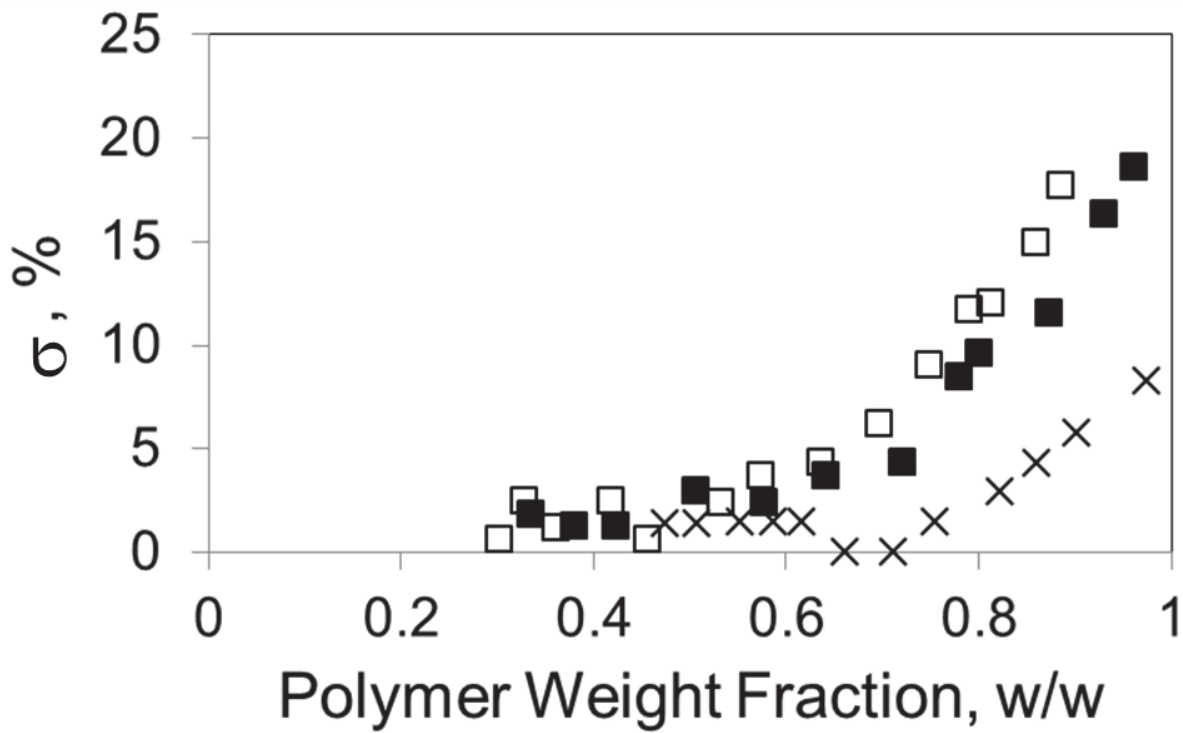


**Figure 5.8.** Percent difference ( $\sigma$ ) in the horizontal and vertical Bragg spacings of an SB film cast from a 20 wt% toluene solution as a function of polymer concentration during solvent removal at 30°C without a sweep gas (■), with a sweep gas (□), and in the presence of excess solvent (x).

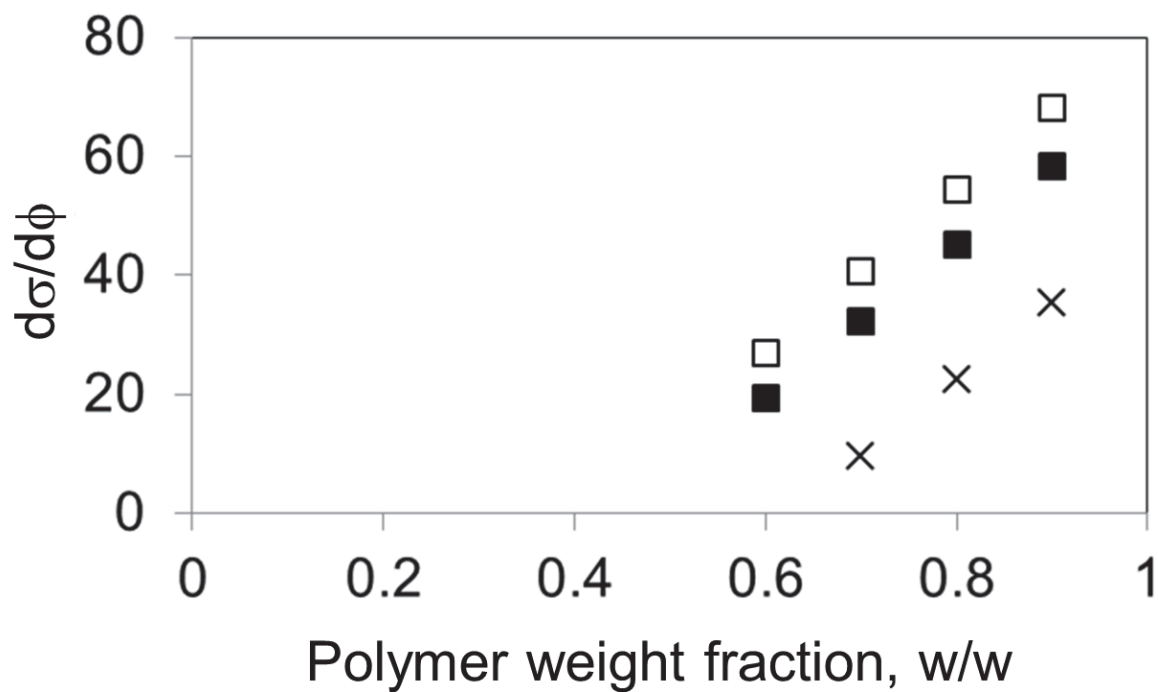


**Figure 5.9.** Rate of change of  $\delta$  with respect to polymer concentration,  $\phi$ , during the removal of solvent from an SB film cast from a 20 wt% solution in toluene at 30°C without a sweep gas (■), with a sweep gas (□), and in the presence of excess solvent (×).

## **Chapter 6**

### **Conclusions & Recommendations**

## 6.1. Conclusions

The following are the conclusions based on the work performed in this dissertation that are pertinent to objectives originally laid out in Chapter 1:

- The iso-concentration ordering of a poly(styrene-*b*-butadiene) block copolymer (SB) in the neutral solvent, toluene, following solvent extraction at room temperature could be tracked by monitoring changes in the dynamic mechanical response (DMR) over time. The measurements were sensitive to both the nucleation and growth events.
- Using small angle X-ray scattering (SAXS) to determine the phase behavior of the SB copolymer in toluene, it was found that the ordered structures were hexagonally-packed cylinders and the order-disorder transition concentration was around 30 wt%. This allowed analysis of the ordering kinetics following concentration quenches, as opposed to following temperature quenches, as is commonly performed in the literature.
- The SAXS data indicated that the ordering process is continuing at higher concentrations than were measurable using DMR and the ordering times are longer than indicated by DMR data. Thus, the DMR measurements are not sensitive to late stages of the ordering process when grains have started to impinge on one another.
- The volume fraction of ordered state in the solution,  $\phi(t)$ , was determined from the DMR data as a function of time by using the parallel and series rules of mixtures for  $|G^*(t)|$ . The  $\phi(t)$  data was then used to assess the ability of the Avrami equation to quantitatively model the ordering kinetics. The following conclusions were made:
  - Because of a large discrepancy existed between the  $\phi(t)$  data calculated using the parallel and series rules of mixtures, while the DMR measurements can be used to

qualitatively describe the ordering kinetics as a function of concentration, they cannot currently be used to model a real solvent extraction process.

- Though the half-times determined by DMR and SAXS differed, the Avrami exponent obtained by both measurement techniques was approximately 1 at all concentrations. The agreement suggests that the DMR measurements were caused by the development of individual microstructures.
- Changing the polymer to the sphere-forming SIS did not affect the Avrami exponent. The DMR measurements performed in this work could not be used to determine microstructure.

Other conclusions from this work based on the in situ SAXS measurements were:

- SAXS can be used to measure the ordering of a block copolymer in solution during solvent removal in situ. This allowed kinetics to be studied in a manner more similar to real processing conditions than iso-concentration measurements.
- It is proposed that in these ordering measurements can be used to compare predictions of the ordering during solvent removal made by modeling iso-concentration kinetics
- These experiments allowed simultaneous identification of the microstructure and determination of changes in the ordering rate and domain dimensions as solvent is removed from a block copolymer film.
- The effect of solvent removal temperature and rate on the ordering kinetics and domain dimensions could be determined.

## **6.2. Recommendations**

### **6.2.1. Materials considerations**

#### **6.2.1.1 Synthesis of block copolymers**

The block copolymers used in this work were purchased from Sigma Aldrich. As such, the molecular weights and polymer compositions that could be used were limited. The high molecular weights of the polystyrene and polybutadiene blocks likely contributed to the relatively slow ordering process. Lower molecular weight polymers would allow faster kinetics to be tracked and would test the capabilities of the method for capturing fast kinetics. By changing the molecular weights of the blocks, the effect of polymer molecular weight can also be included in the work. Further, being able to control the composition would allow access to more microstructures in a neutral solvent. This would allow for a more extensive study of the influence of microstructure on the ordering kinetics. For instance, complex phases, such as the gyroid and perforated lamella structures, can be targeted.

In order to attain lower molecular weight polymers and to better dictate the polymer composition, it would be necessary to synthesize polymers in the lab. Poly(styrene-*b*-isoprene) (SI) can be synthesized by living anionic polymerization following techniques described in the literature [Hanley, 1998]. Though the chemistry is different than the butadiene-containing polymers used in this study, SI should serve as a sufficient model system for the purpose of this work. Both the isoprene and styrene monomers are available for purchase from Sigma-Aldrich®.

#### **6.2.1.2 Selective solvents**

In this dissertation, only a neutral solvent, toluene, was used. In doing so, only disorder-to-order transitions needed to be considered when interpreting the rheology and scattering data.

However, an understanding of ordering in selective solvents is also necessary as selective solvents allow access to more microstructures for a given copolymer composition. In selective solvents, block copolymers will undergo both disorder-to-order (ODT) and order-to-order transitions (OOT) as solvent is extracted. Thus, the dynamic mechanical response of the phase separating block copolymer will be caused by both types of transitions occurring simultaneously. Therefore, these responses must be decoupled.

Two separate experiments using the dynamic mechanical responses of ordering solutions are proposed to decouple the OOT and ODT. In both experiments, the samples are prepared and rheology experiments performed as they were in this thesis. This will be denoted as part 'A' of the experiment. Part 'A' will provide the response of a sample undergoing simultaneous OOT and ODT. After the ordering has stopped, either oscillatory [Wang, 1997] and steady [Soenen, 1997] shear can be used to disorder ordered block copolymers in solution as long as the frequency and strain amplitudes are sufficiently large. Once the sample has been disordered, the strain amplitude and/or frequency can be decreased to the original testing conditions to track ordering of block copolymers from a purely disordered state. The ODT dynamic mechanical response can then be subtracted from the response of the sample during experiment 'A' to deduce the OOT.

Alternatively, after performing experiment 'A' at a concentration  $\phi$ , a fresh sample can be equilibrated at a concentration just below the order-order concentration preceding  $\phi$ . For instance, let  $\phi'$ , which is less than  $\phi$ , represent the OOT concentration for which the equilibrium structure at a concentration greater than  $\phi'$  is the gyroid phase, while below  $\phi'$  the equilibrium structure is hexagonally-packed cylinders. A sample would be equilibrated below  $\phi'$ , then solvent can be rapidly removed until  $\phi$  is reached. Changes in the dynamic mechanical response

can then be tracked. In this manner, only the OOT is being measured. This response can then be subtracted from the simultaneous ODT and OOT responses of part ‘A’.

In order to choose suitable solvent, the selectivity the solvent toward a given block can be determined based the polymer-solvent interaction parameters,  $\chi_{P-S}$  [Prausnitz, 1999]:

$$\chi_{P_i-S} = \frac{V_s}{RT} (\delta_s - \delta_{P_i})^2 \quad (6.2-1)$$

In Eq. 6.2-1,  $i$  denotes the block of the copolymer being considered, while  $s$  refers to solvent.  $V_s$  is the molar volume of the solvent,  $R$  is the gas constant, and  $T$  is temperature.  $\delta_s$  and  $\delta_{P_i}$  are the solubility parameters of the solvent and polymer block, respectively. As  $\chi_{P_i-S}$  for a given block approaches zero, the solvent becomes a better solvent for that block. As the discrepancy between the solvent-polymer interaction parameters of the two blocks increases, the solvent becomes more selective for the polymer with the lower interaction parameter.

Several polystyrene- and polybutadiene-selective solvents have been used in literature. Benzene and cyclohexane have been used as polystyrene-selective and polybutadiene-selective solvents, respectively [Huang, 2004]. These solvents are more volatile than toluene, which will allow them to also be rapidly removed from solution [Huang, 2004]. Carbon tetrachloride can also be used as a volatile, polybutadiene-selective solvent. In the event that volatility is not important, non-volatile phthalates can be used to change the selectivity. Lodge et al. [2002] used the styrene-selective solvents di-*n*-butyl phthalate, diethyl phthalate, and dimethyl phthalate to study the phase behavior of poly(styrene-*b*-isoprene). Though a polyisoprene block was used rather than polybutadiene, both polymers have the same solubility parameters. The solvents presented here are a few commercially available materials that could be used to extend this work to selective solvents. To explore other candidates for this work, Barton [1991] should be consulted for a list of solubility parameters of other solvents to use in conjunction with Eq. 6.2-1.

## **6.2.2 Experimental considerations**

### **6.2.2.1. Transmission in situ Small Angle X-ray Scattering (SAXS) Experiments**

The *in situ* SAXS experiments performed in this work rely on grazing-incidence experiments. This caused a majority of the scattering signal to be collected from the film surface. Further, the range of concentrations that could be studied was limited because of reflection off of the film surface. An improvement on these experiments can be made by performing transmission experiments on the films while solvent is removed. However, because the film flowed at concentrations studied in this work and the film cannot be sealed, it must remain flat as solvent is removed. This requires that the beam, which is originally horizontal, be bent such that it can go through the sample normal to the film surface. The transmitted signal must then be bent again so it will move horizontally to the detector.

### **6.2.2.2. Porous Plate Rheometer**

Currently, the time necessary to extract solvent to the concentrations studied in this work is between 30 and 45 minutes. Though such time is negligible relative to the total ordering time, faster solvent removal times would allow early stages of the nucleation and growth process to be more accurately studied. One way to achieve faster solvent extraction is to make thinner samples. However, the accuracy of the rheometer decreases as the sample thickness decreases. Thus, a method to quickly remove solvent from thick films ( $> 1$  mm) is needed.

A porous-plate rheometer fixture (PPR) is proposed to decrease the solvent removal time from thick samples by extracting solvent from the top and bottom of the sample. A schematic of the fixture is shown in Fig. 6.2.2.2.1.

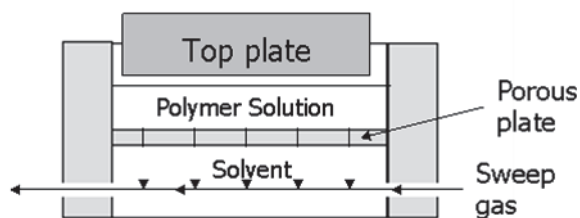


**Fig. 6.2.2.2.1.** Porous-plate rheometer fixture for extracting solvent from top and bottom of polymer solution. The side walls and bottom of the dish are non-porous metal. The porous-plate is a porous stainless steel substrate.

The walls and bottom of the PPR are composed of a non-porous metal, while the porous plate is sintered stainless steel plate. A polymer solution is placed on the porous substrate. Solvent will then evaporate from the top and bottom of the sample. A sweep gas can be flowed underneath the porous plate to facilitate solvent removal. When the desired polymer concentration is attained, the bottom dish can be flooded with a liquid that is immiscible with the sample solvent and a bad solvent for the polymer. This will prevent further removal of solvent from the bottom of the sample. The top of the sample is sealed in the same manner performed in the experiments in Chapter 3. Iso-concentration rheology experiments can then be performed. Alternatively, the dynamic mechanical response of the sample can be continually tracked as solvent is removed only through the bottom dish, providing similar experiments to the *in situ* SAXS work.

The PPR has been fabricated and assembled in Polymer Processing Laboratory at Virginia Tech. The stainless steel sintered porous metal substrates were purchased from Mott Corporation. Pore sizes range from 0.2 to 40  $\mu\text{m}$ . It was found that the available pore sizes were too large for the experiments described above. The porous metal behaved as a filter, with solvent flowing through the plate unimpeded. As such, solvent was removed from the polymer sample nearly instantaneously in an uncontrollable manner. To the author's knowledge, smaller pore sizes are unavailable commercially. The porous metal substrates available must be treated to better control the removal of solvent through the porous plate.

It is proposed that the porous substrate be treated with a hydrophilic polymer, such as a Pluronic, to limit the flow of the organic solvent through the substrate. This effect can be achieved in two possible ways: clogging the pores or increasing the surface energy of the substrate to discourage solvent flow through the plate. By soaking the substrate in a low concentration solution ( $< 1$  wt%) of the Pluronic, the pores will be infiltrated by the water soluble polymer. This will either completely fill some of the pores of the substrate or make the average pore size smaller. Both of these results should be sufficient to lower the total permeability of the substrate. Presumably, different concentrations of the treatment solution and different soak times will yield different resultant substrate permeability. Therefore, these variables should be initially tested to optimize solvent flux.

In the event that filling the pores is found to slow the solvent removal through the porous substrate too much, it is also possible to control solvent extraction by coating the surface of the substrate to change the substrate surface energy. The pores of the substrate should first be filled with a hydrophobic polymer to prevent the Pluronic from entering the pores during surface treatment. This can be achieved by soaking the substrate in a solution of the hydrophobic polymer as described in the preceding paragraph. The surface can then be cleaned with a good solvent for the hydrophobic polymer. With the pores filled and the surface cleaned, a dilute solution ( $< 1$  wt%) of the Pluronic can be coated onto the substrate and dried. Because it will be necessary for the Pluronic coating to be porous so that solvent can move through, the conditions under which water is removed from the Pluronic coating can be tailored to yield voids. The solvent removal can then be controlled by both the change in the surface energy of the substrate and the ability to control the size of the voids in the Pluronic layer. After the Pluronic layer has dried, the hydrophobic polymer in the pores of the substrate can be removed by soaking the plate

in a solvent that is good for the hydrophobic polymer. This will leave a porous metal substrate with a hydrophilic coating to control solvent removal.

### **6.2.2.3. Steady Shear Rheology Experiments**

The dynamic mechanical response of a block copolymer during phase separation cannot be used to identify the microstructure. The data reported in this work indicated that the Avrami exponent is insensitive to the nature of the microstructure. It has also been shown in literature that different microstructures do not generate unique dynamic signatures [Floudas, 1999; Zhao, 1996]. Therefore, it is necessary to explore other dynamic mechanical tests that could be used to extract information regarding the ordered structure.

It may be possible to deduce the microstructure based on the stress growth of an ordered block copolymer solution under steady shear. It has been shown that oscillatory and steady flow fields can be used to orient block copolymer microstructures, including lamella and hexagonally-packed cylinders, in solution [Jain, 2005; Marencic, 2010; Wu, 2005]. Wu et al. [2005] demonstrated that the evolution of the orientation of the lamella microstructure can be monitored over time using dynamic mechanical analysis. Presumably, the same should be true of hexagonally-packed cylinders. It is conjectured that the stress-growth during orientation of these two different microstructures will be different and unique. Although packed spheres will not orient, under steady shear, these microstructures should also possess a unique stress-growth behavior. It is recommended, therefore, that the build-up of stress under steady shear, be assessed as a possible method for identifying microstructures.

#### 6.2.2.4. Polarized Optical Microscopy

Polarized optical microscopy (POM) allows direct observation of the development of ordered grains in an otherwise disordered matrix. POM works by passing polarized light through a sample encapsulated in a clear cell and taking an image of the sample with a camera on the opposite side of the light source. When polarized light is passed through a sample, birefringent ordered structures appear as light or dark regions, while disordered states and isotropic structures are non-birefringent and appear as a uniform gray area. Chastek and Lodge [2003; 2004] were able to use POM to observe the birefringent domains containing lamella and hexagonally-packed cylinders in a disordered solution. Though isotropic phases, such as the gyroid and sphere microstructures, do not birefringe, the transition from hexagonally-packed cylinders to the gyroid structure could still be detected. Using this technique, the authors tracked both ODT and OOT kinetics by measuring the growth rate of the ordered grains. It is proposed that POM be used in a similar manner to track the ordering of block copolymers in solution during solvent removal. Doing so would resolve the remaining unknowns regarding the dynamic mechanical data including: 1) the discrepancy between the ordering times based on dynamic mechanical data and SAXS data; 2) whether the parallel or series approximation of the complex modulus gives a more accurate estimate of the ordering time; 3) the total achievable degree of ordering ( $\phi_\infty$ ) in a sample at a given concentration.

The ordering time measured based on the dynamic mechanical data and the SAXS data did not agree. It was speculated that the dynamic mechanical response is only sensitive to ordering when the ordered grains do not impinge on one another. Repeating these experiments with POM will allow this claim to be confirmed or refuted by measuring the ordering time prior to grain impingement for comparison to dynamic mechanical data.

The half-times calculated based on the parallel and series approximations for the complex modulus did not agree with one another. In some instances, the difference was over 300%. Therefore, while the rules of mixtures were suitable for qualitatively analyzing the trends in the ordering kinetics during solvent removal, the data could not be used to determine absolute ordering times. At the present time, this technique is not useful when trying to quantify kinetics of block copolymers in order to model a real solvent extraction process. It must be determined which rule of mixtures was more representative of the actual ordering times. Because POM allows direct measurement of the growth of an order structure, the absolute ordering time can be accurately determined. Comparison of this ordering time to ordering times based on rules of mixtures will provide insight into which rule of mixture should be used when quantitatively modeling the ordering kinetics.

The ordering of a block copolymer in solution during solvent extraction can be modeled by coupling a mass transfer model with a model for the ordering kinetics. Details regarding several potential mass transfer models are provided in Chapter 2. The model for the ordering kinetics used in this work was the Avrami equation. The Avrami equation is written in terms of the volume fraction of the sample in the ordered state,  $\phi$ , relative to the total achievable volume fraction of the ordered phase,  $\phi_{\infty}$ . In order to model the kinetics during a solvent extraction process,  $\phi_{\infty}$  at each concentration must be known so that the absolute  $\phi$  value can be calculated. Using the current techniques (dynamic mechanical analysis and SAXS),  $\phi_{\infty}$  cannot be determined. POM would allow for this value to be approximated reasonably well based on visual inspection of an image of the phase separated sample after ordering has ended.

Finally, POM would provide a means to verify the *in situ* SAXS measurements. Because of the setup needed for POM, extraction of solvent while images are collected is possible. A

film can be cast onto a glass slide between the light source and the camera. The top surface of the film will be free, allowing solvent to evaporate from the film as images are continually collected. The growth rate of the ordered grain can be compared to the instantaneous rates calculated from the SAXS measurements.

A suitable setup for the POM measurements is available in Dr. Martin's lab at Virginia Tech. The equipment consists of an Olympus BX51 microscope, equipped with a Hamamatsu digital camera. The camera is positioned vertically above the sample. A light source is located below the stage and can be directed through the sample toward the camera. A  $\lambda/20$  waveplate and a green filter will need to be added to the station to enhance the images and resolve the ordered structures. Both add-ons are available for purchase from Olympus.

### 6.2.3 References

1. Barton, A.F.M. *Handbook of Solubility Parameters*; CRC Press: Boca Raton, 1991.
2. Chastek, T.Q.; Lodge, T.P. *Macromolecules* **2003**, *36*, 7672.
3. Chastek, T.Q.; Lodge, T.P. *Macromolecules* **2004**, *37*, 4891.
4. Floudas, G.; Ulrich, R.; Wiesner, U. *J Chem Phys* **1999**, *110*, 652.
5. Hanley, K.J.; Lodge, T.P. *J. Polym. Sci., Polym Phys Ed.* **1998**, *36*, 3101.
6. Huang, H.; Hu, Z.; Chen, Y.; Zhang, F.; Gong, Y.; He, T.; Wu, C. *Macromolecules* **2004**, *37*, 6523.
7. Lodge, T.P.; Pudil, B.; Hanley, K.J. *Macromolecules* **2002**, *35*, 4707.
8. Jain, A.; Hall, L.M.; Garcia, C.B.W.; Gruner, S.M.; Wiesner, U. *Macromolecules* **2005**, *38*, 10095.

9. Marencic, A.P.; Adamson, D.H.; Chaikin, P.M.; Register, R.A. *Phys. Rev. E* **2010**, *81*, 011503.
10. Prausnitz, J.M.; Lichtenthaler, R.N.; de Azevedo, E.G. *Molecular Thermodynamics of Fluid-Phase Equilibria*, 3<sup>rd</sup> ed.; Prentice Hall PTR: Upper Saddle River, 1999.
11. Soenen, H.; Berghmans, H.; Winter, H.H.; Overbergh, N. *Polymer* **1997a**, *38*, 5653.
12. Wang, H.; Kesani, P.K.; Balsara, N.P.; Hammouda, B. *Macromolecules* **1997**, *30*, 982.
13. Wu, L.; Lodge, T.P.; Bates, F.S. *J. Rheol.* **2005**, *49*, 1231.
14. Zhao, J.; Majumdar, B.; Schulz, M.F.; Bates, F.S.; Almdal, K.; Mortensen, K.; Hajduk, D.A.; Gruner, S.M. *Macromolecules* **1996**, *29*, 1204.

## **Appendix A: Dynamic Mechanical Data**

**A.1. Poly(styrene-*b*-butadiene) in toluene Linear Viscoelasticity**  
Strain Sweep – 0.5rad/s; room temperature

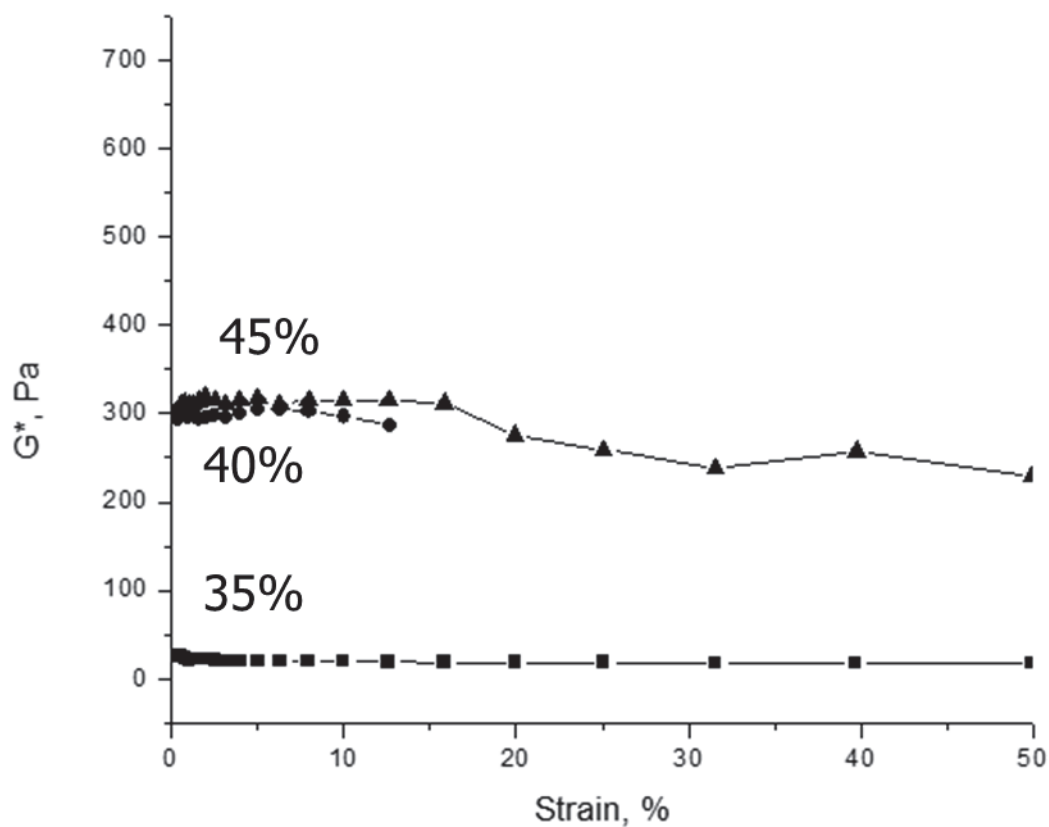


**Figure A.1.1.** Strain sweep of SB copolymer in toluene at room temperature following extraction of solvent from 20 wt% solution (initial concentration) to 35 (■), 40 (●) and 45 (▲) wt% polymer solution. Linear viscoelastic regime occurs up to at least ~15% strain at all concentrations.

## A.2. Poly(styrene) homopolymer in toluene (25 wt% polymer)

The data provided below was used to ensure solvent is not escaping from the rheometer fixture. The dynamic mechanical response of a 25 wt% poly(styrene) / toluene solution was monitored over time using the rheometer fixture equipped with the solvent trap.

<b>Time, s</b>	<b>G', Pa</b>	<b>G'', Pa</b>	<b>G*, Pa</b>
28	11.8694	9.159267	14.9925
550	16.4533	6.212331	17.58704
1073	19.0823	12.48101	22.80153
1598	38.57379	27.41889	47.32582
2121	76.56398	44.88646	88.75155
2644	95.05675	35.38781	101.4302
3168	86.05293	48.63649	98.84643
3691	87.80409	33.49005	93.97415
4214	59.81649	36.58249	70.11627
4739	39.75815	26.07084	47.54365
5262	27.01842	13.95656	30.4102
5785	7.039922	5.10893	8.698374
6309	1.224552	8.553941	8.641147
6833	0.381214	6.068758	6.08072
7356	1.66179	6.34235	6.556442
7881	4.28745	5.713157	7.142999
8404	4.562954	4.557438	6.449093
8927	7.519597	3.21844	8.179405
9451	4.31077	8.20223	9.266031

### A.3. Dynamic Mechanical Data - Poly(styrene-*b*-butadiene) in toluene

50 wt% - room temperature; 2% strain; 0.5 rad/s - Trial 1

Time, s	G', Pa	G'', Pa	G*, Pa
5.00	476.31	436.18	645.85
583	522.78	444.22	686.02
1153	548.33	467.43	720.53
1750	588.78	469.88	753.29
2361	613	485.23	781.8
2932	632.61	493.37	802.25
3515	646.46	502.8	818.98
4106	645.08	510.28	822.5
4696	666.76	509.75	839.29
5274	675.32	513.48	848.36
5846	693.49	524.53	869.52
6444	710.1	524.57	882.84
7009	722.56	524.34	892.76
7594	736.58	530.49	907.73
8165	745.59	533.56	916.83
8725	755.8	542.25	930.2
9307	774.9	547.9	949.03
9892	778.59	549.34	952.88
10472	792.07	559.66	969.84
11067	798.47	563.37	977.21
11670	811.31	567.96	990.36
12237	815.29	573.39	996.73
12803	838.97	576.62	1018
13398	850.63	584.43	1032.1
14001	853.42	586.71	1035.6
14592	862.42	601.67	1051.6
15170	866.25	586.9	1046.3
15748	883.48	589.34	1062
16319	891.02	599.46	1073.9
16916	892.9	594.6	1072.8
17483	904.54	601	1086
18059	903.34	601.06	1085

50 wt% - room temperature; 2% strain; 0.5 rad/s - Trial 2

<b>Time, s</b>	<b>G', Pa</b>	<b>G'', Pa</b>	<b>G*, Pa</b>
5	603.32	231.04	646.05
530	621.5	217.6	658.5
1240	642.58	227.94	681.82
1881	686.32	238.42	726.55
2509	726.7	244.87	766.84
3137	753.12	252.7	794.39
3766	773.39	261.49	816.4
4393	811.66	282.63	859.46
4953	922.73	336.85	982.3
5486	1000.4	330.04	1053.4
6009	1031.1	328.79	1082.3
6532	1036.4	319.95	1084.6
7057	1022.1	323.97	1072.2
7580	1020.6	318.36	1069.1
8104	1009.2	320.35	1058.8
8628	1008	325.27	1059.2
9151	1005.1	330.29	1058
9679	994.73	321.99	1045.5
10202	1012	325.89	1063.2
10726	995.72	335.72	1050.8
11254	993.16	321.28	1043.8
11777	988.39	329.98	1042
12300	985.36	343.32	1043.5
12825	984.04	338.89	1040.8
13355	987.47	335.22	1042.8
13888	993.9	325.61	1045.9

50 wt% - room temperature; 2% strain; 0.5 rad/s - Trial 3

<b>Time, s</b>	<b>G', Pa</b>	<b>G'', Pa</b>	<b>G*, Pa</b>
5	553.02	327.15	642.54
632	617.09	353.46	711.15
1260	661.1	364.7	755.02
1889	698.46	377.87	794.13
2592	749.45	388.16	844.01
3277	784.69	398.81	880.22
3918	819.77	393.19	909.19
4570	834.36	400.09	925.32
5198	853.04	405.3	944.43
5826	866.47	413.76	960.19
6454	888.57	416.52	981.35
7083	887.45	418.02	980.97
7711	901.15	430.02	998.5
8339	913.82	427.4	1008.8
8967	916.21	432.96	1013.4
9595	940.75	430.98	1034.8
10223	940.86	438.71	1038.1
10852	951.35	435.95	1046.5
11488	958.42	437.97	1053.7
12133	971.86	442.28	1067.8
12782	973.15	442.96	1069.2
13440	978.74	451.11	1077.7
14078	994.2	448.01	1090.5
14710	1000.8	450.34	1097.5
15334	999.48	448.37	1095.4
15966	1002.6	457.44	1102

50 wt% - room temperature; 2% strain; 0.1 rad/s - Trial 1

<b>Time, s</b>	<b>G', Pa</b>	<b>G'', Pa</b>	<b>G*, Pa</b>
5	321.6	129.64	346.75
1750	451.94	162.65	480.32
3447	471.04	166.61	499.64
5520	498.57	179.09	529.75
7468	515.35	162.1	540.25
9355	526.69	191.11	560.29
11580	538.83	193.62	572.57
13753	558.95	195.4	592.13
15981	563.81	198.95	597.88

45 wt% - room temperature; 2% strain; 0.5 rad/s - Trial 1

<b>Time, s</b>	<b>G', Pa</b>	<b>G'', Pa</b>	<b>G*, Pa</b>
5	231.24	90.744	248.4
349	308.56	117.15	330.05
700	342.6	126.98	365.38
1065	363.18	133.63	386.98
1410	388.91	138.52	412.84
1762	397.83	151.96	425.86
2114	418.21	143.17	442.04
2472	433.01	153.43	459.39
2825	449.16	161	477.15
3176	454.43	166.14	483.85
3534	477.84	169.08	506.87
3911	494.38	169.18	522.53
4256	517.82	188.54	551.08
4597	549.57	188.44	580.98
4953	571.79	199.38	605.56
5330	590.79	199.6	623.6
5709	613.45	200.97	645.53
6103	633.66	205.84	666.26
6525	660.33	223.31	697.07
6895	676.63	223.4	712.56
7272	683.59	226.11	720.01
7648	687.99	230.47	725.57
8025	694.12	239.14	734.16
8402	714.4	240.19	753.7
8779	721.05	239.76	759.86
9156	730.13	247.48	770.94
9532	733.25	244.67	773
9909	736.26	257.49	779.99
10286	747.53	256.62	790.35
10663	755.24	251.15	795.9
11041	760.83	265.73	805.9
11418	765.8	253.71	806.73
11795	771.76	261.28	814.79
12172	771.87	265.9	816.39
12549	773.77	262.05	816.94
12926	770.5	267.56	815.63

13303	775.95	265.11	819.99
13680	779.06	271.28	824.94
14056	770.1	281.94	820.09
14433	786.77	273.53	832.96
14810	785.99	281.25	834.8
15187	799.59	279.96	847.19
15553	804.09	275.58	850
15929	797.79	276.78	844.44
16306	804.02	276.89	850.36
16682	811.5	274.05	856.52
17060	808.64	279.37	855.54

45 wt% - room temperature; 2% strain; 0.5 rad/s - Trial 2

<b>Time, s</b>	<b>G', Pa</b>	<b>G'', Pa</b>	<b>G*, Pa</b>
5	305.9	29.162	307.29
631	430.69	64.935	435.55
1310	494.81	90.223	502.97
1944	518.73	102.87	528.83
2566	552.92	122.89	566.41
3195	568.97	126.66	582.9
3823	591.43	136.39	606.96
4451	606.98	146.39	624.38
5079	613.02	142.45	629.36
5708	636.88	143.23	652.78
6336	650.08	148.85	666.9
6964	658.97	162.94	678.82
7592	669.95	163.6	689.64
8220	682	162.72	701.15
8849	685.79	174	707.52
9477	694.18	175.61	716.05
10105	702.51	180.08	725.23
10733	704.22	176.01	725.88
11362	714.56	180.16	736.93
11990	723.2	188.76	747.43
12618	730.83	183.82	753.6
13247	742.59	196.79	768.22
13876	744.54	195.3	769.73
14504	750.56	202	777.26
15132	760.11	201.88	786.47
15760	766.91	206.88	794.32
16388	774.12	201.95	800.03
17017	773.55	222.33	804.86
17645	784.97	218.19	814.73
18273	792.02	212.24	819.96
18902	796.22	216.29	825.08

45 wt% - room temperature; 2% strain; 0.5 rad/s - Trial 3

<b>Time, s</b>	<b>G', Pa</b>	<b>G'', Pa</b>	<b>G*, Pa</b>
6	221.05	178.09	283.86
530	306.43	209.92	371.44
1053	361.41	236.85	432.1
1576	395.73	261.26	474.2
2100	422.15	269.91	501.06
2623	447.53	279.14	527.44
3146	471.38	283.07	549.85
3671	489.53	301.25	574.8
4194	513.69	309.12	599.53
4717	523.13	319.08	612.76
5242	547.55	309.92	629.18
5764	554.06	329.5	644.64
6287	573.01	333.2	662.85
6848	585.82	337.8	676.24
7390	594.99	340.42	685.49
7932	603.15	352.77	698.74
8590	623.02	345.23	712.28
9218	627.63	363.5	725.29
9848	651.73	357.63	743.41
10476	658.28	369.17	754.73
11104	664.16	382.07	766.22
11733	684.93	380.68	783.61
12360	686.96	382.84	786.43
12989	698.05	385.29	797.32
13617	721.92	390.82	820.92
14245	721.57	397.51	823.82
14873	735	397.04	835.38
15502	751.72	399.4	851.24
16130	750.19	410.27	855.05

45 wt% - room temperature; 2% strain; 0.1 rad/s - Trial 1

<b>Time, s</b>	<b>G', Pa</b>	<b>G'', Pa</b>	<b>G*, Pa</b>
5	169.04	110.44	201.91
3131	272.97	114.66	296.08
6273	323.02	136.87	350.82
9416	352.15	147.81	381.91
12558	392.83	166.69	426.73
15700	451.88	197.79	493.27
18841	549.07	226.64	594
21984	594.98	254.22	647.01
25126	642.15	275.85	698.9

42 wt% - room temperature; 2% strain; 0.5 rad/s - Trial 1

<b>Time, s</b>	<b>G', Pa</b>	<b>G'', Pa</b>	<b>G*, Pa</b>
5	243.56	128.01	275.15
555	300.32	153.67	337.36
1103	320.14	166.21	360.71
1655	328.59	168.75	369.39
2203	337.26	175.65	380.26
2754	342.09	167.55	380.92
3302	351.97	172.23	391.85
3854	355.75	187.99	402.37
4402	365.11	177.15	405.82
4953	357.68	191.64	405.78
5501	366.12	177.99	407.1
6052	371.63	186.47	415.79
6600	376.13	181.21	417.5
7152	373.78	191.24	419.86
7700	385.13	189.96	429.43
8251	385.25	188.79	429.02
8799	380.48	186.7	423.82
9351	390.57	188.7	433.76
9899	389.28	188.89	432.69
10451	397.06	193.79	441.83
10999	393.69	198.88	441.07
11550	397.21	187.48	439.24
12098	390.73	189.78	434.38
12650	393.82	195.66	439.75
13197	405.23	197.65	450.87
13749	414.97	203.11	462.01

42 wt% - room temperature; 2% strain; 0.5 rad/s - Trial 2

<b>Time, s</b>	<b>G', Pa</b>	<b>G'', Pa</b>	<b>G*, Pa</b>
5	234.23	149.16	277.69
600	301.04	180.12	350.81
1203	359.23	212.59	417.42
1783	409.84	237.13	473.5
2373	442.57	246.27	506.48
2944	468.24	254.08	532.73
3540	499.83	264.94	565.71
4137	516.06	260.03	577.87
4728	529.63	274.34	596.47
5318	555.73	282.82	623.56
5909	561.62	293.73	633.79
6518	593.6	295.49	663.08
7115	603.51	308.9	677.96
7713	607.08	302.86	678.43
8303	619.84	320.12	697.62
8900	636.7	317.74	711.57
9490	642.27	323.64	719.2
10057	666.29	335.73	746.1
10634	671.95	339.07	752.65
11231	685.84	347	768.63
11821	697.51	349.91	780.36
12418	696.2	355.11	781.53
13008	720.27	365.25	807.59
13643	730.83	359.4	814.42
14279	738.4	363.44	823
14943	743.99	367.69	829.9
15590	750.89	379.15	841.18
16287	771.86	385.78	862.9
16917	783.05	384.47	872.34
17583	798.14	392.11	889.26
18210	807.04	398.8	900.2
18838	808.12	396.76	900.26
19467	823.6	403.84	917.29
20095	826.83	408.91	922.42
20710	828.21	410.55	924.38
21338	830.97	418.95	930.61

21942	850.31	412.86	945.24
22570	842.18	423.58	942.71

42 wt% - room temperature; 2% strain; 0.5 rad/s - Trial 3

<b>Time, s</b>	<b>G', Pa</b>	<b>G'', Pa</b>	<b>G*, Pa</b>
5	263.84	63.753	271.43
631	359.76	107.87	375.58
1260	415.24	120.03	432.24
1888	465.26	120.39	480.59
2522	498.91	122.99	513.85
3150	561.15	135.5	577.28
3779	634.96	143.62	651
4407	685.52	150.11	701.76
5035	739.87	154.06	755.74
5663	799.31	160.56	815.28
6292	843.06	164.56	858.97
6920	891.14	169.52	907.12
7548	924.85	181.22	942.44
8176	958.85	195.15	978.51
8805	993.14	195.64	1012.2
9433	1024.1	195.83	1042.6
10061	1048	207.72	1068.4
10689	1092.4	209.37	1112.3
11317	1106.2	205.2	1125.1
11946	1135.1	222.95	1156.7
12588	1145.4	222.39	1166.8
13241	1153.8	221.84	1175
13932	1173.3	229.89	1195.6
14623	1178.5	240.46	1202.7

40 wt% - room temperature; 2% strain; 0.5 rad/s - Trial 1

<b>Time, s</b>	<b>G', Pa</b>	<b>G'', Pa</b>	<b>G*, Pa</b>
5	211.47	157.96	263.95
530	297.83	216.54	368.22
1052	355.39	242.29	430.12
1575	389.92	264.38	471.1
2100	408.96	269.06	489.53
2623	427.58	274.8	508.27
3146	431.59	270.49	509.35
3670	444.2	273.41	521.59
4193	445.25	270.17	520.8
4716	450.27	266.48	523.22
5241	450.95	277.38	529.43
5764	451.22	274.92	528.38
6287	454.65	279.18	533.52
6812	457.28	273.35	532.75
7334	449.24	268.85	523.54
7858	456.46	270.98	530.83
8383	463.69	270.65	536.9
8906	462.67	279.16	540.37
9429	472.07	267.69	542.68
9954	458.65	278.99	536.84
10476	464.45	270.72	537.59
10999	467.54	264.56	537.2

40 wt% - room temperature; 2% strain; 0.5 rad/s - Trial 2

<b>Time, s</b>	<b>G', Pa</b>	<b>G'', Pa</b>	<b>G*, Pa</b>
5	220.15	149.46	266.09
529	296.51	191.6	353.03
1052	321.94	201.88	380
1575	344.92	220.35	409.3
2100	352.53	233.27	422.72
2623	369.99	247.09	444.91
3146	402.64	276.26	488.3
3692	429.88	287.14	516.96
4343	451.64	301.02	542.77
4971	480.48	325.94	580.6
5599	500.53	337.45	603.66
6228	518.47	344.77	622.64

40 wt% - room temperature; 2% strain; 0.1 rad/s - Trial 1

<b>Time, s</b>	<b>G', Pa</b>	<b>G'', Pa</b>	<b>G*, Pa</b>
5	223.57	157.08	273.23
1563	323.02	205.54	382.87
3134	335.3	210.7	396.01
4705	361.11	219.59	422.63
6276	377.21	216.01	434.68
7848	394.39	221.27	452.22
9419	392.88	227.5	454
10990	395.52	238.64	461.94
12561	404.58	229.39	465.08

40 wt% - room temperature; 2% strain; 0.1 rad/s - Trial 2

<b>Time, s</b>	<b>G', Pa</b>	<b>G'', Pa</b>	<b>G*, Pa</b>
5	235.72	100.54	256.26
1564	363.57	135.53	388.01
3135	412.36	150.54	438.98
4706	459.64	169.75	489.98
6427	470.18	185.8	505.56
8123	516.2	183.14	547.72
10072	554.93	191.28	586.97
11954	562.7	220.33	604.29
13839	606.37	213.37	642.82
15724	637.8	214.36	672.86
17608	642.3	230.98	682.57

40 wt% - room temperature; 2% strain; 0.1 rad/s - Trial 3

<b>Time, s</b>	<b>G', Pa</b>	<b>G'', Pa</b>	<b>G*, Pa</b>
5	214.03	162.97	269.01
1473	314.83	221.65	385.02
2948	358.11	210.87	415.59
4422	378.62	239.13	447.81
5896	393.29	226.58	453.89
7370	417.57	236.1	479.69
8844	414.59	239.38	478.73
10319	427.45	246.64	493.5
11782	438.4	248.99	504.17
13256	458.42	254.43	524.29
14731	458.82	251.37	523.17

40 wt% - room temperature; 2% strain; 1.0 rad/s - Trial 1

<b>Time, s</b>	<b>G*, Pa</b>
6	377.7
1501	509.2
3007	545.79
4510	561.65
6017	569.85
7523	577.84
9029	587.7
10536	598.38

37 wt% - room temperature; 2% strain; 0.5 rad/s - Trial 1

<b>Time, s</b>	<b>G', Pa</b>	<b>G'', Pa</b>	<b>G*, Pa</b>
5	105.24	87.433	136.82
587	164.97	107.47	196.89
1135	182.18	111.55	213.62
1686	191.32	114.35	222.89
2234	195.87	114.59	226.92
2785	200.2	115.59	231.17
3333	203.51	118.3	235.4
3885	206.57	118.6	238.19
4433	208.15	120.07	240.3
4984	210.52	119.98	242.31
5532	213.73	121.67	245.93
6083	212.69	123.06	245.72
6631	217.03	122.83	249.38
7220	218.16	124.58	251.22
7849	219.19	127.34	253.5
8503	221.86	129.43	256.85
9131	223.46	130.65	258.84
9759	227.54	131.51	262.81
10387	233.31	135.38	269.74
11015	237.83	136.1	274.02
11643	244.02	141.26	281.96
12271	249.78	144.48	288.56
12900	258.69	148.96	298.51
13528	270.44	150.75	309.62
14156	280.85	158.18	322.33
14784	293.17	162.54	335.21
15412	308.44	170.26	352.31
16040	323.44	176.3	368.37
16646	337.42	182.04	383.39
17243	352.85	188.37	399.98
17799	367.32	194.57	415.67
18347	379.63	201.3	429.69
18895	391.76	205.38	442.33
19448	408.41	211.53	459.94
19998	422.24	218.41	475.39
20547	436.94	224.36	491.17

37 wt% - room temperature; 2% strain; 0.5 rad/s - Trial 2

<b>Time, s</b>	<b>G', Pa</b>	<b>G'', Pa</b>	<b>G*, Pa</b>
5	132.26	143.05	194.82
336	193.38	172.61	259.21
664	237.36	195.65	307.6
996	261.19	206.5	332.96
1324	284.43	206.44	351.45
1655	290.73	213.22	360.53
1983	294.93	214.5	364.68
2315	303.08	221.05	375.13
2643	303.52	219.62	374.64
2974	307.47	220.3	378.25
3303	320.3	215.09	385.82
3634	328.74	234.61	403.87
3962	342.65	227.87	411.5
4294	337.33	224.37	405.13
4622	342.08	235.89	415.53
4953	345.42	233.27	416.81
5281	351.78	231.42	421.07
5613	354.97	232.37	424.26
5941	354.54	230.28	422.76
6273	350.79	237.5	423.63
6601	353.53	243.74	429.4
6932	356.21	246.43	433.14
7260	357.75	240.58	431.12
7592	367.53	238.97	438.39
7920	361.1	228.96	427.57
8251	363.41	239.51	435.24
8580	357.33	235.04	427.7
8911	361.21	243.25	435.48
9239	359.05	241.55	432.74
9571	361.03	244.9	436.25
9900	354.5	241.08	428.71
10231	364.02	237.77	434.8
10559	360.88	239.9	433.34
10891	359.88	229.19	426.67
11219	362.21	236.98	432.85

11551	364.83	245.5	439.74
11879	362.4	235.92	432.43
12210	357.72	244.43	433.25
12538	359.01	250.42	437.72
12870	364.93	234.9	433.99
13198	361.41	239.64	433.64
13530	364.72	238.61	435.84
13858	358.82	235.53	429.21
14189	360.43	239.3	432.64
14517	356.32	248.97	434.68
14849	363.1	241.96	436.33
15177	365.62	239.59	437.13
15508	362.61	236.07	432.68
15836	365.02	238.03	435.77

37 wt% - room temperature; 2% strain; 0.5 rad/s - Trial 3

<b>Time, s</b>	<b>G', Pa</b>	<b>G'', Pa</b>	<b>G*, Pa</b>
7	156.29	96.751	183.81
336	198.95	116.56	230.57
664	205.93	123.49	240.12
996	220.56	119.93	251.05
1324	223.66	120.35	253.98
1656	227.75	121.62	258.18
1984	241.86	125.14	272.31
2315	243.94	127.75	275.37
2643	257.06	130.15	288.13
2975	260.81	132.07	292.35
3303	273.79	137.51	306.39
3634	277.26	147.72	314.15
3963	284.04	140.24	316.77
4294	287.01	148.67	323.23
4622	295.96	144.15	329.2
4953	302.37	142.39	334.22
5282	305.43	146.88	338.91
5613	302.35	150.91	337.92
5941	309.79	146.42	342.65
6273	313.1	154.86	349.31
6601	320.52	163.71	359.91
6933	318.73	153.76	353.88
7261	326.59	158.48	363.01
7593	323.97	156.87	359.95
7921	335.65	161.49	372.48
8253	331.15	166.55	370.68
8581	335.55	164.91	373.88
8912	338.93	174.16	381.06
9240	349.54	166.93	387.35
9572	351.65	170.86	390.96
9900	346.35	171.69	386.57
10231	352.28	172.92	392.43
10559	350.68	181.83	395.02
10891	352.11	171.58	391.69
11219	363.46	180	405.59
11550	369.35	180.71	411.19

11879	368.26	177.34	408.73
12210	378.13	190.96	423.61
12538	385.58	182.92	426.77
12870	387.09	179.5	426.68
13198	384.14	191.68	429.3
13529	395.77	197.77	442.43
13858	396.79	194.61	441.95
14190	394.06	198.98	441.45

37 wt% - room temperature; 2% strain; 0.5 rad/s – Late Start Experiment

Sample was prepared by removing solvent from 20 wt% solution as in all prior experiments. After loading the sample in the rheometer, a single point was collected to ensure the initial modulus of this sample was the same as in previous experiments. The sample was then equilibrated for 35 minutes under static conditions, then shear flow was started and changes in the dynamic mechanical response were measured.

<b>Time, s</b>	<b>G*, Pa</b>
5	191.61
2635	346.88
3183	358.38
3731	370.41
4283	380.62
4831	390.29
5382	397.97
6055	405.98
6733	414.72
7361	423.4
7989	431.89
8617	437.98
9226	447.58
9823	452.54

35 wt% - room temperature; 2% strain; 0.5 rad/s - Trial 1

<b>Time, s</b>	<b>G', Pa</b>	<b>G'', Pa</b>	<b>G*, Pa</b>
5	135.93	95.929	166.37
555	272.93	137.6	305.65
1104	308.78	148.43	342.6
1655	326.15	147.8	358.08
2203	335.67	153.45	369.08
2754	342.37	159.65	377.76
3302	354.29	160.16	388.81
3854	359.72	159.23	393.38
4402	361.3	161.63	395.8
4953	364.28	168.79	401.48
5501	372.08	167	407.84
6052	383.99	167.34	418.87
6600	374.27	172.58	412.14
7152	374.76	170.82	411.85
7700	388.33	175.93	426.33
8251	391.08	173.54	427.85
8799	385.71	176.18	424.04
9350	394.12	181.62	433.96
9899	387.11	174.14	424.47
10463	385.96	169.76	421.65
11011	392.19	179.14	431.17
11563	388.23	183.96	429.61
12111	392.01	179.55	431.17
12662	388.53	189.15	432.12
13210	402.76	172.24	438.04
13762	393.64	181.72	433.56
14310	400.24	175.84	437.16
14861	401.33	181.45	440.44
15420	407.02	196.07	451.78
15968	406.5	192.44	449.75
16519	424.28	189.97	464.87
17099	428.44	183.69	466.16

35 wt% - room temperature; 2% strain; 0.5 rad/s - Trial 2

<b>Time, s</b>	<b>G', Pa</b>	<b>G'', Pa</b>	<b>G*, Pa</b>
5	112.73	118.27	163.39
554	219.41	180.57	284.16
1138	250.89	190.41	314.97
1716	270.69	201.46	337.43
2294	286.7	207.62	353.98
2884	291.81	204.87	356.54
3462	304.15	218.51	374.5
4042	313.37	217.93	381.7
4613	318.92	220.23	387.57
5202	322.83	226.5	394.36
5787	330.58	222.41	398.44
6377	328.38	228.41	400
6968	331.57	228.98	402.96
7552	340.16	235.18	413.55
8124	344.34	236.39	417.67
8720	350.57	242.76	426.42
9330	351.3	246.75	429.3
9903	365.27	242.91	438.67
10499	365.14	248.39	441.62
11085	371.94	247.2	446.6
11674	375.84	259.62	456.79
12265	381.5	254.08	458.36
12836	379.13	256.78	457.91
13421	390	262.12	469.91
14017	392.84	266.98	474.97

35 wt% - room temperature; 2% strain; 0.1 rad/s

<b>Time, s</b>	<b>G', Pa</b>	<b>G'', Pa</b>	<b>G*, Pa</b>
5	116.27	117.48	165.29
1531	268.27	209.89	340.62
3068	294.05	230.13	373.4
4604	284.13	216.16	357.01
6122	286.01	211.23	355.56
7659	275.75	202.62	342.19
9195	277.64	211.77	349.18
10732	277.17	211.66	348.75
12250	280.03	216.47	353.95
13786	284.35	213.49	355.58

35 wt% - room temperature; 2% strain; 1 rad/s

<b>Time, s</b>	<b>G', Pa</b>	<b>G'', Pa</b>	<b>G*, Pa</b>
5	118.29	118.85	167.68
445	178.01	141.55	227.43
885	203.12	145.54	249.88
1324	213.25	151.12	261.37
1764	223.44	151.3	269.84
2204	227.85	160.35	278.62
2643	240.59	163.42	290.84
3083	243.78	168.21	296.18
3523	255.97	169.52	307.01
3963	259.21	173.53	311.93
4403	268.45	173.2	319.48
4843	266.29	177.65	320.11
5282	273.75	182.15	328.81
5722	280.65	177.7	332.17
6162	289.23	179.81	340.56
6601	294.17	185.26	347.64
7041	290.57	184.02	343.94
7482	296.49	189.69	351.98
7921	301.69	183.61	353.17
8361	310.36	193.7	365.85
8801	305.55	193.98	361.92
9240	314.56	196.04	370.65
9680	315.96	204.02	376.11
10120	321.65	203.1	380.4

32 wt% - room temperature; 2% strain; 0.5 rad/s – Trial 1

<b>Time, s</b>	<b>G', Pa</b>	<b>G'', Pa</b>	<b>G*, Pa</b>
5	8.7245	19.231	21.117
644	17.65	24.194	29.948
1337	32.216	27.995	42.68
1958	38.103	28.163	47.382
2541	39.987	29.572	49.734
3089	43.993	30.293	53.414
3803	44.694	28.804	53.172
4432	46.252	30.316	55.302
5059	49.615	30.51	58.245
5687	50.517	30.084	58.796
6315	52.614	30.731	60.931
6943	51.665	30.176	59.832
7571	50.806	31.886	59.983
8199	50.224	31.198	59.125
8828	48.371	30.857	57.375
9455	48.862	29.802	57.233
10073	49.369	31.415	58.516
10728	49.483	33.208	59.593
11339	50.669	32.485	60.188
11995	54.594	33.922	64.274
12672	54.847	34.709	64.907
13388	56.911	35.417	67.032
14107	61.609	38.096	72.436
14773	64.816	37.86	75.064
15401	66.582	38.633	76.979
16030	71.64	42.415	83.255
16658	76.423	43.41	87.892
17286	81.46	45.618	93.364
17914	86.474	49.09	99.436
18542	93.338	50.143	105.95
19170	100.01	52.954	113.17
19799	107.27	57.242	121.59
20427	114.51	60.785	129.64
21055	122.59	61.635	137.21

32 wt% - room temperature; 2% strain; 0.5 rad/s – Trial 2

<b>Time, s</b>	<b>G', Pa</b>	<b>G'', Pa</b>	<b>G*, Pa</b>
5	12.576	15.388	19.873
552	15.795	17.525	23.592
1183	18.375	17.479	25.361
1810	33.685	26.776	43.031
2453	99.654	47.298	110.31
3080	144.88	57.052	155.71
3708	164.9	68.488	178.56
4331	194.42	84.009	211.79
4879	222.21	95.064	241.69
5408	247.89	105.77	269.51
6058	272.9	115.03	296.15
6686	285.76	120.28	310.04
7314	293.94	125.56	319.64
7943	296.71	126.07	322.39
8572	299.95	128.44	326.29
9200	299.21	125.95	324.64
9828	294.32	124.34	319.51
10457	291.4	120.88	315.47
11085	286.26	115.24	308.58
11713	285.5	114.63	307.65
12341	287.13	116.8	309.97
12969	296.59	118.45	319.37
13598	311.99	122.64	335.23

30 wt% - room temperature; 2% strain; 0.5 rad/s

<b>Time, s</b>	<b>G*, Pa</b>
425	19.19
1262	23.63
2101	23.806
2937	23.628
3774	27.321
4613	24.081
5450	15.548
6287	15.939
7127	13.286
7964	14.796
8801	15.54
9640	16.051

#### A.4. Dynamic Mechanical Data - Poly(styrene-*b*-isoprene-*b*-isoprene) in toluene

37 wt% - room temperature; 2% strain; 0.5 rad/s

Time, s	G', Pa	G'', Pa	G*, Pa
5	106.7	54.697	119.9
556	147.93	98.525	177.74
1104	172.11	108.87	203.65
1655	181.54	120.05	217.64
2203	193.81	132.26	234.64
2754	196.74	131.79	236.8
3303	201.96	140.27	245.89
3854	201.22	142.59	246.62
4402	209.65	154.4	260.37
4953	229.97	164.82	282.94
5501	247.96	174.3	303.09
6053	255.86	173.09	308.91
6601	270.35	182.87	326.39
7152	302.22	207.91	366.83
7748	320.83	209.26	383.04
8351	338.73	229.55	409.19
8967	354.59	241.06	428.77
9608	373.6	261.32	455.92
10235	404.96	283.32	494.22
10864	434.63	294.51	525.01
11492	461.5	315.79	559.2
12120	489.51	341.31	596.75
12748	519.72	350.72	626.98
13377	540.13	375.53	657.85
14005	567.05	382.04	683.74
14633	592.77	395.09	712.37
15261	611.32	395.68	728.2
15889	630.11	403.07	748
16517	642.76	403.85	759.1
17146	656.69	405.7	771.91
17774	664.17	412.21	781.69
18402	667.25	404.22	780.14
19030	673.1	407.32	786.74
19659	671.75	416.2	790.24

45 wt% - room temperature; 2% strain; 0.5 rad/s

<b>Time, s</b>	<b>G', Pa</b>	<b>G'', Pa</b>	<b>G*, Pa</b>
5	250.97	191.6	315.74
29	257.81	199.02	325.69
682	313.19	235.45	391.82
1323	357.67	256.8	440.31
1989	389.76	270.99	474.71
2643	416.69	283.68	504.09
3296	448.45	313.3	547.05
3937	500.49	332.45	600.84
4683	539.43	335.48	635.24
5311	568.84	343.76	664.65
5952	588.65	345.5	682.56
6605	613.01	346.62	704.22
7233	636.37	348.76	725.68
7861	646.99	355.4	738.18
8490	657.28	361.79	750.28
9118	678.75	366.97	771.6
9746	681.78	365.52	773.59
10374	684.97	365.36	776.32
11015	690.64	372.06	784.48

50 wt% - room temperature; 2% strain; 0.5 rad/s

<b>Time, s</b>	<b>G', Pa</b>	<b>G'', Pa</b>	<b>G*, Pa</b>
5	315.64	250.53	402.98
29	325.95	250.73	411.23
657	374.49	294.71	476.55
1285	394.08	325.25	510.96
1913	433.9	349.3	557.03
2542	479.27	361.92	600.57
3170	515.07	400.67	652.56
3828	574.95	437.51	722.48
4469	624.9	476.31	785.73
5092	710.43	533.29	888.31
5720	779.42	578.19	970.46
6349	821.43	583.25	1007.4
6977	845.62	588.78	1030.4
7605	871.17	601.68	1058.8
8233	887.57	594.23	1068.1
8861	898.65	594.06	1077.3
9490	907.75	605.1	1090.9
10118	912.68	609.35	1097.4
10746	913.44	602.15	1094.1
11374	914.95	595.01	1091.4
12003	917.17	591.68	1091.5
12632	913.77	591.86	1088.7
13260	905.84	600.08	1086.6
13888	911.19	596.69	1089.2
14517	901.6	596.72	1081.2

## **Appendix B: Small Angle X-ray Scattering Data**

## B.1. SB / toluene Solution Equilibrium Scattering Profiles

25 wt% SB/toluene solution - room temperature; Initial solution concentration: 20 wt% polymer

$q, \text{nm}^{-1}$	$I(q), \text{a.u.}$
0.0011	318
0.0329	319.99
0.0648	321.13
0.0966	907.24
0.1285	596.59
0.1604	504.73
0.1922	473.06
0.2241	458.11
0.2559	442.43
0.2878	425.69
0.3197	411.04
0.3515	402.4
0.3834	398.14
0.4152	390.24
0.4471	386.97
0.479	384.13
0.5108	381.69
0.5427	376.16
0.5745	377.01
0.6064	372.66
0.6383	371
0.6701	371.44
0.702	367.97
0.7338	365.86
0.7657	365.26
0.7976	361.89
0.8294	362.59
0.8613	361.21
0.8931	362.54
0.925	360.31
0.9569	360.26
0.9887	357.07
1.0206	357.86
1.0524	354.76

30 wt% SB/toluene solution - room temperature; Initial solution concentration: 20 wt% polymer

<b>q, nm<sup>-1</sup></b>	<b>I(q), a.u.</b>
0.0011	329
0.0329	330.21
0.0648	331.89
0.0966	1935.6
0.1285	1119.5
0.1604	1415.4
0.1922	4968.4
0.2241	2110.6
0.2559	911.39
0.2878	702.37
0.3197	614.86
0.3515	567.93
0.3834	519.11
0.4152	486.77
0.4471	484.37
0.479	460.74
0.5108	450.77
0.5427	443.46
0.5745	442.11
0.6064	430.31
0.6383	426.83
0.6701	422.37
0.702	414.44
0.7338	415.61
0.7657	410.27
0.7976	408.14
0.8294	403.84
0.8613	403.76
0.8931	398.7
0.925	396.21
0.9569	396.41
0.9887	393.94
1.0206	393.99
1.0524	390.44

60 wt% SB/toluene solution - room temperature; Initial solution concentration: 20 wt% polymer

<b>q, nm<sup>-1</sup></b>	<b>I(q), a.u.</b>
0.0012	3135.6
0.0383	16758
0.0754	4492.1
0.1125	3438.4
0.1496	3241.1
0.1866	3329
0.2237	3207.2
0.2608	3144.1
0.2979	3124.3
0.335	3117.9
0.372	3108.7
0.4091	3104.3
0.4462	3100.9
0.4833	3099.2
0.5204	3098.1
0.5574	3096.8
0.5945	3093.8
0.6316	3094.1
0.6687	3090.6
0.7058	3089.4
0.7428	3088.3
0.7799	3087.6
0.817	3087.6
0.8541	3085.9
0.8912	3084.8
0.9282	3081.8
0.9653	3081.3
1.0024	3080.3
1.0395	3079.1
1.0766	3079.4

## B.2. SIS / toluene Solution Scattering Profiles

41 wt% SIS/toluene solution - room temperature; Initial solution concentration: 20 wt% polymer

<b>q, nm<sup>-1</sup></b>	<b>I(q), a.u.</b>
0.0028	111.85
0.0451	138.04
0.0874	310.62
0.1297	173.96
0.172	143.65
0.2142	145.54
0.2565	129.12
0.2988	122
0.3411	120.35
0.3834	119.31
0.4257	117.46
0.468	116.62
0.5102	117.46
0.5525	116.23
0.5948	116.04
0.6371	114.96
0.6794	115.35
0.7217	114.81
0.7639	115.31
0.8062	115.5
0.8485	114.42
0.8908	113.92
0.9331	113.85
0.9754	114.15
1.0177	113.5

50 wt% SIS/toluene solution - room temperature; Initial solution concentration: 20 wt% polymer

<b>q, nm<sup>-1</sup></b>	<b>I(q), a.u.</b>
0.0028	112.62
0.0451	128.04
0.0874	414.31
0.1297	195.58
0.172	159.77
0.2142	197.42
0.2565	143.42
0.2988	130.88
0.3411	125.5
0.3834	123.46
0.4257	120.58
0.468	118.96
0.5102	118.27
0.5525	117.46
0.5948	116.96
0.6371	116.58
0.6794	116.08
0.7217	116.27
0.7639	115.69
0.8062	115.73
0.8485	115.08
0.8908	115.23
0.9331	115.08
0.9754	115.38
1.0177	115.19

90 wt% SIS/toluene solution - room temperature; Initial solution concentration: 20 wt% polymer

<b>q, nm<sup>-1</sup></b>	<b>I(q), a.u.</b>
0.0028	112.81
0.0451	139.19
0.0874	544.27
0.1297	243.35
0.172	227.96
0.2142	758
0.2565	236.19
0.2988	162.96
0.3411	149.46
0.3834	132.96
0.4257	124.35
0.468	121.96
0.5102	120.65
0.5525	120.77
0.5948	119.08
0.6371	118.42
0.6794	118.62
0.7217	116.65
0.7639	116.77
0.8062	116.58
0.8485	116.23
0.8908	116
0.9331	114.62
0.9754	114.92
1.0177	114.96

SIS/toluene solution scattering profiles - room temperature; Initial solution concentration: 20 wt% polymer

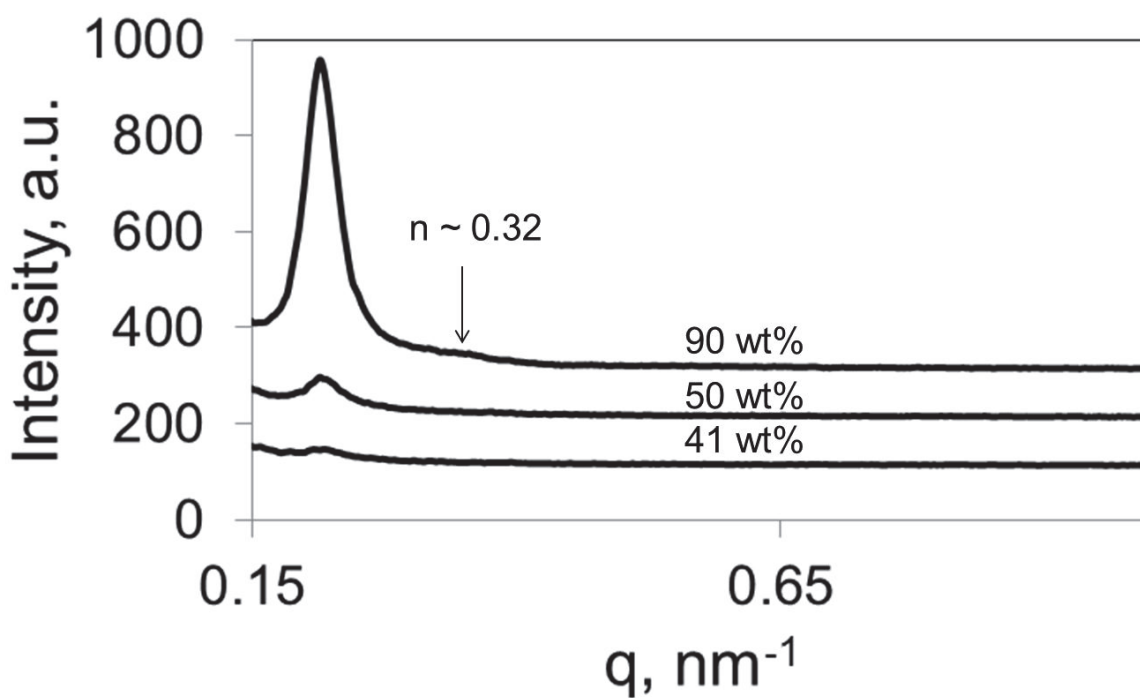


**Figure B.2.1.** Scattering profiles of SIS in toluene at three polymer concentrations during removal of solvent at room temperature.

### B.3. Lorentz Correction & Integration of Primary Scattering Profile Peaks

The following Visual Basic code was used in Excel to perform a Lorentz correction on the primary scattering peak and integrate the area under the primary peak.

```
Sub Lorentz()  
'Define variables for minimum intensity (Min1, Min2), integration rectangle and triangle dimensions, and the bounds of a rectangle  
'for integration by Simpson's rule  
  
Dim Min1, Min2 As Double  
Dim Base1, Base2, Height, Triangle, Rectangle As Double  
Dim SimpsonBase1, SimpsonBase2 As Double  
  
'Label cells  
ActiveSheet.Cells(1013, 1) = "Min1"  
ActiveSheet.Cells(1014, 1) = "q_min1"  
ActiveSheet.Cells(1015, 1) = "Min1"  
ActiveSheet.Cells(1016, 1) = "q_min2"  
ActiveSheet.Cells(1017, 1) = "Triangle"  
ActiveSheet.Cells(1018, 1) = "Rectangle"  
ActiveSheet.Cells(1019, 1) = "Area"  
  
'Step through the columns (data sets)  
For z = 2 To 200  
  
    i = 1021  
    'Initialize all variables for numerical integration  
    Simpson = 0  
    Triangle = 0  
    Rectangle = 0  
  
    'Initialize Min1 and Min2 to large values such that the first intensity is less than Min1 and Min2  
    Min1 = 100000  
    Min2 = 100000  
  
    'Step through the wave-vectors of a given data set to find the first minimum intensity  
    'Min1 and Min2 will give the bounds of the primary scattering peak over which to integrate  
    'The maximum x1 value checked (165 here) should correspond to a wave-vector less than or equal to the wave-vector of the  
    'maximum peak intensity  
  
    For x1 = 87 To 165  
        'If the intensity is less than the previous intensity, it is the new minimum value  
        If ActiveSheet.Cells(x1, z).Value < Min1 Then  
            Min1 = ActiveSheet.Cells(x1, z).Value  
            ActiveSheet.Cells(1013, z) = ActiveSheet.Cells(x1, 1)  
            ActiveSheet.Cells(1014, z) = Min1  
            'Base1 will be the first bound of the integration rectangle  
            Base1 = ActiveSheet.Cells(x1, 1)  
            Min1x = x1  
        End If  
    Next x1  
  
    OldDerivative = 100  
    OldSecondDerivative = 1000  
    For x2 = 168 To 220  
  
        'Determine the second minimum which will be the second boundary of the primary peak  
        'Draw a line between Min1 and Min2 and be sure the line does not cut through the scattering peak  
  
        If ActiveSheet.Cells(x2, z) < Min2 Then  
            Number = 0  
  
            Height = Min1 - ActiveSheet.Cells(x2, z)  
            Base = Base1 - ActiveSheet.Cells(x2, 1)  
            Slope = Height / Base  
            b = Min1 - ActiveSheet.Cells(Min1x, 1) * Slope  
            If Slope <= 0 Then  
  
                For j = Min1x To x2 Step 1  
                    LineValue = Slope * ActiveSheet.Cells(j, 1) + b  
  
                    If LineValue > ActiveSheet.Cells(j, z) Then  
                        Number = Number + 1  
                    End If  
                Next j  
                If Number < 2 Then  
                    Min2 = ActiveSheet.Cells(x2, z).Value  
                End If  
            End If  
        End If  
    Next x2  
End For  
End Sub
```

```

        Base2 = ActiveSheet.Cells(x2, 1).Value
        Minx2 = x2
        ActiveSheet.Cells(1015, z) = Min2
        ActiveSheet.Cells(1016, z) = ActiveSheet.Cells(x2, 1)
    End If
End If

End If

Next x2

'Integrate the area under the peak by Simpson's rule
For x = Min1x - 1 To Minx2 - 1
x = x + 1
Frontx = x - 1
Backx = x + 1

    SimpsonBase1 = ActiveSheet.Cells(Frontx, 1)
    SimpsonBase2 = ActiveSheet.Cells(Backx, 1)
    SimpsonHgt = ActiveSheet.Cells(x, z)
    Simpson = Simpson + SimpsonHgt * (SimpsonBase2 - SimpsonBase1)
    'Calculates scattering power
    PowerIntegral = PowerIntegral + (ActiveSheet.Cells(x, 1) ^ 2) * SimpsonHgt * (SimpsonBase2 - SimpsonBase1)
    Power = (0.5 * (3.14 ^ 2)) * PowerIntegral
Next x

'Define a triangle and rectangle to represent part of the area under the base of the scattering profile which must be
'subtracted off

Height = Min1 - Min2

Base = Base1 - Base2
Triangle = Abs(Base) * Height / 2

Rectangle = Abs(Base) * Min2

'Subtract the area under the scattering profile from the integrated intensity and output results
ActiveSheet.Cells(1020, z) = Simpson - Triangle - Rectangle
ActiveSheet.Cells(1021, z) = Power

For x = Min1x To Minx2
    i = i + 1
Next x
PowerIntegral = 0
Next z

End Sub

```

#### B.4. Iso-concentration SAXS Integrated Intensity vs. time data for SB / toluene solution

40 wt% polymer – room temperature – 30 second exposure

<b>Time, s</b>	<b>Integrated Intensity, a.u.</b>
60	0.017802108
240	0.04973664
420	0.04636854
900	0.064529706
1200	0.017955372
1500	0.133161696
1860	0.10309476
2220	0.139616088
2580	0.16297278
3000	0.177271446
3420	0.380152194
3840	0.194136666
4350	0.269218104
4650	0.402424914
5550	0.31528815
6450	0.363629964
7230	0.93513288
7560	0.99071889
8040	1.103997054
8400	1.194274494
8820	1.165370016
9720	1.006887624
10530	1.303326156
11160	1.023162036
12000	1.639520628
12600	1.690530348
13530	1.612039404
14400	1.663148622
30000	1.938527568

45 wt% polymer – room temperature – 30 second exposure

<b>Time, s</b>	<b>Integrated Intensity, a.u.</b>
330	5.221956624
510	5.68046133
780	6.40021503
1050	7.081968528
1380	7.804972908
1650	8.006229552
1950	8.20516746
3680	8.946778584
4100	9.453474312
4520	10.23161047
4820	10.183404
5120	10.61149878
5480	10.80593518
5870	11.37287293
6200	11.81443763
7100	12.76916668
8000	14.05351158
8900	14.6963045
9800	16.04062136
10700	17.78158916
12500	20.41513189
14150	21.76446568

50 wt% polymer – room temperature – 30 second exposure

<b>Time, s</b>	<b>Integrated Intensity, a.u.</b>
360	4.96850988
540	5.60428356
810	6.303169872
1020	6.503532888
1290	6.782310216
1470	7.008103932
1740	7.404989094
1950	7.599241944
2160	7.890674676
2490	8.52026712
2670	8.657571888
2880	8.962573428
3360	9.527028672
3660	9.94427508
3960	10.01382356
4230	10.52128438
4560	10.93949425
4980	11.50062898
5370	12.05655088
5820	12.75440266
6300	13.53058964
6930	14.52206064
7740	16.24750552
8220	17.04073694
9540	15.8782876
10110	13.32952087

55 wt% polymer – room temperature – 30 second exposure

<b>Time, s</b>	<b>Integrated Intensity, a.u.</b>
420	14.5203599
780	15.06564355
1170	17.05652932
1500	18.77313988
1920	21.47216527
2310	26.23222375
2700	31.44777233
3360	33.73763352
3900	34.88686261
4380	36.36295252
4860	37.7943839
5400	39.70128655
6300	42.33310382
7200	43.92920006
8100	46.04081954
9300	47.6316084

60 wt% polymer – room temperature – 30 second exposure

<b>Time, s</b>	<b>Integrated Intensity, a.u.</b>
360	4.12852428
630	5.165459064
810	5.656778952
990	6.348421068
1230	6.806934426
1590	7.58182176
1950	8.322801288
2310	9.110903934
2670	9.692391876
3030	10.08971891
3390	10.3579649
3750	10.57410854
4110	10.69417111
4470	10.9665954
5190	11.05043143
5550	11.3638903
5910	11.58829228
6270	11.82742738
6630	12.15708835
6990	12.73409765
7350	13.16214608
7710	13.85509094
8070	14.61934002
8910	17.25135073
10110	19.68105542

## B.5. In situ SAXS data – SB in toluene

30°C; No sweep gas

Time, s	Polymer Concentration, w/w	Integrated Intensity, a.u.
600	0.38	1.11
720	0.42	1.73
900	0.51	2.41
1020	0.58	3.85
1140	0.64	4.24
1260	0.72	4.88
1380	0.78	6.06
1500	0.82	6.84
1620	0.87	7.18
1800	0.93	7.14
2040	0.96	6.83

Polymer Concentration, w/w	Horizontal Bragg Spacing, nm	Vertical Bragg Spacing, nm	$\sigma^1$ , n.u.
0.22	34.80	35.78	0.03
0.26	36.29	33.87	0.07
0.30	32.16	31.36	0.02
0.36	32.16	31.56	0.02
0.42	32.16	31.76	0.01
0.53	31.56	30.79	0.02
0.64	32.57	31.36	0.04
0.74	33.87	31.36	0.07
0.82	33.87	29.89	0.12
0.90	33.21	28.38	0.15
0.93	32.78	27.32	0.17
0.96	32.78	27.03	0.18

<sup>1</sup>Fractional difference between horizontal and vertical Bragg spacing

30°C; Sweep gas

Time, s	Polymer Concentration, w/w	Integrated Intensity, a.u.
0	0.20	0.03
240	0.25	0.04
480	0.29	0.19
720	0.34	0.47
900	0.39	0.79
1020	0.44	1.05
1320	0.55	2.04

Polymer Concentration, w/w	Horizontal Bragg Spacing, nm	Vertical Bragg Spacing, nm	$\sigma^1$ , n.u.
0.21	38.79	40.01	0.03
0.24	40.32	40.32	0.00
0.30	31.96	32.16	0.01
0.34	32.16	31.36	0.02
0.42	32.16	31.36	0.02
0.49	30.98	30.06	0.03
0.57	32.57	31.36	0.04
0.66	33.87	31.76	0.06
0.75	33.87	30.79	0.09
0.81	33.87	29.37	0.13
0.86	33.21	28.23	0.15
0.86	32.78	27.92	0.15
0.88	33.21	27.32	0.18

<sup>1</sup>Fractional difference between horizontal and vertical Bragg spacing

40°C; No sweep gas

<b>Time, s</b>	<b>Polymer Concentration, w/w</b>	<b>Integrated Intensity, a.u.</b>
60	0.23	0.02
180	0.27	0.45
300	0.32	1.11
420	0.37	2.47
540	0.44	3.87
660	0.51	6.41
780	0.60	8.92
840	0.64	11.33

<b>Polymer Concentration, w/w</b>	<b>Horizontal Bragg Spacing, nm</b>	<b>Vertical Bragg Spacing, nm</b>	<b><math>\sigma^1</math>, n.u.</b>
0.21	40.01	40.32	0.01
0.34	32.16	31.76	0.01
0.44	32.16	31.76	0.01
0.55	31.76	30.98	0.02
0.67	33.21	30.98	0.07
0.77	33.21	29.37	0.12
0.81	32.78	28.23	0.14
0.83	32.57	27.32	0.16

<sup>1</sup>Fractional difference between horizontal and vertical Bragg spacing

40°C; Sweep gas

Time, s	Polymer Concentration, w/w	Integrated Intensity, a.u.
0	0.21	0.00
195	0.26	0.02
435	0.31	0.40
555	0.34	0.83
735	0.39	0.94
795	0.41	1.65
855	0.43	2.80
915	0.46	4.24

Polymer Concentration, w/w	Horizontal Bragg Spacing, nm	Vertical Bragg Spacing, nm	$\sigma^1$ , n.u.
0.21	40.01	40.32	0.01
0.26	40.32	39.08	0.03
0.30	39.69	40.32	0.02
0.34	32.36	31.17	0.04
0.46	31.56	30.79	0.02
0.52	32.99	31.36	0.05
0.57	33.87	30.98	0.09
0.61	33.21	28.87	0.13
0.63	32.78	28.38	0.13

<sup>1</sup>Fractional difference between horizontal and vertical Bragg spacing

60°C; No sweep gas

<b>Time, s</b>	<b>Polymer Concentration, w/w</b>	<b>Integrated Intensity, a.u.</b>
0	0.22	0.01
110	0.27	0.24
240	0.34	0.80
360	0.41	1.62
420	0.45	2.32
480	0.50	3.66
540	0.53	5.00

<b>Polymer Concentration, w/w</b>	<b>Horizontal Bragg Spacing, nm</b>	<b>Vertical Bragg Spacing, nm</b>	<b><math>\sigma^1</math>, n.u.</b>
0.22	39.69	40.32	0.02
0.30	31.76	31.76	0.00
0.41	32.16	31.76	0.01
0.53	31.76	30.98	0.02
0.64	33.21	31.36	0.06
0.68	32.16	27.32	0.15
0.70	32.57	27.76	0.15

<sup>1</sup>Fractional difference between horizontal and vertical Bragg spacing

30°C; No sweep gas; Chamber saturated with toluene

<b>Polymer Concentration, w/w</b>	<b>Horizontal Bragg Spacing, nm</b>	<b>Vertical Bragg Spacing, nm</b>	<b><math>\sigma^1</math>, n.u.</b>
0.47	30.52	30.94	0.01
0.55	30.94	31.38	0.01
0.66	31.38	31.38	0.00
0.71	31.82	31.82	0.00
0.76	32.76	32.29	0.01
0.86	33.25	31.82	0.04
0.90	33.75	31.82	0.06

<sup>1</sup>Fractional difference between horizontal and vertical Bragg spacing

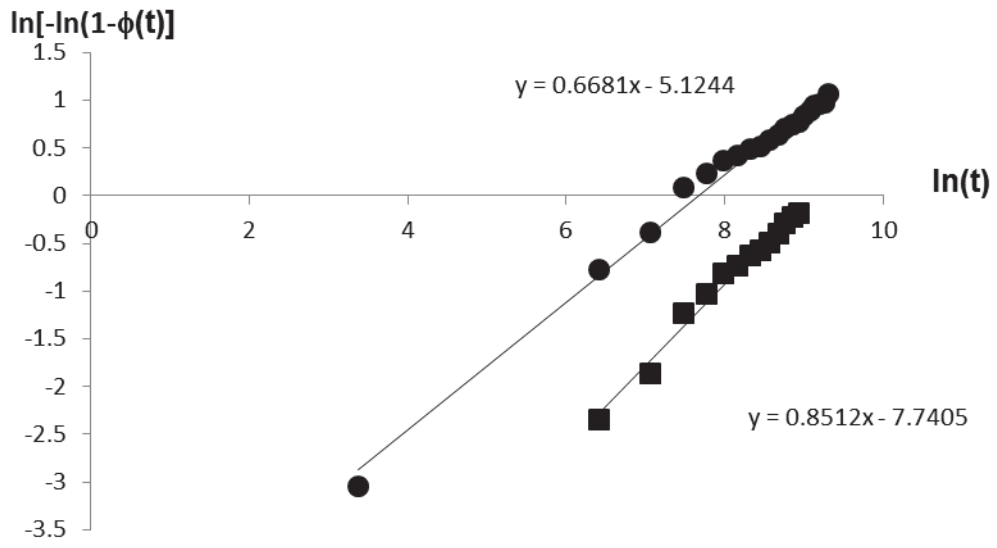
## **Appendix C: Kinetics Data**

### C.1. Iso-concentration SB copolymer in toluene Avrami fits from DMR data

- : Parallel rule of mixture used to calculated  $\phi(t)$
- : Series rule of mixture used to calculated  $\phi(t)$

50 wt% - Trial 1

ln(t)	Parallel		Series	
	$\phi(t)$	$\ln[-\ln(1-\phi(t))]$	$\phi(t)$	$\ln[-\ln(1-\phi(t))]$
3.37	0.01	-4.80	0.05	-3.05
6.41	0.09	-2.35	0.37	-0.78
7.07	0.14	-1.86	0.50	-0.38
7.48	0.25	-1.23	0.67	0.09
7.78	0.30	-1.03	0.72	0.23
7.99	0.36	-0.82	0.76	0.37
8.17	0.38	-0.74	0.78	0.42
8.33	0.41	-0.63	0.80	0.49
8.46	0.43	-0.58	0.82	0.52
8.57	0.46	-0.49	0.83	0.58
8.68	0.49	-0.40	0.85	0.64
8.77	0.53	-0.29	0.87	0.70
8.86	0.55	-0.22	0.88	0.74
8.94	0.57	-0.18	0.88	0.77
9.01	0.61	-0.05	0.90	0.84
9.08	0.64	0.02	0.91	0.89
9.14	0.67	0.10	0.92	0.94
9.20	0.69	0.15	0.93	0.96
9.26	0.69	0.16	0.93	0.97
9.31	0.75	0.31	0.94	1.06
9.37	0.74	0.30	0.94	1.06
9.41	0.78	0.41	0.95	1.12
9.46	0.81	0.49	0.96	1.17
9.50	0.84	0.60	0.97	1.24
9.55	0.87	0.70	0.97	1.30
9.59	0.87	0.72	0.98	1.31
9.63	0.90	0.83	0.98	1.38
9.67	0.91	0.87	0.98	1.40
9.70	0.92	0.93	0.99	1.44
9.74	0.96	1.15	0.99	1.59
9.77	0.96	1.16	0.99	1.60

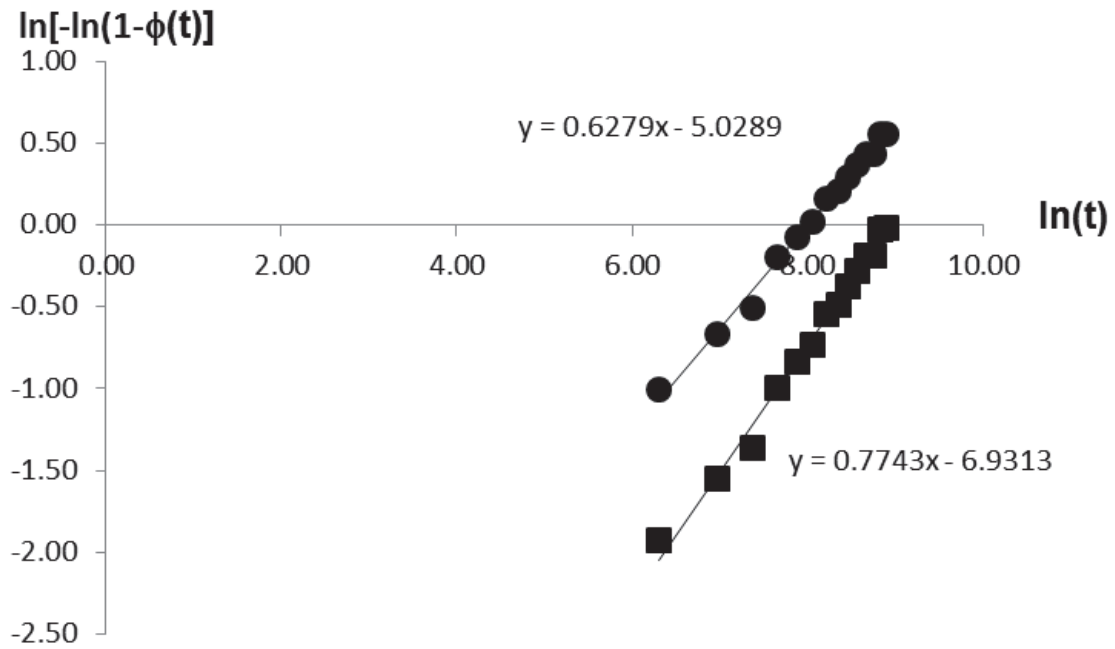


$n_{\text{Parallel}}$	0.85
$Z_{\text{Parallel}}, S^{-n}$	4.8E-4
$n_{\text{Series}}$	0.67
$Z_{\text{Series}}, S^{-n}$	5.5E-3

50 wt% - Trial 2

ln(t)	Parallel		Series	
	$\phi(t)$	$\ln[-\ln(1-\phi(t))]$	$\phi(t)$	$\ln[-\ln(1-\phi(t))]$
6.31	0.13	-1.93	0.31	-1.00
6.98	0.19	-1.55	0.40	-0.67
7.38	0.23	-1.37	0.45	-0.51
7.66	0.31	-1.00	0.56	-0.20
7.88	0.35	-0.84	0.61	-0.07
8.06	0.38	-0.73	0.64	0.01
8.22	0.44	-0.55	0.69	0.16
8.35	0.46	-0.49	0.71	0.20
8.47	0.50	-0.38	0.74	0.29
8.57	0.53	-0.28	0.76	0.36
8.66	0.56	-0.18	0.79	0.43
8.75	0.56	-0.19	0.79	0.43
8.83	0.62	-0.03	0.82	0.55
8.90	0.62	-0.02	0.83	0.56
8.97	0.65	0.06	0.84	0.62
9.04	0.62	-0.04	0.82	0.54
9.10	0.63	-0.01	0.83	0.56
9.15	0.69	0.15	0.86	0.69
9.21	0.70	0.19	0.87	0.71
9.26	0.71	0.23	0.88	0.74
9.31	0.74	0.30	0.89	0.79
9.35	0.73	0.26	0.88	0.76
9.40	0.73	0.27	0.89	0.77
9.44	0.72	0.23	0.88	0.74
9.48	0.76	0.35	0.90	0.83
9.52	0.77	0.40	0.91	0.87
9.56	0.80	0.49	0.92	0.93
9.60	0.78	0.42	0.91	0.88
9.63	0.80	0.47	0.92	0.91
9.66	0.78	0.43	0.91	0.89
9.70	0.82	0.54	0.93	0.97
9.73	0.79	0.45	0.91	0.90
9.76	0.85	0.65	0.94	1.05
9.79	0.84	0.62	0.94	1.03
9.82	0.90	0.86	0.96	1.20
9.85	0.90	0.84	0.96	1.20

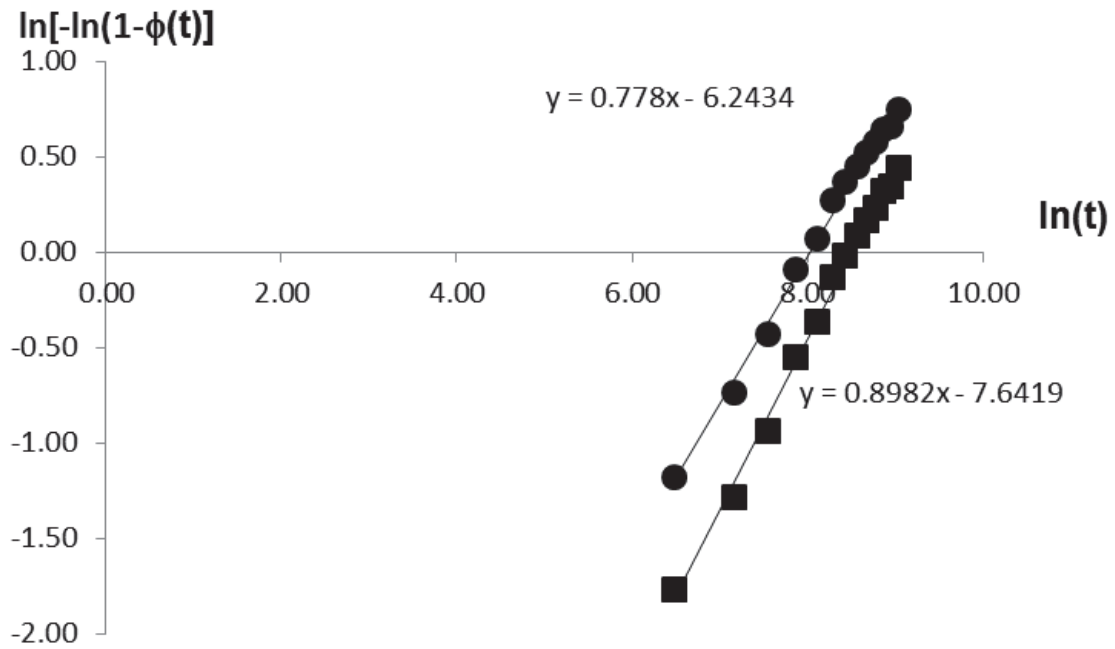
9.87	0.88	0.75	0.95	1.13
9.90	0.89	0.79	0.96	1.16
9.93	0.89	0.81	0.96	1.17
9.55	0.87	0.70	0.97	1.30
9.57	0.86	0.67	0.97	1.28
9.60	0.88	0.74	0.98	1.33
9.62	0.90	0.85	0.98	1.39
9.64	0.91	0.86	0.98	1.40
9.67	0.91	0.87	0.98	1.40
9.69	0.94	1.02	0.99	1.50
9.71	0.93	1.00	0.99	1.49
9.73	0.93	0.99	0.99	1.48
9.75	0.96	1.18	0.99	1.61
9.77	0.96	1.16	0.99	1.60
9.79	0.98	1.43	1.00	1.78



$n_{\text{Parallel}}$	0.77
$Z_{\text{Parallel}}, S^{-n}$	9.8E-4
$n_{\text{Series}}$	0.63
$Z_{\text{Series}}, S^{-n}$	6.5E-3

50 wt% - Trial 3

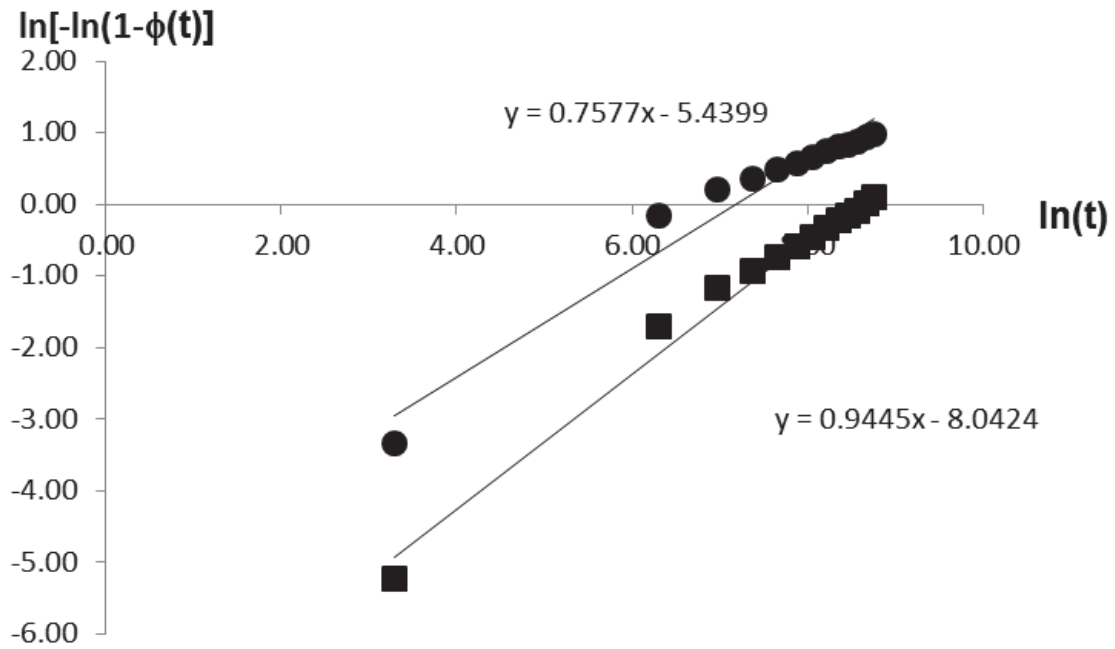
ln(t)	Parallel		Series	
	$\phi(t)$	$\ln[-\ln(1-\phi(t))]$	$\phi(t)$	$\ln[-\ln(1-\phi(t))]$
6.49	0.16	-1.76	0.27	-1.18
7.16	0.24	-1.28	0.38	-0.73
7.56	0.32	-0.94	0.48	-0.43
7.87	0.44	-0.55	0.60	-0.09
8.10	0.50	-0.36	0.66	0.07
8.28	0.58	-0.13	0.73	0.27
8.43	0.63	-0.02	0.76	0.37
8.56	0.66	0.09	0.79	0.45
8.67	0.69	0.17	0.81	0.52
8.78	0.72	0.23	0.83	0.57
8.87	0.75	0.32	0.85	0.64
8.95	0.75	0.34	0.86	0.66
9.03	0.79	0.44	0.88	0.74
9.10	0.81	0.52	0.89	0.81
9.17	0.82	0.53	0.90	0.82
9.23	0.85	0.64	0.92	0.91
9.29	0.86	0.69	0.92	0.95
9.35	0.88	0.76	0.94	1.01
9.41	0.91	0.89	0.95	1.12
9.46	0.91	0.90	0.95	1.12
9.51	0.93	0.99	0.96	1.20
9.55	0.97	1.24	0.98	1.41
9.60	0.99	1.45	0.99	1.59
9.64	0.99	1.48	0.99	1.62
9.68	0.99	1.44	0.99	1.58



$n_{\text{Parallel}}$	0.898
$Z_{\text{Parallel}}, S^{-n}$	4.8E-4
$n_{\text{Series}}$	0.78
$Z_{\text{Series}}, S^{-n}$	1.9E-3

45 wt% - Trial 1

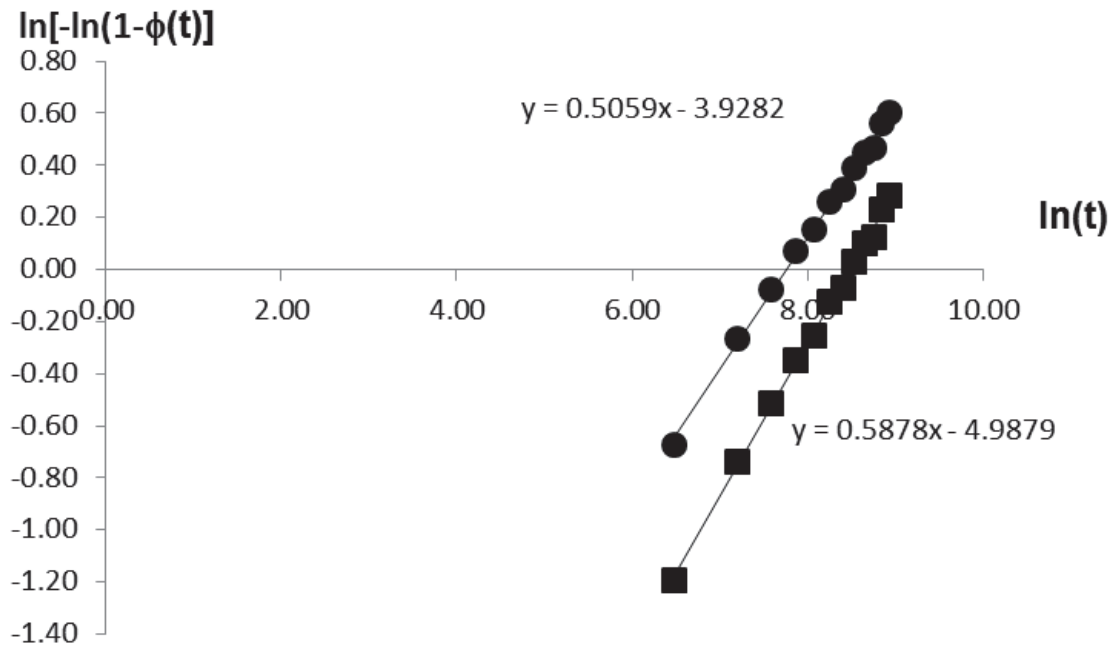
ln(t)	Parallel		Series	
	$\phi(t)$	$\ln[-\ln(1-\phi(t))]$	$\phi(t)$	$\ln[-\ln(1-\phi(t))]$
3.30	0.01	-5.22	0.03	-3.34
6.31	0.17	-1.70	0.57	-0.16
6.98	0.27	-1.16	0.71	0.21
7.38	0.33	-0.93	0.76	0.37
7.66	0.38	-0.73	0.80	0.49
7.88	0.42	-0.60	0.83	0.57
8.06	0.47	-0.46	0.85	0.66
8.21	0.51	-0.32	0.88	0.74
8.35	0.55	-0.21	0.89	0.80
8.46	0.58	-0.15	0.90	0.84
8.57	0.60	-0.09	0.91	0.87
8.66	0.64	0.02	0.92	0.94
8.75	0.67	0.11	0.93	0.99
8.83	0.68	0.12	0.93	1.00
8.91	0.70	0.19	0.94	1.03
8.98	0.73	0.26	0.95	1.08
9.06	0.75	0.31	0.95	1.11
9.13	0.76	0.37	0.96	1.14
9.20	0.79	0.44	0.96	1.18
9.26	0.82	0.54	0.97	1.24
9.32	0.83	0.57	0.97	1.26
9.37	0.86	0.67	0.98	1.32
9.42	0.88	0.76	0.98	1.37
9.47	0.90	0.84	0.98	1.42
9.52	0.92	0.94	0.99	1.48
9.57	0.94	1.01	0.99	1.52
9.61	0.95	1.13	0.99	1.60
9.65	0.97	1.24	1.00	1.67
9.69	0.99	1.63	1.00	1.94



$n_{\text{Parallel}}$	0.94
$Z_{\text{Parallel}}, S^{-n}$	3.2E-4
$n_{\text{Series}}$	0.76
$Z_{\text{Series}}, S^{-n}$	4.3E-3

## 45 wt% - Trial 2

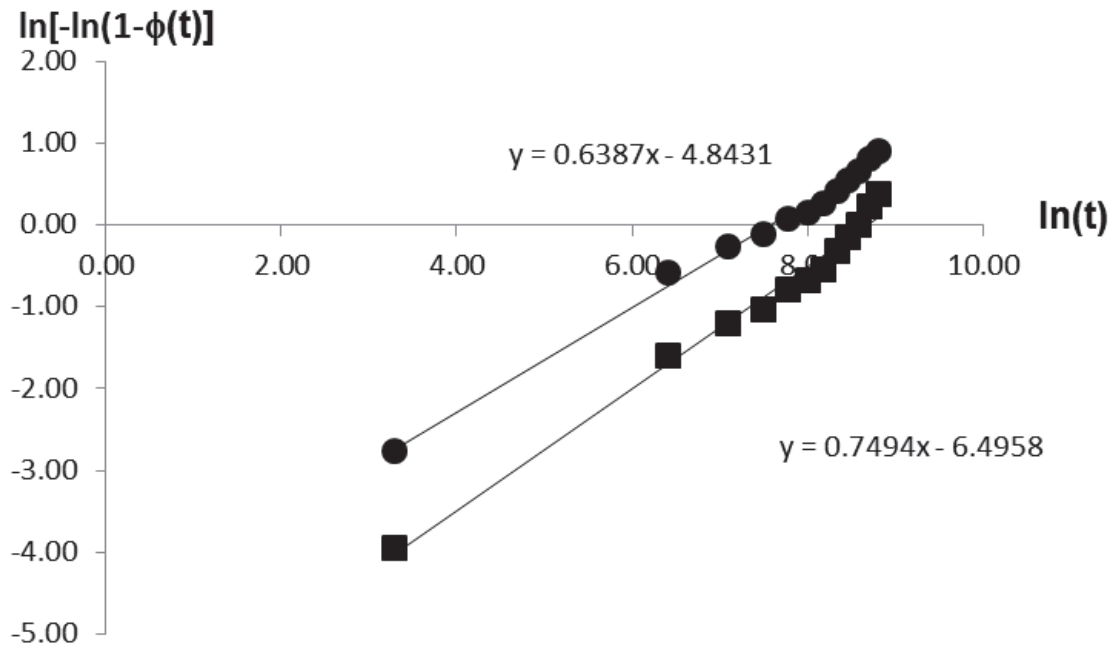
ln(t)	Parallel		Series	
	$\phi(t)$	$\ln[-\ln(1-\phi(t))]$	$\phi(t)$	$\ln[-\ln(1-\phi(t))]$
3.30	0.01	-5.13	0.01	-4.51
6.49	0.26	-1.19	0.40	-0.67
7.20	0.38	-0.74	0.53	-0.27
7.59	0.45	-0.52	0.60	-0.07
7.86	0.51	-0.35	0.66	0.07
8.08	0.54	-0.25	0.69	0.15
8.26	0.59	-0.13	0.73	0.26
8.41	0.61	-0.07	0.74	0.31
8.54	0.64	0.03	0.77	0.39
8.65	0.67	0.10	0.79	0.45
8.76	0.68	0.12	0.80	0.47
8.85	0.72	0.23	0.83	0.56
8.94	0.73	0.28	0.84	0.60
9.02	0.76	0.35	0.85	0.65
9.09	0.78	0.41	0.87	0.71
9.16	0.80	0.47	0.88	0.76
9.22	0.81	0.52	0.89	0.80
9.28	0.82	0.54	0.90	0.82
9.34	0.83	0.56	0.90	0.83
9.39	0.85	0.65	0.92	0.91
9.44	0.87	0.71	0.93	0.95
9.49	0.89	0.78	0.94	1.01
9.54	0.91	0.87	0.95	1.09
9.58	0.93	0.96	0.96	1.16
9.63	0.94	1.01	0.96	1.20
9.67	0.93	0.98	0.96	1.18
9.71	0.95	1.09	0.97	1.27
9.74	0.98	1.37	0.99	1.51
9.78	0.98	1.41	0.99	1.55
9.81	1.00	1.79	1.00	1.89
9.85	1.00	2.00	1.00	2.08



$n_{\text{Parallel}}$	0.59
$Z_{\text{Parallel}, S^{-n}}$	6.8E-3
$n_{\text{Series}}$	0.51
$Z_{\text{Series}, S^{-n}}$	1.9E-2

45 wt% - Trial 3

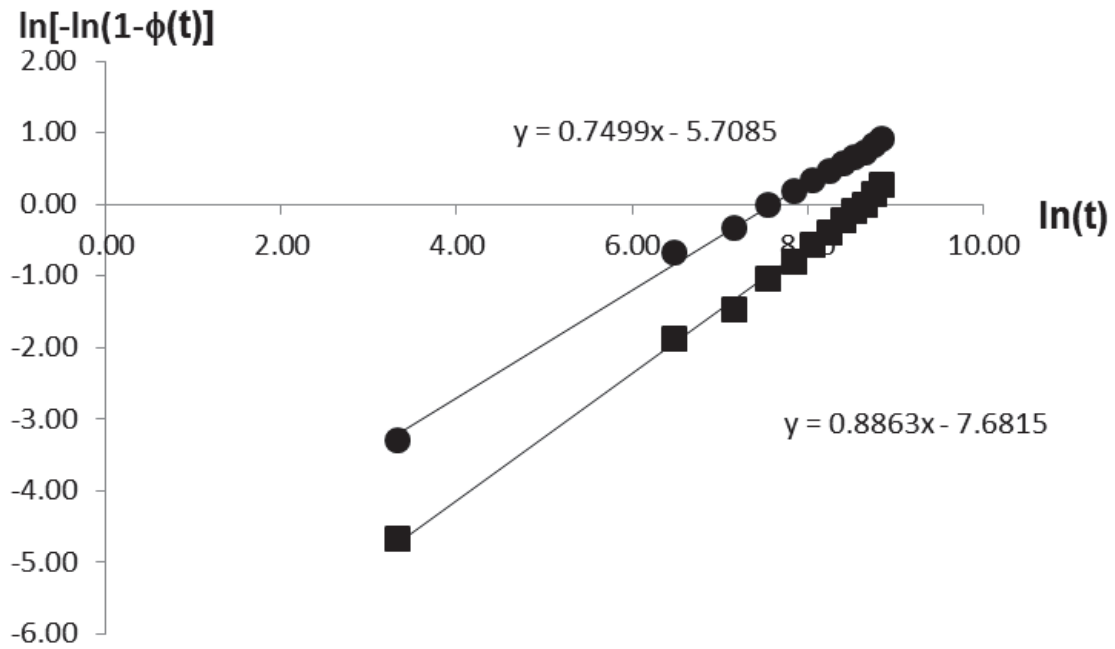
ln(t)	Parallel		Series	
	$\phi(t)$	$\ln[-\ln(1-\phi(t))]$	$\phi(t)$	$\ln[-\ln(1-\phi(t))]$
3.30	0.02	-3.96	0.06	-2.77
6.41	0.18	-1.60	0.43	-0.58
7.10	0.26	-1.21	0.54	-0.26
7.49	0.30	-1.03	0.59	-0.12
7.77	0.37	-0.79	0.66	0.07
8.00	0.40	-0.68	0.69	0.15
8.18	0.44	-0.54	0.73	0.26
8.33	0.52	-0.32	0.78	0.42
8.46	0.58	-0.15	0.82	0.54
8.59	0.63	0.00	0.85	0.65
8.70	0.72	0.23	0.89	0.81
8.81	0.77	0.37	0.92	0.91
8.90	0.80	0.48	0.93	0.98
8.98	0.85	0.63	0.95	1.09
9.05	0.88	0.76	0.96	1.18
9.12	0.89	0.78	0.96	1.20
9.19	0.91	0.78	0.97	1.20
9.25	0.94	0.78	0.98	1.20
9.31	0.94	0.78	0.98	1.20
9.37	0.97	0.78	0.99	1.20
9.42	0.96	0.78	0.99	1.20
9.47	0.98	0.78	0.99	1.20
9.52	0.99	0.78	1.00	1.20



$n_{\text{Parallel}}$	0.64
$Z_{\text{Parallel}}, S^{-n}$	$1.5E-3$
$n_{\text{Series}}$	0.75
$Z_{\text{Series}}, S^{-n}$	$7.8E-3$

45 wt% - Trial 4

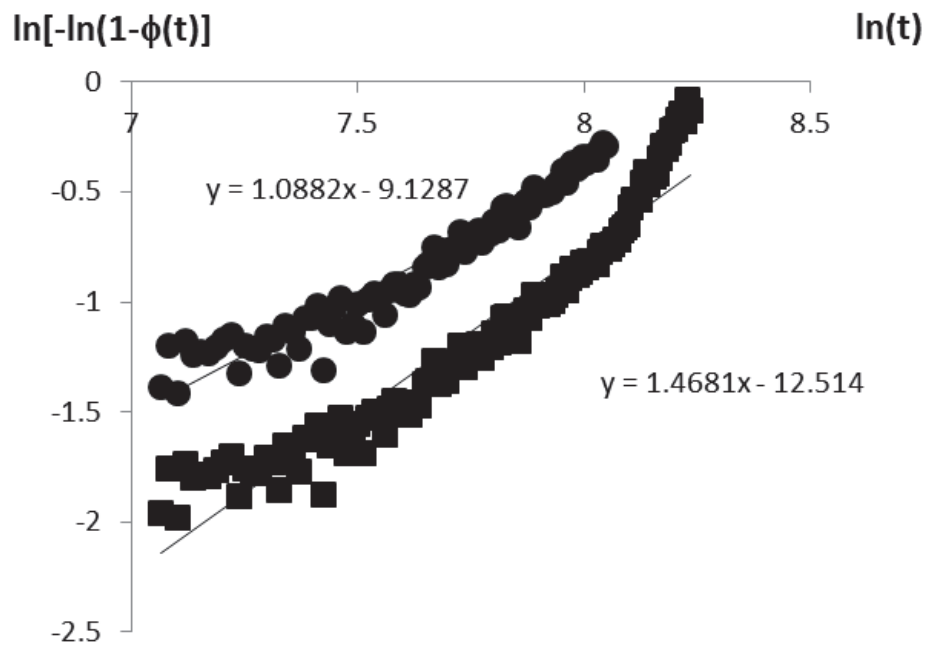
ln(t)	Parallel		Series	
	$\phi(t)$	$\ln[-\ln(1-\phi(t))]$	$\phi(t)$	$\ln[-\ln(1-\phi(t))]$
3.33	0.01	-4.68	0.04	-3.29
6.49	0.14	-1.88	0.40	-0.67
7.16	0.20	-1.48	0.51	-0.34
7.56	0.30	-1.05	0.63	0.00
7.84	0.36	-0.80	0.70	0.18
8.06	0.43	-0.57	0.75	0.34
8.24	0.49	-0.40	0.80	0.46
8.40	0.55	-0.22	0.83	0.58
8.53	0.60	-0.09	0.86	0.67
8.66	0.63	0.00	0.87	0.73
8.76	0.68	0.14	0.90	0.82
8.85	0.73	0.27	0.92	0.91
8.94	0.77	0.39	0.93	0.99
9.02	0.80	0.49	0.94	1.06
9.09	0.84	0.60	0.95	1.13
9.16	0.86	0.69	0.96	1.19
9.22	0.89	0.81	0.97	1.27
9.28	0.90	0.85	0.97	1.30
9.34	0.92	0.93	0.98	1.35
9.39	0.92	0.94	0.98	1.36
9.45	0.95	1.11	0.99	1.48
9.49	0.95	1.13	0.99	1.49
9.54	0.96	1.18	0.99	1.53
9.58	0.98	1.32	0.99	1.64
9.63	0.98	1.42	1.00	1.71
9.67	0.99	1.61	1.00	1.86



$n_{\text{Parallel}}$	0.75
$Z_{\text{Parallel}}, S^{-n}$	4.6E-4
$n_{\text{Series}}$	0.89
$Z_{\text{Series}}, S^{-n}$	3.3E-3

42 wt% - Trial 1

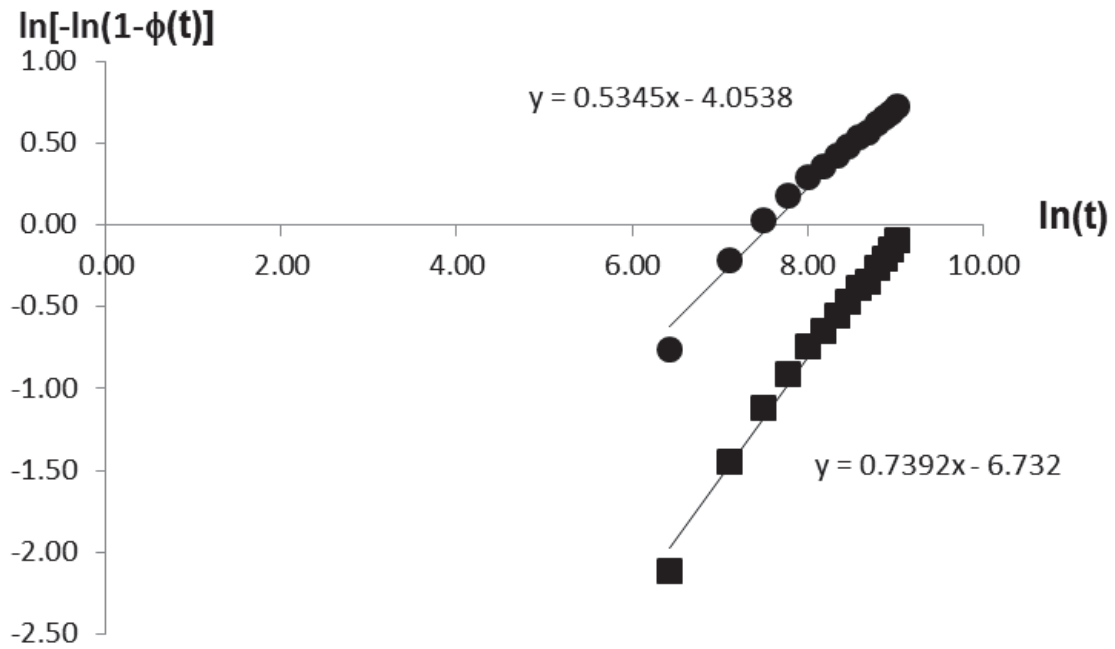
ln(t)	Parallel		Series	
	$\phi(t)$	$\ln[-\ln(1-\phi(t))]$	$\phi(t)$	$\ln[-\ln(1-\phi(t))]$
3.30	0.02	-4.02	0.03	-3.41
6.36	0.11	-2.12	0.19	-1.54
7.03	0.16	-1.74	0.26	-1.18
7.42	0.14	-1.88	0.24	-1.31
7.71	0.24	-1.28	0.37	-0.76
7.93	0.31	-1.00	0.45	-0.50
8.11	0.44	-0.53	0.60	-0.09
8.27	0.64	0.02	0.77	0.38
8.42	0.86	0.66	0.92	0.91
8.55	0.93	0.95	0.96	1.16
8.67	0.97	1.30	0.99	1.46



$n_{\text{Parallel}}$	1.47
$Z_{\text{Parallel}}, S^{-n}$	3.7E-6
$n_{\text{Series}}$	1.09
$Z_{\text{Series}}, S^{-n}$	1.1E-4

42 wt% - Trial 2

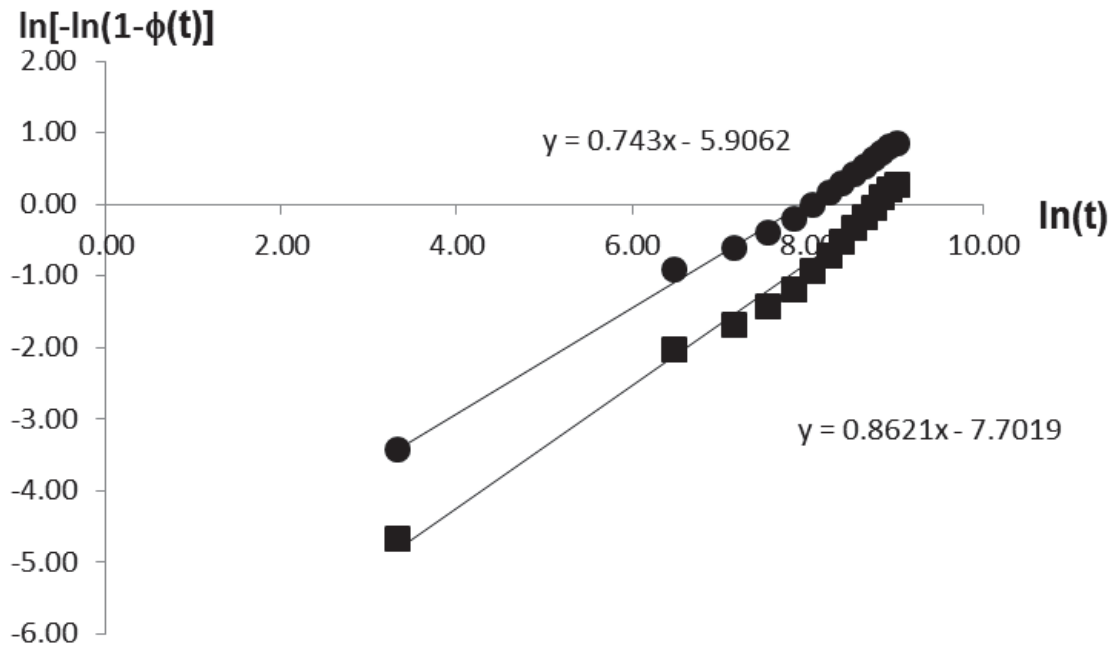
ln(t)	Parallel		Series	
	$\phi(t)$	$\ln[-\ln(1-\phi(t))]$	$\phi(t)$	$\ln[-\ln(1-\phi(t))]$
6.43	0.11	-2.11	0.37	-0.76
7.11	0.21	-1.44	0.55	-0.22
7.50	0.28	-1.12	0.64	0.03
7.78	0.33	-0.91	0.70	0.17
8.00	0.38	-0.74	0.74	0.30
8.18	0.41	-0.65	0.76	0.36
8.33	0.44	-0.55	0.78	0.42
8.47	0.46	-0.47	0.80	0.48
8.58	0.49	-0.39	0.82	0.53
8.69	0.51	-0.35	0.83	0.56
8.79	0.54	-0.26	0.84	0.62
8.87	0.56	-0.20	0.85	0.65
8.95	0.58	-0.15	0.86	0.69
9.03	0.60	-0.10	0.87	0.72
9.10	0.61	-0.07	0.88	0.74
9.16	0.64	0.01	0.89	0.79
9.22	0.67	0.09	0.90	0.85
9.27	0.67	0.10	0.90	0.85
9.33	0.69	0.17	0.91	0.90
9.38	0.70	0.18	0.91	0.90
9.43	0.72	0.24	0.92	0.94
9.48	0.74	0.28	0.93	0.97
9.52	0.75	0.32	0.93	0.99
9.57	0.77	0.39	0.94	1.03
9.61	0.78	0.43	0.94	1.06
9.66	0.81	0.52	0.95	1.12
9.70	0.83	0.56	0.96	1.14
9.74	0.84	0.59	0.96	1.16
9.78	0.87	0.70	0.97	1.23
9.81	0.87	0.70	0.97	1.24
9.84	0.88	0.75	0.97	1.27
9.88	0.90	0.82	0.98	1.31
9.91	0.90	0.85	0.98	1.33
9.94	0.91	0.87	0.98	1.35
9.97	0.92	0.94	0.98	1.39



$n_{\text{Parallel}}$	0.74
$Z_{\text{Parallel}}, S^{-n}$	1.2E-3
$n_{\text{Series}}$	0.53
$Z_{\text{Series}}, S^{-n}$	1.7E-2

## 42 wt% - Trial 3

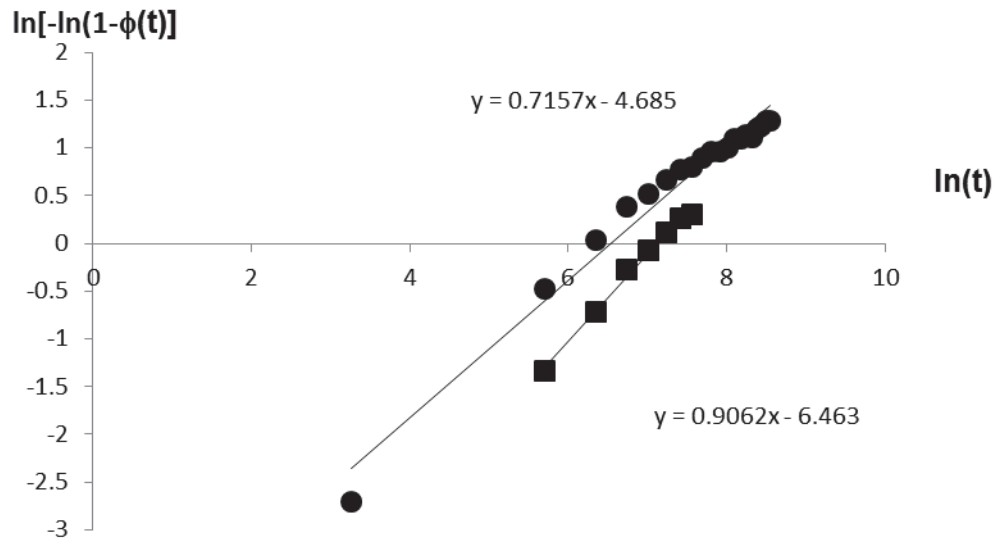
	Parallel		Series	
ln(t)	$\phi(t)$	$\ln[-\ln(1-\phi(t))]$	$\phi(t)$	$\ln[-\ln(1-\phi(t))]$
3.33	0.01	-4.67	0.03	-3.42
6.49	0.12	-2.04	0.33	-0.92
7.16	0.17	-1.68	0.42	-0.61
7.56	0.21	-1.42	0.49	-0.39
7.84	0.27	-1.18	0.56	-0.20
8.06	0.33	-0.93	0.63	-0.01
8.24	0.39	-0.72	0.69	0.16
8.40	0.45	-0.53	0.74	0.29
8.53	0.51	-0.34	0.79	0.43
8.65	0.56	-0.19	0.82	0.54
8.75	0.61	-0.06	0.85	0.63
8.85	0.67	0.09	0.87	0.73
8.93	0.70	0.20	0.89	0.81
9.01	0.73	0.28	0.91	0.86
9.09	0.77	0.39	0.92	0.94
9.15	0.80	0.49	0.94	1.01
9.22	0.83	0.59	0.95	1.07
9.28	0.87	0.73	0.96	1.17
9.34	0.89	0.81	0.97	1.23
9.39	0.92	0.91	0.97	1.31
9.44	0.93	0.98	0.98	1.35
9.49	0.94	1.03	0.98	1.39
9.54	0.97	1.26	0.99	1.56
9.59	0.96	1.19	0.99	1.51
9.63	0.99	1.48	1.00	1.73



$n_{\text{Parallel}}$	0.86
$Z_{\text{Parallel}}, S^{-n}$	4.5E-4
$n_{\text{Series}}$	0.74
$Z_{\text{Series}}, S^{-n}$	2.7E-3

40 wt% - Trial 1

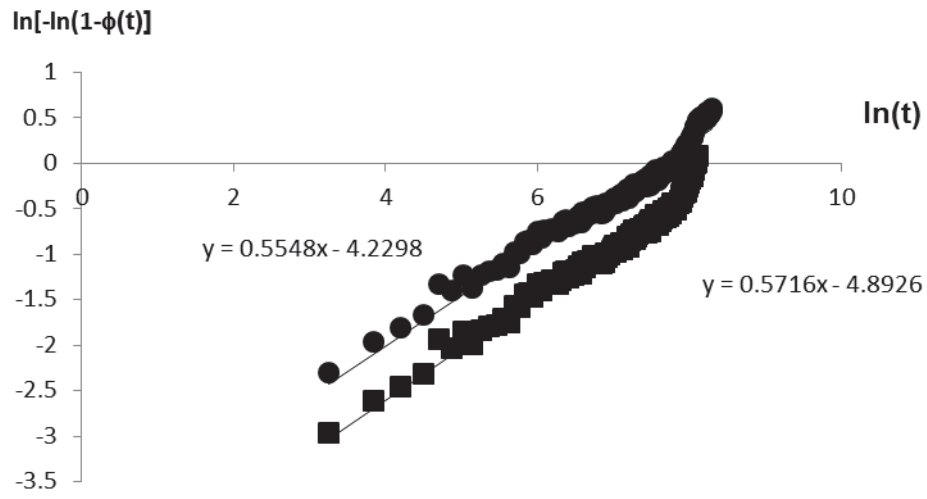
	Parallel		Series	
ln(t)	$\phi(t)$	$\ln[-\ln(1-\phi(t))]$	$\phi(t)$	$\ln[-\ln(1-\phi(t))]$
3.2581	0.0232	-3.7533019	0.0643	-2.7116759
5.7004	0.2301	-1.3412717	0.464	-0.472315
6.3456	0.385	-0.7214333	0.6444	0.03350059
6.7382	0.5329	-0.2728581	0.7676	0.37808007
7.0166	0.6039	-0.0768965	0.8153	0.52416339
7.2349	0.6723	0.1094052	0.8559	0.66134632
7.4146	0.7284	0.26511368	0.8859	0.77523742
7.5663	0.7433	0.30743524	0.8935	0.8061363
7.6976	0.7865	0.43438455	0.9143	0.89882506
7.8148	0.8143	0.52092973	0.927	0.96212193
7.9186	0.8156	0.52523152	0.9276	0.96527237
8.013	0.8333	0.58319864	0.9354	1.00777631
8.0999	0.8655	0.696143	0.9491	1.09094533
8.1789	0.8678	0.70463914	0.95	1.09722483
8.2524	0.8833	0.76446902	0.9564	1.14155413
8.3212	0.8736	0.72659475	0.9524	1.11346948
8.3853	0.9032	0.84807838	0.9643	1.2038632
8.4453	0.9119	0.88780001	0.9677	1.23363283
8.5025	0.9239	0.94633659	0.9724	1.27772254
8.556	0.9258	0.95592336	0.9731	1.28496964
8.607	0.8921	0.80064399	0.9599	1.16845782
8.6559	0.9063	0.86173327	0.9655	1.21408403
8.702	0.9032	0.84793396	0.9643	1.20375518
8.7462	0.9368	1.01574449	0.9772	1.33036949
8.7887	0.9296	0.9757763	0.9745	1.30000205
8.8294	0.9442	1.05965932	0.98	1.36390301
8.8683	0.9438	1.05761986	0.9799	1.36234166
8.9061	0.9143	0.89905439	0.9687	1.24208877
8.9422	0.9397	1.03266995	0.9783	1.34327257
8.9773	0.9514	1.10652702	0.9827	1.39989491
9.0113	0.9326	0.99209833	0.9756	1.31238632
9.0438	0.9606	1.17366294	0.986	1.45183826



$n_{\text{Parallel}}$	0.91
$Z_{\text{Parallel}, S^{-n}}$	1.6E-3
$n_{\text{Series}}$	0.72
$Z_{\text{Series}, S^{-n}}$	9.2E-3

40 wt% - Trial 2

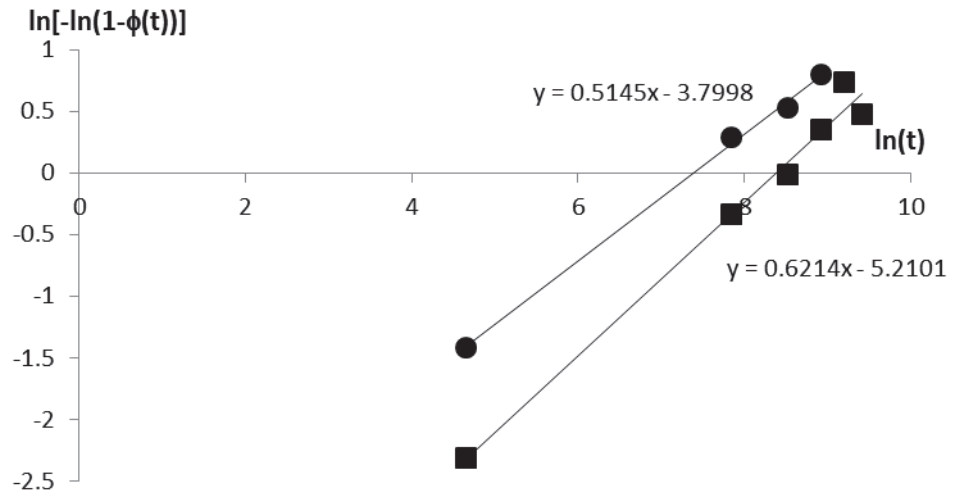
	Parallel		Series	
ln(t)	$\phi(t)$	$\ln[-\ln(1-\phi(t))]$	$\phi(t)$	$\ln[-\ln(1-\phi(t))]$
3.2581	0.0504	-2.9621833	0.095	-2.3042744
5.6971	0.1875	-1.5718319	0.3135	-0.9778709
6.3456	0.2605	-1.1978876	0.4107	-0.6369763
6.737	0.3015	-1.0250907	0.4606	-0.4825145
7.0166	0.3312	-0.9106784	0.4949	-0.3813663
7.2349	0.3668	-0.7832349	0.534	-0.2697669
7.4146	0.3945	-0.6897213	0.5631	-0.1885952
7.5663	0.4332	-0.5659241	0.602	-0.0820559
7.6976	0.4254	-0.5905945	0.5942	-0.1032048
7.8148	0.4543	-0.5013404	0.6222	-0.0268817
7.9186	0.5001	-0.3661701	0.6644	0.08772995
8.013	0.5669	-0.1780765	0.7214	0.24541187
8.1017	0.6453	0.03584997	0.7826	0.42259016
8.1856	0.6882	0.15300658	0.8137	0.5188709
8.2726	0.6939	0.16885567	0.8177	0.53186471
8.3528	0.7344	0.28205298	0.8455	0.62450646
8.427	0.8111	0.51089256	0.8947	0.81137684
8.4962	0.8182	0.5334229	0.899	0.82978085
8.5606	0.8555	0.65998232	0.9214	0.93331034
8.6214	0.8979	0.8250884	0.9457	1.06903293
8.6785	0.9562	1.14030933	0.9774	1.33186561
8.7326	0.9505	1.10074653	0.9744	1.29853269



$n_{\text{Parallel}}$	0.57
$Z_{\text{Parallel}}, S^{-n}$	$7.5E-3$
$n_{\text{Series}}$	0.55
$Z_{\text{Series}}, S^{-n}$	$1.4E-2$

40 wt% - 0.1 rad/s - Trial 3

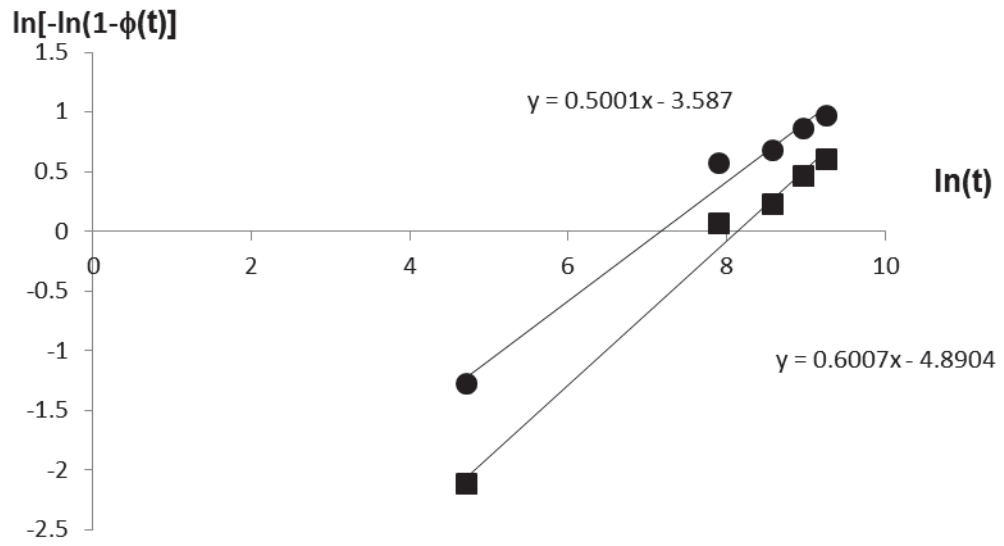
<b>ln(t)</b>	<b>Parallel</b>		<b>Series</b>	
	<b><math>\phi(t)</math></b>	<b><math>\ln[-\ln(1-\phi(t))]</math></b>	<b><math>\phi(t)</math></b>	<b><math>\ln[-\ln(1-\phi(t))]</math></b>
4.66	0.09	-2.31	0.22	-1.41
7.85	0.51	-0.33	0.74	0.29
8.52	0.63	-0.01	0.82	0.53
8.92	0.76	0.35	0.89	0.80
9.20	0.88	0.74	0.95	1.10
9.42	0.80	0.48	0.92	0.90
9.60	0.95	1.11	0.98	1.38



$n_{\text{Parallel}}$	0.62
$Z_{\text{Parallel}, S^{-n}}$	5.6E-3
$n_{\text{Series}}$	0.51
$Z_{\text{Series}, S^{-n}}$	2.2E-2

40 wt% - 0.1 rad/s - Trial 1

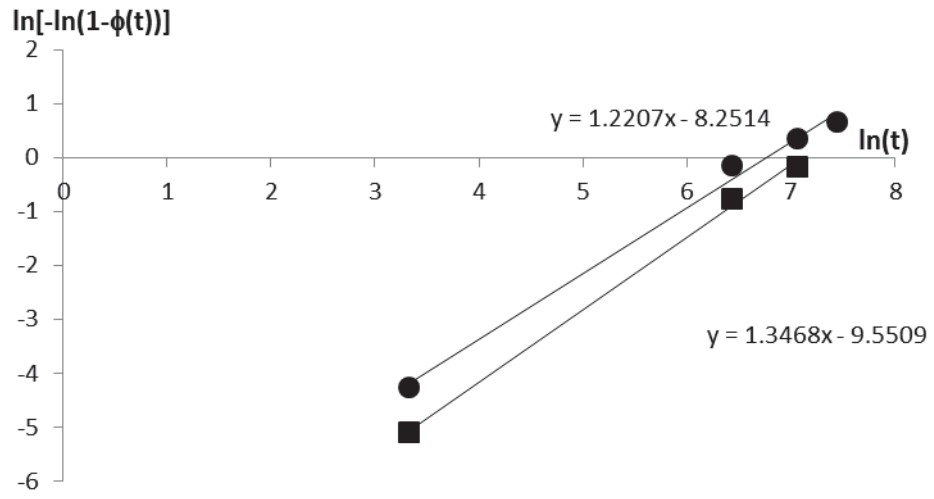
ln(t)	Parallel		Series	
	$\phi(t)$	$\ln[-\ln(1-\phi(t))]$	$\phi(t)$	$\ln[-\ln(1-\phi(t))]$
4.72	0.11	-2.11	0.24	-1.28
7.91	0.66	0.07	0.83	0.57
8.58	0.71	0.23	0.86	0.68
8.98	0.79	0.46	0.91	0.86
9.27	0.84	0.60	0.93	0.97



$n_{\text{Parallel}}$	0.6
$Z_{\text{Parallel}}, S^{-n}$	7.5E-3
$n_{\text{Series}}$	0.5
$Z_{\text{Series}}, S^{-n}$	2.8E-2

37 wt% - Trial 1

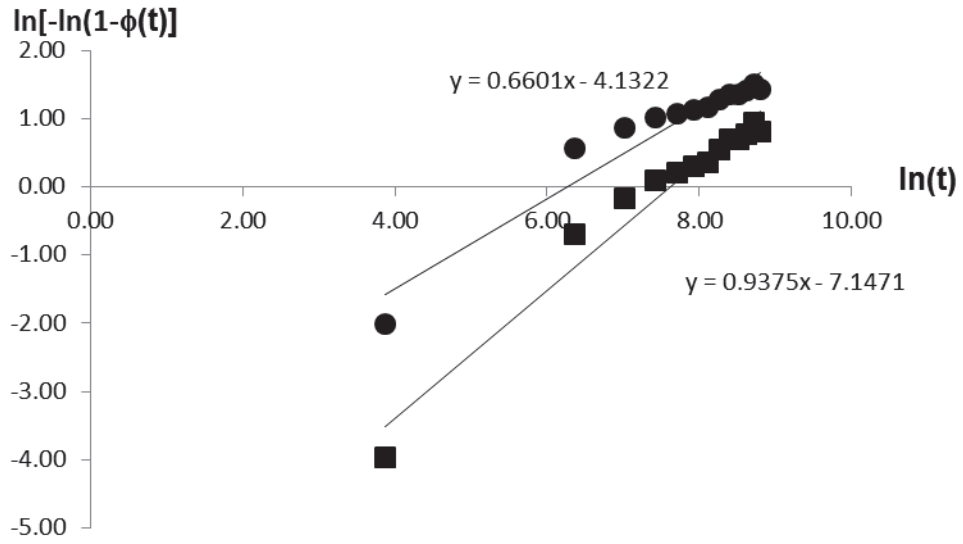
ln(t)	Parallel		Series	
	$\phi(t)$	$\ln[-\ln(1-\phi(t))]$	$\phi(t)$	$\ln[-\ln(1-\phi(t))]$
3.33	0.01	-5.09	0.01	-4.25
6.43	0.38	-0.75	0.58	-0.14
7.06	0.57	-0.16	0.76	0.35
7.45	0.72	0.24	0.86	0.66
7.73	0.82	0.55	0.91	0.90
7.94	0.90	0.83	0.95	1.12
8.12	0.96	1.16	0.98	1.39
8.27	0.99	1.55	1.00	1.71
8.40	0.99	1.60	1.00	1.76



$n_{\text{Parallel}}$	1.3
$Z_{\text{Parallel}, S^{-n}}$	7.1E-5
$n_{\text{Series}}$	1.2
$Z_{\text{Series}, S^{-n}}$	2.6E-4

37 wt% - Trial 2

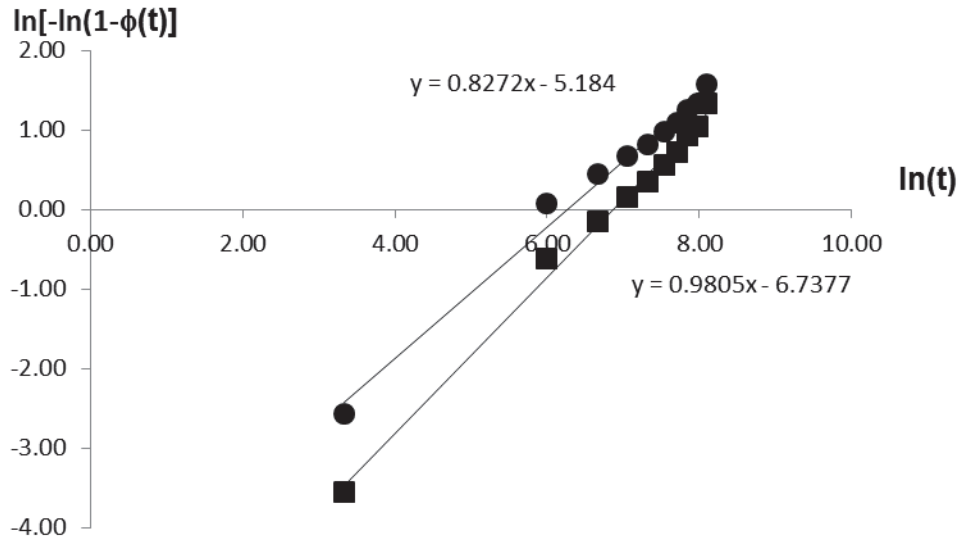
ln(t)	Parallel		Series	
	$\phi(t)$	$\ln[-\ln(1-\phi(t))]$	$\phi(t)$	$\ln[-\ln(1-\phi(t))]$
3.87	0.02	-3.97	0.12	-2.02
6.36	0.39	-0.70	0.83	0.56
7.03	0.57	-0.18	0.91	0.86
7.42	0.66	0.09	0.94	1.01
7.71	0.71	0.21	0.95	1.08
7.93	0.74	0.30	0.96	1.13
8.11	0.76	0.35	0.96	1.16
8.26	0.82	0.55	0.97	1.27
8.40	0.87	0.70	0.98	1.36
8.51	0.87	0.70	0.98	1.36
8.62	0.89	0.77	0.98	1.40
8.71	0.92	0.95	0.99	1.51
8.80	0.89	0.81	0.98	1.42
8.88	0.91	0.90	0.99	1.48
8.95	0.94	1.06	0.99	1.57
9.02	0.94	1.03	0.99	1.56
9.09	0.95	1.12	0.99	1.61
9.15	0.95	1.13	0.99	1.62
9.20	0.95	1.07	0.99	1.58
9.26	0.94	1.02	0.99	1.55
9.31	0.94	1.05	0.99	1.57
9.36	0.96	1.13	0.99	1.62
9.40	0.95	1.11	0.99	1.61
9.45	0.95	1.08	0.99	1.59
9.49	0.95	1.12	0.99	1.61
9.53	0.95	1.09	0.99	1.59
9.57	0.96	1.18	0.99	1.66



$n_{\text{Parallel}}$	0.94
$Z_{\text{Parallel}}, S^{-n}$	$7.8E-4$
$n_{\text{Series}}$	0.66
$Z_{\text{Series}}, S^{-n}$	$1.6E-2$

37 wt% -Trial 3

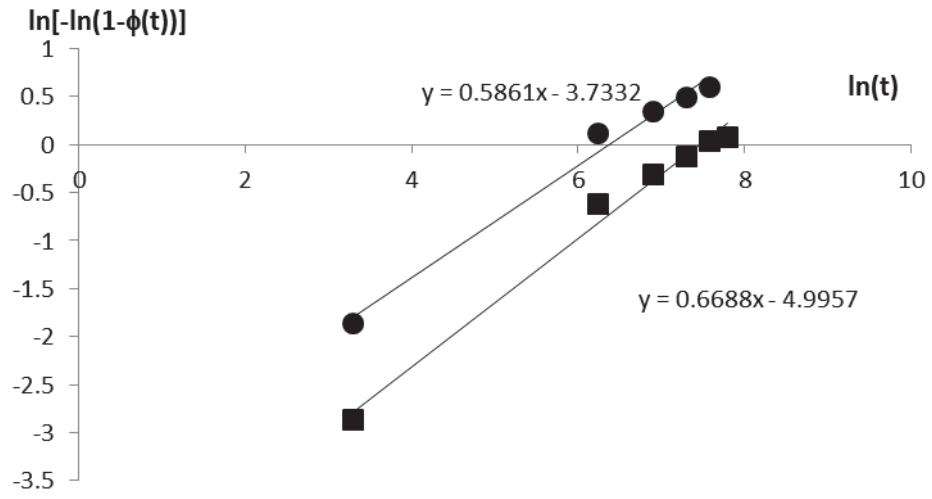
ln(t)	Parallel		Series	
	$\phi(t)$	$\ln[-\ln(1-\phi(t))]$	$\phi(t)$	$\ln[-\ln(1-\phi(t))]$
3.33	0.03	-3.56	0.07	-2.57
6.00	0.42	-0.61	0.66	0.08
6.66	0.58	-0.15	0.79	0.44
7.05	0.69	0.16	0.86	0.67
7.32	0.76	0.36	0.90	0.82
7.54	0.83	0.57	0.93	0.98
7.71	0.87	0.73	0.95	1.10
7.84	0.92	0.92	0.97	1.24
7.97	0.94	1.05	0.98	1.34
8.10	0.98	1.34	0.99	1.57



$n_{\text{Parallel}}$	0.98
$Z_{\text{Parallel}}, S^{-n}$	<b>1.1E-3</b>
$n_{\text{Series}}$	0.83
$Z_{\text{Series}}, S^{-n}$	5.6E-3

35 wt% -Trial 1

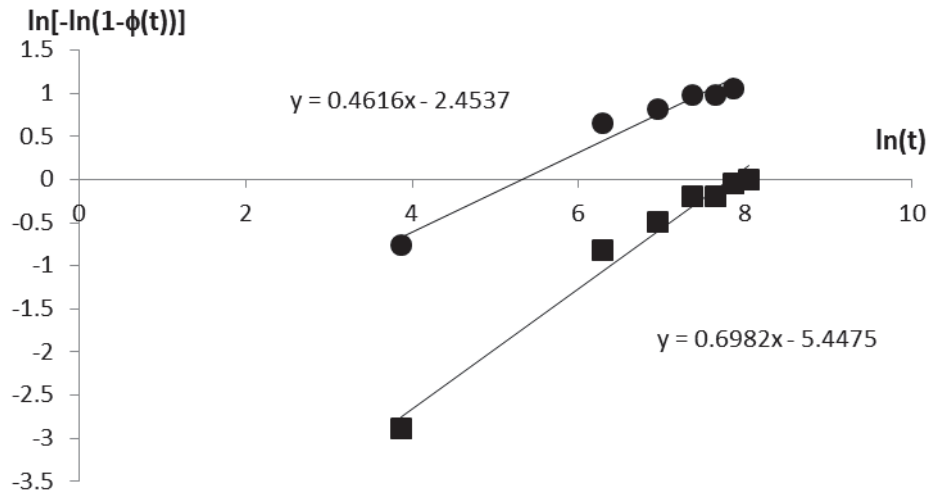
ln(t)	Parallel		Series	
	$\phi(t)$	$\ln[-\ln(1-\phi(t))]$	$\phi(t)$	$\ln[-\ln(1-\phi(t))]$
3.30	0.06	-2.87	0.14	-1.86
6.24	0.42	-0.62	0.67	0.11
6.90	0.52	-0.31	0.76	0.35
7.30	0.59	-0.12	0.80	0.49
7.58	0.64	0.03	0.84	0.60
7.80	0.66	0.08	0.85	0.64
7.98	0.69	0.17	0.87	0.70
8.14	0.70	0.18	0.87	0.71
8.27	0.73	0.27	0.89	0.78
8.39	0.76	0.34	0.90	0.83
8.49	0.75	0.31	0.89	0.81
8.58	0.77	0.39	0.91	0.87
8.67	0.76	0.34	0.90	0.83
8.75	0.80	0.47	0.92	0.93
8.82	0.79	0.45	0.92	0.91
8.89	0.80	0.49	0.92	0.94
8.96	0.81	0.52	0.93	0.96
9.02	0.83	0.59	0.94	1.01
9.08	0.82	0.55	0.93	0.98
9.13	0.80	0.49	0.92	0.94
9.18	0.84	0.59	0.94	1.01
9.23	0.82	0.55	0.93	0.98
9.28	0.83	0.57	0.93	1.00
9.32	0.83	0.57	0.93	1.00
9.36	0.85	0.64	0.94	1.05
9.40	0.85	0.65	0.94	1.06
9.44	0.83	0.58	0.93	1.00
9.48	0.84	0.59	0.94	1.01
9.52	0.85	0.63	0.94	1.04
9.55	0.85	0.66	0.94	1.06
9.59	0.87	0.71	0.95	1.10
9.62	0.88	0.77	0.96	1.14
9.65	0.87	0.70	0.95	1.09
9.68	0.90	0.82	0.96	1.18
9.71	0.94	1.03	0.98	1.34
9.74	0.96	1.15	0.98	1.43



$n_{\text{Parallel}}$	0.59
$Z_{\text{Parallel}, S^{-n}}$	6.8E-4
$n_{\text{Series}}$	0.67
$Z_{\text{Series}, S^{-n}}$	2.4E-2

35 wt% - Trial 2

	Parallel		Series	
ln(t)	$\phi(t)$	$\ln[-\ln(1-\phi(t))]$	$\phi(t)$	$\ln[-\ln(1-\phi(t))]$
3.87	0.05	-2.88	0.37	-0.76
6.29	0.36	-0.82	0.85	0.65
6.95	0.46	-0.49	0.90	0.82
7.36	0.56	-0.19	0.93	0.98
7.64	0.56	-0.19	0.93	0.98
7.86	0.62	-0.04	0.94	1.06
8.04	0.63	0.00	0.95	1.08
8.19	0.67	0.10	0.95	1.13
8.32	0.67	0.09	0.95	1.12
8.44	0.71	0.22	0.96	1.19
8.54	0.72	0.24	0.96	1.20
8.64	0.71	0.22	0.96	1.19
8.73	0.75	0.34	0.97	1.25
8.81	0.77	0.37	0.97	1.27
8.88	0.77	0.40	0.97	1.28
8.95	0.79	0.44	0.97	1.30
9.01	0.81	0.51	0.98	1.34
9.08	0.84	0.60	0.98	1.39
9.14	0.84	0.60	0.98	1.38
9.19	0.86	0.67	0.98	1.42
9.24	0.87	0.72	0.99	1.45
9.29	0.91	0.88	0.99	1.54
9.34	0.92	0.95	0.99	1.58
9.38	0.92	0.94	0.99	1.58
9.42	0.93	1.00	0.99	1.61
9.46	0.95	1.10	0.99	1.67
9.50	0.93	1.00	0.99	1.61
9.54	0.96	1.17	1.00	1.71
9.58	0.95	1.12	1.00	1.68

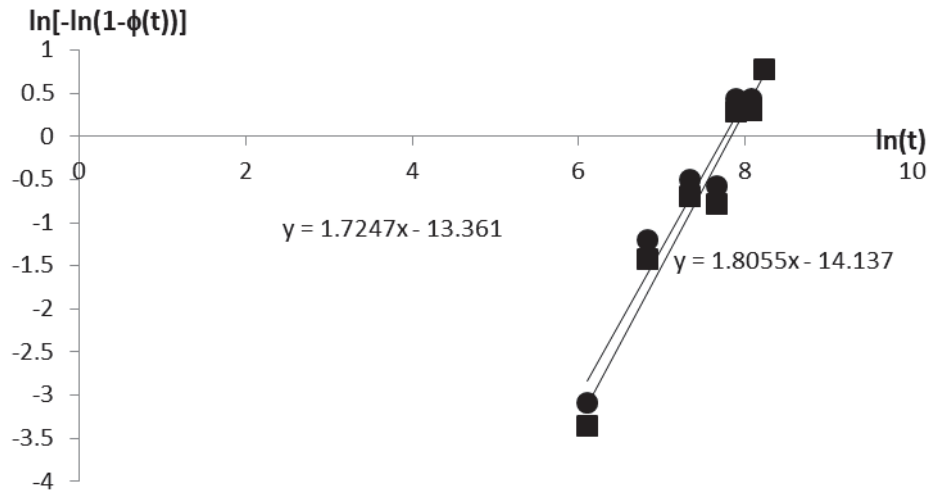


$n_{\text{Parallel}}$	0.7
$Z_{\text{Parallel}}, S^{-n}$	4.3E-3
$n_{\text{Series}}$	0.46
$Z_{\text{Series}}, S^{-n}$	8.6E-2

32 wt% - Trial 1

Time is shifted such that  $t = 0$  corresponds to the start of the growth period

<b>ln(t)</b>	<b>Parallel</b>		<b>Series</b>	
	<b><math>\phi(t)</math></b>	<b><math>\ln[-\ln(1-\phi(t))]</math></b>	<b><math>\phi(t)</math></b>	<b><math>\ln[-\ln(1-\phi(t))]</math></b>
6.10	0.03	-3.35	0.04	-3.09
6.83	0.21	-1.43	0.26	-1.20
7.33	0.39	-0.70	0.45	-0.50
7.65	0.37	-0.78	0.43	-0.58
7.89	0.74	0.29	0.79	0.43
8.07	0.74	0.30	0.79	0.44
8.23	0.89	0.78	0.91	0.89

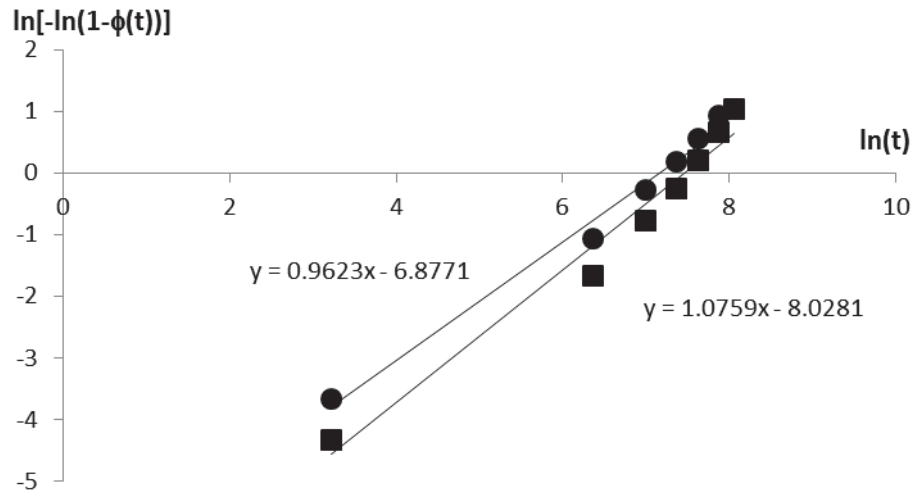


$n_{\text{Parallel}}$	1.8
$Z_{\text{Parallel}, S^{-n}}$	7.25E-07
$n_{\text{Series}}$	1.7
$Z_{\text{Series}, S^{-n}}$	1.57E-06

32 wt% - Trial 2

Time is shifted such that  $t = 0$  corresponds to the start of the growth period

<b>ln(t)</b>	<b>Parallel</b>		<b>Series</b>	
	<b><math>\phi(t)</math></b>	<b><math>\ln[-\ln(1-\phi(t))]</math></b>	<b><math>\phi(t)</math></b>	<b><math>\ln[-\ln(1-\phi(t))]</math></b>
3.22	0.01	-4.33	0.03	-3.66
6.36	0.17	-1.66	0.29	-1.06
7.00	0.37	-0.76	0.54	-0.26
7.36	0.54	-0.25	0.70	0.18
7.63	0.71	0.21	0.83	0.56
7.87	0.86	0.66	0.92	0.93
8.06	0.94	1.04	0.97	1.24

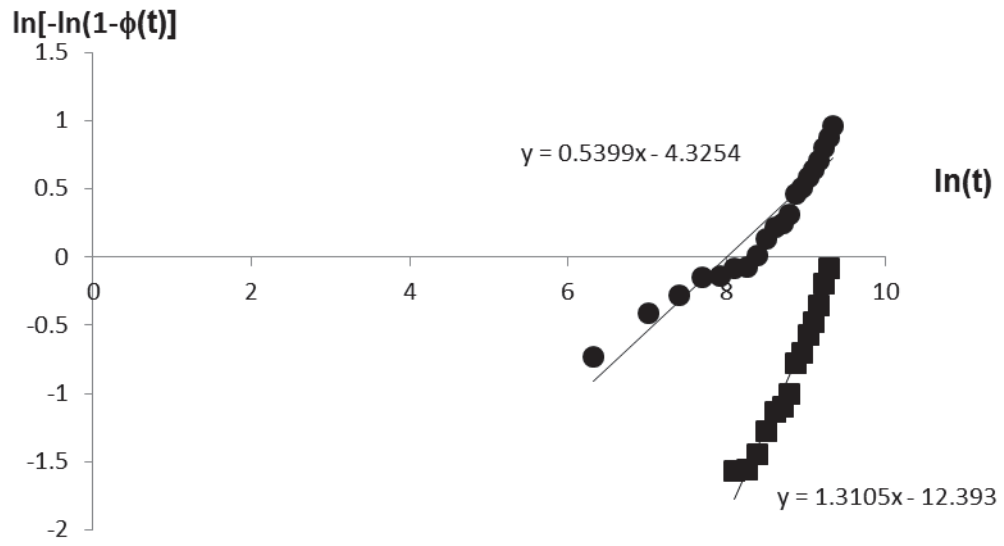


$n_{\text{Parallel}}$	1.08
$Z_{\text{Parallel}}, S^{-n}$	3.2E-4
$n_{\text{Series}}$	0.96
$Z_{\text{Series}}, S^{-n}$	1.0E-3

## C.2. Iso-concentration SIS copolymer in toluene Avrami fits from DMR data

37 wt%

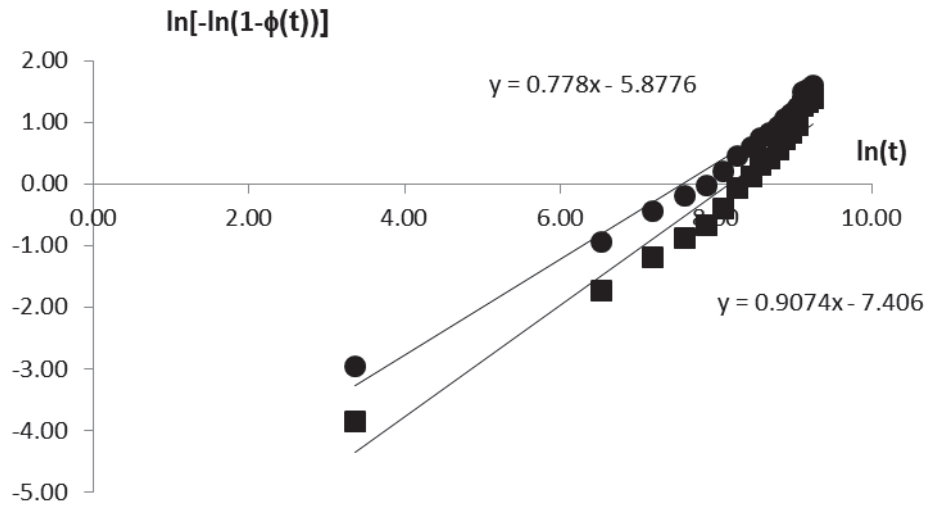
ln(t)	Parallel		Series	
	$\phi(t)$	$\ln[-\ln(1-\phi(t))]$	$\phi(t)$	$\ln[-\ln(1-\phi(t))]$
6.32	0.09	-2.41	0.38	-0.73
7.01	0.12	-2.01	0.48	-0.41
7.41	0.15	-1.85	0.53	-0.28
7.70	0.17	-1.67	0.58	-0.15
7.92	0.17	-1.65	0.58	-0.14
8.10	0.19	-1.57	0.60	-0.08
8.26	0.19	-1.56	0.61	-0.07
8.39	0.21	-1.45	0.64	0.01
8.51	0.24	-1.28	0.68	0.13
8.61	0.27	-1.14	0.71	0.22
8.71	0.28	-1.10	0.72	0.25
8.79	0.31	-1.00	0.75	0.31
8.88	0.37	-0.78	0.79	0.46
8.96	0.39	-0.70	0.81	0.51
9.03	0.43	-0.57	0.83	0.58
9.10	0.46	-0.48	0.85	0.64
9.17	0.50	-0.36	0.87	0.71
9.23	0.56	-0.20	0.89	0.80
9.29	0.60	-0.08	0.91	0.88
9.35	0.66	0.06	0.93	0.96
9.40	0.71	0.22	0.94	1.05
9.45	0.76	0.35	0.95	1.12
9.50	0.80	0.48	0.96	1.20
9.55	0.84	0.61	0.97	1.28
9.59	0.88	0.77	0.98	1.37
9.63	0.91	0.87	0.98	1.43
9.67	0.94	1.02	0.99	1.53
9.71	0.95	1.12	0.99	1.59
9.75	0.97	1.28	1.00	1.70
9.79	0.99	1.47	1.00	1.83
9.82	0.98	1.43	1.00	1.80
9.85	0.99	1.66	1.00	1.97



$n_{\text{Parallel}}$	1.31
$Z_{\text{Parallel}, S^{-n}}$	4.15E-6
$n_{\text{Series}}$	0.54
$Z_{\text{Series}, S^{-n}}$	1.3E-2

45wt%

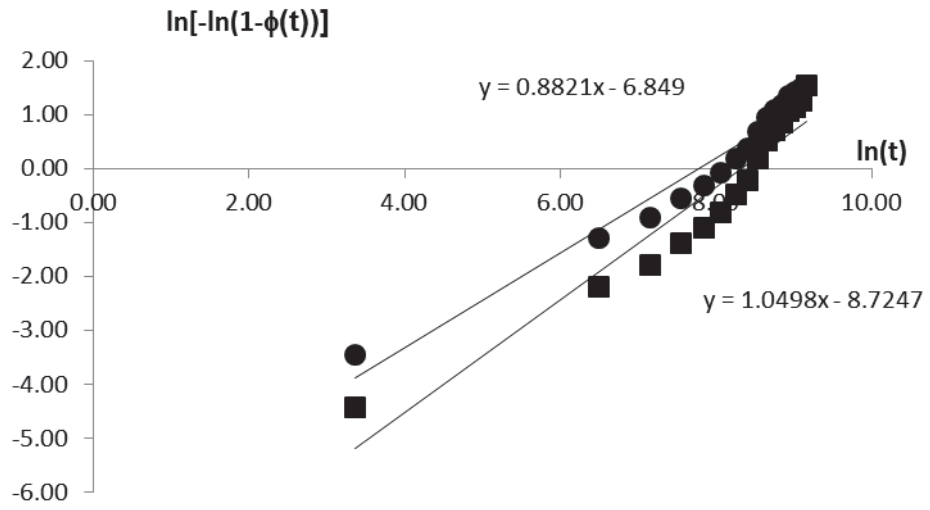
ln(t)	Parallel		Series	
	$\phi(t)$	$\ln[-\ln(1-\phi(t))]$	$\phi(t)$	$\ln[-\ln(1-\phi(t))]$
3.37	0.02	-3.84	0.05	-2.95
6.53	0.16	-1.73	0.32	-0.93
7.19	0.27	-1.17	0.47	-0.44
7.60	0.34	-0.88	0.56	-0.20
7.88	0.40	-0.67	0.63	-0.02
8.10	0.49	-0.39	0.71	0.21
8.28	0.61	-0.06	0.79	0.46
8.45	0.68	0.13	0.84	0.61
8.58	0.74	0.31	0.88	0.75
8.69	0.78	0.42	0.90	0.83
8.80	0.83	0.57	0.92	0.94
8.89	0.87	0.73	0.95	1.07
8.97	0.90	0.84	0.96	1.15
9.05	0.93	0.96	0.97	1.25
9.12	0.97	1.28	0.99	1.50
9.18	0.98	1.33	0.99	1.54
9.25	0.98	1.40	0.99	1.60



$n_{\text{Parallel}}$	0.91
$Z_{\text{Parallel}}, S^{-n}$	$6.1E-4$
$n_{\text{Series}}$	0.78
$Z_{\text{Series}}, S^{-n}$	$2.8E-3$

50 wt%

ln(t)	Parallel		Series	
	$\phi(t)$	$\ln[-\ln(1-\phi(t))]$	$\phi(t)$	$\ln[-\ln(1-\phi(t))]$
3.37	0.01	-4.43	0.03	-3.44
6.49	0.11	-2.19	0.24	-1.27
7.16	0.16	-1.78	0.33	-0.90
7.56	0.22	-1.38	0.44	-0.55
7.84	0.28	-1.09	0.52	-0.31
8.06	0.36	-0.81	0.60	-0.08
8.25	0.46	-0.48	0.70	0.18
8.40	0.55	-0.22	0.77	0.38
8.54	0.70	0.18	0.86	0.69
8.65	0.82	0.53	0.92	0.95
8.76	0.87	0.71	0.95	1.09
8.85	0.90	0.85	0.96	1.19
8.94	0.94	1.06	0.98	1.35
9.02	0.96	1.15	0.98	1.42
9.09	0.97	1.26	0.99	1.51
9.16	0.99	1.54	1.00	1.73

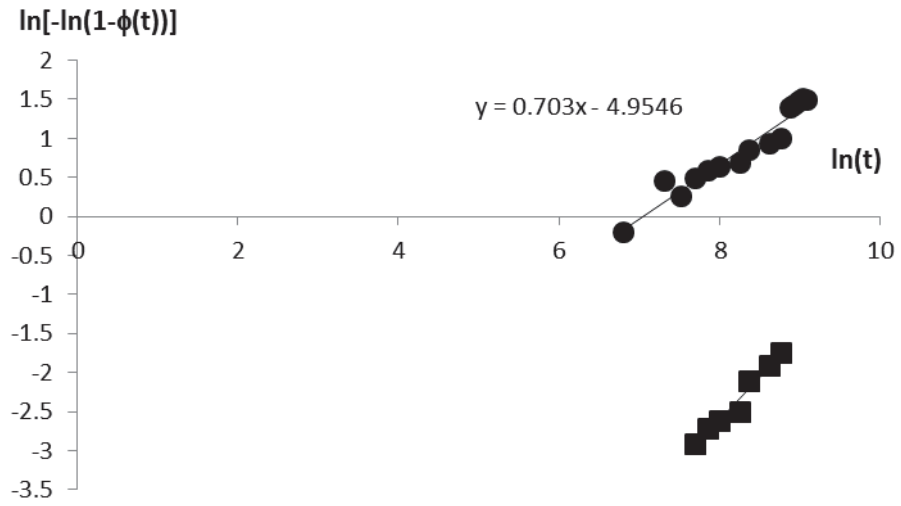


$n_{\text{Parallel}}$	1.05
$Z_{\text{Parallel}, S^{-n}}$	1.6E-4
$n_{\text{Series}}$	.88
$Z_{\text{Series}, S^{-n}}$	1.0E-3

### C.3. Iso-concentration SB copolymer in toluene Avrami fits from SAXS data

40 wt% - 30 second exposure

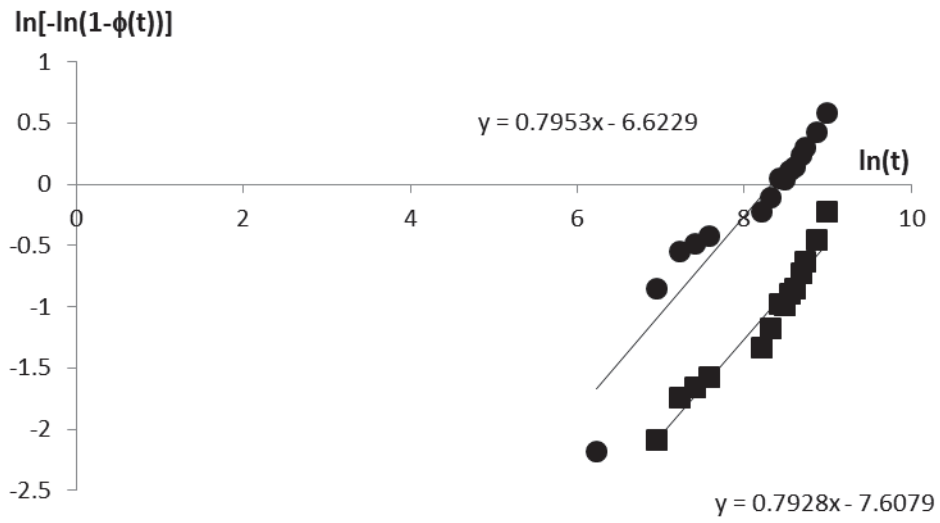
ln(t)	Parallel		Series	
	$\phi(t)$	$\ln[-\ln(1-\phi(t))]$	$\phi(t)$	$\ln[-\ln(1-\phi(t))]$
6.8024	0.0169	-4.072016048	0.5578	-0.203378948
7.3132	0.0496	-2.979153299	0.7928	0.453747404
7.5283	0.0353	-3.327273653	0.7284	0.264929963
7.7053	0.0526	-2.917412908	0.803	0.485366347
7.8555	0.0638	-2.719957374	0.8333	0.582919874
8.0064	0.0706	-2.614924855	0.8478	0.632683408
8.1374	0.1671	-1.698968147	0.9364	1.013506045
8.2532	0.0786	-2.502896961	0.8622	0.684212497
8.3779	0.1143	-2.10863008	0.9045	0.853873188
8.4446	0.1777	-1.631263368	0.9407	1.03850519
8.6216	0.1363	-1.920905666	0.9205	0.928915318
8.7718	0.1593	-1.751725665	0.9329	0.993774376
8.886	0.4313	-0.572052377	0.9823	1.395465898
8.9306	0.4577	-0.491017307	0.9841	1.421235404
8.9922	0.5117	-0.333055629	0.9872	1.471375857
9.036	0.5546	-0.212161515	0.9892	1.509822752
9.0848	0.5409	-0.25049981	0.9886	1.497613407



$n_{\text{Parallel}}$	1.1
$Z_{\text{Parallel}}, S^{-n}$	1.2E-5
$n_{\text{Series}}$	.703
$Z_{\text{Series}}, S^{-n}$	7.0E-3

45 wt% - 30 second exposure

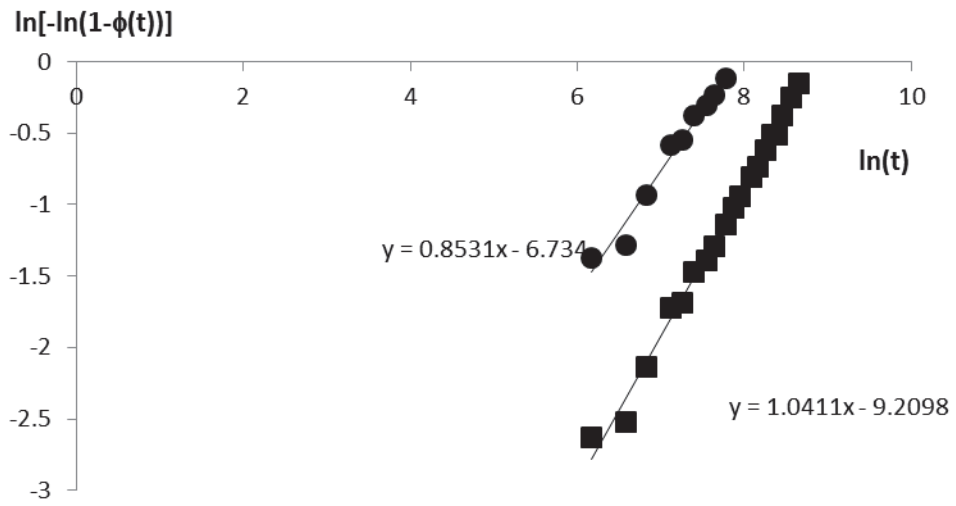
ln(t)	Parallel		Series	
	$\phi(t)$	$\ln[-\ln(1-\phi(t))]$	$\phi(t)$	$\ln[-\ln(1-\phi(t))]$
6.2344	0.0286		0.107	-2.178705305
6.9565	0.1161	-2.092565018	0.3482	-0.848515201
7.2298	0.1612	-1.738649079	0.4388	-0.548793026
7.4085	0.1737	-1.656308128	0.4611	-0.480959401
7.5756	0.1862	-1.579975942	0.482	-0.41874486
8.2107	0.2324	-1.32983296	0.552	-0.219471785
8.3187	0.264	-1.182258906	0.5935	-0.105254332
8.4163	0.3126	-0.981260447	0.6492	0.046356889
8.4805	0.3096	-0.992977696	0.646	0.037641647
8.5409	0.3363	-0.891764717	0.6734	0.11243341
8.6089	0.3484	-0.84774134	0.6851	0.144623827
8.6776	0.3838	-0.725244852	0.7171	0.233145195
8.7323	0.4114	-0.634967696	0.7398	0.29743641
8.8679	0.4709	-0.451524807	0.7836	0.425802155
8.9872	0.5511	-0.221994574	0.8332	0.582729368
9.09381	0.59119	-0.111474047	0.85474	0.657125371
9.19014	0.67508	0.117046847	0.89422	0.809339738
9.278	0.78371	0.426021661	0.93648	1.013941945
9.43348	0.94805	1.08430709	0.98671	1.463439211



$n_{\text{Parallel}}$	0.79
$Z_{\text{Parallel}}, S^{-n}$	5.0E-4
$n_{\text{Series}}$	.79
$Z_{\text{Series}}, S^{-n}$	1.3E-3

50 wt% - 30 second exposure

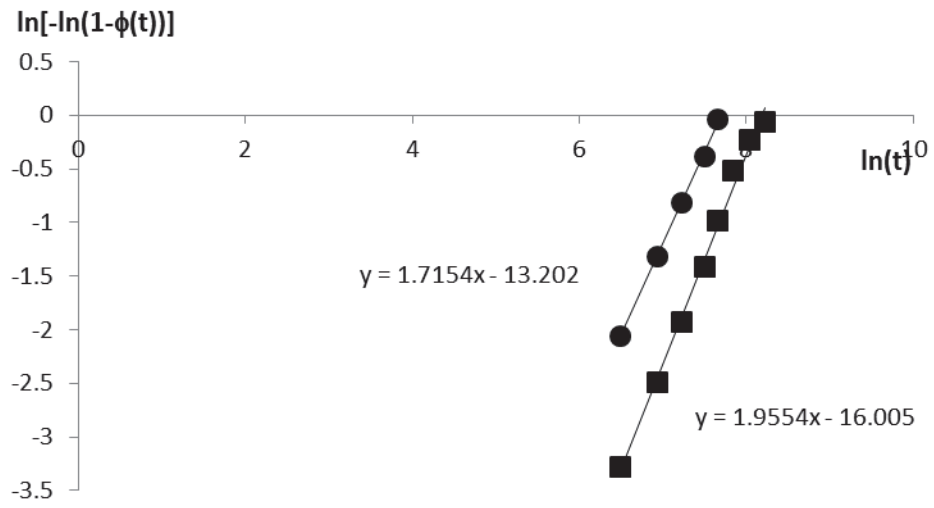
ln(t)	Parallel		Series	
	$\phi(t)$	$\ln[-\ln(1-\phi(t))]$	$\phi(t)$	$\ln[-\ln(1-\phi(t))]$
6.1738	0.0698	-2.626788154	0.2233	-1.375391778
6.5793	0.0773	-2.520431943	0.2431	-1.278370987
6.8352	0.1115	-2.134784317	0.325	-0.933940844
7.1148	0.1634	-1.723504889	0.4283	-0.581441443
7.2513	0.169	-1.686986393	0.4381	-0.550968039
7.3902	0.2055	-1.469695213	0.4979	-0.372607158
7.5443	0.2203	-1.390675229	0.5201	-0.309026434
7.6353	0.2405	-1.290442343	0.5484	-0.229375532
7.7832	0.2736	-1.140395636	0.5909	-0.112230448
7.8671	0.3015	-1.025011227	0.6234	-0.023839849
7.94449	0.32301	-0.941361886	0.64659	0.03933547
8.09255	0.36023	-0.80599925	0.68345	0.140000945
8.16337	0.38055	-0.736227711	0.702	0.191157437
8.26101	0.41719	-0.616387124	0.73297	0.277921717
8.32845	0.45245	-0.506996979	0.76011	0.355974286
8.39841	0.44964	-0.515532686	0.75803	0.349921143
8.45105	0.49514	-0.380563547	0.78995	0.444944955
8.56598	0.54046	-0.251643439	0.8185	0.534452449
8.64822	0.57507	-0.155673039	0.83844	0.600402615
8.7291	0.6591	0.073444149	0.8812	0.756087678
8.8349	0.74	0.298027669	0.9161	0.907390209
8.9385	0.8435	0.617748472	0.9539	1.123585598
8.9922	0.8919	0.799743696	0.9694	1.248687619



$n_{\text{Parallel}}$	1.0
$Z_{\text{Parallel}}, S^{-n}$	$1.2\text{E-}4$
$n_{\text{Series}}$	0.85
$Z_{\text{series}}, S^{-n}$	$1.1\text{E-}3$

55 wt% - 30 second exposure

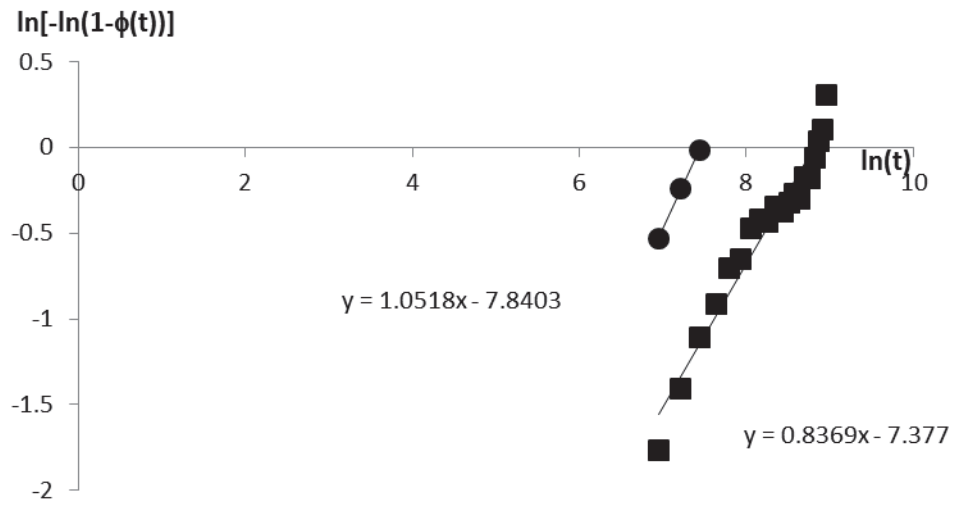
ln(t)	Parallel		Series	
	$\phi(t)$	$\ln[-\ln(1-\phi(t))]$	$\phi(t)$	$\ln[-\ln(1-\phi(t))]$
6.4922	0.0368	-3.284403846	0.1198	-2.0584203
6.9276	0.0797	-2.488118673	0.236	-1.312226088
7.2298	0.1352	-1.929470433	0.3579	-0.813989384
7.4955	0.2159	-1.413656571	0.4955	-0.379425939
7.6497	0.3111	-0.987186333	0.6169	-0.041261027
7.8438	0.4481	-0.520335092	0.7433	0.307376996
8.0359	0.5476	-0.231744106	0.8119	0.513390182
8.2215	0.6078	-0.066290393	0.8468	0.629079749
8.3428	0.6491	0.046116143	0.8684	0.706963376
8.4511	0.7156	0.229117067	0.8998	0.833006795
8.537	0.7431	0.306847036	0.9116	0.88642179
8.6995	0.8112	0.511093817	0.9387	1.027041216
8.8393	0.8871	0.77990393	0.9655	1.214385841
8.96188	0.91817	0.917520525	0.97562	1.312131188
9.07108	0.97595	1.315816843	0.99314	1.605839263



$n_{\text{Parallel}}$	1.96
$Z_{\text{Parallel}}, S^{-n}$	$1.12\text{E-}7$
$n_{\text{Series}}$	1.72
$Z_{\text{Series}}, S^{-n}$	$1.84\text{E-}6$

60 wt% - 30 second exposure

ln(t)	Parallel		Series	
	$\phi(t)$	$\ln[-\ln(1-\phi(t))]$	$\phi(t)$	$\ln[-\ln(1-\phi(t))]$
6.9565	0.1576	-1.763268508	0.4445	-0.531299952
7.2079	0.218	-1.402916924	0.5438	-0.242178799
7.4442	0.2806	-1.110793806	0.6252	-0.018832914
7.6353	0.3307	-0.912617759	0.6788	0.127146746
7.7956	0.391	-0.701374631	0.733	0.278117933
7.9338	0.4064	-0.65095304	0.7454	0.313493534
8.0552	0.4645	-0.470800047	0.7877	0.438000644
8.1634	0.4825	-0.417341667	0.7995	0.474422823
8.261	0.4772	-0.432963681	0.7961	0.463802335
8.35	0.5072	-0.345736426	0.8149	0.52287051
8.4316	0.498	-0.372324934	0.8093	0.504924354
8.50714	0.51541	-0.322353617	0.81979	0.538612214
8.57735	0.53315	-0.272140457	0.83006	0.572293613
8.64294	0.52352	-0.299297957	0.82454	0.554097583
8.7045	0.56798	-0.175194296	0.84902	0.636887848
8.76249	0.56641	-0.179551997	0.84819	0.633995642
8.8173	0.60883	-0.063347256	0.8694	0.710806615
8.86926	0.64659	0.039345656	0.88669	0.778236121
8.91865	0.66986	0.102766673	0.89668	0.819728444
8.96572	0.74309	0.306780662	0.92521	0.952861393
9.0107	0.7952	0.460904858	0.9432	1.053634811
9.1345	0.9719	1.273602285	0.9933	1.61048822



$n_{\text{Parallel}}$	1.05
$Z_{\text{Parallel}}, S^{-n}$	$3.9\text{E-}4$
$n_{\text{Series}}$	0.84
$Z_{\text{Series}}, S^{-n}$	$1.84\text{E-}6$